

© 2019 by Eric J. Meier. All rights reserved.



MOMENTUM-SPACE LATTICES FOR ULTRACOLD ATOMS

BY

ERIC J. MEIER

DISSERTATION

Submitted in partial fulfillment of the requirements  
for the degree of Doctor of Philosophy in Physics  
in the Graduate College of the  
University of Illinois at Urbana-Champaign, 2019

Urbana, Illinois

Doctoral Committee:

Professor Brian DeMarco, Chair  
Assistant Professor Bryce Gadway, Director of Research  
Professor Taylor L. Hughes  
Assistant Professor Seppe Kuehn

# Abstract

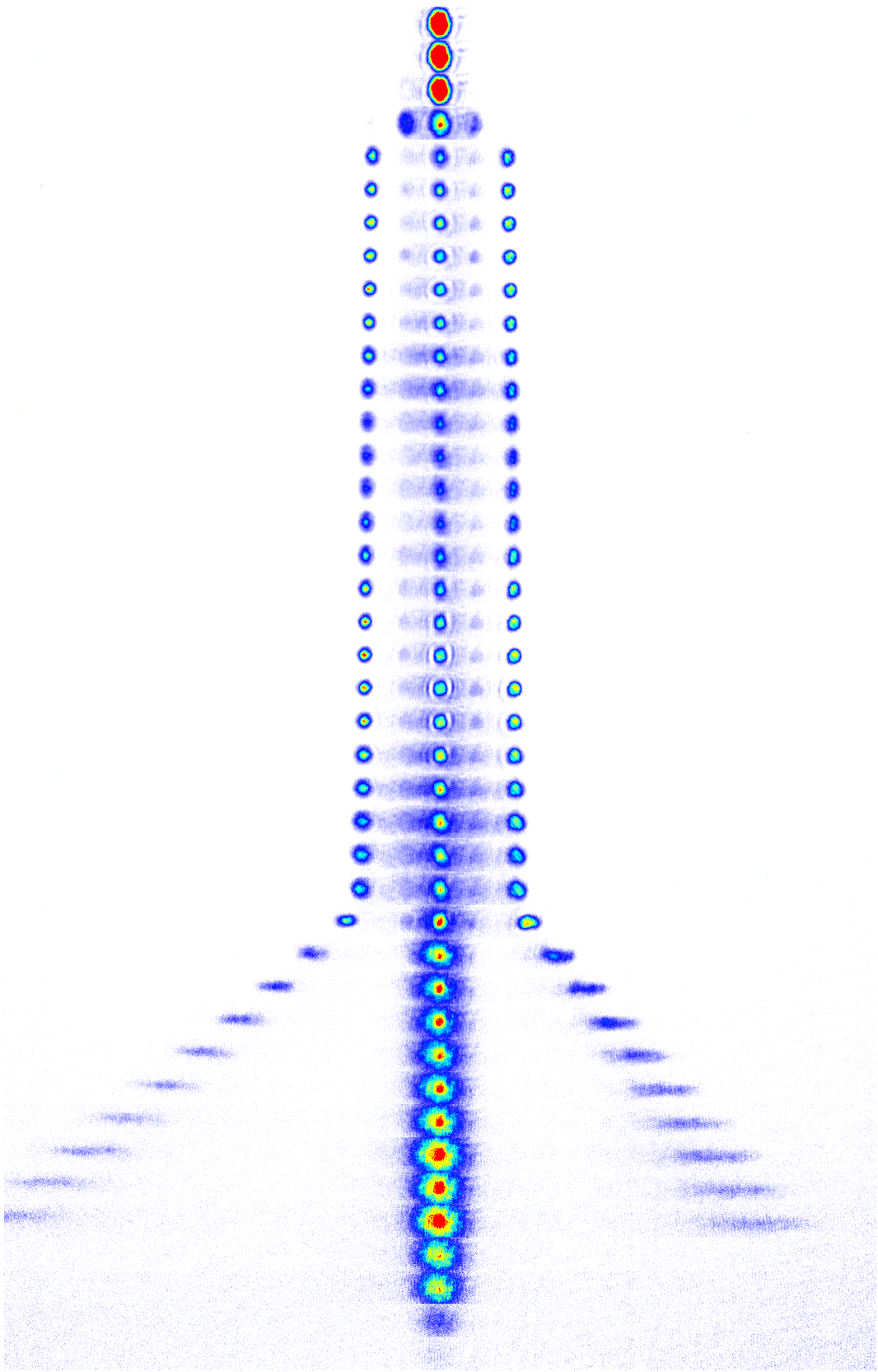
As the progress of science pushes the frontiers of studying nature to both the extremely large scale and the incredibly small scale, experiments can become increasingly difficult to perform. Therefore, a scale model experiment for these kinds of physics can be useful as long as it is relatively easy to access and control. This is the idea of quantum simulation, where one system exactly mimics another when they are subjected to equivalent physical scenarios. Topological systems, those with a property that is stabilized by their specific configuration, are often quite challenging to experimentally probe. Therefore, test bed systems have been widely and successfully applied to studying topology in an effort to advance the field, which promises enticing applications such as robust quantum technology.

Our particular scheme uses a novel type of “synthetic” dimension for atoms of a Bose–Einstein condensate, which we call a momentum-space lattice, to emulate one-dimensional lattice models. The idea of a synthetic dimension or synthetic lattices is a useful construct to describe how the particle dynamics can evolve in degrees of freedom that are not directly related to transport in real space. This can relate to population dynamics in an internal degree of freedom, such as spin, or, in our case, in the dynamics of free-particle-like atomic momentum states. We expose a Bose–Einstein condensate to two laser fields that are capable of driving transitions between different momentum states of the condensate atoms through a two-photon Bragg diffraction process. Neighboring states in the free-particle dispersion relation are characterized by a unique momenta and energy spacing such that we can independently control every aspect of their coupling.

In this thesis, we report on the design and construction of an apparatus for the production of  $^{87}\text{Rb}$  Bose–Einstein condensates as well as the partial construction of an apparatus for the

production of  $^{39}\text{K}$  Bose–Einstein condensates. We also discuss the experimental realization of, and theoretical background for, our momentum-space lattice. Using the momentum-space lattice, we perform experiments on not only topological systems, but also on driven artificial spins featuring chaotic dynamics, as well as faster-than-adiabatic quantum state control and preparation. Our measurements of topological systems are based in the 1D Su–Schrieffer–Heeger model, where we report on the direct observation of the localized, solitonic edge state created by the topology inherent in the system. Through the addition of exactly tunable tunneling disorder, we observe the destruction of the band topology due to disorder at a random-singlet transition. Furthermore, we drive a trivial system into a topological phase through the addition of disorder, observing a counter-intuitive phenomenon known as the topological Anderson insulator for the first time. We go on to report on our driven, tunable spin experiment, where we probe effective spin “squeezing” (in the absence of any entanglement in our noninteracting system), the out-of-time-ordered correlation function, and chaos. And finally, we use our momentum-space lattice to demonstrate a technique which allows a system to be transformed faster than the adiabatic limit with no diabatic transitions in a highly non-trivial regime.

Due to the versatility of the momentum-space lattice, the results detailed here have a broad impact. Our observations of topological phenomena in elementary and canonical 1D systems are some of the first experimental verifications of long-standing predictions. Further, our studies of the interplay between classical chaos and quantum systems may help shed light on this complex and rich problem. And from a more “applied science” perspective, our demonstrations of generalized counter-diabatic techniques are widely beneficial and applicable to many systems where adiabaticity is challenged.



*For Tina, Arty, and B-Boy*

*In memory of Ace*

# Acknowledgments

I sincerely thank Bryce Gadway for being a fantastic adviser. He has a great sense for experiments and intuition for physics. But what I am most grateful for is his dedication to treating his students with respect and dignity. Most advisers are good at physics but far fewer truly care for their students/employees. I additionally thank the rest of my committee—Brian DeMarco, Taylor L. Hughes, and Seppe Kuehn—for their helpful advice at my preliminary examination and general support throughout my graduate work.

I thank my Mom & Dad for showing me how to be an independent and creative thinker and for always making ‘home’ a place where I felt comfortable and happy. I thank my Grandpa Don, Grandma Betty, Grandpa Marvin, and Granny Joan for their love and support throughout my childhood. And I thank my brother and sister for teaching me how to share. I thank my oldest friends, Scott and Tyler, for distracting me from afar and coming to visit.

My chief pillars of support throughout my graduate school career have been my partner Kristina, my son Arthur, and my dogs Ace and Baron. I thank Kristina for helping me become a better person and for her love. She has always been my toughest critic and biggest advocate, keeping my ego at an optimal size. Further, I love spending time with her and she always knows when I need to be dragged out of the house to have some fun and unwind. Ace, who passed away in 2018, always greeted me at the door with a whine and a wagging tail when I got home. Arthur, who turned eight months old two days before my defense, simultaneously made the writing process more stressful by taking up my time and less stressful with his absurdly cute smile and giggle. I am grateful to Baron (my 110 lb. lap dog), who looked out for my mental health by making sure I took breaks from writing to play with him and take him on long walks.



Ace



Baron



Arthur

I thank all the Gadway Lab members over the years—Shraddha Agrawal, Fangzhao Alex An, Ritika Anandwade, Jackson Ang’ong’a, Cait Battle-McDonald, Michael Castle, Andrew Eberlein, Michael “Micheal” Highman, Samantha Lapp, Zejun Liu, Hannah Manetsch, Gilad Margalit, Kinfung “Frankie” Ngan, Yuhao Pan, Myeonggon Park, Sai Naga Manoj Paladugu, Derek “DJ” Ping, Hannah Ullberg, Zhenyu Wei, Garrett Williams, Lingfeng Yan, and Autumn Zender—for their contributions to this work. Specifically, I thank Alex (co-author on most of the work described here) for making me laugh and being such a great experimentalist. It was always fun building stuff or doing experiments because we work so well together. I thank Jackson Ang’ong’a for all his experimental assistance over the years and for making me laugh as well. I also thank Michael Highman for being constantly ready to drop anything and help me (possibly to a fault) as well as for making me laugh. I thank Alex An and Michael Highman for their careful reading of this thesis and helpful comments. I wish Sai and Shraddha luck as they take over Alex and my apparatus and drag it into a new era.

I further thank Brian DeMarco and his group members through the years William “Old Will” McGehee, David Chen, Carolyn Meldgin, Wenchao Xu, Philip Russ, William Morong, Laura Wadleigh, Pei-Wen Tsai, Nick Kowalski, and Nathan Fredman. We have a really friendly and collaborative environment which helps when you need to borrow some equipment or ask a question. I further thank Brian and the older members of the group, who have mostly passed on now, for teaching me a lot of the basics of working in cold atoms in my first few years as a graduate student.

Jerry Cook and Kelly Sturdyvin have my gratitude for tirelessly working to minimize

disruptions to our lab as the physics building was continuously renovated over the last five years. I thank Cheryl Sabas for putting through all my orders in a very timely manner and helping expedite my work. Thank you to Betsy Greifenkamp for helping with all my conference travel, reimbursements, and other administrative assistance. I thank the physics machine shop crew Jim Brownfield, Ernest Northen, and Lucas Osborne for their help on several projects which went into this work. And further gratitude to Jim for training me to use the student shop. I also thank Ralf Möller of the Rapid Prototyping Lab for working with me to make the 3D printed parts discussed here. I thank Debbie McCarter and Tommie Wininger for receiving, storing, and delivering all my packages. I thank the Graduate Office run by Lance Cooper and Wendy Wimmer for being so kind and approachable and making the department more welcoming.

I also acknowledge theory assistance for the work shown here from several sources. On the topological wires Taylor L. Hughes and Ian Mondragon-Shem were indispensable and we thank Smitha Vishveshwara for helpful discussions. I also thank Pietro Massignan and his group members Alexandre Dauphin and Maria Maffei for their contributions to the disordered topological wires project. Finally I thank Dries Sels and Kinfung “Frankie” Ngan for their work on the counter-diabatic driving experiment.

This material is based upon work supported by the National Science Foundation under Grant No. PHY1707731 and by the Air Force Office of Scientific Research under Grant No. FA9550-18-1-0082.

# Table of Contents

<b>List of Figures</b> . . . . .	<b>xii</b>
<b>Chapter 1: Introduction</b> . . . . .	<b>1</b>
1.1 Topology . . . . .	4
1.2 The Su–Schrieffer–Heeger Model . . . . .	8
1.2.1 SSH Band Structure and Edge States . . . . .	9
1.2.2 Discussion . . . . .	16
1.3 Outline . . . . .	18
<b>Chapter 2: The Momentum Space Lattice</b> . . . . .	<b>19</b>
2.1 Mathematical Basis . . . . .	20
2.2 Tunability . . . . .	24
2.3 Limitations . . . . .	25
2.4 Experiment Types . . . . .	27
2.5 Experimental Demonstrations . . . . .	28
2.5.1 Continuous-Time Quantum Walk . . . . .	28
2.5.2 Bloch Oscillations . . . . .	30
2.5.3 Phase Reversal . . . . .	32
2.6 Extensions to Higher Dimensions . . . . .	33
2.7 Interactions . . . . .	35
<b>Chapter 3: Methods</b> . . . . .	<b>41</b>
3.1 Apparatus Overview . . . . .	42
3.1.1 The Vacuum Chamber . . . . .	42
3.1.2 Atom Source . . . . .	45
3.1.3 Hardware, Software, and Control Mechanisms . . . . .	46
3.1.4 Momentum-Space Lattice Creation . . . . .	51
3.2 $^{87}\text{Rb}$ BEC Creation . . . . .	53
3.2.1 The Magneto-Optical Trap . . . . .	55
3.2.2 Further Cooling and Optical Pumping . . . . .	62
3.2.3 The Optical Dipole Trap and Evaporative Cooling . . . . .	64
3.2.4 Imaging . . . . .	67
3.3 $^{39}\text{K}$ BEC Creation . . . . .	69
3.3.1 Feshbach Resonance . . . . .	71
3.3.2 The Magneto-Optical Trap . . . . .	72
3.3.3 Magnetic Field Upgrades . . . . .	75

3.3.4	Gray Molasses . . . . .	86
3.4	Performing an Experiment . . . . .	87
3.4.1	Arbitrary Waveforms . . . . .	88
3.4.2	Data Collection and Processing . . . . .	92
<b>Chapter 4:</b>	<b>Clean Topological Wires . . . . .</b>	<b>97</b>
4.1	Introduction . . . . .	97
4.2	Results . . . . .	99
4.2.1	Single-Site Injection . . . . .	99
4.2.2	Phase-Sensitive Injection . . . . .	102
4.2.3	Adiabatic Preparation . . . . .	105
4.3	Discussion . . . . .	107
<b>Chapter 5:</b>	<b>Disordered Topological Wires . . . . .</b>	<b>109</b>
5.1	Introduction . . . . .	109
5.2	Results . . . . .	112
5.2.1	Topological to Trivial Transition . . . . .	112
5.2.2	Observation of the Topological Anderson Insulator . . . . .	115
5.2.3	Disordered Topological Charge Pumping . . . . .	119
5.3	Discussion . . . . .	122
<b>Chapter 6:</b>	<b>Studying Chaos with a Synthetic Spin . . . . .</b>	<b>125</b>
6.1	Introduction . . . . .	125
6.2	The Kicked-Top Model . . . . .	127
6.2.1	The Momentum-Space Lattice as a Synthetic Spin . . . . .	128
6.2.2	Linear Spin Operators: Rotations . . . . .	129
6.2.3	State Preparation . . . . .	131
6.2.4	State Measurement . . . . .	132
6.2.5	Implementing the Nonlinear Kick Operation . . . . .	133
6.3	Results . . . . .	134
6.3.1	Nonlinear Dynamics of the Effective Spin . . . . .	134
6.3.2	Chaotic Behavior in the Kicked-Top Model . . . . .	138
6.4	Discussion . . . . .	141
<b>Chapter 7:</b>	<b>Counter-Diabatic Driving . . . . .</b>	<b>143</b>
7.1	Introduction . . . . .	143
7.2	Results . . . . .	146
7.2.1	Lattice Tilt Inversion . . . . .	148
7.2.2	Preparing the Eigenstates of a 1D Square Well . . . . .	152
7.3	Discussion . . . . .	159
<b>Appendix A:</b>	<b>Custom Lab Hardware and Software . . . . .</b>	<b>161</b>
A.1	Analog Isolation Circuit . . . . .	161
A.2	Laser Offset Locking Scheme . . . . .	163
A.3	Andor Neo Camera Program . . . . .	166

A.4	Magnetic Field Estimation . . . . .	172
A.4.1	Feshbach Coils . . . . .	173
A.4.2	Square Coil Formulae . . . . .	174
<b>Appendix B:</b>	<b>Simulation Techniques . . . . .</b>	<b>177</b>
B.1	Ideal Approximation Simulations . . . . .	177
B.2	Non-Approximated Simulations . . . . .	181
B.3	Simulations with Interactions . . . . .	184
B.4	Python Simulations . . . . .	186
B.4.1	QuTiP . . . . .	187
B.4.2	QuSpin . . . . .	189
B.5	Corrections for Time Dependent Lattices . . . . .	191
<b>References</b>	<b>. . . . .</b>	<b>197</b>
<b>Index</b>	<b>. . . . .</b>	<b>209</b>

# List of Figures

1.1	The Möbius strip . . . . .	5
1.2	The SSH model of <i>trans</i> -polyacetylene . . . . .	9
1.3	Band structure of the SSH model without an edge . . . . .	13
1.4	Edge states in the SSH model . . . . .	15
2.1	Introduction to the momentum-space lattice . . . . .	20
2.2	Tuning parameters in the momentum-space lattice . . . . .	25
2.3	Quantum walk in momentum space . . . . .	29
2.4	Bloch oscillations in momentum space . . . . .	31
2.5	Reversal of dynamics through temporal switching of the tunneling phase . . . . .	33
2.6	The Bogoliubov picture . . . . .	37
2.7	Interaction shifts of Bragg tunneling resonances . . . . .	38
3.1	Schematic of the vacuum chamber . . . . .	43
3.2	Optical layout used to create the momentum space lattice . . . . .	52
3.3	Level diagram of relevant transitions for the $^{87}\text{Rb}$ $D_2$ line . . . . .	57
3.4	The 2D MOT . . . . .	59
3.5	The 3D MOT . . . . .	61
3.6	Beam layout for the science cell . . . . .	62
3.7	Diagram of $^{87}\text{Rb}$ optical pumping . . . . .	63
3.8	Images at different points in the cooling and evaporating sequence . . . . .	64
3.9	“Site”-resolved absorption imaging . . . . .	68
3.10	Feshbach resonance mechanism . . . . .	72
3.11	Level diagram of relevant transitions for the $^{39}\text{K}$ $D_2$ and $D_1$ lines . . . . .	73
3.12	Upgraded magnetic field configuration for the 2D MOT . . . . .	76
3.13	Magnetic field produced by the 2D MOT coils . . . . .	78
3.14	Science cell shimming field configuration . . . . .	80
3.15	3D MOT magnetic field configuration . . . . .	82
3.16	Feshbach coil holder . . . . .	83
3.17	Complete science-side magnetic field configuration . . . . .	85
3.18	Fourier spectrum of example arbitrary waveform . . . . .	90
3.19	Calculation of optical depth from three absorption images . . . . .	94
4.1	The SSH model revisited . . . . .	98
4.2	Nonequilibrium quench dynamics in the SSH model . . . . .	100
4.3	Phase-sensitive injection into the SSH model edge state . . . . .	102
4.4	Adiabatic preparation of the topological soliton state in the SSH model . . . . .	106

5.1	Synthetic chiral symmetric wires engineered with atomic momentum states . . . . .	111
5.2	Disorder-driven transition from topological to trivial wires . . . . .	113
5.3	Observation of the topological Anderson insulator phase . . . . .	116
5.4	Probing the topological Anderson insulating phase in BDI class wires . . . . .	119
5.5	Breaking a topological charge pump with tunneling disorder . . . . .	121
5.6	Numerical simulation hinting at a possible interaction-induced topological phase transition . . . . .	123
6.1	Experimental scheme for realizing a synthetic spin . . . . .	127
6.2	Demonstrations of linear rotations . . . . .	129
6.3	State preparation and measurement . . . . .	132
6.4	Squeezing of the artificial spin . . . . .	135
6.5	Out-of-time-ordered correlation function . . . . .	137
6.6	Chaotic behavior in the kicked-top model . . . . .	139
7.1	The counter-diabatic server . . . . .	144
7.2	Enhancement of population transfer by CD driving . . . . .	150
7.3	Preparing the eigenstates of an $L$ -site lattice with counter-diabatic driving . . . . .	153
7.4	Testing the phase structure of the counter-diabatically prepared eigenstates . . . . .	156
7.5	Evidence for dressed states of the lattice with CD driving . . . . .	158
A.1	Circuit diagrams for the analog isolator . . . . .	162
A.2	Block diagram of electronics for the $^{87}\text{Rb}$ offset lock . . . . .	164
A.3	Dimensional layout for a square coil . . . . .	175
B.1	Population dynamics for example ideal simulation . . . . .	180
B.2	Population dynamics for example full simulation . . . . .	183
B.3	Population dynamics for example interacting ideal simulation . . . . .	185
B.4	Corrections for time dependent lattices . . . . .	193



# Chapter 1

## Introduction

I love working on puzzles—jigsaw puzzles, mechanical puzzles, word puzzles<sup>1</sup>—any kind of puzzle really. I also love to make things, both touchable and untouchable. In fact, some of my greatest moments of satisfaction have been when I finished making something well. This is to say that my personal motivation for performing this research is that I found it to be *fun*, because most of the time I was doing one of my favorite activities (please note that writing was not listed among these). My decision to start as one of the first two graduate students in the newly established Gadway Lab was based almost entirely on my desire to build something from nothing, and a new lab is a great place to do that. Further, I am fascinated with atoms and it is hard to find another type of experimental physics lab where the research is cooler than a microkelvin.

On the other hand, the scientific motivations for our specific works are varied because the works themselves are varied, and that is the first point I want to make about our system. Based on a new technique using laser-coupled atomic momentum states, our apparatus is a test bed for other physics. Most of our efforts in the laboratory are put toward building and maintaining our apparatus and yet the physics that we study has little to do with the fact that we are even using atoms. This is made possible, in the words of William Morong of the Brian DeMarco lab, “through either a remarkable accident or powerful display of the universality of physical law” where one system can completely mimic or emulate another if they are governed by the same Hamiltonian. This idea is often called analog “quantum simulation” as first proposed by Richard Feynman decades ago [1]. At first glance this might seem unnecessary, but some systems can be incredibly difficult to work with and explore experimentally, whereas other systems can be very well controlled and easy to measure. Therefore, if one wants to probe certain kinds of subtle physical phenomena, it may be

---

<sup>1</sup>My personal best for the New York Times Saturday crossword is 27 minutes and 4 seconds set on Jan. 26, 2019.

more tractable to emulate the physics of interest in a well-controlled test bed system. Cold atom platforms are one of the most prominent examples of this kind of approach. While not necessarily easy to work with, they are extremely well controlled and therefore lend themselves naturally to realizing physics not readily found in nature. I do not wish to imply that cold atom simulators are superior to the systems they seek to emulate, but rather that a symbiotic relationship exists between the two. For example, if a quantum computer is ever to be made small enough to fit in one's pocket, it will probably not be based on cold atom architecture. Our contribution with cold atom emulation then is to help test certain physics with the goal of advancing the interdisciplinary field as a whole.

Over the past several years we have used our cold atom system to mimic primarily condensed matter phenomena, making some observations that had never been made in their parent systems and lending experimental credence to long-established but untested theories. Namely, we observed topological edge states and further measured disorder-driven topological transitions in one-dimensional (1D) topological wires. We also emulated a tunable, driven spin that displayed quantum signatures of chaos. And finally, we demonstrated a general technique for deforming a Hamiltonian faster than the adiabatic limit without generating any diabatic transitions. These different experiments have vastly different scientific motivations, however our exploration of topological band structures represents the main focus of this thesis.

One of the simplest systems giving rise to a topological band structure is the dimerized lattice described by the Su–Schrieffer–Heeger (SSH) model [2]. The band structure of a material is a plot of the energies of the eigenstates with respect to their crystal momentum (a quantity that takes the place of momentum for the states in the crystal structure). There are  $N \sim 10^{23}$  eigenstates in a crystal with  $N$  lattice sites, however, so the discrete plot of eigenenergies is effectively a continuum of states, referred to as bands. The SSH model gives rise to gapped energy bands characterized by a topological invariant known as the winding number, and additionally hosts a topological mid-gap eigenstate that is localized to the boundary of the open 1D system (see Sec. 1.2 and Chaps. 4 and 5). Even with this being one of the simplest 1D topological models, it is still rather difficult to probe in most cold atom experiments, which are often based on systems of neutral atoms subjected to

real-space optical lattice potentials formed from the interference of counterpropagating laser beams. In such real-space schemes, band structures can be naturally realized through the hybridization of energy levels at the sites of the lattice due to quantum tunneling. This approach has its selling points: it is free of disorder and can be controlled in some fashion by the parameters of the applied laser field. However, the natural homogeneity in real-space systems can also be a limitation in the context of studying topological models and related phenomena. Specifically, the parameters of the optical lattice and the related tight-binding Hamiltonian cannot easily be tuned on an individual, site-by-site basis, as they are derived from global laser fields. Additionally, the topological boundary states appearing in systems with sharp open boundary conditions can be hard to probe in real-space experiments, since the boundaries of such systems are typically derived from smoothly varying global trapping potentials.

In an effort to gain more/different controls over system parameters, many alternatives to real-space optical lattices have been developed, and not all of them are in the framework of cold atoms. Eigenmodes of mechanical oscillators (using fidget spinners [3] and phonons [4]), photonic waveguides [5–9], and microwave circuits [10] are a few examples that still utilize real space as one of their dimensions. However, some advantages can be gained by abandoning real space altogether and instead using states *internal* to the particles being considered. Any set of states that is not real-space has been given the name “synthetic,” and I will adopt that terminology in this thesis as well. Examples of synthetic lattices include atomic internal states [11, 12] and atomic momentum state lattices, which are the basis of this work.

Our specific choice of atomic momentum states for our Hamiltonian engineering experiments is motivated by the level of control that is naturally present in this system. As discussed in detail in Chap. 2 this scheme provides us with the ability to tune almost any system parameter of a 1D (or higher) tight-binding model in a site-dependent and time-dependent way, along with naturally defining edges to our system. These controls, coupled with the fact that we have atoms hosting inherent interactions, give us some advantages over the systems listed above. But, there are specific models and measurements that the other systems are better for as well, thus creating a veritable menagerie of experimental platforms capable of exploring new physical phenomena. Given some of the strengths of our

approach based on atomic momentum states, much of my research has focused on realizations of topological lattice systems with relevance to condensed matter physics. As such, I begin in earnest with a primer on this topic.

## 1.1 Topology

Topology is a mathematical concept which encapsulates the phenomenon that some properties of specific geometric shapes are invariant under continuous changes to that shape. Perhaps the most famous example of this idea is the Möbius strip as shown in Fig. 1.1. This interesting shape has fascinated humankind since at least the Roman Empire [13] but was first mathematically described in the modern era by August Ferdinand Möbius and, independently, Johann Benedict Listing in 1858. One can imagine creating a Möbius strip by taking a long slip of paper and bringing the two ends together to form a band. Before connecting the two ends however, one end is turned such that the twisted loop shown in Fig. 1.1 is produced.

As the blue and red lines in Fig. 1.1 illustrate, once in the Möbius strip configuration the shape has only one side and only one edge. It turns out that no matter what is done to this shape—spinning it, twisting it, crumpling it up into a ball—it will always have only one side unless a discontinuous change is made (like cutting). If the strip were cut back into a sheet of paper, it would make the sudden transformation from a one-sided object back to a two-sided object. We can therefore refer to the number of sides of the paper as its topological index, a number which tells us that some feature of the shape is robust to continuous deformations. If the topological index of the strip of paper is 1 we know it is in the Möbius configuration, and if it is 2 we know it must have been cut. There are many examples of topology similar to the Möbius strip. Another common one, which is popular among physicists, uses doughy foods—a loaf of bread, a donut, and a pretzel, say—with a topological index equal to the number of holes in the food. Each item starts out topologically identical as a ball of dough with no holes. The loaf of bread stays that way, the donut is blessed with one hole, and a classic pretzel is given three. These three forms of dough are topologically distinct because there is no way to transform one into the other without cutting or drilling. On the other

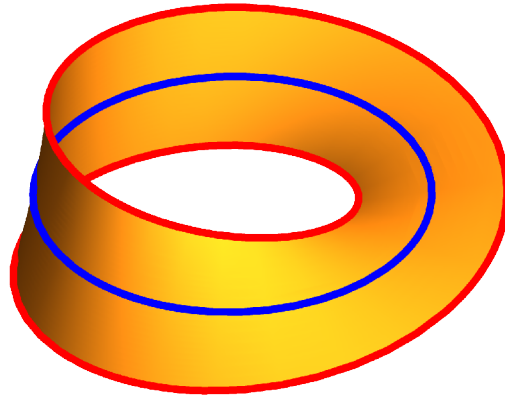


Figure 1.1: The Möbius strip is an example of a topologically nontrivial shape. The blue line wraps endlessly upon itself without ever going over an edge, demonstrating that the strip has only one side even though it appears to have two. Further, there is only one red line demarcating the edge of the band, showing that it has only one edge whereas it appears to have two. If cut perpendicularly to the blue line, the band goes through a topological phase transition where its one side and edge become two sides and edges.

hand, the coffee mug that you may be dipping your one-hole donut into happens to have the same topology as said donut. The coffee mug has only one hole (the handle) and so therefore its shape can be continuously deformed into a donut.

While these topological properties were fascinating mathematicians for decades, the concept had not yet been adopted into mainstream physics. That is, until the 1980s when it was realized that topology could be used to explain the astounding quantization of the integer quantum Hall effect [14]. The integer quantum Hall effect manifests itself as a perfectly (to parts-per-billion levels) quantized conductance in a two-dimensional electronic system subjected to a uniform magnetic field [15]. As it turns out, this quantized conductance even persists in the presence of disorder and across different samples owing to the fact that it is a topologically protected effect. Just like in the previous examples where the geometries can be twisted and bent and crumpled without affecting the topology, the quantized Hall conductance is, in a way, a topologically protected quantity. For a while, it was believed that topological effects in materials only became relevant at high external fields, but with the discovery of topological insulators [16–19] it was shown that topology is actually an intrinsic property in a wide range of systems and materials causing all sorts of effects with potentially useful applications. Even more recently, a technique based on the underlying symmetry of a material has been developed to predict whether it will exhibit topological properties or

not [20, 21].

Another important point to be made that is relevant to this work in particular is that topology can be relatively hard to detect. Most of the intrinsic properties of solids can be uncovered by performing a “local” measurement, a probe over just part of the system. For example, the color, specific heat, melting point, density, etc. of a piece of copper can be determined by measuring just one small part of the whole system. However, since the topology of a sample stems from its geometry—in particular the global geometry of its eigenstates—a local probe will not reveal it. Consider taking a small bite out of a particularly large donut for example. If one were blindfolded and being fed the donut, one would have no way of knowing there was a hole in the middle. If the blindfold were removed however, a more global measurement could be made with the eyes and the topology could be detected. A similar consideration appeared in the Möbius strip example: if an ant were to crawl along the strip it would have no way of knowing that there was only one side to the strip until it crawled all the way around. For this reason detecting topology usually requires some type of global or at least semi-global measurement and there are significant theoretical and experimental efforts focused on determining new, and more experimentally viable, ways of detecting topology. For example, our study of disorder-induced topological transitions in Chap. 5 was delayed and initially thought to be impractical because we did not have a convenient way to directly measure band topology until a new observable was formulated [8].

In the context of physics, a system is dubbed topological when it has some property that is both created and protected by its underlying structure. In lattice systems, the band topology will thus relate to how exactly the lattice is constituted, in terms of the symmetries of the Hamiltonian that result from the various intersite coupling terms (tunneling amplitudes and phases) as well as the landscape of site energies. In its most interesting form, this can relate to the ground state properties of a many-body system, whereas here we will restrict to considering the topology of single-particle band structures. The topological properties of a condensed matter system can often times be revealed by looking at its band structure. The band structure gives one a sense of what properties a certain material might have: whether it be insulating, conducting, or a semi-conductor for example. But it may also reveal underlying topological properties of the material.

The most common method of detecting the topology of a system is by computing a number corresponding to some property of the wavefunction in these energy bands. In some cases it is the number of times a wavefunction’s phase “winds” by  $2\pi$  across the band as a function of crystal momentum. These winding numbers are, in general, related to the famous Berry phase [22, 23] with a simple mapping from the phase acquired in a two-band model upon returning to an initial state to the geometric phase acquired by closed paths on the Bloch sphere of a spin-1/2 system. They are computed differently for 2D (Chern number) and 1D (Zak phase [24]) systems, but all give a measure of the topology of a specific band. These observables are usually tricky to measure directly in experiment. In the 2D case there has been progress in condensed matter systems using graphene layers [25, 26] and in cold atom experiments in real-space optical lattices [27, 28]. In 1D, the first direct measurement of the Zak phase was performed in 2013 in a cold atom platform [29]. But even in these systems where higher levels of control and direct observability can be attained, it is still rare for the measurement of a Berry phase to be possible. This difficulty spurred the formulation of a new measure of the topological index for 1D systems based on the dynamical evolution of a particle starting in a superposition of many eigenstates called the chiral displacement [30], which was first measured in photonic systems [8]. Discussed in more detail in Chap. 5 (where we used it to measure a transition to a topological Anderson insulator phase) this observable allows one to measure the topological index through the nonequilibrium dynamics from easily prepared initial conditions, as opposed to a more complex interferometric measurement based on individually prepared eigenstates [29]. Moreover, this chiral displacement remains a valid observable for topology in the presence of disorder, even when the concept of energy bands breaks down.

Many topological band structures also have “edge states” that can be easier to observe. For example, the 2D electronic system that hosts the integer quantum Hall effect has a gapped band structure. However, between the bands (and at the edges of the system) are states which carry a quantized charge even in the regime that would normally be insulating [14, 15]. These states are referred to as edge states because they often manifest at the boundaries of their system and are a common property of topological systems. In the 2D quantum Hall effect, the edge state is a 1D wavefunction which exists around the edge of

the system and in the 1D SSH model the edge state is a 0D localized state at the end of the chain [2]. As von Klitzing *et al.* can attest, the robust conductance allowed by these states can be observed without measuring (or even knowing about the existence of) the topology of the system. Therefore, edge effects provide an indirect window into the topology of a material and have been utilized in many systems [8, 29, 31], including our own [32, 33].

The fact that many of the first observations of these basic topological phenomena have been in artificial quantum materials based on atoms or photons, for example, shows how powerful these techniques are [34]. Many other specific models and phenomena have been observed not only with cold atom platforms as summarized nicely in the recent review by Cooper *et al.* [35], but also with photonic systems [9]. These techniques benefit not only from their generally high levels of microscopic control but also from their direct access to microscopic dynamics and the properties of individual eigenstates. This makes measurements of edge states and winding numbers possible in these systems.

The motivation for studying topology is twofold. First, one of the main goals of science is to understand nature and  $\approx 27\%$  [21] of the materials around us have topological properties that we were unaware of just a few years ago. Most of these materials have not been studied in depth but may hold important keys to the development of our understanding of nature. Therefore, from a fundamental science perspective, the study of topology continues to develop, shedding light on the unknown. From an applications-driven perspective, one can imagine that being able to protect a certain useful property of a system against disorder and sample-to-sample variations is a very enticing possibility for manufacturing and the development of small-scale future technologies. Indeed, this robustness to disorder has already earned topology a place in the International System of Units and even provides some benchmarking measurements of fundamental quantities (like the fine structure constant) based on materials systems.

## 1.2 The Su–Schrieffer–Heeger Model

Since the context of this work is strongly connected to the SSH model, we present a brief discussion on its properties to preface the main experimental results outlined in Chaps. 4 and 5.

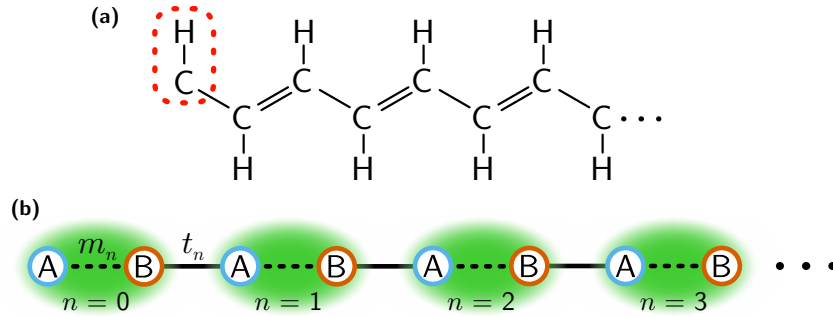


Figure 1.2: The SSH model of *trans*-polyacetylene. **(a)** Chemical structure of *trans*-polyacetylene. The ‘C’s represent carbon atoms and the ‘H’s represent hydrogen atoms. An edge to the system such as the one shown encircled by the red dashed line can result in the presence of a localized edge state in the system. The single lines are single bonds and the double lines represent double bonds. **(b)** The SSH, tight-binding model for *trans*-polyacetylene. The sites A and B represent two carbon atoms in the lattice which are singly bonded to form a unit cell as indicated by the green oval. The unit cells are indexed by  $n$ . The intra-cell tunneling on cell  $n$  is given by  $m_n$  and the inter-cell tunneling between cells  $n \rightarrow n + 1$  by  $t_n$ .

The SSH model was originally formulated to help explain the unusually high conductivity of the polymer *trans*-polyacetylene [see Fig. 1.2(a)] that arises when it is doped [2, 36–38]. The explanation for this at the time was given in terms of a solitonic electronic state that is localized to a defect in the crystal, gaining mobility when the crystal is doped [2]. But, it was eventually realized that this was not the whole picture as the solitonic state in this model is also a topologically protected boundary mode between two distinct topological phases [36, 39], and indeed the energy bands of the system have a non-zero winding number. It is now classified as a chiral orthogonal (BDI) class topological insulator, possessing chiral symmetry. As with all members of the BDI class, the SSH model also exhibits particle-hole and time-reversal symmetry. With the addition of alternating signs of the tunneling, the system is classified as a chiral unitary (AIII) topological insulator and the time-reversal and particle-hole symmetries are broken.

### 1.2.1 SSH Band Structure and Edge States

The actual SSH model consists of a tight-binding approximation to the molecular structure as shown in Fig. 1.2(b). The unit cells, indexed by  $n$ , are defined by pairs of carbon atoms which act as the sites of the lattice and the two sites in a single unit cell are given labels A and B. In the chemical structure the bonds between carbon atoms are alternating single

and double bonds and this is reflected in the tight-binding model as an alternating tunneling strength. We define the inter-cell and intra-cell tunneling terms as

$$t_n = t \quad (1.1)$$

$$m_n = mt, \quad (1.2)$$

where  $t$  corresponds to the characteristic inter-cell tunneling energy of the lattice and  $m$  the ratio between the intra- and inter-cell tunneling energies. The model additionally fixes all site energies to zero and we subsequently define the following Hamiltonian.

$$H = t \sum_n \left[ mc_n^\dagger \sigma_1 c_n + \left( c_{n+1}^\dagger \frac{(\sigma_1 - i\sigma_2)}{2} c_n + \text{H.c.} \right) \right], \quad (1.3)$$

where  $c_n^\dagger = (c_{n,A}^\dagger, c_{n,B}^\dagger)$  with  $c_{n,A}^{(\dagger)}$  and  $c_{n,B}^{(\dagger)}$  representing the annihilation (creation) operators for a particle at site A or B of unit cell  $n$ , and  $\sigma_{\{1,2,3\}}$  are the Pauli matrices. If we rewrite this Hamiltonian in terms of the single-site creation and annihilation operators  $(c_{n,A}^\dagger, c_{n,B}^\dagger)$  we get something a little easier to look at:

$$H = t \sum_n \left[ mc_{n,B}^\dagger c_{n,A} + c_{n+1,A}^\dagger c_{n,B} + \text{H.c.} \right]. \quad (1.4)$$

To find the band structure of this Hamiltonian we first define the discrete Fourier transform of our operators into reciprocal space,  $q$ , as

$$c_{q,j} = \frac{1}{\sqrt{N}} \sum_n c_{n,j} e^{iq(an+d_j)}, \quad (1.5)$$

$$c_{n,j} = \frac{1}{\sqrt{N}} \sum_q c_{q,j} e^{-iq(an+d_j)}, \quad (1.6)$$

where  $j$  is a placeholder for the A or B site and  $d_{\{A,B\}}$  represents the position in the unit cell of the A or B site with the condition  $d_B - d_A = a/2$  with  $a$  the lattice spacing. We can

now rewrite our term in the real-space Hamiltonian as:

$$\sum_n c_{n,B}^\dagger c_{n,A} = \frac{1}{N} \sum_n \sum_q \sum_{q'} c_{q,B}^\dagger e^{iq(an+d_B)} c_{q',A} e^{-iq'(an+d_A)} \quad (1.7)$$

$$= \frac{1}{N} \sum_n \sum_q \sum_{q'} c_{q,B}^\dagger c_{q',A} e^{i(q-q')an} e^{i(qd_B - q'd_A)} \quad (1.8)$$

$$= \sum_q \sum_{q'} c_{q,B}^\dagger c_{q',A} \left[ \frac{1}{N} \sum_n e^{i(q-q')an} \right] e^{i(qd_B - q'd_A)}. \quad (1.9)$$

Now replacing the quantity in brackets with the Kronecker delta we get

$$\sum_n c_{n,B}^\dagger c_{n,A} = \sum_q \sum_{q'} c_{q,B}^\dagger c_{q',A} [\delta_{q,q'}] e^{i(qd_B - q'd_A)} \quad (1.10)$$

$$= \sum_q c_{q,B}^\dagger c_{q,A} e^{iq(d_B - d_A)} \quad (1.11)$$

$$= \sum_q c_{q,B}^\dagger c_{q,A} e^{iqa/2}. \quad (1.12)$$

And equivalently for the form of the other term in the Hamiltonian, we have

$$\sum_n c_{n+1,A}^\dagger c_{n,B} = \sum_q c_{q,A}^\dagger c_{q,B} e^{iqa/2}. \quad (1.13)$$

Now rewriting the Hamiltonian shown in Eq. 1.4 by substituting in the  $q$ -space forms for the terms as found above and explicitly including the Hermitian conjugates we arrive at

$$H = t \sum_q \left[ m e^{iqa/2} c_{q,B}^\dagger c_{q,A} + e^{iqa/2} c_{q,A}^\dagger c_{q,B} + m e^{-iqa/2} c_{q,A}^\dagger c_{q,B} + e^{-iqa/2} c_{q,B}^\dagger c_{q,A} \right] \quad (1.14)$$

$$= t \sum_q \left[ (m e^{iqa/2} + e^{-iqa/2}) c_{q,B}^\dagger c_{q,A} + (m e^{-iqa/2} + e^{iqa/2}) c_{q,A}^\dagger c_{q,B} \right] \quad (1.15)$$

$$= t \sum_q \begin{pmatrix} c_{q,A}^\dagger & c_{q,B}^\dagger \end{pmatrix} \begin{pmatrix} 0 & m + e^{-iqa} \\ m + e^{iqa} & 0 \end{pmatrix} \begin{pmatrix} c_{q,A} \\ c_{q,B} \end{pmatrix}, \quad (1.16)$$

where we have absorbed a phase factor. This finally leaves us with the reciprocal Hamiltonian

$$H_q = t \begin{pmatrix} 0 & m + e^{-iqa} \\ m + e^{iqa} & 0 \end{pmatrix}. \quad (1.17)$$

To make this reciprocal Hamiltonian even simpler to look at and diagonalize we can break it up into a new function,  $\mathbf{h}(q)$ , and the Pauli matrices  $\boldsymbol{\sigma} = \{\sigma_1, \sigma_2, \sigma_3\}$  by defining

$$\mathbf{h}(q) = t\{m + \cos(qa), \sin(qa), 0\}, \quad (1.18)$$

$$H_q = \mathbf{h}(q) \cdot \boldsymbol{\sigma}. \quad (1.19)$$

This notation allows for the simple determination of the eigenvalues of  $H_q$  as

$$E_{\text{SSH},\pm} = \pm |\mathbf{h}(q)| = \pm t \sqrt{m^2 + 1 + 2m \cos(qa)}, \quad (1.20)$$

which describes a band structure as shown in Fig. 1.3(a) for  $m = 1/3$  and both  $m$  and  $t$  positive and real.

The band structure displays several important features. The width of each of the two bands is  $2mt$ , meaning that when  $m = 0$  (the fully dimerized limit) the bands become perfectly flat. This is the limit of many degenerate (and disconnected) pairs of symmetric and antisymmetric states residing within each unit cell. In addition the band gap is set by  $2t(1 - m)$  so if  $m = 1$  then the band gap drops to zero and the bands touch. This is the critical point for the model: when  $m < 1$  the bands are topologically nontrivial, but when  $m = 1$  the bands touch and a topological phase transition occurs, sending the system into the trivial regime for all  $m > 1$ . This can be further visualized by finding the eigenvectors of the system that can be written in terms of  $\mathbf{h}(q)$  as

$$|\psi_{\pm}\rangle = \frac{1}{\sqrt{2}} \begin{pmatrix} \pm \frac{|\mathbf{h}(q)|}{h_x + ih_y} \\ 1 \end{pmatrix}. \quad (1.21)$$

As long as the system is gapped ( $h_x(q) = h_y(q) \neq 0$ ), the denominator can be rewritten as

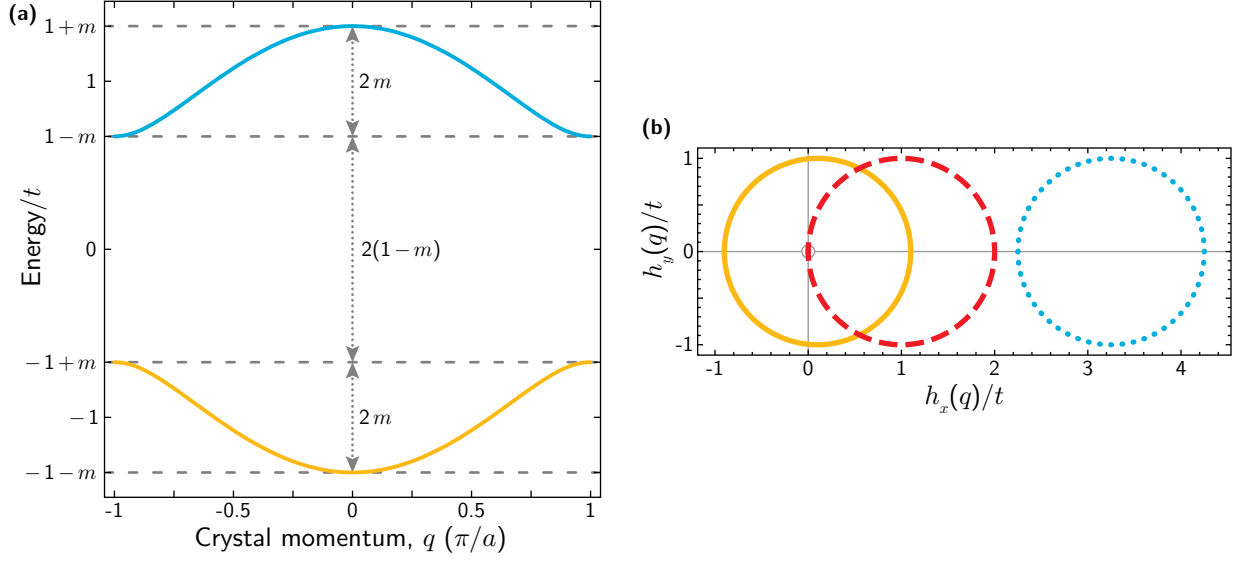


Figure 1.3: Band structure of the SSH model without an edge. **(a)** The band structure as plotted from Eq. 1.20 versus crystal momentum. The lower energy band  $E_{\text{SSH},-}$  is in yellow and the higher energy band  $E_{\text{SSH},+}$  is in teal. Both bands have a width of  $2mt$  and the gap between them is  $2t(1-m)$ . Parameters for the plot are  $m = 1/3$  with both  $m$  and  $t$  being positive and real. **(b)** Parametric plot of  $h_x(q)$  vs.  $h_y(q)$  for  $-\pi/a \leq q < \pi/a$  forming a circle in parameter space with radius  $t$  and horizontal position  $mt$ . When the circle encompasses the origin (yellow circle,  $m = 0.1$ ), the system is in the topological phase with winding number 1. As  $m$  is increased to 1 the circle moves to the right until its left edge passes through the origin (red dashed circle). This is the critical point where the band gap closes and Eq. 1.22 breaks down. With a further increase to  $m = 3^{1/3}$  the origin lies completely outside the circle (blue dotted circle) and the system is topologically trivial.

$h_x(q) + ih_y(q) = |\mathbf{h}(q)|e^{i\varphi(q)}$  with  $\varphi(q) = \arctan[h_y(q)/h_x(q)]$ , yielding

$$|\psi_{\pm}\rangle = \frac{1}{\sqrt{2}} \begin{pmatrix} \pm e^{-i\varphi(q)} \\ 1 \end{pmatrix}. \quad (1.22)$$

Now that a general form for the wavefunction is known, we can calculate the winding number  $N$  for these bands, which corresponds to the number of times the phase  $\varphi(q)$  winds by  $2\pi$  over the entire range of crystal momentum. In terms of the Zak phase,  $\phi_{\text{Zak}}$ , [24] the winding number is

$$N = -\frac{1}{\pi}\phi_{\text{Zak}} = \frac{1}{2\pi} \int_{-\pi/a}^{\pi/a} \frac{\partial\varphi_q}{\partial q} dq = 1; \quad \forall \quad -1 < m < 1. \quad (1.23)$$

Therefore, we see that as long as we are in the topological regime ( $-1 < m < 1$ ) we get an integer winding number for our bands. To reiterate, this analysis only holds as long as  $\varphi(q)$

is well defined, that is to say as long as  $h_x(q) = h_y(q) \neq 0$ . This zero crossing represents the critical point of the system directly because it is the point when the band gap vanishes, *i.e.*, if  $m = 1$ , then  $\mathbf{h}(q) = \{0, 0, 0\}$  at the band edge  $q = -\pi/a$ . This idea can be visualized by looking at the parametric plot of  $h_x(q)$  vs.  $h_y(q)$  over the entire range of crystal momentum as shown in Fig. 1.3(b). In parameter space a circle is formed for any  $m$  and  $t$  values. The radius of the circle corresponds to  $t$  and its central position on the horizontal axis is given by  $mt$  such that when the system is deep in the topological phase at, say,  $m = 0.1$  the circle (yellow solid circle) encompasses the point  $\{h_x(q), h_y(q)\} = \{0, 0\}$  at the origin of the graph. We have shown that the system encounters its critical point when the circle passes through the origin, and the first part of the circle to cross the origin with increasing  $m$  will be the left edge which has coordinates  $\{h_x, h_y\} = \{0, t(m - 1)\}$ . When  $m = 1$ : the band gap closes, Eq. 1.20 breaks down, the left edge of the circle passes through the origin (red dashed circle), and the system is at its critical point. For values of  $m$  larger than 1, the origin is completely outside the circle (blue dotted circle) and the system is in a trivial phase. Perhaps the most physical argument for the presence of this phase transition is in terms of symmetries. The underlying chiral symmetry present in the lattice is also broken when  $m = 1$ , meaning that this topological phase is stabilized by the presence of this symmetry and without it the phase does not exist.

Although we have calculated the winding number, we have so far neglected to mention the edge, or boundary, states of this system. In this 1D model a 0D “edge” is created at the point at which the chain is terminated or, as in the case of *trans*-polyacetylene, a defect in the chain may cause a boundary between two distinct topological phases, as shown in Fig. 1.4(a) by the red dashed line. The band structure including one defect state at the center of the lattice is shown in Fig. 1.4(b). Instead of an analytical form for the band structure, the system has been solved via numerical diagonalization of the Hamiltonian. The bands in Fig. 1.4(b) look identical to the analytical case presented with periodic boundary conditions in Fig. 1.3(a) but are shown only for positive crystal momenta. A new zero-energy state has appeared in the band gap at  $|q| = \pi/a$  corresponding to the boundary state.

The wave function of this boundary state is shown in Fig. 1.4(c). Notice that, for this eigenstate, there is exactly zero wave function amplitude at any of the B sublattice sites in

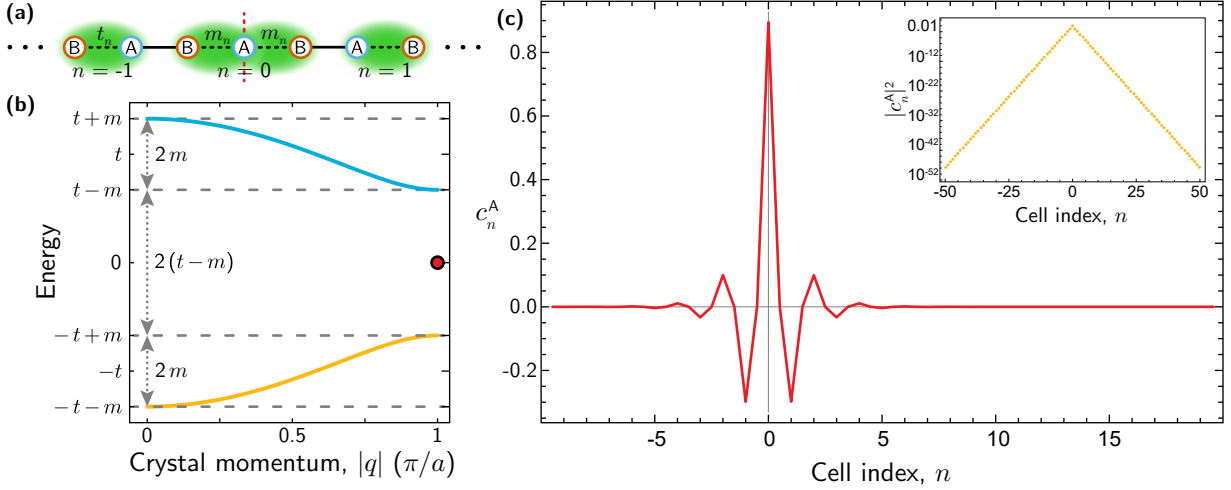


Figure 1.4: Edge states in the SSH model. **(a)** Structure of the SSH model with a central defect at the red vertical dashed line. This can be understood as the interface between two topologically distinct phases with winding numbers  $\pm 1$ . **(b)** The band structure for the SSH model with a central defect with  $m = 1/3$ . The energy bands shown in blue and yellow are identical to those shown before without a defect but a new state has appeared at zero energy and at the band edge shown as a red dot. **(c)** The amplitude of the wave function versus the cell index  $n$ . The wave function is real everywhere with a  $\pi$  phase inversion at every other A sublattice site and a decaying envelope spreading away from the defect location. **(c, inset)** The probability amplitude of the wave function at A sublattice sites versus the unit cell index  $n$  on a log scale showing the exponential decay of the wave function amplitude centered on the defect sublattice site.

the entire system. The amplitude of the wave function at the A sublattice sites, however, can be written in the following analytical form:

$$c_n^A \propto (-1)^n \left( \frac{1}{m} \right)^{N_{\text{cells}} - |n|}. \quad (1.24)$$

The wave function is centered at the A sublattice site of the unit cell where the two topological phases meet, that is to say, the defect site. In addition, it decays exponentially as it moves away from the defect site. To calculate the characteristic decay length the probability amplitudes can be written as  $|c_n^A|^2 = |c_0^A|^2 \exp(-\xi n)$  with the decay length defined as  $\xi = -2 \ln(m)$ . For the plotted values of  $m = 1/3$ , the wave function is almost completely localized to within 8 unit cells with a decay length of  $\xi \approx 2.2$  cells. This exponential decay is further illustrated by the semilog plot shown in the inset of Fig. 1.4(c). Finally, the wave function also features a  $\pi$  phase inversion at every other A sublattice site and is real everywhere.

### 1.2.2 Discussion

The SSH model was one of the first condensed matter systems to have its effects explained through topology and it is a canonical teaching model in introductory condensed matter courses. Yet, outside of the conductivity effects observed in the molecule that the model was originally based on, there were no direct measurements of the topology of the model or its edge states for many years. Then, in 2013 the Zak phase was measured in a real-space superlattice cold atom platform [29], but the edge states were not observed until we applied our momentum-space lattice techniques to the problem in 2016 [33]. This relative lack of experimental verification is what motivated us to study this problem in the first place.

Another area of this specific model that had been examined in theory but not realized in a systematic experiment is the effect of adding disorder. It is a general feature of topologically protected states that they persist, largely unaltered, even in the presence of relatively strong disorder. The original conductivity effects in *trans*-polyacetylene were certainly observed in the presence of disorder (thermal and static) since it is very difficult to make a perfect lattice structure in organic polymer systems, which additionally live in some surrounding environment. But this disorder is impossible to systematically control because of its natural, random presence. In our system, however, we can start with a lattice which is free from any disorder and add it in by randomly changing the tunneling parameters connecting any pair of sites. This allowed us to extend this model to a disordered regime and observe the persistence of the topological phase. In addition, we were able to increase the disorder up to a point where the band gap closes and the topology is destroyed, marking the first such observation of the “random-singlet” transition [40]. In the past, observations of robustness to disorder and the absence of topology in the presence of very high disorder had been measured in photonic systems [8] but the phase transition itself had not yet been observed due to the difficulty in exactly controlling disorder in most systems.

In addition, there is a counter-intuitive phenomenon in this system in the presence of a specific model of disorder. The system can start at zero disorder in a trivial phase with  $m \approx 1.1$  and actually become topological with the addition of strong disorder [see Fig. 5.3(a)] before eventually transitioning back to a trivial phase with very strong disorder. This in-

icates that this topological phase is not only persistent in the presence of disorder but can actually be created by it. This phenomenon is referred to as the topological Anderson insulator in reference to P. W. Anderson’s famous 1958 work on the localization of a particle in a random potential due to wave interference [41]. The topological Anderson insulator was first theoretically predicted in 2009 [42] and has since been the subject of much theoretical investigation [43–47], but it was never experimentally demonstrated until 2018 by two concurrent measurements. One measurement, based in photonic systems [5], found evidence for a topological phase by adding disorder to a topologically trivial system. The other was our observation of the transition from trivial to topological and back again as a function of disorder strength through measurement of the mean chiral displacement [30, 48].

## 1.3 Outline

The rest of this manuscript is organized as follows:

- [Chapter 2: The Momentum-Space Lattice](#). We start by presenting the mathematical basis of the momentum-space lattice as a tool for engineering effective tight-binding Hamiltonians. Then we expound on its tunability and limitations before showing some experimental demonstrations. We finish by discussing the methods by which it can be extended to more than one dimension and the effects of interactions in the system. These last two items are relatively unimportant for the work described here since it is 1D and interactions do not play a major role, and are only given for larger context and overview.
- [Chapter 3: Methods](#). This chapter gives a detailed synopsis of the experimental apparatus used to take the measurements presented here. We describe how we create BECs of  $^{87}\text{Rb}$  and how we will in the future create Bose–Einstein condensates of  $^{39}\text{K}$ . The section on  $^{39}\text{K}$  contains extensive detail on the design and realization of magnetic field controls for the new apparatus. We finish the chapter by discussing the unique procedure for performing quantum simulation with the apparatus, including writing and implementing arbitrary waveforms.
- [Chapter 4: Clean Topological Wires](#). In this chapter, we present our realization of the SSH model with our momentum-space lattice. After a brief overview of the SSH model, we display our observations of the edge states of this model in the absence of disorder.
- [Chapter 5: Dirty Topological Wires](#). We extend the work shown in Chap. 4 through the addition of controlled tunneling disorder. We begin with an introduction to the interplay of topology and disorder and subsequently present our observations of topological phase transitions and the topological Anderson insulator. In addition, some speculative simulations are shown of the SSH model in the presence of interactions.
- [Chapter 6: Studying Chaos with a Synthetic Spin](#). We present here a drastically different experiment using the momentum-space lattice to simulate an artificial driven spin. We subject the spin to both linear and non-linear operations and measure an effective “squeezing” of the spin and the out-of-time-ordered correlation function. Then we proceed to implement a “kicked top” Hamiltonian where we observe the onset of classical chaos in this quantum system.
- [Chapter 7: Counter-Diabatic Driving](#). We describe our implementation of a type of “shortcut-to-adiabaticity” protocol using dynamic Hamiltonian engineering for countering diabatic terms. This illustrates a generic technique for deforming a Hamiltonian faster than the adiabatic limit with no detrimental consequences. We prepare both extended states and quantum-well eigenstates much faster than adiabatically allowed when starting with all population in one site.

The appendices detail simulations, software, and hardware that we have created which may be useful to future researchers in the lab.

# Chapter 2

## The Momentum Space Lattice

“We use heavy photons called rubidium.”

---

Bryce Gadway

The full detail of the “momentum-space lattice” scheme can be found in Ref. [49], but a brief discussion of the important operating principles is reproduced here. The momentum-space lattice is a type of synthetic lattice for ultracold atoms or, more specifically, Bose–Einstein condensates (BECs). The synthetic dimension in this case is the set of discrete atomic momentum states which become resonantly coupled by the use of two interfering laser fields. When the atoms first condense they collapse into the ground state of the optical trap and have a momentum of zero (with some small spread). If we ignore both the trap<sup>1</sup> and atomic interactions, these atoms act essentially as free particles having an energy  $E = p^2/2M$ , where  $p$  is momentum and  $M$  the mass of the particle. We then expose the BEC to a laser field [Fig. 2.1(a)] that satisfies the momentum and energy conservation needed to connect multiple points on this dispersion relation, thereby defining the set of momentum states  $\psi_n$  to be used as synthetic lattice sites.

The laser wavelength  $\lambda = 1064$  nm sets the momentum of the states  $\psi_n$  to be  $p_n = 2n\hbar k$ , where  $k = 2\pi/\lambda$ . Atoms may undergo a transition via the stimulated exchange of photons between the right-going laser field (properties of which are denoted with a superscript +)  $\omega^+$  and one of frequency components of the left-going, multifrequency laser field  $\omega_j^-$  (properties of which are denoted with a superscript –), as shown in Fig. 2.1(a). The frequencies  $\omega_j^-$  are all very near to  $\omega^+$ , only detuned on the kHz level from a beam with a frequency of roughly 282 THz, and therefore using a single  $k$  to define the momentum states is a very

---

<sup>1</sup>We assume the population stays near the trap center, which is approximately flat, during the entire experiment. Further, the coherence length of the BEC, which is essentially set by the trap frequency, is much longer than the spacing of the “Bragg grating” the atoms diffract from, making this a good approximation.

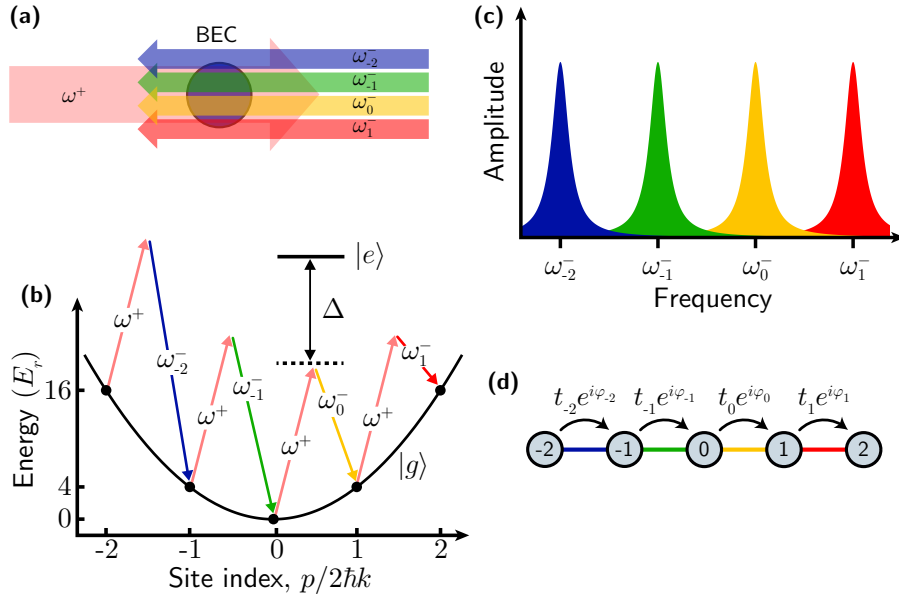


Figure 2.1: Introduction to the momentum-space lattice. **(a)** The right-going laser field, with frequency  $\omega^+$  and left-going laser field with many frequencies  $\omega_j^-$  incident on the BEC. **(b)** The dispersion relation of free-particles (condensate atoms) exposed to the counterpropagating laser field. **(c)** The frequency spectrum of the left-going laser field depicting amplitude at the necessary weight and frequency to resonantly couple 5 sites with equal tunneling energy. **(d)** A schematic of the resultant tight-binding model lattice with five sites.

good approximation. Additionally, both  $\omega^+$  and  $\omega_j^-$  are roughly 98 THz detuned from the nearest electronic transition, shown as  $|g\rangle \rightarrow |e\rangle$  in Fig. 2.1(b). These transitions can be understood as a two-photon Bragg diffraction process as the different combinations of  $\omega_j^-$  link distinct points on the free-particle dispersion relation [see Fig. 2.1(b)]. In this limit, each laser frequency of the  $-$  beam, in tandem with the  $+$  beam, independently addresses a specific transition between pairs of momentum states. Therefore, by controlling the frequency components of  $\omega^-$  we can independently control the parameters in our simulated Hamiltonian. There are, however, several approximations and operational limits that must be respected for this picture to be accurate and a more detailed mathematical treatment helps make them more explicit.

## 2.1 Mathematical Basis

The Hamiltonian for an atom simultaneously experiencing the full laser field can be written  $H(\tau) = H_0 + V(\tau)$ , where  $\tau$  is time. In this case,  $H_0$  relates to the energies of the states  $\psi_n$

linked by the laser fields. It can be written as  $H_0 = \sum_n E_n |\psi_n\rangle\langle\psi_n|$  where  $E_n = p_n^2/2M = 4n^2 E_r$ , with the recoil energy (the amount of energy an atom “recoils” with when it emits a photon) of the lattice laser  $E_r = \hbar^2 k^2/2M$ . The second part of the Hamiltonian describes the interaction between an atom and the laser field and is written as

$$V(\tau) = \sum_n (\chi(\tau) |\psi_n\rangle\langle\psi_{n+1}| + \chi^*(\tau) |\psi_{n+1}\rangle\langle\psi_n|), \quad (2.1)$$

with

$$\chi(\tau) = \sum_j \hbar \tilde{\Omega}_j e^{i\varphi_j} e^{-i\tilde{\omega}_j \tau}. \quad (2.2)$$

Here,  $\tilde{\omega}_j = \omega^+ - \omega_j^-$  and  $\varphi_j = \varphi^+ - \varphi_j^-$  give the angular frequency and phase difference, respectively, between the right-going laser and the  $j^{\text{th}}$  component of the left-going field. The coupling strength  $\tilde{\Omega}_j = \Omega^+ \Omega_j^- / 2\Delta$  is given in terms of the one-photon Rabi strengths of the right-going field  $\Omega^+$  and the  $j^{\text{th}}$  component of the left-going field  $\Omega_j^-$ , where  $\Delta$  refers to the detuning from the one-photon transition to the electronic excited state [the  $|g\rangle$  to  $|e\rangle$  transition in Fig. 2.1(b)].

The coupling term  $\chi(\tau)$  contains the multifrequency field which links all the different states  $\psi_n$  together. However, it is not immediately obvious how this allows for individual control of each transition between states  $\psi_n$  because  $\chi(\tau)$  is a common coupling term between all nearest-neighbor states. That is to say, it appears in all the off-diagonals of the Hamiltonian, thereby linking each state to its neighbors with the identical complicated coupling term  $\chi(\tau)$ . To see how this individual transition control arises, it is helpful to move to the interaction picture and eliminate the diagonal terms in the Hamiltonian. Doing this transformation gives the interaction-picture Hamiltonian  $H^{\text{int}}(\tau) = V^{\text{int}}(\tau) = e^{iH_0\tau/\hbar} V(\tau) e^{-iH_0\tau/\hbar}$ . Plugging in  $V(\tau)$  and distributing our exponential terms leaves us with

$$\begin{aligned} H^{\text{int}}(\tau) &= \sum_n (\chi(\tau) e^{i(E_n - E_{n+1})\tau/\hbar} |\psi_n\rangle\langle\psi_{n+1}| + \chi^*(\tau) e^{-i(E_n - E_{n+1})\tau/\hbar} |\psi_{n+1}\rangle\langle\psi_n|) \\ &= \sum_n (\tilde{\chi}_n(\tau) |\psi_n\rangle\langle\psi_{n+1}| + \tilde{\chi}_n^*(\tau) |\psi_{n+1}\rangle\langle\psi_n|), \end{aligned}$$

where the new coupling, defined in terms of  $\omega_n^{\text{res}} = (E_n - E_{n+1})/\hbar$ , is given by

$$\tilde{\chi}_n(\tau) = \chi(\tau)e^{i\omega_n^{\text{res}}\tau} \quad (2.3)$$

$$= \sum_j \hbar\tilde{\Omega}_j e^{i\varphi_j} e^{i(\omega_n^{\text{res}} - \tilde{\omega}_j)\tau} \quad (2.4)$$

as is illustrated in Fig. 2.1(c).

For each transition  $n \rightarrow n + 1$  (that is to say, at each off-diagonal position in our Hamiltonian) there is now a unique coupling  $\tilde{\chi}_n(\tau)$ . However, this unique coupling still contains many terms, each one from a different frequency component of the left-going laser field. Remediating this complication requires the use of a rotating-wave-like approximation, which drops all the rapidly oscillating terms in a specific  $\tilde{\chi}_n(\tau)$ , leaving only a static coupling term. This can be done in the weak coupling limit where the only frequency component present in  $\tilde{\chi}_n(\tau)$  which will affect a specific transition is the one which is near-resonant to it. This point is illustrated in Fig. 2.1(c) where the frequency spectrum of the left-going laser field is shown. Each peak addresses a specific Bragg resonance frequency and its overlap with other transitions can be ignored in the weak-driving limit.

As an explicit example, consider a many-site system under resonant coupling of all sites. The coupling term  $\tilde{\chi}_n(\tau)$  linking site  $n \rightarrow n + 1$  becomes

$$\tilde{\chi}_n(\tau) = \dots + \hbar\tilde{\Omega}_{n-1} e^{i\varphi_{n-1}} e^{i(\omega_n^{\text{res}} - \tilde{\omega}_{n-1})\tau} + \hbar\tilde{\Omega}_n e^{i\varphi_n} e^{i(\omega_n^{\text{res}} - \tilde{\omega}_n)\tau} + \hbar\tilde{\Omega}_{n+1} e^{i\varphi_{n+1}} e^{i(\omega_n^{\text{res}} - \tilde{\omega}_{n+1})\tau} + \dots \quad (2.5)$$

Since the coupling is resonant  $\omega_n^{\text{res}} - \tilde{\omega}_n = 0$  and

$$\tilde{\chi}_n(\tau) = \dots + \hbar\tilde{\Omega}_{n-1} e^{i\varphi_{n-1}} e^{i(\omega_n^{\text{res}} - \omega_{n-1}^{\text{res}})\tau} + \hbar\tilde{\Omega}_n e^{i\varphi_n} + \hbar\tilde{\Omega}_{n+1} e^{i\varphi_{n+1}} e^{i(\omega_n^{\text{res}} - \omega_{n+1}^{\text{res}})\tau} + \dots \quad (2.6)$$

As is evident, in this case we have a static coupling term relating to frequency component  $n$  of the left-going field and many off-resonant terms related to the other frequency components of the left-going field. Dropping these rapidly-oscillating terms leaves only the static term. This approximation is valid when the drive-field energy scales  $\hbar\tilde{\Omega}_j$  are much less than the lowest

oscillation frequencies that are being dropped. In this case, which happens to be the most stringent case, the lowest oscillation frequencies are  $\omega_n^{\text{res}} - \omega_{n+1}^{\text{res}} = (E_n - 2E_{n+1} + E_{n+2}) / \hbar = 4E_r(n^2 - 2(n+1)^2 + (n+2)^2) / \hbar = 8E_r / \hbar$  as shown in the two oscillating terms in the equation above. So, in most scenarios, for the approximation to remain valid the coupling strength for any two sites in the system must remain much less than the fixed value of 8 recoil energies. This value can be intuitively understood from the fact that the Bragg resonance conditions are linearly spaced by this same amount. For our chosen lattice wavelength of  $\lambda = 1064$  nm the recoil energy is  $E_r / h = 2027.8$  Hz. For our approximation to remain valid, this sets a practical limit on the tunneling energy of

$$\hbar\tilde{\Omega}_j \ll 8E_r \approx h \times 16222.5 \text{ Hz} \quad \forall j. \quad (2.7)$$

To practically define the symbol  $\ll$  in the above equation, deviations from the approximate form of the Hamiltonian tend to appear at a deleterious level when  $\hbar\tilde{\Omega}_j$  exceeds roughly  $h \times 1200 \text{ Hz} \approx 0.6 E_r$ .

Considering the non-resonant driving case, the coupling term  $\tilde{\chi}_n(\tau)$  linking sites  $n \rightarrow n+1$  becomes

$$\tilde{\chi}_n(\tau) = \sum_j \hbar\tilde{\Omega}_j e^{i\varphi_j} e^{i\delta_j\tau} \quad (2.8)$$

where  $\delta_j = \omega_n^{\text{res}} - \tilde{\omega}_j$ . As before, in the weak driving limit, the only term of  $\tilde{\chi}_n(\tau)$  which will drive any appreciable population across the transition  $n \rightarrow n+1$  is the near-resonant term ( $j = n$ ). Therefore, in the spirit of a rotating-wave approximation as defined above, all other rapidly oscillating terms may be ignored resulting in an effective coupling which contains only one term per transition

$$\tilde{\chi}_n^{\text{eff}}(\tau) \approx \hbar\tilde{\Omega}_n e^{i\varphi_n} e^{i\delta_n\tau}. \quad (2.9)$$

Further absorbing the remaining weak time-dependence related to  $\delta_j$  into the diagonal terms through local frame transformations results in a single-particle, tight-binding Hamiltonian

of the form:

$$H^{\text{eff}} \approx \sum_{n=N_i}^{N_f} \epsilon_n c_n^\dagger c_n + \sum_{n=N_i}^{N_f-1} \left( t_n e^{i\varphi_n} c_{n+1}^\dagger c_n + \text{H.c.} \right) \quad (2.10)$$

where  $\delta_n = (\epsilon_{n+1} - \epsilon_n)/\hbar$  relates the site energies to the detuning of the drive-fields,  $t_n = \hbar\tilde{\Omega}_n$  relates to the strength of the drive fields, and  $\varphi_n$  is the tunneling phase. In addition,  $N_i$  and  $N_f$  relate to the first and last sites in the system with the total number of sites given by  $N = N_f - N_i + 1$  as shown in Fig. 2.1(d). The number of sites is controlled exactly by the presence of specific frequency components of the  $\omega^-$  laser field. Each term in the second sum of the Hamiltonian links sites  $n$  and  $n + 1$  and therefore the sum runs to the second-to-last site, resulting in the next site being the final site in the system.

## 2.2 Tunability

The momentum-space lattice technique allows for the creation of nearly any one-dimensional finite size tight-binding model with local connectivity. The tunneling energy  $t_n$ , tunneling phase  $\varphi_n$ , and site energy  $\epsilon_n$  in Eq. 2.10 can all be changed locally and in a time-dependent way through the control of the multifrequency laser field as illustrated in Fig. 2.2. First, by tuning the laser power present at a specific frequency we can directly tune the coupling strength  $t_n$  between the two sites associated with that frequency. Second, adding a relative phase to a specific frequency component in the laser field adds that phase directly onto the system as a tunneling phase which a particle acquires when undergoing that transition. Third, by slightly detuning a specific frequency component of the multifrequency beam we can create an effective energy difference between the two sites that it couples. This gives us control not only over the local parameters in Eq. 2.10 but also time-dependent control as well.

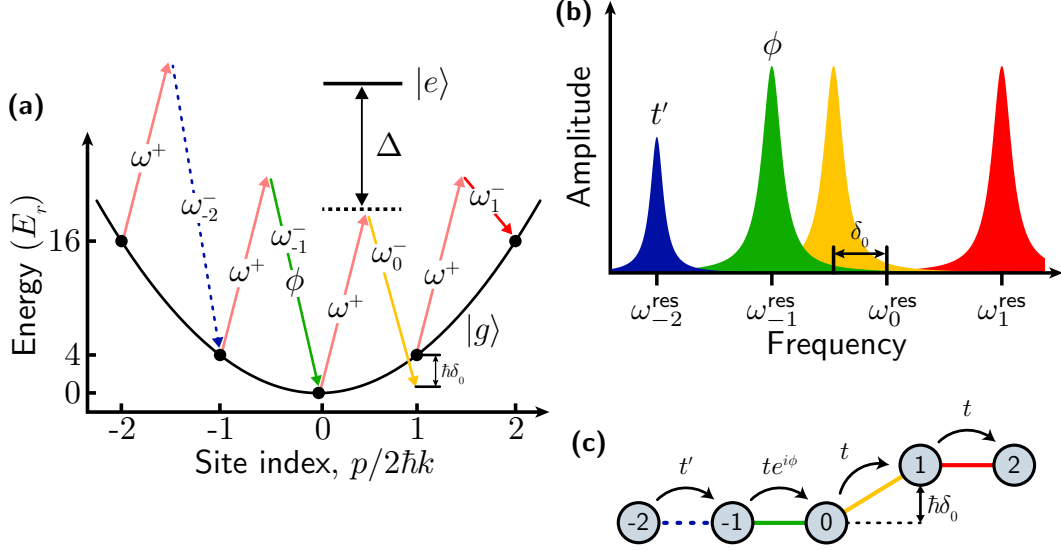


Figure 2.2: Tuning parameters in the momentum-space lattice. **(a)** Dispersion relation showing the counter-propagating laser field.  $\omega_{-2}^-$  is dashed to represent a lesser beam intensity than the rest of the multifrequency field.  $\omega_{-1}^-$  has a relative phase  $\phi$ , and  $\omega_0^-$  is detuned from its respective resonance by an amount  $\delta_0$ . **(b)** The spectrum of the multifrequency laser field showing a lesser weight at  $\omega_{-2}^-$ , a phase  $\phi$  on  $\omega_{-1}^-$  and a detuning  $\delta_0$  on  $\omega_0^-$ . **(c)** The resultant lattice picture showing a reduced tunneling energy  $t'$  associated with  $\omega_{-2}^-$ , a tunneling phase associated with  $\omega_{-1}^-$ , and an energy offset  $\epsilon_0$  associated with  $\omega_0^-$ .

## 2.3 Limitations

There are several practical operational limitations that are relevant to the momentum-space lattice scheme. As already discussed there exists a limit on the tunneling energy,  $t_n \ll 8E_r$ . Using our practical limit given above of  $t/h = 1200$  Hz, this translates into the fact that one tunneling time in our experiment is, at its shortest,  $\hbar/t \approx 130 \mu\text{s}/\text{rad}^2$ . If we exceed this limit, we start to suffer from off-resonant driving. Essentially the approximation that each frequency component present in the  $\omega_j^-$  beam addresses only one transition breaks down and multiple frequency components may address each transition off-resonantly. This causes tunneling to occur which does not follow the simulated rotating-wave approximated Hamiltonian and thus provides a limit to how fast the system can be driven, at least with respect to idealized dynamics. By itself this limitation is not concerning, as we may simply make the experiment duration longer to compensate for the long tunneling times. However,

<sup>2</sup>The unit  $\hbar/t$ , or “tunneling time”, is formulated in the context of a two-level system where  $\pi/2$  tunneling times corresponds to all population being transferred from one state to the other. In addition, tunneling times are often given with the rad unit suppressed but it can be important to remember.

there exists another more fundamental limit in our system which constrains the experimental duration by restricting the time during which coherent dynamics may take place.

Since we are using momentum states, when an atom is excited into a state  $\psi_n$  it begins to move with a velocity related to its momentum  $p_n$  as long as it stays near the center of the trap (we note that this is true so long as there are no lattice fields on, such that the bare momentum states are the good system eigenstates, as opposed to light-atom dressed states). This presents a fundamental problem for this scheme because the atoms cannot undergo coherent quantum dynamics once the spatial wavepackets relating to different momentum values become spatially separated. The speed at which they separate is  $v_n = p_n/M = 2n\hbar k/M \approx n \times 8.63 \mu\text{m}/\text{ms}$ . To give this speed a sense of scale, the world record for a garden snail was set at  $2.75 \mu\text{m}/\text{ms}$  in 1995 by Archie and his trainer, six-year-old Carl Bramham of the UK [50]. The radial size of the condensate is initially roughly  $15\text{--}45 \mu\text{m}$  giving us a practical constraint of  $1\text{--}2 \text{ms}$  to perform an experiment. This constraint on how slowly we can go coupled with the off-resonant driving limitation on how fast we can go means we can evolve our Hamiltonian at best for about 10 tunneling times before dynamics stop due to the momentum modes losing spatial overlap.

This also depends on the actual experiment being performed. For example, if only two-site Rabi oscillations between sites  $n \leftrightarrow n+1$  are being observed, any given atom will have an average momentum  $2\hbar k$  for half the time and zero momentum for the other half of the time. Therefore, these two modes will separate more slowly than the modes of a system with many sites and population spread out very far in momentum space. More to the point, a strong Bragg coupling between states  $n$  and  $n+1$  can result in light-atom dressed states that relate to superpositions of the two bare momentum states. Preparation of such states will result in no separation of momentum wavepackets. This is much the same way as atoms adiabatically loaded into a deep, stationary optical lattice will be stationary, while still having non-zero projections onto multiple momentum states (*e. g.*, zero and  $\pm 2\hbar k$ ). In cases dealing with “dressed states,” much longer experimental timescales may be explored.

## 2.4 Experiment Types

The momentum-space lattice technique naturally lends itself to dynamical measurements due to the fact that every experiment begins with a BEC of atoms at zero momentum and this is almost never an eigenstate of the actual Hamiltonian that is being studied. So the most natural measurement for us to make is the evolution of the localized condensate after “turning on” the Hamiltonian, which we term a quench measurement. This type of measurement can be useful and often times gives access to rich and interesting physics. However, many of the more subtle measurements carried out in the course of this work require additional tricks to obtain the desired observables. Fortunately, and due to our high level of control over the system, we can additionally prepare certain eigenstates (either adiabatically or manually) before exposing them to the full Hamiltonian in question. This can be helpful for a number of measurements, specifically those in Chapters 4, 6, and 7. Regardless of the method, preparing eigenstates before an experiment takes valuable time so it must be done with speed in mind.

Adiabatic preparation of a particular state is typically done by slowly changing the potential that the atoms are exposed to so that the initial state connects to some final state of interest in a lossless manner. Typically, the starting eigenstate is simply the at-rest BEC and the Hamiltonian is slowly deformed from there to adiabatically connect this state to the desired eigenstate. This can be useful in its own right, as preparing a certain state or detecting the presence of a certain state can be an experiment in and of itself as in Chapters 4 and 7. Additionally, the adiabatically prepared state may be subjected to some further experimental probing or be the starting off point for some other measurement as in Chapters 4 and 6.

If the state to be prepared is relatively simple or localized in space it may be possible to prepare it manually. To manually prepare an eigenstate, we selectively move population through the lattice by individually turning specific links on and off in time. In this way population can be moved one site at a time from the zero-momentum mode to where it should be to realize a certain eigenstate. This is only faster and more successful than adiabatic preparation if the state in question only has population distributed over a few

lattice sites with simple phase structure. This technique was used to detect the phase structure of a topological edge state, as discussed in Chapter 4.

Lastly, we have had recent success with a method of preparing states called counter-diabatic driving or shortcut-to-adiabaticity protocols. The idea behind these schemes is to counter out unwanted diabatic terms that crop up when you change a Hamiltonian in time by direct cancellation. When changing a Hamiltonian for the adiabatic preparation of a certain eigenstate, the added time-dependence may introduce couplings between eigenstates, the very thing that imposes a speed limit on adiabatic processes in the first place. In some cases these undesired couplings can be solved for mathematically ahead of time and added into the Hamiltonian directly. That way when the Hamiltonian is changed in time the manually added counter-diabatic terms cancel with the terms which arise because of the time dependence. This has the potential to be a hugely useful technique for momentum-space lattice experiments because it drastically reduces the amount of time necessary for preparing eigenstates via the adiabatic approach. This is the premise of the measurements discussed in Chapter 7.

## 2.5 Experimental Demonstrations

In late 2015, we tested the capabilities of this scheme through observations of quantum walking, Bloch oscillations, and phase reversal experiments and published the results in Ref. [51]. The experiments shown in this section were performed by Fangzhao Alex An and myself under the guidance of Bryce Gadway.

### 2.5.1 Continuous-Time Quantum Walk

The first of these demonstrations, the observation of a continuous-time quantum walk, exhibits many of the hallmark features displayed by discrete time quantum walks [52], as realized in experiments with single atoms [53], ions [54], and photons [55, 56]. Starting from an initially localized state, we observe the spread of the atomic wavefunction in momentum space as characterized by its standard deviation or width  $\sigma_p = \sqrt{\langle p^2 \rangle - \langle p \rangle^2}$ . A

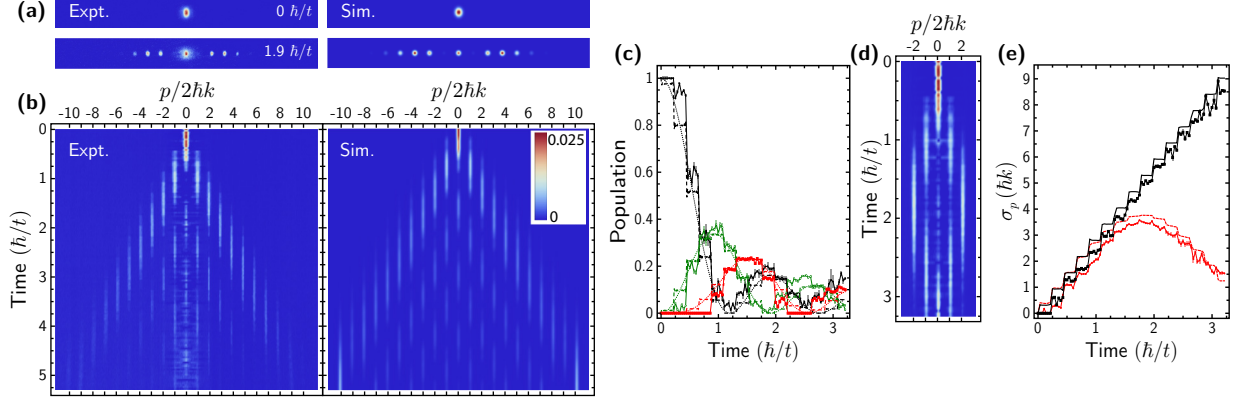


Figure 2.3: Quantum walk in momentum space. **(a)** Comparison of experiment (left) and simulation (right) for data taken right when the Hamiltonian is switched on ( $0 \hbar/t$ ) and after some evolution time  $1.9 \hbar/t$  with  $t/E_r \approx 0.3$ . **(b)** Comparison of data (left) and simulation (right) for a continuous-time quantum walk in a 21-site lattice showing population spreading from site zero all the way to the edges of the system. **(c)** The normalized populations extracted from the data shown in (b) for sites  $n = \{0, 1, 2\}$  shown as solid black dots, open green circles, and solid red squares. The black, green, and red lines show simulations of Eq. 2.11 for each mode and the dashed lines show a more complex simulation including off-resonant driving. **(d)** Data for a quantum walk in a five site system showing population rebounding from the edges of the system. **(e)** The width of the state in momentum space  $\sigma_p$  as a function of evolution time. Data from (b) in black squares with accompanying black simulation line as well as data from (d) in red dots with red, dashed simulation line showing good agreement with simulation and reflection from the system boundaries. All error bars denote one standard error of the mean. This figure was adapted from Ref. [51].

quantum walk leads to ballistic wave-packet spreading characterized by a linear increase of the momentum-space width ( $\sigma_p \propto \tau$ ), where  $\tau$  is the evolution time. On the other hand, a classical random walk would result in diffusive spreading reflected in the width by an increase with the square-root of time ( $\sigma_p \propto \tau^{1/2}$ ).

Our observations of quantum walks were done with a quench protocol and the results are summarized in Fig. 2.3. Once the BEC is created, we turn on a static Hamiltonian of the form

$$H = \sum_{n=-10}^9 t \left( c_{n+1}^\dagger c_n + \text{H.c.} \right). \quad (2.11)$$

This Hamiltonian represents a uniform lattice with equal tunneling rate  $t \approx 0.3E_r$  between all sites and no relative tunneling phases or energy structure. When exposed to this Hamiltonian the atoms undergo a quantum walk spreading uniformly outward from the center site as shown in Figs. 2.3(a,b), which show good agreement between data and a simulation of Eq. 2.11 with no free parameters. This agreement between data and simulation is further

validated by the more qualitative comparison shown in Fig. 2.3(c), where the populations of sites  $n = \{0, 1, 2\}$  are shown as a function of evolution time as solid black dots, open green circles, and red squares respectively. There are two types of simulations shown in this figure for all three modes as well. Direct numerical simulations of Eq. 2.11 are shown as dotted red, green, and black lines and more complex simulations including off-resonant driving are shown as dashed red, green, and black lines. We find that both simulations agree qualitatively with the data while the off-resonant simulation additionally captures the step-like behavior of the data.

For the data shown in Figs. 2.3(a–c) the atoms only begin to approach the edge of the system at the end of the experimental time. However, since we can locally control our Hamiltonian, we can set the system size at will. To test this control, we create a system with only five sites, centered about  $n = 0$ , as presented in Fig. 2.3(d). In this limit, we observe population spreading until it “hits” and rebounds off the edges of the system, causing it to refocus at  $n = 0$  at a later time (roughly  $3\hbar/t$ ). Additionally, we check that the atoms spread out in a ballistic fashion (as is found in a quantum walk) by calculating the width  $\sigma_p = \sqrt{\langle p^2 \rangle - \langle p \rangle^2}$  of the observed momentum distribution as a function of evolution time. For the 21-site lattice we observe  $\sigma_p$  (black points) expanding linearly over the entire range of sampled evolution times and for the 5-site lattice (red points) we see an initial linear expansion followed by a rounded turn-over as the atoms rebound off the engineered system boundaries as shown in Fig. 2.3(e). These observations agree well with a numerical simulation including off-resonant effects (solid black and dashed red lines) in both cases.

This first experiment shows simply that the system behaves as we expect it to in a simple scenario and also showcases our ability to create system boundaries. That is to say, our ability to locally control the tunneling amplitude. We further test our ability to create a site-energy landscape through Bloch oscillation measurements.

## 2.5.2 Bloch Oscillations

We test our control over the site-energy landscape of our momentum-space lattice by performing a tilted-lattice experiment and thereby observing Bloch oscillations of our atomic

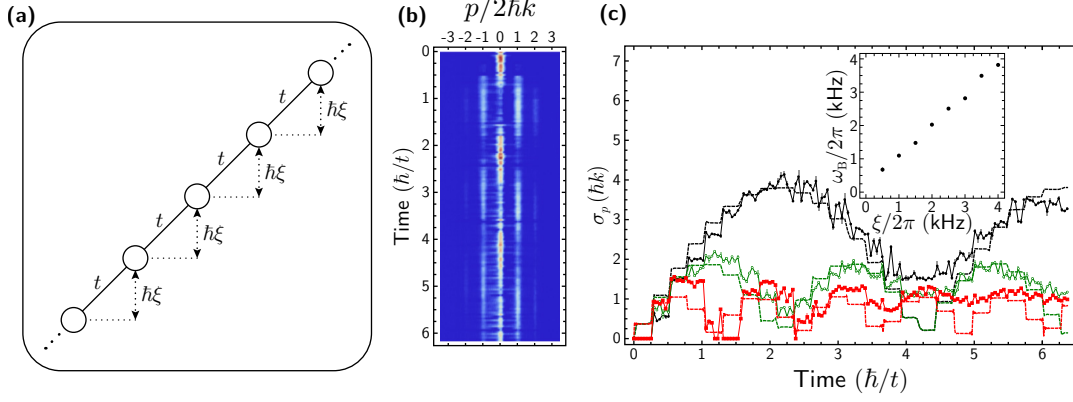


Figure 2.4: Bloch oscillations in momentum space. **(a)** Schematic of the tilted lattice showing five (of the 21 total) sites (black circles) separated in energy by  $\hbar\xi$  and coupled uniformly with tunneling  $t$ . **(b)** Integrated absorption images versus evolution time for a 21-site lattice with  $t/E_r \approx 0.33$  and  $\hbar\xi = E_r$ . **(c)** The momentum-width  $\sigma_p$  for the tilt values  $\hbar\xi/E_r \approx 0.5, 1.0$ , and  $1.75$  (black dots, open green circles, and red squares). Accompanying dashed lines show the results of a numerical simulation including off-resonant effects. **(c, inset)** The measured Bloch frequency  $\omega_B$  of the oscillations in  $\sigma_p$  for  $n = 0$  as a function of the lattice tilt  $\xi$ . All error bars denote one standard error of the mean. This figure was adapted from Ref. [51].

population as summarized in Fig. 2.4. The effective Hamiltonian for this experiment is

$$H = \hbar\xi \sum_{n=-10}^{10} n c_n^\dagger c_n + t \sum_{n=-10}^9 \left( c_{n+1}^\dagger c_n + \text{H.c.} \right), \quad (2.12)$$

where  $\hbar\xi$  represents the energy offset between each set of sites  $n$  and  $n + 1$  and  $t$  is the uniform coupling energy as shown in Fig. 2.4(a).

Nearly a century ago, the motion of particles in a periodic potential under the influence of a uniform force was predicted to result in oscillatory motion, Bloch oscillations [57, 58], rather than uniform drift or free acceleration. Over the past several decades, this coherent wave effect has been experimentally studied in electronic systems [59], with cold atoms in optical lattices [60], in optics [61], and even in the rotational excitations of  $\text{N}_2$  molecules [62]. The absence of dissipation in our system prohibits transport of our initially localized wave packets in the tilted potential, so instead we expect periodic spreading and refocusing in momentum space, as recently observed using cold atom microscopy [63]. Here again we make use of the momentum width of the observed atomic distribution  $\sigma_p$  to quantify this oscillatory spreading.

Starting with all the population at the center site  $n = 0$  we quench on the Hamiltonian

with the parameters  $t \approx 0.33E_r$  and  $\hbar\xi = E_r$ . This results in the onset of Bloch oscillations as shown in the integrated absorption images in Fig. 2.4(b) as a function of evolution time. It is important to note that the number of sites coupled in this experiment is 21, which is larger than the oscillation amplitude, so the atoms do not sample the edges of the system. We further show the clear oscillation in the extracted momentum width  $\sigma_p$  as a function of evolution time in Fig. 2.4(c) for  $\hbar\xi/E_r \approx 0.5$  (black dots),  $\hbar\xi/E_r \approx 1.0$  (open green circles), and  $\hbar\xi/E_r \approx 1.75$  (red squares) and compare each of these to a simulation (dashed lines) which includes the effects of off-resonant driving. Finally, by varying the tilt  $\hbar\xi$  we observe a linear dependence on the resultant Bloch frequency as shown in the inset of Fig. 2.4(c) as we expect. These observations confirm our ability to tune the site energies of our momentum-space lattice.

### 2.5.3 Phase Reversal

We now turn to testing our ability to control the relative tunneling phases present in our system. In testing our other control parameters we were able to use static Hamiltonians but we must use a time-varying Hamiltonian to test the phase structure. This is a result of any relative phase structure being inconsequential on population dynamics (in one-dimensional systems with only nearest-neighbor coupling) as it can be “gauged away” via local transformations. Specifically, we demonstrate the reversal of momentum-space dynamics by periodic phase inversions of the form  $\phi \rightarrow \phi + \pi$  in the effective Hamiltonian

$$H(\tau) = \sum_{n=-10}^9 t \left( e^{i\phi(\tau)} c_{n+1}^\dagger c_n + \text{H.c.} \right). \quad (2.13)$$

For a dispersive lattice with uniform tunneling amplitudes  $t$ , this phase inversion can be thought of as a band inversion  $t \rightarrow -t$ , leading to a complete reversal of dynamics, and is reminiscent of a higher-spin version of a rotary-spin-echo sequence [64].

We summarize our results for this demonstration in Fig. 2.5 for several different phase switching rates. We observe a reversal of dynamics in a 21-site lattice with a phase reversal occurring after roughly  $1.4 \hbar/t$ , allowing population to move out to sites  $\pm 5$  before returning

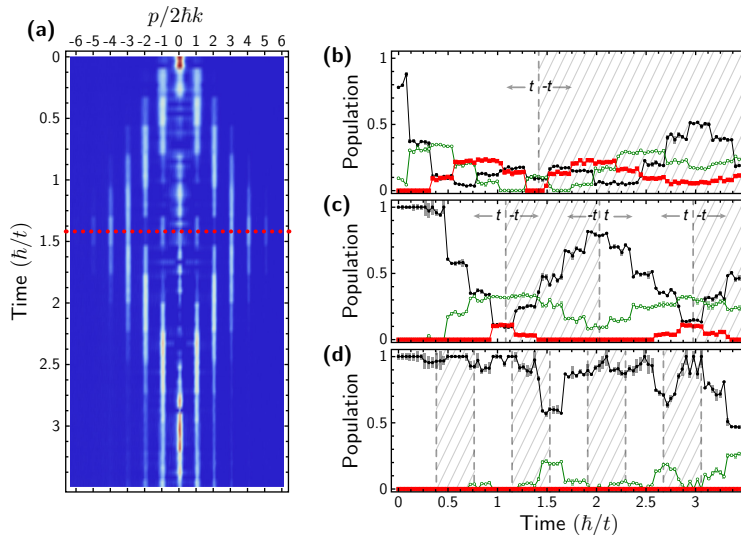


Figure 2.5: Reversal of dynamics through temporal switching of the tunneling phase. **(a)** Integrated absorption images vs evolution time, with  $t/E_r \approx 0.3$  in a 21-site lattice. The tunneling phases are switched by  $\pi$  resulting in  $t \rightarrow -t$ , at roughly  $1.4 \hbar/t$  (indicated by the red dotted line). **(b–d)** Normalized populations of the zeroth, first, and second (black circles, open green circles, red squares) momentum orders vs evolution time. As indicated by the dashed vertical lines and shaded regions, the phase is switched one time, three times, and eight times for panels (b), (c), and (d), respectively. All error bars denote one standard error of the mean. This figure was adapted from Ref. [51].

to the central order as shown in the integrated absorption images in Fig. 2.5(a). By increasing the rate at which we switch the phase we are able to go from this clear case of spreading and refocusing to a case where dynamics effectively cease because population has no time to spread from the central order before being driven back. Figure 2.5(b–d), which shows the population of  $n = 0, 1, 2$  for three different switching rates, illustrates this freezing of dynamics when the phase is switched every roughly  $0.38 \hbar/t$ .

## 2.6 Extensions to Higher Dimensions

So far the discussion of momentum-space lattices has been limited to one-dimension. However, the scheme can be easily extended to higher dimensions through either of two independent mechanisms. The first method is to use higher-order, next-nearest-neighbor tunneling (or beyond) to create a system which is effectively two-dimensional, through higher order connectivities of the states. For the addition of next-nearest-neighbor terms, this type of procedure basically produces two one-dimensional systems connected in some way along

their length and is more akin to a quasi-two-dimensional system. The second method is to introduce more laser fields capable of coupling other momentum states. This extension does indeed create true higher dimensionality but is much more experimentally difficult. Fangzhao Alex An has been the lead student on the experiments we have done in higher dimensions so we only briefly discuss them here as examples of this technique.

The next-nearest-neighbor technique works through second-order, four-photon Bragg transitions. These transitions impart  $4\hbar k$  momentum on an atom making the transition and so link next-nearest-neighbor sites. The set of frequencies needed to link these transitions is also unique and independent of the first-order transitions as they are spaced by the same  $8E_r$  but offset to land exactly in between the first-order transitions, allowing for the same kind of controls to be implemented on these next-nearest-neighbor transitions as can be implemented on the nearest-neighbor transitions as discussed above. One interesting side effect of this is that the resonant frequency to link sites  $n = -1 \rightarrow n = 1$  is 0 Hz, meaning a standing wave resonantly couples these sites.

In general, tailoring specific lattice models with next-nearest-neighbor tunneling can be extremely tricky because unintended couplings can occur when linking certain sites and not others. For example, if the transitions  $n = 0 \rightarrow 2$  at  $8E_r$  and  $n = 2 \rightarrow 4$  at  $24E_r$  are both present then an atom at site  $n = 1$  can be virtually excited by the  $24E_r$  field and unexcited by the  $8E_r$  field for a net change of  $16E_r$  and a momentum shift of  $4\hbar k$ . As it is, the resonant frequency for the  $n = 1 \rightarrow 3$  transition is  $16E_r/h$  and so sites  $n = 1$  and  $n = 3$  have been unintentionally coupled. In addition, the unintentional coupling in this case would be weaker than the intentional couplings because of the detuning of the constituent two-photon transitions from the virtual momentum mode  $n = 2$ . We note that somewhat complicated “echo” sequences can be used to cancel out some of these unwanted processes.

Despite these challenges, we have used the next-nearest-neighbor technique to realize a quasi-two-dimensional model we call a “zigzag” lattice [65]. This model consists of all nearest-neighbor and next-nearest-neighbor couplings being present with a tunable ratio of their strengths. This model was subjected to tunable disorder, flux, and tunneling ratio to observe a flux-dependent mobility edge among other things.

The second method for achieving a multi-dimensional system is the addition of more

lasers. This is much more straightforward and more general in the systems it can create, but it is more experimentally challenging and exacerbates the natural limitations of decoherence and wavepacket spreading. This second laser field works the same way the first laser field works (as described previously) but it couples a different, distinct set of momentum states from the first laser field. When atoms are exposed to both beams they may make transitions between the two sets of states as allowed by the laser frequencies present. This creates a full two-dimensional manifold of states that may be coupled. In addition, this second laser field may be directed along *any* spatial direction as long as the resulting momentum states are not overlapped after time of flight. To note, in our realization of this technique we directed the second laser field along the same direction as the first. This is truer to the spirit of a synthetic lattice where the different synthetic dimensions do not need to be spatially orthogonal as long as they are effectively independent of one another. We have used this technique to create a two-dimensional square lattice with a tunable flux [32] where we observed magnetic reflection and chiral currents. There is ongoing work to extend these capabilities, for the creation of larger, truly 2D momentum-space lattices with tunable parameters.

## 2.7 Interactions

While we have shown that momentum-space lattices have the ability to engineer diverse single-particle Hamiltonians, we have not yet examined the prospects for studying interactions and correlated dynamics. Reference [66] goes through the mechanism by which interactions are realized in the momentum-space lattice in detail. Here, we reproduce a brief discussion of how these interactions arise and display an experimental observation of correlated dynamics.

At first glance, the interactions in this system, resulting from real-space contact interactions, would appear to lead only to all-to-all interactions in momentum space. Ignoring energy-dependent corrections (*i. e.*, finite-range effects), these all-to-all interactions would be incapable of driving correlated behavior, as the total interaction energy would be a constant of motion. However, the same quantum statistics which promotes Bose–Einstein condensation in gases with weak repulsive interactions [67] comes into play with our identical bosons

in distinguishable momentum states. That is to say, the added exchange energy (for pairs of atoms colliding in distinguishable momentum states [68–71]) associated with the symmetry of the two-boson wavefunction results in an effectively attractive interaction between atoms in the same momentum state.

Some intuition of the form of these interactions can be gained by considering the limit where the entire condensate (assumed to be at low density satisfying  $na^3 \ll 1$ , with  $n$  the real-space density and  $a$  the scattering length) is in one momentum state and by considering weakly-populated excitations of this macroscopically-populated condensate. In this case the mean-field energy associated with the condensate of interacting particles leads to the modified dispersion relation given by the Bogoliubov spectrum [68, 72, 73]. A comparison of the parabolic free-particle dispersion and the Bogoliubov dispersion relation is displayed in Fig. 2.6(a) for an average mean-field energy given by  $U = 4 E_r$ . This magnitude of mean-field energy (relating to the density and scattering properties of the gas) yields a modified site energy landscape in momentum space as shown in Fig. 2.6(b). An atom added near zero momentum (relative to the condensate) requires an added energy  $U$ , while an atom added at a large momentum compared to that of the condensate requires roughly  $2U$ , due to the added exchange energy. Subtracting off an overall energy of  $U$ , related to a redefinition of the single-particle states, this form of energies relates to an effective attractive interaction dip at the central, macroscopically populated site. Moreover, this dip has a finite range, due to the partial indistinguishability even for neighboring momentum orders. The general form of these interactions (for the case where population is distributed amongst many orders) is nontrivial, but simple approximate forms hold in certain limits (*e. g.*, the attractive dips are roughly delta-like in momentum space when  $U \ll 2E_R$ ).

Alternatively, the attractive dip in the weak-excitation limit can be thought of as arising from the detunings from Bragg resonance which are introduced when considering the Bogoliubov dispersion, tying back into how we control the site energies in the momentum-space lattice. When we drive transitions at the single-particle resonances these frequencies are actually slightly detuned from the real resonance frequencies when interactions are taken into account. This results in the resonant frequency, which maps directly onto the site energy, being dependent on the number of atoms in a given mode. This picture also provides

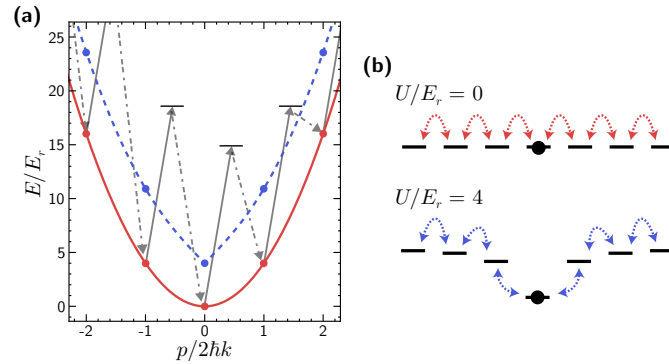


Figure 2.6: The Bogoliubov picture. **(a)** Energy dispersion of noninteracting massive atoms (red solid line) and Bogoliubov dispersion of a homogeneous gas with weak repulsive interactions and a mean-field energy  $U = 4E_r$  (blue dashed line). Gray lines denote laser fields used to couple adjacent momentum states. **(b)** Depiction of site energies shifted by interactions with a  $p = 0$  condensate for  $U/E_r = 0$  and  $U/E_r = 4$ . This figure was adapted from Ref. [66].

an intuitive way to verify and quantify the interactions in our system since we can easily perform Bragg spectroscopy and measure these detunings directly. Figure 2.7(a) shows such a measurement. We drive a zero-momentum condensate with a single variable frequency (characterized by its detuning from single-particle resonance  $\Delta$ ) nearest to the  $n = 0 \rightarrow 1$  transition and observe how much population is transferred after a  $400 \mu\text{s}$  pulse time. We observe a maximum in the transferred population (dashed line) which is detuned from the single-particle resonance (solid line) by  $1.31(3) \text{ kHz} = 0.65(2) E_r/h$ . Figure 2.7(b) shows our measurements (open blue circles) for the Bragg spectroscopy of both the  $n = 0 \rightarrow 1$  and  $n = 0 \rightarrow -1$  transitions and the Bogoliubov dispersion (dashed blue line) is compared to the single-particle dispersion (solid black line) and single-particle resonances (black dots).

As a first experimental demonstration of these interactions we perform a site-energy sweep procedure in a two-site (double-well) system. The protocol, which is illustrated in Fig. 2.7(c), begins with all population in the left well at zero momentum with a large site-energy offset  $\Delta_i$  between this site and site  $n = 1$ . Site  $n = 1$  begins at either a positive or negative energy offset and sweeps through the single-particle resonance with site  $n = 0$  to a final energy offset  $\Delta_f = -\Delta_i$  in a time of 1 ms (this is similar to an adiabatic rapid passage). The initial energy offset is  $|\Delta_i|/h = 8 \text{ kHz}$  such that the coupling strength  $t/h \approx 390 \text{ Hz}$  causes negligible population transfer.

The experimental results of these two sweeps are shown in Fig. 2.7(d) with the positive

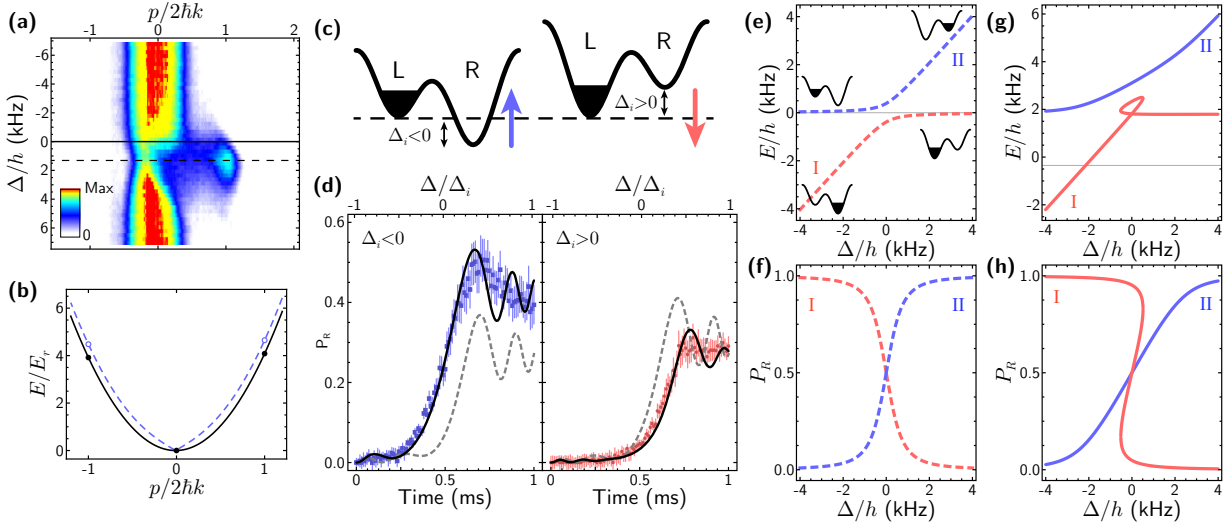


Figure 2.7: Interaction shifts of Bragg tunneling resonances. **(a)** Bragg spectroscopy of the  $0 \rightarrow 1$  transition showing an interaction-driven shift (dashed line) of  $1.31(3)$  kHz from single particle resonance (solid line). The momentum distributions, show population transferred to the state  $p = 2\hbar k$  by a  $400 \mu\text{s}$ -long Bragg pulse vs. detuning from single-particle resonance  $\Delta$ . **(b)** Measured shifts for both  $0 \rightarrow \pm 1$  transitions overlaid onto the Bogoliubov dispersion (dashed blue, shifted by initial condensate momentum  $-0.018 \hbar k$ ) with single-particle dispersion for comparison (solid black). **(c)** Experimental protocol for double well sweeps. Population begins in left well ( $L$ ) and transfers to the right well ( $R$ ) as the imbalance  $\Delta$  is swept linearly across 0 (dashed line) in the positive (left, blue arrow) and negative (right, red arrow) directions over 1 ms. **(d)** Population in the right well  $P_R$  plotted vs. time (lower horizontal axis) and vs. the ratio of the bias to the initial bias  $\Delta/\Delta_i$  (upper horizontal axis). Positive (left, blue squares) and negative (right, red dots) sweeps are shown with single-particle predictions (dashed gray curves) and predictions taking into account the inhomogeneous density distribution with an average mean-field energy  $U/\hbar \approx 2\pi \times 1.81$  kHz (solid black curves). **(e)** Adiabatic energy levels (I and II) of the non-interacting double well vs.  $\Delta$ . Cartoon insets depict the population distributions for large  $|\Delta/h|$ . **(f)** Population projection of the adiabatic levels in **(e)** onto the right well vs.  $\Delta$ . **(g, h)** Energy levels and population projections as in **(e, f)**, but with an added homogeneous mean-field energy of  $U/\hbar \approx 2\pi \times 1.81$  kHz. Error bars in **(b)** and **(d)** denote one standard error of the mean. This figure was adapted from Ref. [66].

sweep in blue in the left panel and the negative sweep data in red in the right panel. We observe a much larger population transfer for the positive sweep than for the negative sweep. In the non-interacting limit this asymmetry would not appear but instead the transferred population would be identical for both sweep directions as is reflected in the single-particle simulations (shown in dashed gray lines in both panels). The data displays much better agreement when considering interactions (shown in solid black lines) where many numerical simulations of a homogeneous nonlinear Schrödinger equation are averaged for different mean-field interaction values using a local density approximation and an average mean-field energy of  $U/\hbar = 1.81$  kHz (see Ref. [66] for more details).

The asymmetry present in the total transferred population can be better understood

by examining the behavior of the adiabatic energy levels of this system. If there are no interactions present a canonical avoided level crossing diagram is produced as shown in Fig. 2.7(e) and population is completely transferred from one well to the other regardless of sweep direction in the adiabatic limit as depicted in Fig. 2.7(f). However, when interactions are added into this calculation, a loop [74–76] (sometimes called a “swallow tail” for its resemblance to the bird) appears in the energy level diagram in the lower branch as is shown in Fig. 2.7(g), which prevents population from transferring adiabatically from one well to the other in the case of a negative sweep. For the upper branch (a positive sweep) the energy levels remain smooth and population may be transferred from one well to another, thus explaining why more population was transferred in our experiment with a positive sweep than a negative sweep as is illustrated in Fig. 2.7(h).

The presence of interactions in this system opens up many possibilities for future study, all of which will be enhanced by the ability to tune interactions. Since the interaction strength in this system is governed by the scattering properties of the gas, if those properties can be controlled then the interactions can be controlled. At these low temperatures the scattering can be well described by two-body elastic collisions. Further, the cross section of colliding atoms in this low-temperature or low-collision-energy limit is given by  $4\pi a^2$ , where  $a$  is the scattering length. The scattering length in our current experiments with  $^{87}\text{Rb}$  is  $a \simeq 100 a_0$  where  $a_0 \approx 0.53 \text{ \AA}$  is the Bohr radius. The principal approach for tuning the scattering length of an atomic species is through a Feshbach resonance [77], which we describe in Sec. 3.3.1. However, the Feshbach resonances present in  $^{87}\text{Rb}$  have a narrow width with respect to an external magnetic field. Since it is difficult to make a magnetic field extremely stable on the sub-milligauss level, this sensitivity makes  $^{87}\text{Rb}$  more difficult to work with in comparison to other atomic species. This leaves us with more or less fixed “attractive” interactions in our momentum-space lattice (they can still be modified with the density of the gas but this does not provide wide, systematic control). This motivated our switch to  $^{39}\text{K}$ , as its Feshbach resonance near 400 G [78] has a practical tuning range on the Gauss level.



# Chapter 3

## Methods

“It’s the worst MOT in the world.”

---

Brian DeMarco on our first  $^{87}\text{Rb}$  3D MOT

“Ralf’s not going to give you what you want. He’s going to give you what you need.”

---

Jackson Ang’ong’a

In our experiments, we use a common (but still complex) method of producing a Bose–Einstein condensate (BEC) from dilute neutral atomic vapors. In fact, for either of the two atomic species to be discussed, none of the techniques we employ are novel, rather they are tried methods developed over the last three decades. For this reason we do not supply an exhaustive discussion of many of these techniques but we do attempt to provide brief descriptions of the physics at work behind them and point the reader to references where detailed information can be found. Our use of a momentum-space lattice, however, is unique and we have devoted Chap. 2 to the theoretical framework of this topic, although the experimental hardware for its creation is discussed here. In addition, we discuss the methods and techniques used for performing the experiments detailed in this manuscript. We include information on how our apparatus was constructed for use with  $^{87}\text{Rb}$ , how it is currently being modified for use with  $^{39}\text{K}$ , how (separate) BECs are made of these two atomic species, and some practical and technical details on how we perform experiments.

## 3.1 Apparatus Overview

### 3.1.1 The Vacuum Chamber

It is certainly true that atomic BECs would not be possible without a vacuum chamber and in this section we discuss the design and construction of ours. A vacuum is necessary because once the atoms have been cooled and trapped, stray particles colliding with them heat them back up and knock them out of their trapping potential. This is indeed the limiting factor on the BEC lifetime in most experiments of this nature, even with pressures in the  $10^{-11}$  Torr regime.

The initial assembly of our chamber (shown in Fig. 3.1) was performed in September of 2014 primarily by Alex An, Bryce Gadway, and myself. This first iteration operated for roughly 4 years until, in the summer of 2018, the vacuum pressure suddenly jumped and we slowly ran out of rubidium slightly ahead of schedule. We suspect either some kind of bad chemistry took place with the dispensers or a leak somewhere else allowed air into the system, or both. The original source cell contained both  $^{87}\text{Rb}$  and  $^{39}\text{K}$  sources and when we went to test the  $^{39}\text{K}$  source in spring 2019 we found it did not work. We tested the dispensers by looking for fluorescence with light resonant with the cycling transition borrowed from another, functional, apparatus in the lab and saw nothing. We decided to replace the atom source with a two-armed cell featuring 6  $^{39}\text{K}$  metal dispensers (SAES), to replace a 25 L/s ion pump (which was reading high pressure) with a 45 L/s ion pump, and to replace the science cell with a larger version. These upgrades were completed in July 2019.

In both incarnations, the vacuum chamber consists of the following parts, with numbering corresponding to Fig. 3.1:

1. Atom Source and Source Cell - For our source we use alkali metal dispensers encased in a forked glass cell blown by Precision Glassblowing in Colorado. We create a two-dimensional magneto-optical trap in this chamber as a source for cold atoms.
2. Differential Pumping Tube I - This is a roughly 0.5 cm inner-diameter tube which is about 6 in long braised into a vacuum flange. This allows for a high differential pressure between the source cell and the science cell without obstructing the beam of cold atoms

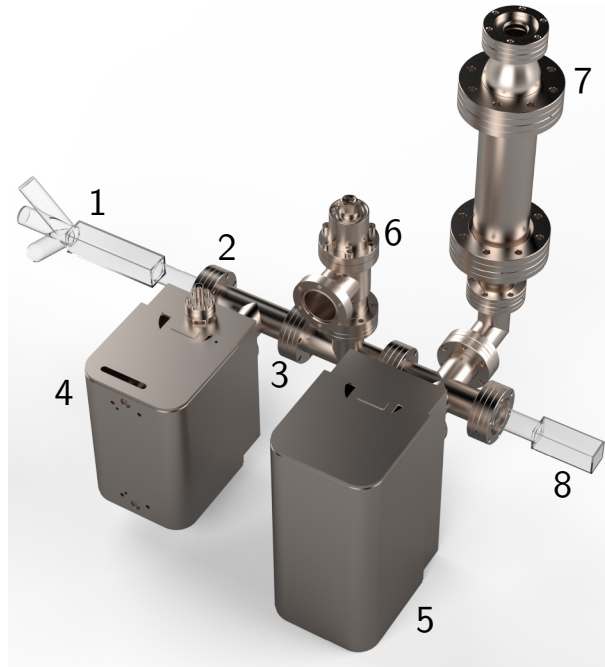


Figure 3.1: Depiction of the vacuum chamber. The different parts as labeled are: (1) The atom source and 2D MOT cell, (2) differential pumping tube I, (3) differential pumping tube II, (4) ion pump I, (5) ion pump II, (6) all-metal valve, (7) titanium sublimation pump, and (8) science cell.

coming from the source cell. The flange holding the tube is sandwiched between the source cell (item 1) and the tee joint which leads to the rest of the chamber and the tube extends several inches in both directions inside the chamber.

3. Differential Pumping Tube II - Same as item 2 but on the other side of the first ion pump to provide additional isolation of the science cell.
4. Ion Pump I - Initially, this was a 25 L/s Gamma Vacuum ion pump but was replaced with a 45 L/s pump in July 2019.
5. Ion Pump II - A larger, 75 L/s Gamma Vacuum ion pump which primarily pumps on the science cell.
6. Valve - An all-metal gate valve which allows for a secure connection to the vacuum chamber. This is usually only used for attaching a turbo pump during a pump-out and bake-out of the chamber.
7. Titanium Sublimation Pump - This is used to coat the inside of the chamber with

titanium to prevent outgassing of other materials from the vacuum parts. We typically only fire this once after a bake but we used it again when the vacuum pumps started reading high as discussed above.

8. Science Cell - Made by Precision Glassblowing as well, the cell was initially  $1.2 \times 0.4 \times 0.8$  in. It was replaced with a  $3 \times 1 \times 1$  in cell in July 2019. This is where the atoms from the source cell are cooled to a BEC and experiments are performed.

The vacuum parts were cleaned prior to assembly with the “AIM” technique (cleaning with acetone, isopropyl alcohol, and finally methanol) in a commercial sonic cleaning bath. We then assembled the parts and attached a turbo pump to begin lowering the pressure in the chamber. When baking the chamber we wrap the apparatus with heater tape ([Omega DHT051040LD](#), seven of these work well for our size chamber) and further wrap everything in vacuum safe metal foil. The heater tape is wrapped directly on the metal vacuum parts and ion/Ti-Sub pumps. However, for the glass cells we build a cage with optomechanics and wrap that with foil, then wrap heater tape around that and then wrap more foil around that to create a small oven. This is done to avoid scratching the glass cells and directly heating the glass-metal interface which can be sensitive due to the different thermal expansion coefficients of the metal and glass. During the wrapping we installed  $\approx 10$  thermocouples to different locations around the vacuum chamber to monitor the temperature.

We then connect each heater tape to an independent variable AC source (variac). Each variac should ideally be connected to an isolated circuit as they are prone to tripping breakers and, more importantly, the turbo pump should *not* share a circuit with a variac. To heat up the apparatus we increase the output voltage of each variac slightly and monitor the thermocouples to ensure we heat up the chamber uniformly. We attempt to increase the temperature by  $+10$  C per hour, or less, until we reach 190 C. We then ease the temperature up slowly to 205–210 C and stop adjusting the variacs. This temperature allows us to keep the magnets on the ion pumps and use them to monitor the pressure during the bake while still achieving  $10^{-11}$  Torr pressures after cooling down.

We baked the chamber for roughly one week with the turbo pump attached and then closed the valve and turned off the turbo pump and continued to bake for another week.

After this we began cooling down the chamber at roughly the same 10 C per hour rate that we used to heat it up. We achieved a final pressure on the 25 L/s ion pump of  $10^{-11}$  Torr, which is the minimum value that the pump can read. The 75 L/s pump stopped at  $\approx 2 \times 10^{-8}$  Torr during cool down which we think was a leakage current causing a false reading. We never had any further problems from this pump and the pressure slowly came down to low  $10^{-10}$  Torr.

This procedure was repeated in July 2019 when we replaced the source cell, science cell and 25 L/s ion pump but with one added layer of complexity. Since we had filled the chamber with  $^{87}\text{Rb}$  for years (and possibly also  $^{39}\text{K}$  toward the end) we were concerned that when we opened the chamber the alkali metal would react with the water vapor in the air in a disastrous way. If the entire inside of the chamber was coated in enough alkali and we exposed it to air it would at best coat the inside of the chamber in a film produced by the reaction which would necessitate a complete disassembly and recleaning of the entire chamber and at worst explode. We did *not* want this to happen so we attached a tank of compressed argon to the valve with a funnel and duct tape before opening the chamber. Then when we opened the angle valve we released a flow of argon into the chamber rather than air. This way when we removed pieces of the chamber argon would flow out of the opened holes, preventing air from flowing in and possibly reacting. There was one issue however, which was the outside of the differential pumping tube which would not have argon flowing across it when we removed the source cell. We prepared a backup tube in case it reacted but no visible reaction took place so we reused the old pumping tube. This allowed us to simply swap the parts we wanted to replace and rebake the apparatus following the procedure detailed above.

### 3.1.2 Atom Source

We use alkali metal dispensers (AMDs) as a source of alkali atoms in our experiments. They are available for a select variety of alkali atoms and we have used them for sourcing  $^{39}\text{K}$  and  $^{87}\text{Rb}$  (with natural isotopic abundances). The alkali metal is stored in a small millimeter by millimeter by inch scale trough containing a proprietary alkali salt chemical. The trough is connected to electrical leads on both ends and sealed inside a custom blown glass cell. When current is sent through the AMD the alkali salt is heated such that a chemical reaction takes

place and the desired alkali atom is given off in gaseous form and escapes the AMD through a small slit.

After working with these devices for a few years we have learned some important practical information about their successful use for this kind of experiment. First, before their first use the AMDs must be activated, which essentially means getting rid of the sealant which is placed on them to protect them until their first use. This is done by passing a current (of 4–6 A for  $^{87}\text{Rb}$  or  $^{39}\text{K}$ ) through them until the vacuum pressure near the source cell increases appreciably. Then the current is lowered until the pressure returns to its base level and the process is repeated. Each subsequent increase in pressure should happen at a lower and lower current until an asymptote is reached or nearly reached. This as-low-as-possible current for our  $^{87}\text{Rb}$  dispensers turned out to be around 3.9 A and for our  $^{39}\text{K}$  dispensers around 4.0 A. While taking data we keep the dispensers on around these values continuously to provide a steady supply of the alkali needed.

Additionally, the wire leads which supply current to the AMD often create leaks in the vacuum system if not handled carefully. They usually come from the manufacturer with heat shrink tubing on them but this will not survive the bake so it has to be carefully removed. After baking we replace the heat shrink tubing around the leads but only shrink it near the top away from the glass-metal interface where the leads come out. Additionally, we connect them to their power source with strain relieved gator clips because we would rather risk this flaky connection than yank the wires and create a leak trying to connect them more securely. We suspected both our initial  $^{87}\text{Rb}$  AMD and our newer  $^{39}\text{K}$  AMD of leaking at this juncture after the bake and in both cases applying a small amount of [Vacseal](#) seemed to fix the problem.

### 3.1.3 Hardware, Software, and Control Mechanisms

To perform an experiment first a BEC must be created, then a lattice must be realized for the atoms, and finally an image must be taken to collect the results. This entire process takes roughly 25 seconds to be completed in our experiments. Often the data we take is as a function of evolution time, such as for the data already presented in Fig. 2.3, or some other

finely sampled variable. Coupling this fine sampling of data with repeated measurements for good statistics results in a measurement consisting of typically thousands of images. With each image taking about 25 s this means that tens of hours of continuous operation is usually necessary. For example, when taking the data on disordered topological wires displayed in Chapter 5 we ran the apparatus around the clock, stopping only to recalibrate every few hours, for six days. In addition, a single experimental cycle requires many different stages to perform, with many lasers and magnetic fields turning on and off or having their power or strength adjusted as a function of time. This is all to say that the remote and automated computer control over as much of the system as possible is all but necessary.

The brain controlling all this automation is a Windows XP computer from the early 2000s running a program specifically designed for cold atom laboratories called Cicero Word Generator [79], which was written by Aviv Keshet of Wolfgang Ketterle’s lab at MIT (based off of original word generator programs developed by, *e. g.*, Til Rosenband). The program uses a field-programmable gate array (we use an Opal Kelly XEM3001) and interfaces directly with other National Instruments (NI) hardware to control timing and send signals to the apparatus. We use Cicero (and hardware interfacing program Atticus) to communicate with other hardware through 0–10 V analog signals, 5 V digital (TTL) signals, and GPIB-class serial communication. The analog, digital, and serial signals are created by an NI PXIe-1073 chassis. It has an NI PXIe-6535 digital I/O card passing to an NI SCB-68A pinout for the digital signals which are optically isolated before being sent to the apparatus. For the analog signals, an NI PXIe-6733 card passes the signals to an NI BNC-2110 pinout which feeds into basic optical isolation circuits (see Sec. A.1) before heading to the apparatus. Also in the chassis is the processing card for the GPIB signals, an NI PXIe-GPIB. Analog signals are used to control things which need to have their magnitude changed in time, like the power of a laser beam or the strength of a magnetic field. Digital signals are used primarily as switches to turn on or off AOMs, open or close shutters, switch magnetic fields on or off, and finally send triggers to other hardware like the arbitrary waveform generator (AWG) (Keysight 33612A) that drive the AOMs that create the momentum-space lattice. The serial communication is used to change the waveform being output by the AWG between runs, which enables us to change a parameter of the experiment which is encoded in the waveform

itself.

The ability to change the waveform translates into the ability to modify the specific Hamiltonian being studied—*i. e.*, our effective Hamiltonian is spectrally engineered through the Bragg laser frequency spectrum. Coupled with the built in control afforded by Cicero to change the experimental time, this allows us to procedurally change almost any parameter we like. Automation at this level makes for very efficient data taking, allowing us to preprogram “runs” where thousands of images are taken over several hours and freeing us to do other work (or occasionally goof off) while the data is being taken. Taking data all at once is beneficial because it helps to reduce the chances that something will go wrong or become misaligned with the apparatus before all the data is taken, which serves to ensure some consistency in experimental factors between measurements. This mode of operation results in the vast majority of the time spent on a specific experiment being devoted to planning, analysis, and writing, rather than taking data.

## Lasers

Several lasers are necessary for these experiments, both for the creation of the BEC and for its subsequent manipulation and probing. The roles of the lasers will be discussed more thoroughly in the sections regarding the specifics for creating BECs. Here, we discuss the basics of how different frequencies are created and controlled. During parts of the experimental sequence we need to manipulate both the power and frequency of the lasers present. To control the power we can physically block the laser using an electronically-actuated shutter or by switching off the acousto-optic modulator (AOM) that is deflecting the beam along a path leading to the experiment (typically through an optical fiber). AOMs shift the frequency of a laser as well as deflect the laser’s path and we use this to provide many of the required laser frequencies. We use a variety of AOMs for different frequency shifts and optical wavelengths, including Gooch & Housego [R23080-1-1.06-LTD](#) for the 1064 nm and 1070 nm laser power controls, Gooch & Housego [3080-120](#) and [3200-121](#) for light in the 767-780 nm range, and also Isomet [1205C-843](#) for the two lattice creation AOMs (see Subsec. [3.1.4](#)) at 1064 nm.

We use Vincent Associates Uniblitz drivers and shutters to physically block and unblock lasers remotely as part of the experimental sequence. For high powered lasers we use the reflective model of shutter [VS25S1ZM0](#) in conjunction with a beam dump to prevent a fire, but for low power lasers we use Teflon coated shutters [VS25S1T0](#). All of these shutters are driven by either [VCM-D1](#) or [VMM-D4](#). The drivers take in 5 V signals to open and close the shutters they control. We typically mount them on top of [Sorbothane](#) to dampen the mechanical shock produced by their rapid movement. These shutters take roughly 6.00(2) ms to close or open fully, but by aligning the beam right on the center of the shutter aperture, faster actual times can be achieved because the beam waist is much smaller than the roughly 1 in opening of the shutter. For faster and more reliable switching (but potentially less complete) the AOM which is “creating” the specific laser can be turned on or off by its supply RF (RF control is discussed in detail below). This is much faster, on the order of a hundred nanoseconds, as the electronics are much quicker to respond than a mechanical shutter. However, to be absolutely sure a laser is or is not present we often incorporate both shutters and AOMs into a single path.

The primary use of an AOM in the path of a laser is to change its frequency to align with some desired value, such as an atomic transition for example. But another utility is for power stabilization using a feedback circuit. This is typically only done with lasers whose power stability is very important, like those used as optical dipole traps for creating the BEC, or the lattice laser. This is done by measuring the power of the laser as close as practically possible to the atoms using a beam pick off and photodiode. The signal from this photodiode is then sent to an active feedback loop that sets the output RF power to the AOM by comparing the measured beam power to a set point value supplied by the computer. This feedback is done with a PID (proportional–integral–derivative) circuit (Stanford Research Systems [SIM960](#) module housed in a [SIM900](#) mainframe). Then by controlling the set point via Cicero the laser power can be controlled in a fast, time-dependent way. This is used to program the optical trap power to decay exponentially for evaporative cooling, among other things.

In addition to these controls, the main lasers used for any near-resonant tasks must be frequency stabilized with respect to the atomic transition with which they will be used. This is commonly referred to as “locking” the laser because a feedback loop circuit is used

to compare the laser frequency with a reference point and it adjusts the laser diode controls to keep the frequency stable. The reference point can be provided by using a small amount of the laser power to excite an electronic transition in a vapor cell using one of a myriad of different spectroscopy techniques. In the case of our  $^{87}\text{Rb}$  apparatus, we have two lasers which need to be locked. The first, the laser near resonant with the  $F = 2 \rightarrow F' = 3$  transition (cycling, see Fig. 3.3), is locked via polarization spectroscopy [80]. The second laser, near-resonant to the  $F = 1 \rightarrow F' = 2$  transition (repump) is instead locked to a signal generated electronically via mixing both the cycling and repump lasers with a controlled rf signal. This is performed by first mixing the cycling and repump lasers in free space and shining them on a photodiode with a bandwidth high enough to detect the difference frequency. This difference frequency is divided by 64 electronically and then mixed with an rf signal provided by a voltage controlled oscillator (VCO) around 100 MHz. This produces a locking signal for the repump laser with reference to the already locked cycling laser. This is called an offset lock and we discuss it in further detail in Sec. A.2.

In the case of our  $^{39}\text{K}$  apparatus we again have two lasers to lock but this time one is near-resonant to the  $D_2$  transition and one is near-resonant with the  $D_1$  transition, and these lasers are both locked via polarization spectroscopy. Each one is still split into a cycling and repump transition as well but in  $^{39}\text{K}$  the required optical frequencies are only split by  $\approx 460$  MHz (rather than  $\approx 6.6$  GHz for  $^{87}\text{Rb}$ ) and so the repump light for both lasers is created from the cycling with AOMs or electro-optic modulators.

### Radio Frequency Signals

Radio frequency (RF) signals are used to drive many AOMs in the apparatus. A variety of different hardware is used to create the RF signals used to power the AOMs depending on the specific application. Our typical RF source is a Voltage Controlled Oscillator (VCO) like MiniCircuits ZX95-100-S+. These are good for lasers that need to have their frequency changed throughout the experimental sequence as these sources can be tuned through a simple control voltage signal. For the power control AOMs on the optical trapping and lattice beams we use a Wenzel crystal oscillator (SC Sprinter 501-09133) because we only need a

pure, fixed frequency for these paths. Finally, to create the lattice we need a multifrequency RF drive for the lattice AOMs. For this we use an arbitrary waveform generator (Keysight 33612A) programmed to output the multifrequency signal. We further control the power of the RF signals through the use of switches (MiniCircuits ZASWA2-50DR-FA+) and Voltage Variable Attenuators (VVAs, MiniCircuits ZX73-2500-S+). The switches turn the RF on or off based on a 5 V input controlled by computer, and the VVAs take an analog control voltage signal in and attenuate the RF power based on that control voltage.

### 3.1.4 Momentum-Space Lattice Creation

To create the multifrequency beam needed to make the momentum-space lattice we use an optical layout as shown in Fig. 3.2. The laser used for the lattice beam is one of the optical dipole trap beams after it has passed through the science cell. By creating the lattice out of a trapping beam we ensure near perfect alignment of the lattice with the BEC. The lattice beam enters the setup with a right-circular polarization  $\hat{R}$  which is immediately switched to vertical  $\hat{V}$  with a quarter-wave plate. After a polarizing beam splitter and two steering mirrors the beam passes into the first of two AOMs which create the multifrequency field used to create/control the momentum-space lattice. This first AOM is driven with a single frequency at 80 MHz (the center frequency of the AOM's response) and the +1<sup>st</sup> order is taken. The orders of the AOM correspond to how many integer frequency shifts the laser light gained, *i. e.*, the  $\pm i^{\text{th}}$  order corresponds to the laser frequency shifting by  $\pm i \times 80$  MHz in this case. The second AOM in the setup is where the lattice frequencies are written onto the laser beam. This AOM is driven with  $80 \text{ MHz} - \sum_n \tilde{\omega}_n$  where the  $\tilde{\omega}_n \ll 80 \text{ MHz}$  and we take the -1<sup>st</sup> order. Since we first took the +1<sup>st</sup> order and then the -1<sup>st</sup> order, the overall 80 MHz shifts from the two AOMs cancel each other out and the final beam has only the set of frequencies  $\omega^+ + \tilde{\omega}_n$ , where  $\omega^+$  is the base frequency of the laser corresponding to  $\lambda = 1064 \text{ nm}$ .

The presence of the multifrequency drive has the effect of essentially splitting the -1<sup>st</sup> order of the second AOM into many independent (but phase-stable) laser fields, each with a frequency  $\omega^+ + \tilde{\omega}_n$ . Because the angular deflection of a diffracted beam depends on the

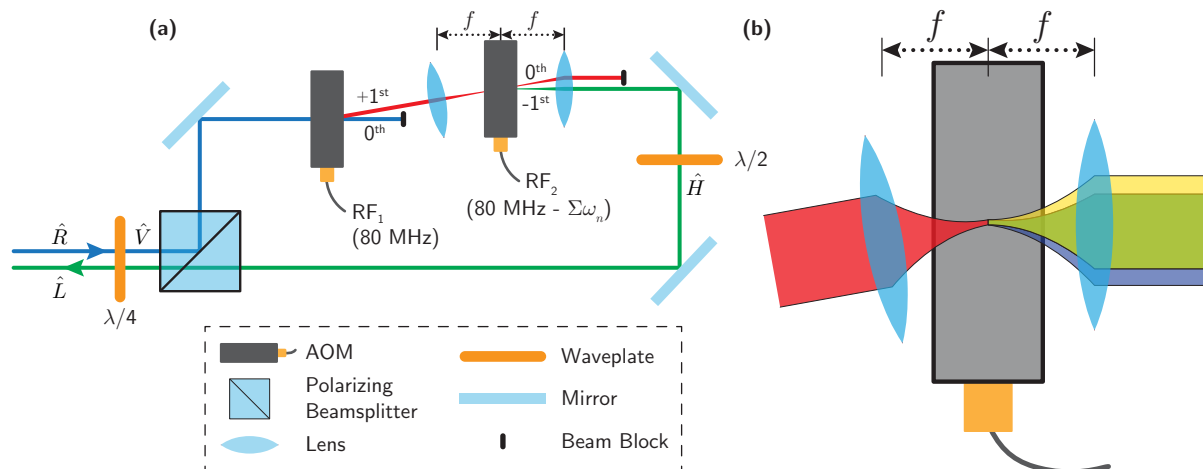


Figure 3.2: Optical layout used to create the momentum space lattice. **(a)** Overview of the beam path that creates the multifrequency field.  $RF_1$  is a constant 80 MHz driving field and  $RF_2$  is a multifrequency drive. In experiment the incoming and outgoing beams are aligned to be perfectly counterpropagating. **(b)** Close up of the second AOM from **(a)** being driven by a two-frequency drive. The incoming red beam is diffracted into the  $-1^{st}$  order ( $0^{th}$  order not shown) of the AOM which is split into two separate beams by the two-frequency drive (yellow and blue beams shown at right). These two beams are recollimated and made parallel to each other by the second lens.

frequency shift it received, these new beams are also spreading apart from one another as they move away from the second AOM, and this is where the lenses straddling the second AOM serve their purpose. The first lens is placed one focal length before the AOM so that the incoming beam [the red beam at left in Fig. 3.2(b)] gently focuses at the center of the AOM. This beam is diffracted into the  $-1^{st}$  order of the AOM which is split into many beams by the multifrequency drive. These diffracted beams—two representative beams are shown in yellow and blue in Fig. 3.2(b)—are at the same time individually diverging themselves and separating from each other. Then the second lens, placed one focal length after the AOM, both recollimates each beam and stops the beams from spreading further apart in space. If the second lens is close enough (this is rather easy experimentally) then the effective operation of this setup is to generate a single laser field with many discrete frequencies, which is shown as the green laser formed by the overlap of the yellow and blue lasers in Fig. 3.2(b). The transverse displacement of the various frequency components can be made small in experiment.

Now that the multifrequency field has been created it needs to be directed onto the atoms to counterpropagate with the incoming beam and create a lattice. This is accomplished by

changing the polarization from vertical to horizontal  $\hat{H}$  so that the beam can pass through the polarizing beam splitter from which it initially reflected. The figure shows these two beams [blue and green in Fig. 3.2(a)] separated in space only for ease of illustration. In experiment, these beams are aligned to be perfectly counterpropagating. Following the quarter wave plate, the resulting counterpropagating beam with left-handed circular polarization leads to interference with the forward-traveling (and right-circularly polarized beam).

## 3.2 $^{87}\text{Rb}$ BEC Creation

The prediction by Bose and Einstein in 1925 [81, 82] of a sudden macroscopic population of the ground state in a bosonic gas due to quantum statistics initiated a quest which has been likened to the search for the holy grail. After 70 years of scientific effort and advancement, the first BEC was finally created by the group of Eric Cornell and Carl Wieman with  $^{87}\text{Rb}$  [83] and separately by the group of Wolfgang Ketterle with sodium atoms [84]. The discovery resulted in the 2001 Nobel Prize in physics. The group of Randy Hulet also achieved the same feat using lithium [85]. However, the experiment was more controversial at the time due to the attractive interactions present in the system which made the signatures of condensation less clear. Our procedure for creating a  $^{87}\text{Rb}$  BEC relies heavily on the work of these groups and others who paved the way in the last few decades in the development of laser cooling, trapping, and evaporation techniques.

To create a BEC, not only must the temperature of the gas be lowered below some level but the number density  $n_d$  of the gas must also be high enough (these two quantities are intertwined, as the critical temperature is dependent on the particle density). Intuitively, this can be understood by the fact that for the properties of an ensemble to depend on the quantum statistics of the constituent particles, the average space between them must be similar to their characteristic “size”, relating to their thermal de Broglie wave coherence length. This idea is captured by a dimensionless metric called the phase-space density  $\rho_{\text{ps}} = n_d \lambda_{\text{dB}}^3$ , which combines the number density  $n_d$  and the thermal de Broglie wavelength  $\lambda_{\text{dB}} = h/\sqrt{2\pi m k_{\text{B}} T}$  with  $m$  the mass of the atom and  $k_{\text{B}}$  the Boltzmann constant. In terms of this convenient metric, BEC is reached in a dilute atomic gas when  $\rho_{\text{ps}} \geq 2.612$  [86], which

happens to be a universal value regardless of the trapping potential. The trap does have a significant effect on the critical temperature however, because it affects the volume of the gas. If we approximate our trap as an isotropic harmonic oscillator with a trap frequency of 100 Hz, and say we have  $5 \times 10^5$  atoms in the trap, the critical temperature would be  $T_c \approx 450$  nK [86] and indeed the first  $^{87}\text{Rb}$  BEC had a reported temperature of 170 nK [83]. This means the atoms must be cooled from, say, 300 K to 300 nK, nine orders of magnitude. For comparison, the surface of the sun is only about 20 times hotter than 300 K.

The rest of this section details how this is done in our apparatus. We begin with an overview of the process:

- (i) A 2D Magneto-Optical Trap (MOT) is initially loaded from our alkali metal dispenser sources. This pre-cools the atoms in two dimensions and leaves them untrapped in the third dimension. In addition, a pushing beam is added along the untrapped dimension to create a beam of atoms traveling through the vacuum chamber.
- (ii) This beam of atoms is collected in a 3D MOT at the other side of the vacuum chamber where the background pressure is much lower than at the source side. This MOT collects  $\sim 10^9$  atoms in roughly 10 seconds from the atomic beam. In the MOT the atoms are cooled by radiative cooling to temperatures in the mK regime.
- (iii) Several stages of further cooling are performed to increase the density and reduce the temperature of the gas, including a compressed MOT, a temporal dark MOT, and optical molasses. These procedures lower the temperature of the atoms to the  $\mu\text{K}$  regime.
- (iv) The atoms are then optically pumped such that they are made to all occupy the same internal (hyperfine and Zeeman) state, such that they can be trapped solely by a magnetic quadrupole field.
- (v) With the atoms trapped in the magnetic trap they are loaded into an optical dipole trap (which is offset from the field zero) with around 1% efficiency, leaving us with a few  $10^6$  atoms left.

- (vi) Once the atoms are loaded into the optical dipole trap, the quadrupole magnetic field is switched off (with a dc bias field remaining) and the power in the beams is lowered exponentially in time to perform evaporative cooling. This last stage decreases the temperature into the nK regime, increasing the phase-space density to a point that a BEC forms.

In the rest of this section we discuss these techniques in more detail and give additional information on their specific realizations in our apparatus.

### 3.2.1 The Magneto-Optical Trap

A MOT consists of a specific arrangement of lasers and a magnetic field and we begin our discussion with the lasers. To trap  $^{87}\text{Rb}$  in a MOT there are two laser-driven atomic transitions that come into play which are conventionally called the cycling and repump transitions. The cycling laser addresses the transition  $5^2\text{S}_{1/2} F = 2 \leftrightarrow 5^2\text{P}_{3/2} F' = 3$  (the prime in  $F'$  denotes the excited state) which are two electronic hyperfine levels as shown in Fig. 3.3. The standard notation for defining these energy levels in terms of the quantum numbers of the atoms as used above is  $n^{2S+1}L_J$ , where  $n$  is the principal quantum number,  $S$  is the electron spin  $1/2$ ,  $L$  refers to the orbital angular momentum of the electron (S for  $L = 0$ , P for  $L = 1$ , D for  $L = 2$ , ...), and  $J = L + S$  gives the total electronic angular momentum (note:  $S$  refers to the electron spin of  $1/2$ , not to be confused with the electron orbital angular momentum for  $L = 0$  which is given the shorthand S). Further, the nuclear spin  $I$  (for both  $^{87}\text{Rb}$  and  $^{39}\text{K}$   $I = 3/2$ ) must be taken into account to get the electronic levels  $F = I + J$ .

It so happens that this “cycling” transition in  $^{87}\text{Rb}$  is nearly closed, meaning that once in the excited state the atom has only a small probability of decaying to any other level than the one in which it started. This means that a given atom may absorb and reemit many photons from the cycling laser before it makes an undesired transition into a state not resonant with the cycling laser. Hence, one can use the “cycling” laser to perform this cycle of excitation and decay many, many times. In addition, the cycling lasers are slightly red-detuned (by  $\sim 10$  MHz) from the transition frequency, such that when an atom is traveling with some

velocity into the beam it sees the laser as on-resonance through a Doppler shift. In this way, an atom is more likely to damp its motion rather than to speed up, i.e. more likely to scatter a photon when it is moving towards the laser source, rather than away from it. Since the photons from the laser have a momentum opposite of the moving atom they have a net effect of slowing the atom down when absorbed. If the photon is reemitted backward, the atom will speed back up to its original momentum, but the emission process happens randomly in any direction thereby slowing the atom down on average and removing its kinetic energy. One common and not too wrong analogy of this is slowing down a speeding semi truck by bouncing many ping pong balls off of it.

This cycling transition is very efficient at removing energy from the atom but it is not perfect as mentioned above. Sometimes the cycling light excites an atom from  $F = 2 \rightarrow F' = 2$  and from this state the atom may decay to  $F = 1$ . It is now 6.83 GHz (the hyperfine ground state splitting) away from resonance with the cycling laser and therefore no longer feels its effects. This necessitates the use of a repump laser as shown by the light blue wavy line in Fig. 3.3. For atoms amenable to laser cooling such as  $^{87}\text{Rb}$ , only one repump laser is necessary and it is conventionally tuned to the transition  $F = 1 \leftrightarrow F' = 2$ . When an atom initially in the cycling laser loop falls to the  $F = 1$  state it becomes resonant with this laser and makes the transition from  $F = 1 \rightarrow F' = 2$ . Once in  $F' = 2$ , the atom may decay to either  $F = 1$  or  $F = 2$  and when it enters the  $F = 2$  state it is back on resonance with the cycling laser and continues to be cooled on this transition. For  $^{87}\text{Rb}$  the transition rates work out such that the repump light requirements are very forgiving; we use a ratio of approximately  $< 10\%$  repump to cycling power.

These two lasers are typically directed at the atoms from six directions for a standard 3D MOT although other geometries can be used. Three pairs of counterpropagating beams are arranged, each perpendicular to the others. At their intersection [as shown in Fig. 3.5(a)], they form a region in which atoms moving in any direction are slowed down. These six beams form what is called an optical molasses [90] because the velocity-dependent damping force, caused by the Doppler effect as described above, makes the atoms behave as if they were particles submerged in molasses regardless of their direction of travel. This is not the whole story however, as just the presence of this drag force from the lasers does not constitute

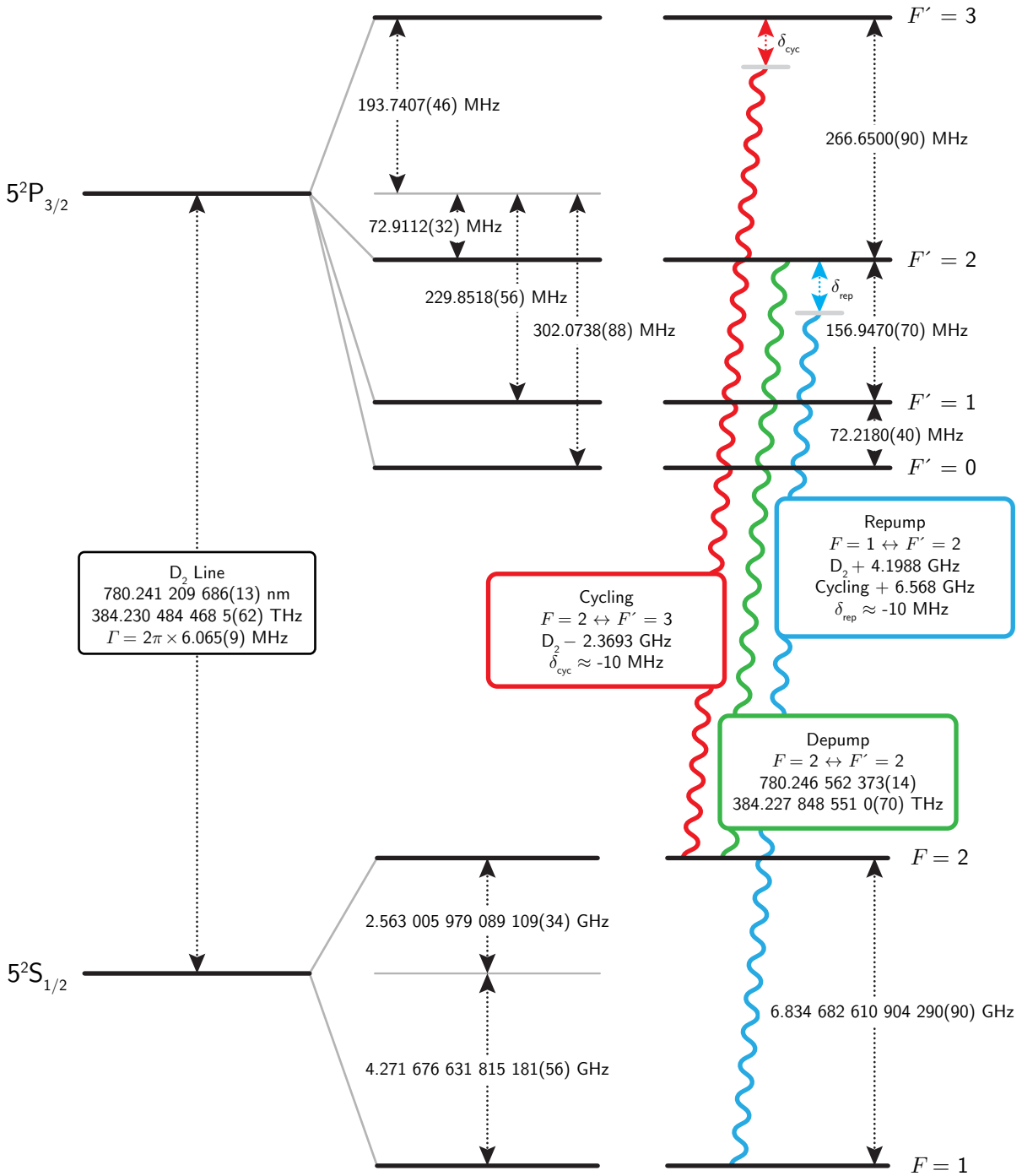


Figure 3.3: Level diagram of relevant transitions for the  $^{87}\text{Rb}$   $D_2$  line. The cycling laser (red wavy line) is shown connecting  $F = 2 \leftrightarrow F' = 3$ , the repump laser (light blue wavy line) is shown connecting  $F = 1 \leftrightarrow F' = 2$ , and the depump laser (green wavy line) used for optical pumping is shown connecting  $F = 2 \leftrightarrow F' = 2$ . This figure was adapted from Ref. [87] with numbers from Refs. [87–89].

a trap. In order to form a trap, the atoms must also feel a position-dependent force, one drawing them to the intersection of the lasers. This position-dependent force is provided by a quadrupole magnetic field. In total, the combination of radiative and magnetic forces form the trapping and cooling of the MOT.

The magnetic field works on the atoms by shifting the energy of the Zeeman levels to bring the lasers into resonance when the atom is not at the trap center. These Zeeman levels are the previously degenerate  $m_F$  sublevels (as long as the magnetic field is relatively weak) whose degeneracy is now broken by the presence of the magnetic field. The quadrupole configuration of the field is such that the zero-point of the field coincides with the intersection of the laser beams. When an atom is offset from the center of the trap, its energy levels are shifted by the magnetic field gradient such that the further from the center the atom goes the larger the shift. If the polarizations of the different laser beams are set properly with regard to the magnetic field direction, this shift from the magnetic field will result in the atom becoming closer to resonance with the cycling or repump lasers and getting pushed back toward the center of the trap. Therefore, through the combination of the lasers and the magnetic field, the atoms feel velocity- and position-dependent forces which both remove their kinetic energy and force them toward the trap center. In a 3D MOT the quadrupole field is typically provided by a single pair of anti-Helmholtz (*i. e.*, currents traveling in opposite directions) circular coils positioned close to the atoms. To transition this into a 2D MOT the quadrupole can be provided by rectangular coils which have an elongation along one dimension resulting in a weakened gradient along that dimension. To go even further, one can use two pairs of quadrupole coils which are all elongated in the direction parallel with the axis of no or weak trapping. This two-pair scheme results in a much more ideal 2D quadrupole field along its axis and results in a more uniform gradient in the cooling plane. To change the laser configuration for a 2D MOT, one pair of counterpropagating lasers is removed along the axis where trapping is not desired, resulting in two pairs of counterpropagating beams coming in along the cooling and trapping axes perpendicular to each other as shown in Fig. 3.4(a).

Now that the basic workings of a MOT have been explained, we turn to the specific case of our apparatus. The 2D MOT is made in the source chamber (item 1 in Fig. 3.1) where

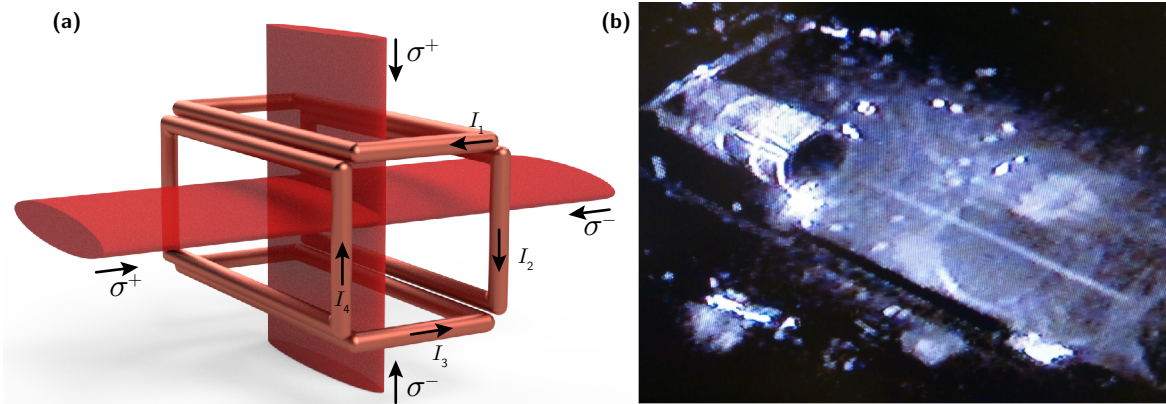


Figure 3.4: The 2D MOT. **(a)** Schematic of lasers and magnetic field for the 2D MOT. The copper-colored rectangles represent the quadrupole coils which are roughly  $5 \times 2$  in carrying currents  $I_1$ ,  $I_2$ ,  $I_3$ , and  $I_4$ . These currents are each independently adjusted to control the field center. The circular polarizations used for the six laser beams are shown as  $\sigma^+$  for right-handed circular and  $\sigma^-$  for left-handed circular. **(b)** Picture of the two-dimensional magneto-optical trap. The image shows a close-up of the source cell with the end of the transfer tube in the upper-left. The 2D MOT is the bright line of fluorescing atoms which appears in front of the tube at the same angle.

the dispensers provide a high vapor pressure of  $^{87}\text{Rb}$ . The atoms are tightly confined in the plane perpendicular to the transfer tube and weakly confined parallel to the transfer tube creating a line of trapped atoms by the combination of lasers and magnetic field shown in Fig. 3.4(a). In addition, blue and red detuned (from the cycling transition) pushing beams [91] are directed along the length of the vacuum chamber to create a beam of atoms moving from the atom source side to the science cell.

Our cycling and repump lasers (two Toptica DL100 external-cavity diode lasers), are slightly red-detuned (roughly 10 MHz) from the D2 line [see Fig. 3.3]. They are combined using a  $2 \times 2$ , 50:50 fiber coupler (Thorlabs PN780R5A2) yielding two fiber outputs each containing both cycling and repump light. The beams are shaped to be elliptical using cylindrical lenses and have visual dimensions  $5 \times 1$  cm. Roughly 35–40 mW of power per beam of cycling light and 2–3 mW of repump light are used. After these two beams pass through the atoms (one in the vertical dimension and one in the horizontal dimension) they are reflected and aligned to counterpropagate with themselves to create the four cooling light fields as shown in Fig. 3.4(a). The figure also shows the polarizations of the beams which are essential for the interplay of the lasers and magnetic field.

The magnetic quadrupole field is created with four independent wire coils made from

22-gauge magnet wire. The coils are rectangular with an aspect ratio similar to the atom source cell and are placed around the cell, offset from the top and bottom and sides as shown in Fig. 3.4(a). Each pair of coils (top and bottom and side-to-side) is arranged to be anti-Helmholtz and the two pairs of coils have their currents configured such that their individual quadrupole fields add constructively. We adjust the current in each coil independently to control the field center and thus the position of the MOT. We have also used permanent magnets in the past to successfully form a 2D MOT but this method lacked the ability to finely adjust the position of the field zero and was abandoned. The atoms which leave the source cell with the right velocity make their way through the vacuum chamber and into the science cell (item 8 in Fig. 3.1). In this region we have a 3D MOT setup capable of capturing some fraction of the atoms coming from the source cell. With this scheme we are able to load a 3D MOT of around  $10^9$   $^{87}\text{Rb}$  atoms in about 10 s.

The laser arrangement for the 3D MOT is similar to the 2D MOT but with an additional beam in the horizontal plane perpendicular to the other two beams as shown in Figs. 3.5(a) and 3.6. We have a total of 80 mW of cycling power for our 3D MOT which is split evenly between two fibers. The power is distributed unevenly along the three final beam paths with the light from one fiber supplying the vertical beam and the light from the other fiber split with a polarizing beam splitter to supply 20 mW each to the two horizontal paths. The vertical path is larger however, resulting in similar but still slightly imbalanced intensities at the atoms between the three paths. A second fundamental difference between our 3D and 2D MOT setups is the repump configuration. In the 2D MOT the repump and cycling light are combined directly with a fiber coupler, but in the 3D MOT the 4–5 mW of repump light is directed along the imaging path, totally separated from the MOT beam paths as shown in Fig. 3.6. This works for  $^{87}\text{Rb}$  because the cycling transition is closed such that the cycling light does most of the cooling and trapping so the need for repump light is very modest in terms of power, alignment, and polarization.

The magnetic field for the science cell is treated more carefully than for the source cell and a schematic is shown in Fig. 3.5(a). We have a single pair of circular coils arranged to form a quadrupole field and placed with roughly 1 cm of clearance above and below the edge of the cell in the vertical dimension. This creates the trapping field necessary for

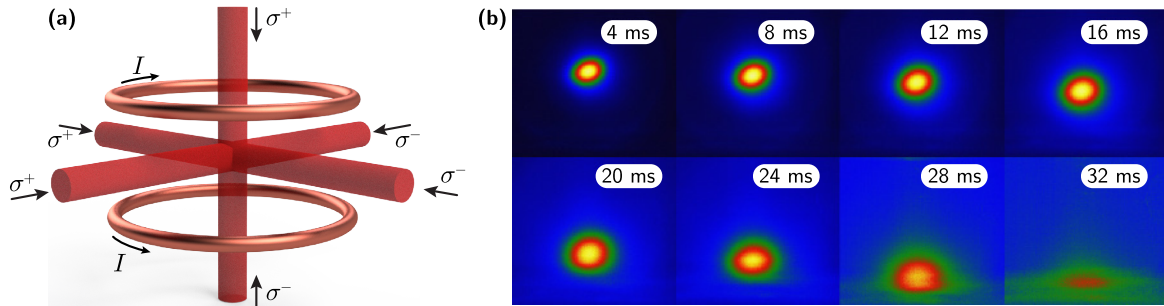


Figure 3.5: The 3D MOT. **(a)** Schematic of lasers and magnetic field for the 3D MOT. The circular coils are connected in series and carry a current  $I$  in an anti-Helmholtz configuration to produce a quadrupole at the position of the atoms. The circular polarizations used for the six laser beams are shown as  $\sigma^+$  for right-handed circular and  $\sigma^-$  for left-handed circular. **(b)** Fluorescence images of the 3D MOT as it falls during a time of flight period, eventually hitting the bottom of the science cell at 26 ms.

forming the MOT but we also employ a cube of rectangular shimming coils offset from cell by several inches in all dimensions. These shimming coils are not shown in Fig. 3.5 but can be seen in Figs. 3.14 and 3.17. They consist of a Helmholtz and anti-Helmholtz set of coils along all three dimensions, and are used to cancel out any stray fields that may be passing through our science cell (Earth's field included) as well as to shift the position of the 3D MOT quadrupole field zero. Magnetic fields are used not only for the 3D MOT but also for magnetic levitation of optically pumped atoms, providing a quantization axis for imaging, and evaporation.

The MOT is an excellent and very important tool for trapping and cooling hot or room temperature atoms. However, the near-resonant processes and constant photon cycling which make it capable of trapping and cooling very hot atoms also place a natural limit on how cold the atoms can get in the MOT. Since the atoms are constantly cycling photons, the minimum velocity they can obtain is the amount of momentum imparted on them when they emit a photon in a random direction, called the recoil energy. This effect coupled with radiation pressure, impose limitations which prevent a MOT from coming anywhere near the temperatures and densities needed to achieve a BEC and thus more cooling and state manipulation is needed.

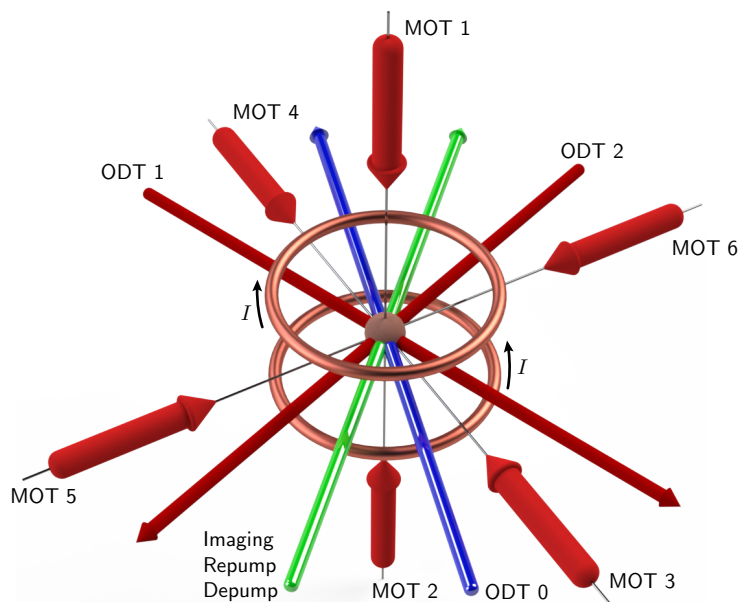


Figure 3.6: Beam layout for the science cell. The two rings represent the coils used to produce the quadrupole field. They are connected in series with current  $I$  traveling in opposite directions (anti-Helmholtz). The six MOT beams are shown as red arrows offset from the atoms for ease of illustration. In addition, the DSPOT repump beam is also directed along these six pathways. The green beam represents the path that hosts the main repump light, the depump light used in optical pumping, and the imaging beams at various different times in the experimental cycle. The blue beam represents the path of ODT 0, the 1070 nm large-volume trap which is turned off after the evaporation sequence. The perpendicular dark red beams represent the paths of ODT 1 and ODT 2, which form the 1064 nm small-volume trap at their intersection. ODT2 is used as the lattice beam after the BEC has been produced. The atoms are represented by the sphere in the center of the beams. Note that the size of beams and the atomic cloud are not to scale.

### 3.2.2 Further Cooling and Optical Pumping

After the 3D MOT has been loaded with enough atoms to eventually get to a BEC we “turn off” the atom source by extinguishing the 2D MOT cycling, repump, and pushing beams. At this point the 3D MOT atoms have too much energy and are not in the right Zeeman level to be optically trapped so we perform Compressed MOT (CMOT) [92, 93] and Dark SPontaneous-force Optical Trap (DSPOT) [94, 95] stages to further cool the atoms and increase their density. The CMOT consists of a linear ramp of the magnetic quadrupole field to physically push them closer together and increase the density. The DSPOT allows the atoms to be pushed closer together by reducing scattered radiation pressure as they are shelved in a dark state through the absence of repump light near the trap center. This way atoms only cycle photons when they near the trap edge and are pushed back into the dark trap center when they do. In experiment, this absence of repump light at the trap center

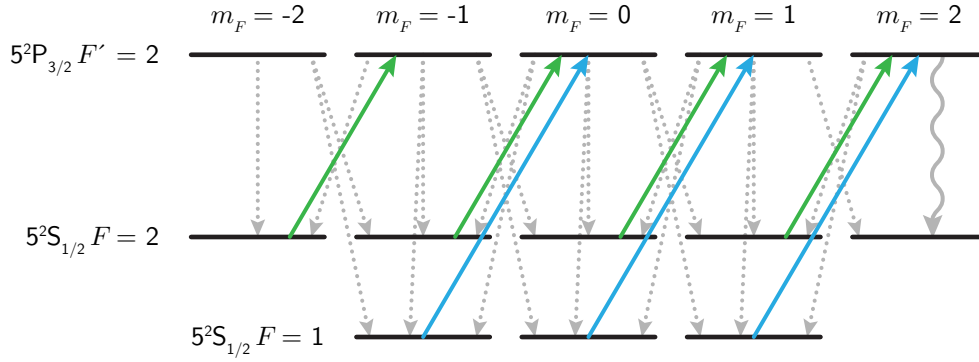


Figure 3.7: Diagram of  $^{87}\text{Rb}$  optical pumping. The depump (green arrows) and repump (blue arrows) lasers are tuned to be right-handed circular  $\sigma^+$  such that  $m_F \rightarrow m_F + 1$  when an atom makes a transition. An atom starting in any state shown will make its way to  $|F, m_F\rangle = |2, 2\rangle$  via driven transitions and spontaneous emission. Atoms that make it to this long-lived state are insensitive to the repump and depump lasers because of their polarization and remain in this state for the duration of the experiment.

is achieved by switching to a repump beam path containing a mask on a glass microscope slide which blocks the beam center and leaves a ring of repump light. Next, the atoms are subjected to a few millisecond long optical molasses [90] period as described above, allowing us to achieve sub-Doppler cooling.

Once the molasses period is complete the atoms are optically pumped into the Zeeman sublevel  $|F, m_F\rangle = |2, 2\rangle$  with which we perform our final experiments. This is achieved by exposing the atoms to repump and depump light as shown by the blue and green arrows, respectively, in Figs. 3.3 and 3.7. The optical pumping protocol used here works by first applying a magnetic quantization axis to the atoms along the direction of propagation of the light field. This defines the  $m_F$  states with respect to the polarization axis of the repump and depump beams. The polarization of the repump and depump beams is set to be  $\sigma^+$  such that they drive transitions which increase  $m_F$  by 1 upon the absorption of a photon as shown in Fig. 3.7. With both the repump and depump beams present population is continually moved to higher and higher  $m_F$  values by making transitions driven by the repump or depump laser and ends up in the desired final state with the help of spontaneous emission [the gray dotted lines in Fig. 3.7]. An atom starting in any given state will make transitions in this state space until it ends up decaying into the state  $|F, m_F\rangle = |2, 2\rangle$  from  $|F', m_{F'}\rangle = |2, 2\rangle$  as shown by the large gray wavy arrow. Once an atom reaches this state it is no longer effected by the repump and depump light because there is no state in the excited manifold with  $m_F = 3$  for

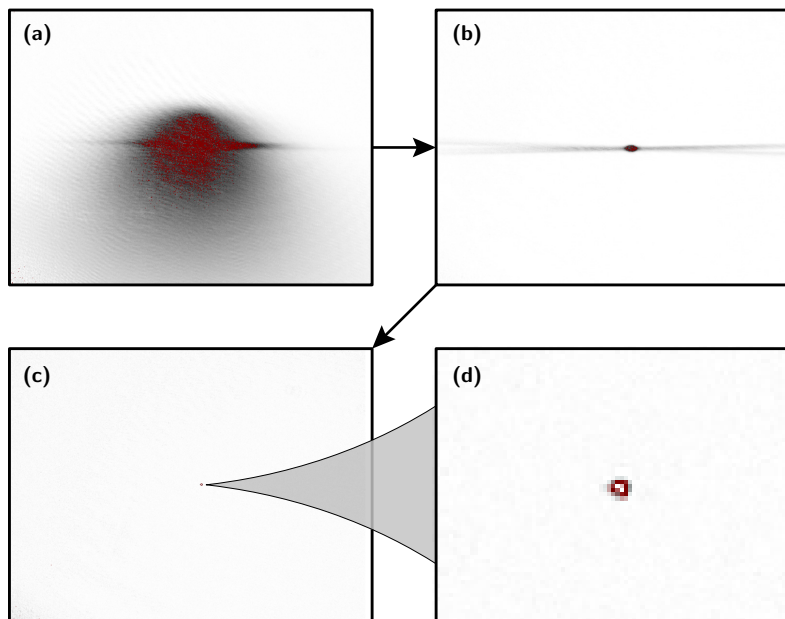


Figure 3.8: Images at different points in the cooling and evaporating sequence. For orientation, these images are from the point of view of the imaging beam as shown in Fig. 3.6. **(a)** An image of the magnetically levitated cloud of  $^{87}\text{Rb}$  atoms in state  $5^2\text{S}_{1/2} |2, 2\rangle$ . This image was taken during the optical dipole trap loading period. The circular, red ball is the levitated atoms which is slightly smaller than the original MOT size. The shadow spreading and falling away from the main ball of atoms is made up of atoms which were not optically pumped into the proper state and so are not being levitated properly against gravity. The streak through the middle is the crossed set of three optical dipole trapping beams being loaded during this stage as viewed from the side. **(b)** This image is taken in the very beginning of the evaporation stage. The gradient supporting the cloud of atoms has been lowered and those not trapped in the optical dipole trap have fallen away. The remaining atoms are supported by the optical dipole trap and appear as the dark oval in the center of the image. The horizontal stripe shows atoms which were cool enough to remain trapped in one of the individual dipole trapping beams but didn't make it into the crossed trap. **(c)** The BEC at the end of the evaporation stage is shown here near the center of the image. This image illustrates the scale of the BEC as compared to the MOT and crossed trap as it is nearly invisible at this scale. The dipole trapping beams, while still present, are invisible at this level as well since their power has been reduced to the point that no atoms are trapped in the individual beams. **(d)** This image is a blown up copy of (c) showing the BEC.

it to transition to. This results in a dark state that accumulates population.

### 3.2.3 The Optical Dipole Trap and Evaporative Cooling

The atoms, now all with the same magnetic moment, are levitated against gravity through the use of a magnetic field gradient. They are held for  $2.35\text{ s}^1$  while some fraction of them

<sup>1</sup>This value has changed throughout the life of the experiment in the range 2–5 s. While a sizable fraction of the ODT atoms are captured within milliseconds of turning on the ODT, we find that waiting for this long, seconds-scale “Ehrenfest time” allows for other atomic trajectories within the quadrupole trap to find their way into the ODT.

collects in the now present optical dipole trap (ODT) [96] beams which intersect in the middle of the cold cloud of atoms as shown in Fig. 3.6 and Fig. 3.8(a). An ODT works by taking advantage of the ac Stark effect and the Gaussian intensity profile of a laser beam as a trap for neutral atoms. The ac Stark effect [97] describes how the oscillating electric field from the far off-resonant light couples to the atom to shift its energy, as a second-order perturbative effect. If the laser is red detuned from the nearest atomic transition this results in the atom minimizing its energy by locating itself at the place of highest laser intensity, thus creating an attractive potential for the atom at the beam’s radial center. The trap depth for our ODT is low enough that the effect is negligible until after the atoms have been cooled to the  $\mu\text{K}$  level. A single laser beam provides a good trap for the atoms in the radial direction but the variation in its intensity in the axial direction as provided by its divergence angle is typically much smaller, resulting in weak trapping along the beam. For this reason and to increase the overall trap depth, ODTs typically consist of two or more beams which cross at their foci. In this way, a more-or-less spherically symmetric trap can be made for the cold atoms. At different points in the life of the experiment our ODT has consisted of three or four separate crossed beams with combinations of orthogonal polarizations and distinct frequencies to avoid interferences. In either case, two IPG Photonics fiber lasers are used to supply the laser light. One IPG Photonics fiber laser centered at 1070 nm (nearly a nanometer in spectral width) with a maximum power of 10 W creates the large-volume trap (beam waist  $\approx 250 \mu\text{m}$ )<sup>2</sup>. And a second IPG Photonics 20 W narrow-line (linewidth  $\sim 150 \text{ kHz}$ ) laser centered at 1064 nm is split into two beams (beam waists  $\approx 80 \mu\text{m}$ ) with separated frequencies (using AOMs) and intersected to form a small-volume optical trap. All three beams intersect to form a variant of a “dimple trap” [98] where we collect a few million atoms.

After the atoms have been collected in the optical trap, the final evaporation to condensation begins. Evaporatively cooling a collection of atoms consists of simply getting rid of the hottest atoms in the sample, allowing the sample to rethermalize, and repeating the process.

---

<sup>2</sup>This laser can also be used as a second ODT as it was during some points of the experiment’s life. It was reflected after passing through the science cell and recycled as a second large-volume ODT and this layout can be seen in the supplement of Ref. [51].

When the hottest atoms leave the trap, the atoms' velocity distribution is thrown out of equilibrium. The equilibrium (Maxwell–Boltzmann) distribution is regained after some time through collisions between the atoms still in the trap but the atoms have had their average energy reduced. In reality, these loss and rethermalization processes happen simultaneously, with a rethermalization rate that ideally exceeds the loss rate. This is like a hot cup of coffee cooling by sitting out uncovered while the hottest particles evaporate off the top. Evaporative cooling is commonly done in one of two ways. First, forced RF evaporation [99] is a common and very efficient way to cool magnetically trapped atoms to a condensate. In short, the technique works by trapping a single Zeeman level and then using an oscillating magnetic field to excite transitions to untrapped Zeeman levels in only the hottest atoms. The name “forced” comes from the fact that the atoms are driven out of the trap. The second way, and the one employed in this work, is a less efficient but experimentally easier and faster approach using only the ODTs themselves to evaporatively cool the atoms. This “all-optical” evaporation is done by simply lowering the trap depth exponentially in a way that progressively removes colder and colder atoms. As the trap depth is lowered, the hot atoms near the top of the trap are lost taking greater than the average particle energy with them and the entire ensemble is thereby cooled.

Our evaporation sequence was initially completed in roughly 6 s but toward the end of the experiment's life the process was sped up to around 2.5 s. The optimal procedure for our particular apparatus was to immediately turn off the magnetic levitation field at the start of the evaporation. Then, the ODT beam powers are exponentially turned down until condensation is reached. The atoms condense into the small volume trap and to make sure that no ill effects of our broad 1070 nm laser take place, this beam is turned all the way down to zero and then blocked. Thus the initial trap for the produced condensate consists of just the two crossed small-volume beams. One of these two beams serves double duty as not only a trapping beam but, at later times, the lattice beam as well. In order to mitigate the effects of spatial separation on the subsequent experiments, the trap is further deformed adiabatically to turn the power in the “lattice” ODT beam up while turning the power in the other trapping beam down. This results in an ovoid shaped trap and condensate which is extended along the direction of the lattice beam. This extended shape allows for a longer

spatial extent (and, coherence length) along the direction in which momentum is imparted, and correspondingly for the momentum orders to remain overlapped with one another for longer durations than they would be in a tighter trap. With the condensate now living in the final trap, the lattice can be turned on and an experiment can be performed.

### 3.2.4 Imaging

When the experiment is finished the atoms of the condensate have a wave function can be, to some approximation, written in the basis of the plane-wave momentum states  $|\psi_n\rangle$  considered in the experiment as  $|\Psi\rangle = \sum c_n |\psi_n\rangle$ . We measure the set of probability amplitudes  $|c_n|^2$  of the wave function in this basis by measuring the relative fraction of the condensate atoms that are in each momentum state. This measurement is done by first turning off all trapping lasers and adiabatically orienting the magnetic field to align with the imaging laser beam. The imaging frequency is near-resonant to the cycling transition [see Fig. 3.3] making the atoms very good absorbers of its light because they are in the state  $5^2S_{1/2} |F, m_F\rangle = |2, 2\rangle$ . The condensate, now released from the trap, falls due to gravity for 18 ms, corresponding to a drop distance of roughly 1.6 mm as shown in Fig. 3.9(a). During this “time-of-flight” period, an atom that has ended in a state  $|\psi_n\rangle$  begins to move perpendicularly to the direction of gravity according to its momentum  $p_n = 2n\hbar k$ . So, as the condensate falls, the atoms which are in different momentum orders spread out in space. Then, after the momentum orders have spread out far enough to be easily resolved by our imaging system, we shine the imaging laser on the atoms as depicted in Fig. 3.9(b). An atom anywhere in the field of the imaging laser will absorb some light from the beam, so the condensate fraction at each lattice site absorbs photons from the imaging laser corresponding to how many atoms are in that site. In the most basic picture, the atoms cast a shadow in the laser beam and this shadow is then imaged directly on a digital camera as illustrated in Fig. 3.9(b).

By looking at the profile of the laser beam on a camera we can tell how many atoms are at any point in space based on how much of the laser beam was absorbed. This process results in a kind of negative image of the population in each lattice site. For this to work well, the laser must have enough power or be far enough detuned such that even the most

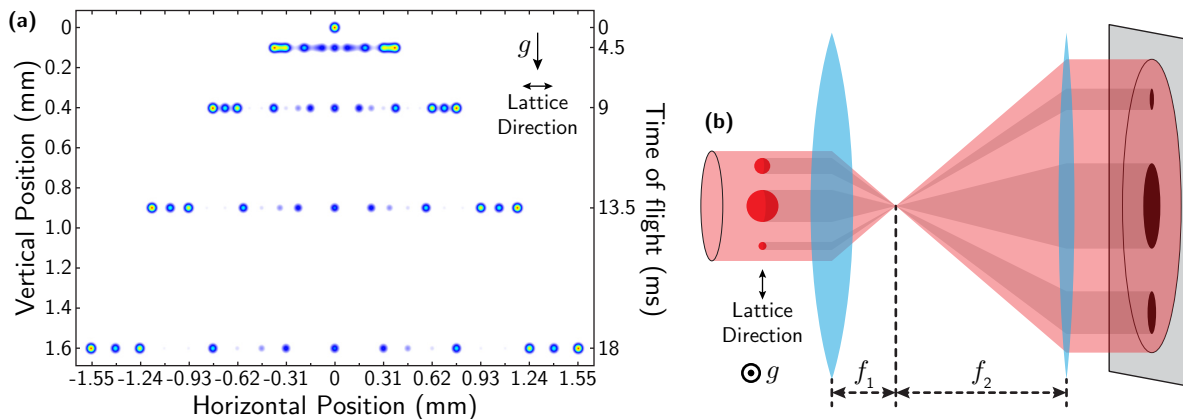


Figure 3.9: “Site”-resolved absorption imaging. **(a)** Five separate simulated absorption images showing the momentum orders spreading out as they fall due to gravity (down on the page) (for 0, 4.5, 13.5, and 18 ms) during time of flight. The distribution of atoms over the sites is based on a simulation of a uniform tunneling lattice with 21 sites after an evolution time of  $5.25 \hbar/t$ . **(b)** A cartoon depicting absorption imaging. After some time-of-flight, atoms in the different momentum states (red spheres) have spread out horizontally (up and down on the page) as they fell due to gravity (out of the page). Then the imaging laser (red beam coming from left) passes through the balls of atoms in the different momentum states and has its intensity absorbed according to their locations and volumes. The imaging beam then passes through the two telescopic lenses which magnify the beam by  $f_2/f_1$  and is imaged directly on a digital camera (gray screen). It is not reflected in this cartoon but in actuality the individual balls of atoms are not just larger or smaller based on the number of atoms they contain, but are also more or less transparent to the beam.

dense momentum order does not absorb all the photons from the beam that hit it but some make it through. As discussed further in Subsec. 3.4.2 and shown in Fig. 3.19 in the final image each momentum mode imprints its integrated density profile in the imaging plane. The recorded image shows intensity variations of the laser beam due to not only the presence of atoms but also due to the intensity profile of the laser itself. To correct the image for this unavoidable fact, a second image is taken immediately after the atoms have fallen out of the path of the laser and dropped onto the bottom of the science cell. Additionally, the dark counts and noise associated with the camera are corrected for by taking a third image with no atoms and no imaging laser present. This third image captures what the noise profile of the camera was as close as possible to the time of the measurement. By combining all three of these measurements a positive image of the momentum distribution is generated. This process is discussed in more detail in the section regarding data collection and processing (Subsec. 3.4.2).

### 3.3 $^{39}\text{K}$ BEC Creation

In general the process for making a BEC of  $^{39}\text{K}$  is very similar to the process discussed in the previous section for  $^{87}\text{Rb}$ , with the exception of a few key points.  $^{39}\text{K}$  can be more difficult to work with because it has less favorable vapor pressures, a closely-spaced excited state hyperfine structure [see Fig. 3.11], and, most importantly, undesirable collisional properties for cooling [100, 101]. The methods of cooling described in the previous section work well for atoms with a positive scattering length like  $^{87}\text{Rb}$ , which has a scattering length of roughly  $100 a_0$ . Moderately large (in magnitude) scattering lengths allow atoms to rethermalize efficiently during evaporative cooling while avoiding a large three-body loss rate. To cool to ultralow temperatures, however, positive scattering lengths are generally required. It so happens that at zero magnetic field  $^{39}\text{K}$  has a scattering length of around  $-30 a_0$  [100, 102]. Unfortunately, this negative scattering length prevents  $^{39}\text{K}$  from being directly cooled to a BEC because at low magnetic fields the attractive interactions cause instabilities leading to collapse [103, 104] which has been observed in both  $^{39}\text{K}$  [105] and  $^{85}\text{Rb}$  [106].

This hurdle was initially partly overcome through the use of sympathetic cooling using a second atomic species more amenable to laser cooling (typically  $^{87}\text{Rb}$ ) as a bath for the  $^{39}\text{K}$  [107]. Adding another species into a cold atom apparatus is in no way a simple task however, and still does not solve the entire problem. Using sympathetic cooling,  $^{39}\text{K}$  can be cooled down to around  $1 \mu\text{K}$  [100]. While this is significant cooling, it does not address the core problem of a negative scattering length and therefore prevents the production of a pure  $^{39}\text{K}$  BEC as evaporative cooling is still ineffective. Another method of improving the collisional properties of  $^{39}\text{K}$  is by directly manipulating its scattering length through the use of an external magnetic field, *i. e.*, through a Feshbach resonance. By first sympathetically cooling with  $^{87}\text{Rb}$  and then introducing a positive scattering length with a magnetic field during evaporation, the first pure BEC of  $^{39}\text{K}$  was created [107]. This was a milestone in the field but the procedure was still not very desirable due to the difficulties in working with two atomic species.

Shortly thereafter, new ways of performing optical molasses for  $^{39}\text{K}$  were realized which involved time-dependent manipulations of the laser frequencies and intensities [108–110].

This turns out to be quite tricky and hard to reproduce in generic experiments, and alternative methods were soon developed based on what is known as gray molasses cooling using light that is blue-detuned from the  $D_1$  transition (discussed further in Subsec. 3.3.4). Using a conventional  $D_2$  molasses followed by a  $D_1$  gray molasses enables cooling of  $^{39}\text{K}$  down to  $< 10 \mu\text{K}$  [111, 112]. These temperatures are sufficiently cold to have some sizable fraction of the atoms loaded directly into an optical dipole trap. This still leaves the problem of the negative scattering length preventing evaporative cooling, but this can be solved by tuning the scattering length with an external magnetic field to a positive value during evaporation [113] as discussed in Sec. 3.3.1.

Our approach to realizing a  $^{39}\text{K}$  BEC will rely heavily and entirely on these techniques and the more universal techniques which we have already employed for  $^{87}\text{Rb}$  as discussed in the previous section. In this section I will discuss in detail only the differences between our approaches for  $^{39}\text{K}$  and  $^{87}\text{Rb}$ . At an overview, our procedure for reaching a  $^{39}\text{K}$  BEC is:

- (i) Capture  $^{39}\text{K}$  atoms from a vapor alkali metal dispenser in a 2D MOT. This precools the atoms in a plane perpendicular to the direction that they are pushed to reach the science cell.
- (ii) Collect the atoms from the 2D MOT which reach the science cell in a 3D MOT.
- (iii) Perform stages of magnetic compression,  $D_2$  molasses, and  $D_1$  gray molasses, further cooling the atoms to the  $\mu\text{K}$  regime.
- (iv) Perform optical pumping to place the atoms in a specific Zeeman sublevel.
- (v) Load the atoms into an optical dipole trap with a higher-power 50 W IPG fiber laser.
- (vi) Evaporatively cool the atoms in the presence of an external magnetic field to provide a positive scattering length. At this point a BEC will be produced and an experiment can be performed.

It should be pointed out that we are currently in the process of completing these necessary tasks and so this section will only discuss technical information for the steps that have been successfully completed (steps i and ii).

### 3.3.1 Feshbach Resonance

Generally, the term Feshbach resonance relates to modification of the free-atom states in the presence of other atoms and near degeneracies of atom-atom and molecular energy levels. Associated with this are the ability to modify the scattering properties of colliding atoms by the use of external dc magnetic fields, as well as enhanced three-body loss at degeneracy, as atom pairs can be resonantly converted into loosely-bound "Feshbach molecules," which can then be lost in collisions with a third atom. Reference [77] has a very detailed and clear treatment of this topic and since we only use this phenomenon here as a tool and not as a subject of study we only briefly discuss its operational principles. The bottom line we need to get across for this work is that through the physics of a Feshbach resonance, an external magnetic field can tune the scattering properties of  $^{39}\text{K}$ .

We begin our description by considering three cold atoms in a trap coming together in a collision. The atoms may simply bounce off of one another but they also have some probability of entering a molecular bound state. To conserve energy and momentum the released molecular binding energy is converted into kinetic energy of both the new molecule and a third bystander atom. This results in the loss of all three atoms from the trap as the binding energy tends to be much larger than a typical trap depth. A Feshbach resonance refers to the resonant enhancement of this loss mechanism by coupling the incoming partial waves of the two colliding atoms with a molecular bound state.

As illustrated in Fig. 3.10(a) the two colliding atoms have a potential described by the entrance channel curve with a relative energy above any bound states in that curve. This potential curve depends on the specific angular momentum quantum numbers of the colliding atoms such that, for modified quantum numbers, the exit channel curve in Fig. 3.10(a) exists. Since the angular momentum quantum numbers are in this case magnetic Zeeman sublevels and the exit and entrance channels represent different sublevels, the relative energy between the channels can be controlled through the use of an external magnetic field. Therefore, this three-body decay process can be resonantly enhanced by tuning the incoming atoms to be the same energy as a molecular bound state in the exit channel. The goal here however is not to resonantly remove atoms from our BEC, but rather to take advantage of the dramatic

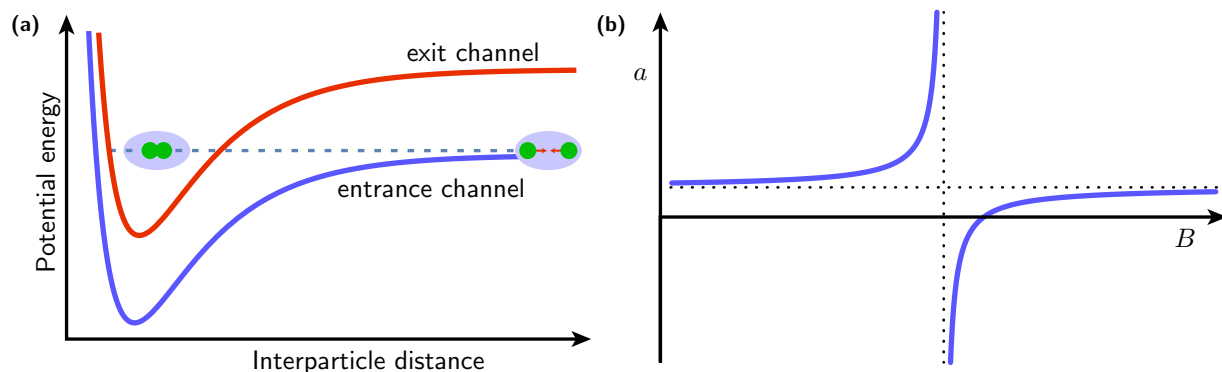


Figure 3.10: Feshbach Resonance Mechanism. **(a)** Potential energy schematic for a Feshbach resonance. Atoms colliding in the entrance channel can resonantly scatter into the molecular bound state in the closed channel and escape the trap. **(b)** Cartoon diagram of a magnetic Feshbach resonance illustrating the tunability of the scattering length  $a$  with the external magnetic field  $B$ . These figures adapted from Ref. [114].

modifications to the scattering properties which occur near this resonance.

In Fig. 3.10(b) we show a cartoon depiction of a typical Feshbach resonance curve. The scattering length displays a resonant behavior as the external magnetic field is tuned so as to introduce a new molecular bound state. Feshbach resonances have been a major tool in cold atom experiments over the past two decades, allowing for even higher levels of control over the underlying Hamiltonian (see Ref. [77]).  $^{39}\text{K}$  hosts a fairly broad Feshbach resonance near 400 G [78] which we access through the use of water-cooled electromagnets as described in Subsec. 3.3.3. With this capability we will be able to realize tunable interactions in a momentum-space lattice, paving the way for studies on the rich physics surrounding correlated dynamics in a highly controlled system.

### 3.3.2 The Magneto-Optical Trap

The unfavorable hyperfine structure of  $^{39}\text{K}$  also affects the approach to making a MOT. In  $^{87}\text{Rb}$  the cycling and repump lasers are detuned by about 10 MHz to the red of their respective transitions. It turns out that  $^{39}\text{K}$  and  $^{87}\text{Rb}$  have the same nuclear spin,  $I = 3/2$ , so their hyperfine structure is similar, meaning the cycling and repump transitions would ideally be tuned to the same transitions:  $F = 2 \leftrightarrow F' = 3$  and  $F = 1 \leftrightarrow F' = 2$  respectively. However, the spacing between the  $F' = 2$  and  $F' = 3$  states in  $^{39}\text{K}$  is only 21.1 MHz (Fig. 3.11) whereas in  $^{87}\text{Rb}$  this spacing is 266.7 MHz (Fig. 3.3). Therefore a -10 MHz detuning on

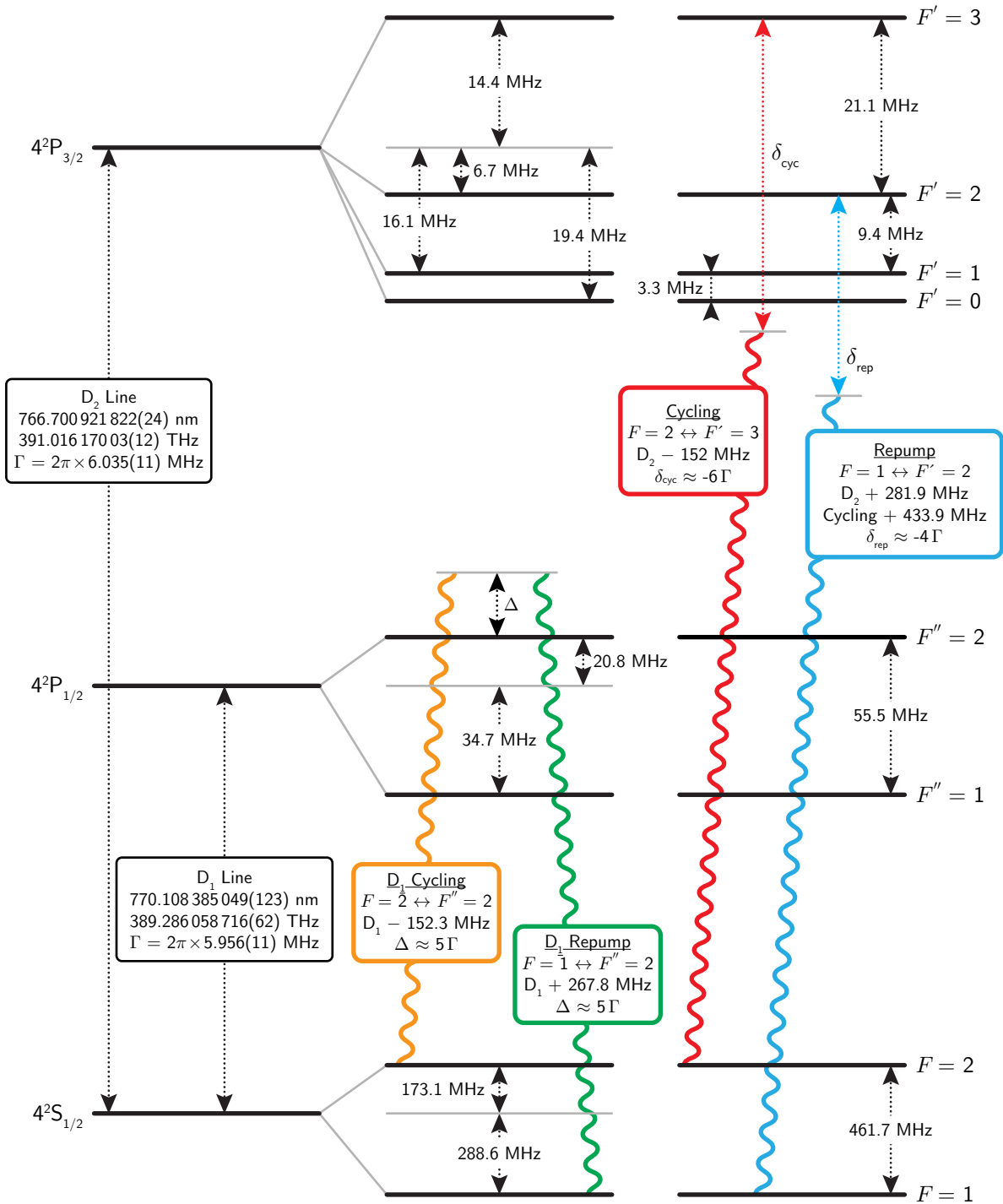


Figure 3.11: Level diagram of relevant transitions for the  $^{39}\text{K}$  D<sub>2</sub> and D<sub>1</sub> lines. The cycling (red wavy line) laser is shown connecting  $F = 2 \leftrightarrow F' = 3$  with detuning  $\delta_{\text{cyc}} \approx 6\Gamma$ , the repump (light blue wavy line) is shown connecting  $F = 1 \leftrightarrow F' = 2$  with detuning  $\delta_{\text{rep}} \approx 4\Gamma$ . The D<sub>1</sub> gray molasses beams are shown in orange and green for the cycling and repump respectively. The gray cycling beam is detuned  $\Delta$  from the  $F = 2 \rightarrow F'' = 2$  transition and the gray repump is detuned by the same amount from the  $F = 1 \rightarrow F'' = 2$  transition. This figure was adapted from Ref. [115] with numbers from Refs. [115–117].

the cycling transition in  $^{39}\text{K}$  would put it halfway between these two levels resulting in an equivalent blue detuning from the  $F' = 2$  state. This severely affects the ability to use this same scheme as a mechanism for cooling  $^{39}\text{K}$  because when the beam is detuned to achieve efficient cooling it starts exciting other states. The solution to this problem is to use the poorly spaced hyperfine structure to one's advantage. The cycling and repump beams are both detuned completely below the entire  $4^2\text{P}_{3/2}$  hyperfine manifold as shown in Fig. 3.11, in this way they act as red-detuned cooling beams for atoms in any of the excited hyperfine levels, working less efficiently for some than others. The optimal detuning for the cycling is around  $\delta_{\text{cyc}} \approx -6\Gamma \approx -36$  MHz and for the repump  $\delta_{\text{rep}} \approx -4\Gamma \approx -24$  MHz. In some ways it is more helpful to think of the two beams used for this type of MOT not as a cycling and repump but really just as two cycling transitions because neither of the beams addresses a specific transition in reality and so there is not one dominant transition with a small leak but many transitions being simultaneously cooled with both beams. For this reason, the repump requirements of  $^{39}\text{K}$  are much more demanding than  $^{87}\text{Rb}$ , with typical ratios of repump to cycling power of 1:2 or even 1:1. We use Thorlabs DL100 external cavity diode lasers (along with several Eagleyard tapered amplifiers) to source all of the near-resonant laser light for this cooling.

Another consideration for the use of  $^{39}\text{K}$  is the much lower vapor pressure. A 2D MOT can be easily made for  $^{87}\text{Rb}$  by just using the alkali metal dispensers to produce some appreciable pressure of  $^{87}\text{Rb}$  in the source cell. For  $^{39}\text{K}$ , however, the source cell must be heated externally in order to really make good use of the alkali metal dispenser. Otherwise, the  $^{39}\text{K}$  which comes off the dispensers will just adsorb to the glass cell rather than being trapped in the MOT. We use Minco heating strips ([HK6908/HK6904](#)) which are adhered directly to the edges of the source cell and dispenser arms and near the glass-to-metal seal. We heat the source cell to around 50 C when making a 2D MOT.

### 3.3.3 Magnetic Field Upgrades

#### Atom Source

In addition to changing the laser systems to accommodate  $^{39}\text{K}$  we have made upgrades to the technical side of both the 2D and 3D MOT magnetic field configurations. Figure 3.12 shows the updated design of the coil holders for the 2D MOT. The assembled holder [shown in Fig. 3.12(i)] consists of four parts, one for each side where coils are needed to create the 2D quadrupole field. The holder was designed as four separate parts so that we could assemble it around the source cell after baking the chamber. This is made necessary because the forked dispenser arms [see item 1 in Fig. 3.1] prevent us from sliding the source cell through a single piece without placing the coils too far away to be practical. This design also makes the coils a little easier to wind as they can be wound separately in the same orientation and then assembled afterward. The only drawback of this approach is the possibility that the coils may be slightly misaligned since they are on separate pieces, creating an imperfect magnetic quadrupole field. However, we believe this effect is negligible compared to the other limiting factors of our implementation (no field control along the axial direction, anisotropy in the winding, etc.).

The motivation for changing the design for the 2D MOT from what was used previously for  $^{87}\text{Rb}$  (as discussed in Sec. 3.2.1) was to generate a more ideal 2D quadrupole field. Previously we ran separate currents through all four quadrupole coils as shown in Fig. 3.4(a) and adjusted these currents to adjust the location of the magnetic field zero. This only works well if the field zero only needs very small adjustments, otherwise changing these currents results in very pronounced anisotropy in the trapping plane gradient as well as introducing an undesirable nonzero gradient in the axial direction. If the four coils are connected in series, however, they are forced to have the same current and they create a “perfect” 2D quadrupole field. That is to say, in the trapping plane the field is isotropic and in the axial direction there is no gradient anywhere along the field zero as shown in Fig. 3.13. However, if these four coils are all run in series we have removed the ability to tune the position of the field zero. This problem is overcome through the addition of four more coils wound around the outside of the quadrupole coils and in the same channel on the holders. These loops are

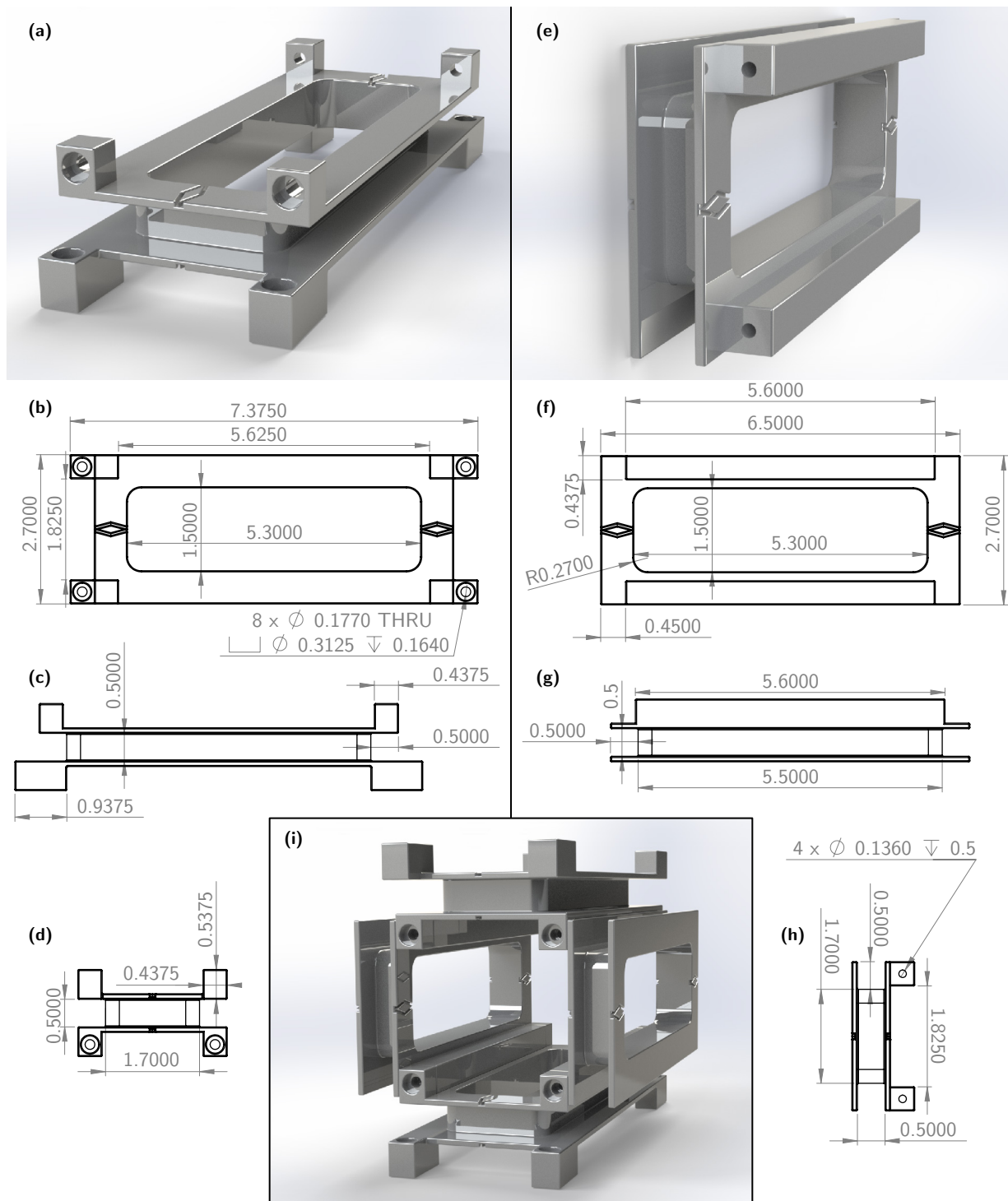


Figure 3.12: Upgraded magnetic field configuration for the 2D MOT. **(a)** Image of the magnetic field coil holder for the top and bottom coils. The holes pointing downward are for mounting to optomechanics and subsequently to the optical table and the holes pointing into the page are for attaching to the side pieces. **(b–d)** Schematics of the top/bottom coil shown in **(a)** from the top **(b)**, side **(c)**, and end **(d)**. **(e)** Image of the magnetic field coil holder for the side coils. The holes pointing into the page are threaded 8-32 for attaching to the top and bottom pieces. **(f–h)** Schematics of the side coil holders shown in **(e)** from the top **(f)**, side **(g)**, and end **(h)**. **(i)** Assembled 2D MOT coil holder. All values in the schematics are in inches.

arranged in a Helmholtz style configuration such that they produce a uniform offset field. The two pairs of offset coils (in the vertical and horizontal direction) are still kept in series so as to create homogeneous fields but their current can be tuned to adjust the position of the field zero while only very slightly affecting the quadrupole field.

On each holder we wound two coils of 22-gauge magnet wire (CNC Tech [610222](#)) into the  $1/2 \times 1/2$  in channel. We prefer to use polyurethane coated wire as opposed to polyamide coated because it is a little easier to wind and a little thinner, allowing for more turns with the same gauge. The first 175-turn loop is one of the four loops used to create the quadrupole field and the second 50-turn loop is one of the four loops used to create the uniform offset field. The dimensions of the loops after winding is identical on all four sides and measures roughly  $6 \times 2.2$  in as shown in Fig. [3.12](#). These holders were fabricated by Ralf Möller of the Rapid Prototyping Lab at the University of Illinois using an EOS Formiga P100 3D printer with PA2200 plastic (a powdered, polyamide-based plastic). The only feature added after printing is the 8-32 tapped holes in the side pieces. The 3D printer made the 0.136 in diameter hole and then it was hand-tapped with 8-32 threading after printing.

Figure [3.12\(a\)](#) is a rendered image of the coil holder used for the top and bottom of the final assembly and drawings of this piece are shown from three angles in Figs. [3.12\(b-d\)](#). The eight counter-bored holes on each piece are intended for 8-32 socket head cap-screws with the four holes pointing down used for mounting the whole assembly (designed for easy use with Thorlabs  $1/2$  in posts) and the four holes pointing into and out of the page used to attach the side pieces. The diamond shaped relief notch is a reference for aligning the holder to the cell and aligning lasers to the magnetic field center and appears on both the top and bottom of the part. When fully assembled the four rectangles sticking up from the top piece (which are used for mounting the bottom piece) can be left unused or used for additional mounting. They are not necessary for the design but leaving them on simplifies the whole assembly to only two parts rather than three.

A 3D rendering of the side piece is shown in Fig. [3.12\(e\)](#) with schematic drawings showing its dimensions in Figs. [3.12\(f-h\)](#). The channel for the coils has the exact same dimension as the top and bottom pieces and this part also has diamond reliefs marking its center for beam alignment. The protruding rectangles shown on the right face have two tapped 8-32

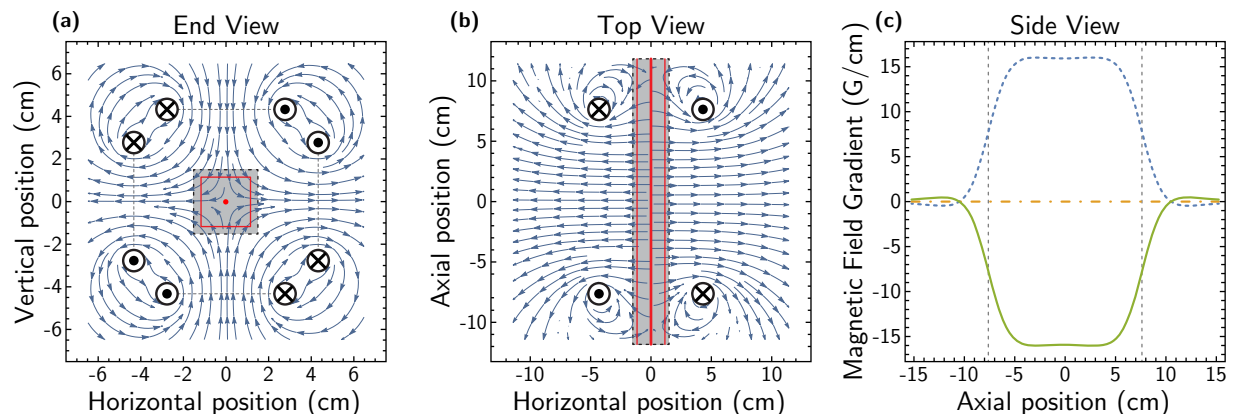


Figure 3.13: Magnetic field produced by the 2D MOT coils. **(a)** A contour plot of the 2D MOT magnetic field as viewed looking along the axial direction, perpendicular to the trapping plane showing the isotropic quadrupole field. The current direction at the eight intersections of the four coils with the trapping plane are shown with vector notation. The red dot represents the point at which the magnetic field is zero and the gray box represents the cross-sectional area of the source cell. The red box within the area of the cell represents the available tuning area of the field zero position using the offset field. **(b)** A contour plot of the 2D MOT magnetic field as viewed from the top. As in **(a)** the red line at a horizontal position of zero represents the magnetic field zero and the gray box the cross sectional area of the source cell. The four intersections between the two side-mounted current loops and the viewing plane are shown with vector direction notation indicating the direction of the current. The red lines on either side of the field zero line represent tuning range of the field zero position using the offset field. **(c)** The magnetic field gradient produced by the current configuration as shown in **(a)** and **(b)** as viewed from the side. Plotted are the gradient in the vertical (green solid line), horizontal (blue dashed line), and axial (yellow dot-dashed line) directions for a current in the quadrupole coils of 1.6 A. The gray dashed vertical lines represent the edges of the current loops.

holes on each end such that when this piece is slotted in between the raised rectangles on the top and bottom part the tapped holes line up with the clearance holes on the top and bottom part for attaching the four pieces together.

The finished product results in four coils for the quadrupole field and four coils for the uniform field, one on each of the four sides. This results in a magnetic field as depicted in Fig. 3.13. By running the four quadrupole loops in series a gradient of 10.3(4) G/cm/A is measured (in agreement with a predicted gradient of 9.9 G/cm/A) and the 22-gauge wire has an operational limit of 2 A without active cooling, giving a maximum gradient of 20.6(8) G/cm (see Tab. 3.1). The offset field coils are capable of supplying an 8 G uniform field at the center of the cell in the vertical and horizontal directions, defining a square field-zero tuning area of approximately 2.3 cm on a side as depicted by the red rectangle in Fig. 3.13(a). The field is also shown in a top view in Fig. 3.13(b) with the source cell indicated by the gray box and the tuning range and field zero indicated by red lines. Figure 3.13(c)

shows the calculated gradient from a side view with the gradient in the vertical direction shown in green, the horizontal direction shown as the blue dashed line, and the zero-field axial direction shown as the dot-dashed yellow line. The gray vertical lines indicate the position of the coils. The field as shown in the figure is estimated using the equations derived from the Biot–Savart law for a rectangular coil as outlined in Sec. A.4 and the estimations agree with the measurements quite well.

### Science Cell: Shimming Fields

The magnetic field hardware surrounding the science cell and used for the 3D MOT, compression, optical pumping, levitation, etc. was also redesigned when we began switching from  $^{87}\text{Rb}$  to  $^{39}\text{K}$ . This change was motivated not only because we desired to improve the field quality, but also because we needed to alter the field arrangement to fit in the new, bulky Feshbach coils which we would be using with  $^{39}\text{K}$ . In this section, we discuss the technical information and performance of the different coils. In all, there are 18 separate coils of wire to provide these fields. Twelve of them make up the “shimming” fields which consist of six pairs of coils: three pairs create uniform offset fields for the science cell in all three dimensions and the other three pairs create gradient canceling fields in all three dimensions. These are arranged on a large rectangular frame offset several inches in all dimensions from the cell. Next, there is a pair of coils positioned very close (0.36 in clearance) to the cell in the vertical dimension which creates the primary magnetic quadrupole field for the science chamber. Another pair of coils with a small number of turns is co-wound with the quadrupole coils to provide a quickly varying magnetic field as this pair has a low inductance. Finally, the last pair of coils is the Feshbach coils. These are very different from the other 16 coils because they are designed to be able to support over 100 A of current to reach the  $\approx 400$  G field necessary for the Feshbach resonance.

We will start our discussion of this relatively complex array of electromagnets with those furthest away from the cell, the shimming fields. Figure 3.14 shows the single piece which defines the rectangular frame for the 12 coils. In each  $1/2 \times 1/2$  in channel are two coils of 22-gauge magnet wire with 100 turns each. One pair of the corresponding loops on opposite

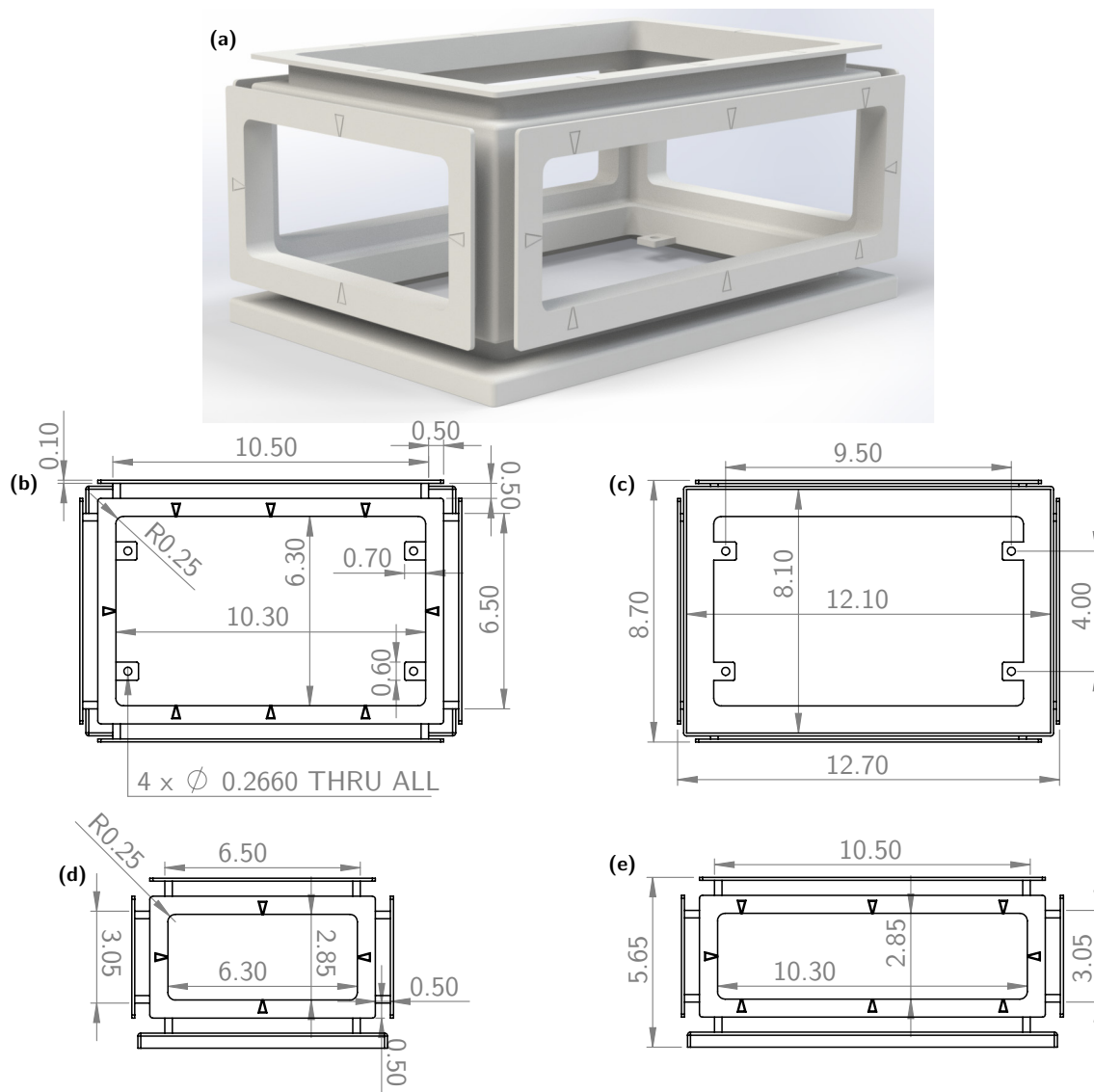


Figure 3.14: Science cell shimming field configuration. **(a)** Image of the magnetic field coil holder for the shimming fields. Each face of the rectangular frame has a  $\frac{1}{2} \times \frac{1}{2}$  in channel girding it where the wire is wrapped. The triangular reliefs in each face are for rough-aligning lasers to the field center at angles normal to the face and at the  $45^\circ$  paths on the two vertical faces which they intersect as well as the top and bottom. The holes pointing downward are  $\frac{1}{4}$  in clearance holes for mounting to a custom-made breadboard measuring  $12 \times 8$  in. **(b–e)** Schematics of the shimming field holder as viewed from the top **(b)**, bottom **(c)**, small side **(d)**, and large side **(e)**. All values in the schematics are in inches. The thickness of all the walls of the part is 0.1 in.

sides of the cube are arranged to produce a uniform field and the other are arranged to produce a quadrupole field. The coils in the vertical dimension produce a field of 8 G/A and 0.75(4) G/cm/A at their center. In the long horizontal dimension the coils produce a field of 1.5 G/A and 0.26(1) G/cm/A at their center. Finally, in the short horizontal dimension the coils produce a field of 3.4 G/A and 0.79(4) G/cm/A at their center (see Tab. 3.1). These fields are primarily used to shift the field zero crossing of the quadrupole coils as well as to cancel out any stray fields which may be affecting the atoms, such as Earth's field and fields from the magnets on the ion pumps. This part was also created via 3D printing by Ralf Möller of the Rapid Prototyping Lab at the University of Illinois using an EOS Formiga P100 3D printer with PA2200 plastic.

### Science Cell: MOT Coil

Next, we move on to the main quadrupole field coils which we commonly call the MOT coils as that is one of their main purposes. We use a highly-specialized coil holder for the MOT designed to fit inside the Feshbach coils. Figure 3.15(a) shows an image of this part with schematic drawings shown in Figs. 3.15(b–d). This part features a very narrow channel for the coils but a nearly Helmholtz configuration, *i.e.*, the coil radius is very near to the separation. The channel is  $\frac{1}{8}$  in tall and just over 1 in deep. We wound 140 turns into each channel to be used for the quadrupole field and 5 turns into each channel for a fast-response field. The quadrupole field was measured to produce a gradient of 8.4(6) G/cm/A in the vertical direction at the center and the extra pair of coils can produce a uniform field of approximately 0.7 G/A at the center (see Tab. 3.1). The part was originally designed as two separate pieces with no support pillars but, being printed in PA2200, the top plate of the channel area flared up significantly after winding. This reduced the gap between the two parts such that they would no longer fit around the science cell. So the part was redesigned with the support pillars and as one piece. This new design still flared up but the pillars held it down in the middle to allow the cell to pass through unobstructed. The triangular reliefs mark every  $45^\circ$  to help with rough beam alignment to the field center. The eight mounting arms have a counter-bored clearance hole designed for a  $\frac{1}{4}$  in socketed-head cap screw. The

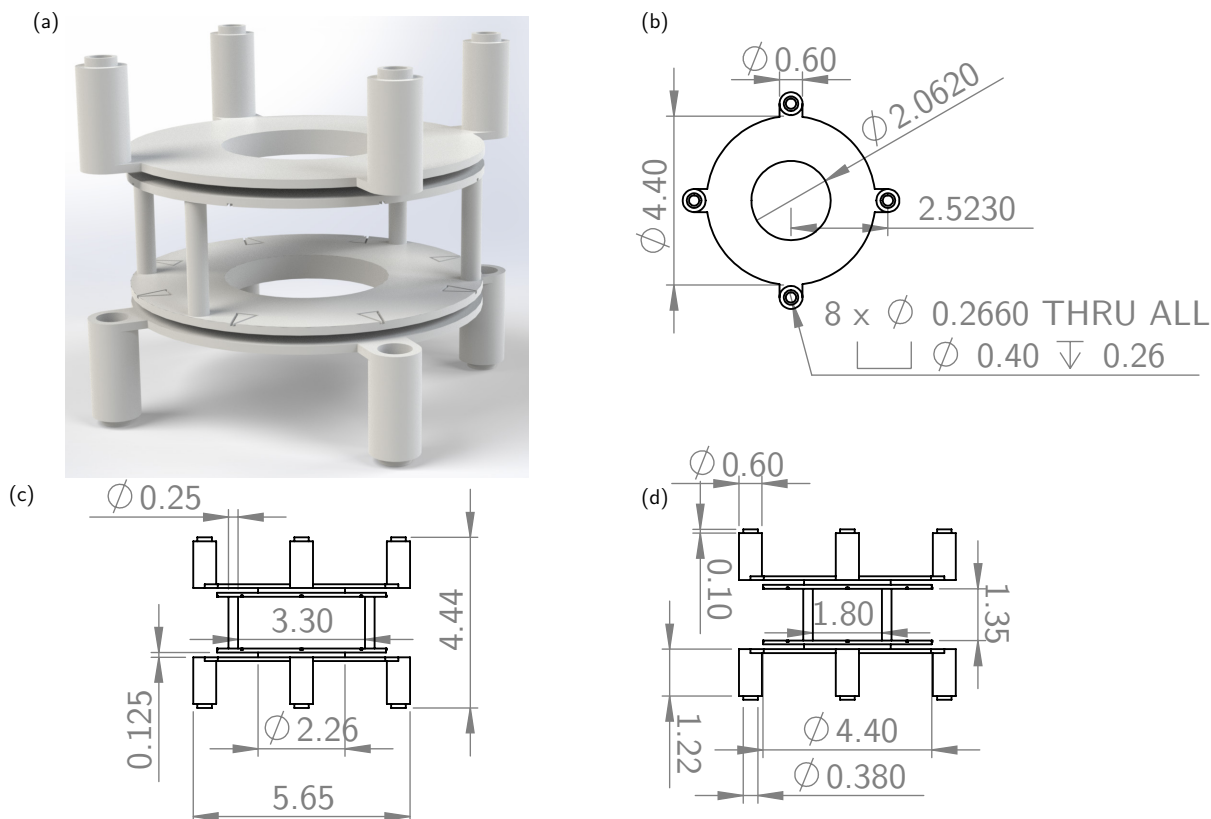


Figure 3.15: 3D MOT magnetic field configuration. **(a)** Image of the magnetic field coil holder for the 3D MOT. The channels for the wire have a height of  $\frac{1}{8}$  in and an inner radius of 2.26 in and are separated by 1.675 in. The four pillars hold the two top plates of the channels apart so that they do not bow in from the force of the wound wires and they are offset from the  $45^\circ$  degree lines for optical access. The triangular reliefs mark the field center at every  $45^\circ$ . The eight mounting arms have  $\frac{1}{4}$  in clearance holes and are counter-bored for a socket-head cap screw. **(b–d)** Schematics of the coil holder shown in **(a)** from the top **(b)**, the side with a large opening between the pillars **(c)**, and the side with a small opening between the pillars **(d)**. All values in the schematics are in inches. The thickness of all the walls of the part is 0.1 in.

mounting arm spacing is defined relative to the Feshbach coils as we will discuss next.

### Science Cell: Feshbach Coil

The Feshbach coils are a much more complex electromagnet than all the other coils discussed herein. This complexity primarily stems from the fact that we need these coils to produce fields two orders of magnitude larger than the others. To achieve fields in the vicinity of 400 G, the coils will require high currents and have significant power dissipation, and so they have to be actively water cooled. To ensure our coils have good thermal contact with the cooling water, we use  $\frac{1}{8}$  in refrigerator tubing (McMaster Carr [5174k1](#)) to carry the

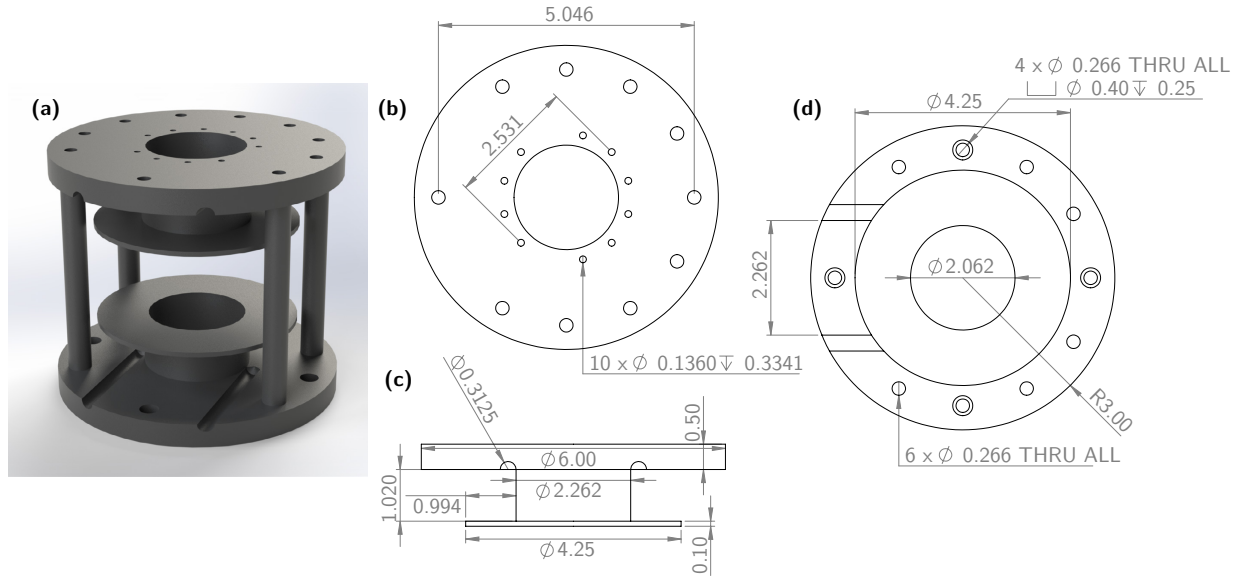


Figure 3.16: Feshbach coil holder. **(a)** An image of the assembled Feshbach coil holder. The outer ring of holes in the spool piece have several  $\frac{1}{4}$  in clearance holes. The four counter-bored holes were used to mount the piece to the rotary table for winding and in the final configuration are where the 3D MOT coil holder attaches. Four of the other six holes are used for attaching the two spools via the four pillars. The extra holes are for mounting some future optics or to have flexibility in where the pillars are placed to avoid a beam path. The inner ring of holes near the central opening of the spool are a series of tapped 8-32 holes to allow for the possibility of mounting optics to the coils themselves. The pillars themselves are each 4.250(4) in long and have tapped  $\frac{1}{4}$ -20 holes in each end. The two channels cut into the base of the spools are for the refrigerator tubing to come in and go out under the stack of wound tubing. **(b–d)** Schematic drawings of the spool part of the coil holder shown from the front **(b)**, bottom **(c)**, and top **(d)**. All units are in inches.

current instead of conventional magnet wire. The cooling water flows through the inside of the tubing and the tubing itself carries the current. Working with refrigerator tubing rather than magnet wire introduces a much higher level of complexity to the winding and mounting process. The initial design for the holders, electronic controls, and plumbing was done by Michael Highman for a different apparatus in the Gadway Lab. We made slight improvements to the coil holder design but the plumbing and electronics are copied directly from his plans.

First, we insulated the bare tubing by wrapping it with heat shrink tubing. Since kinking the tubing will result in a water blockage and prevent cooling and since the tubing is much too stiff to be easily workable by hand, we wound the tubing around the holders with a rotary table (Phase II [H220-006](#)). For all of these reasons, the holders must be made of a durable, rigid material that is not metallic to prevent eddy currents and other undesirable effects. We made our holders from polyoxymethylene plastic (sold under the name Delrin by

DuPont). The machining of the stock Delrin was performed by myself, Ernest Northen, and Lucas Osborne of the University of Illinois physics machine shop. The holder consists of two main parts, the spools (stock Delrin: McMaster Carr [9986k35](#)) which are wound with the refrigerator tubing, and four pillars (stock Delrin: McMaster Carr [8576k15](#)) which attach the two pieces and keep them a set distance apart as shown in Fig. [3.16](#).

To wind the coil holder, a block of Teflon with a guide channel cut into it was used to provide tension and straighten the tubing. We started at the bottom and wound a six-tube high stack vertically and then covered the whole thing in epoxy. Then we moved on to the next set of six wraps, this time starting at the top and working back to the bottom. We continued in this fashion until we wound the coils with  $35\frac{1}{2}$  turns, sending the tube out in the same direction it came in and adding a layer of epoxy between every column of six tubes and a healthy coat over the entire thing when it was finished. To make the electrical connection, the tubes were cut roughly one foot away from the holders and were soldered onto custom-machined copper blocks with a  $\frac{3}{8}$  in through-hole for attaching leads. The coils were measured to produce a field at their center of  $3.920(3)$  G/A (see Tab. [3.1](#)) meaning we need to supply the coils with a current of just over 100 A to reach our target magnetic field of just over 400 G.

The full assembly is shown in Fig. [3.17](#). In this configuration the entire structure can be slid around the science cell [see item 8 in Fig. [3.1](#)]. The breadboard which the structure rests upon was custom-machined to fit the holes in the Feshbach coil in the center. Everywhere else it has the standard 1 in spaced  $\frac{1}{4}$ -20 holes except for the four counter-bored clearance holes at the corners for mounting the whole assembly as well as the four oddly placed holes on the short edges for attaching to the shimming field coil holder. We mounted the breadboard on locking, adjustable-height posts (Thorlabs [BLP01](#)) to center the holder assembly on the science cell vertically. The main advantage of this complicated design is that all the different holders are squared up and attached to one another to keep their centers as close as possible to the same point in space.

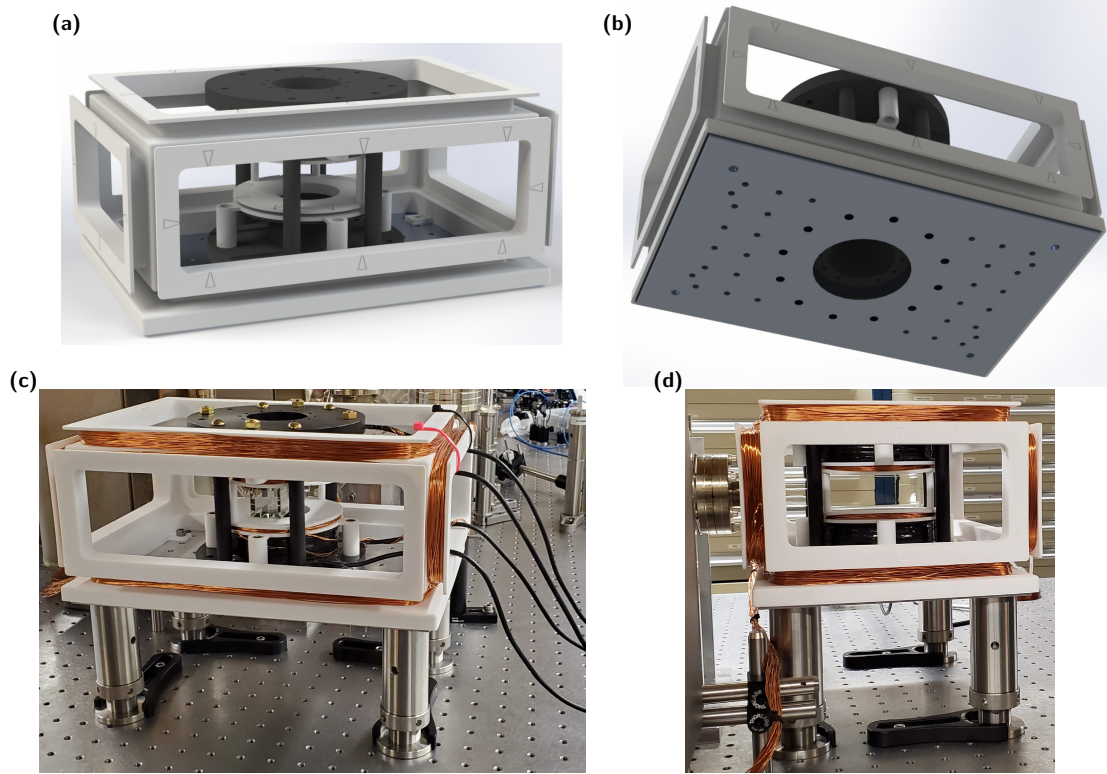


Figure 3.17: Full science-side magnetic field configuration as seen from **(a)** the front and **(b)** showing how the shim field coil holder (outer white rectangular prism), Feshbach coil holder (black central piece), MOT coil holder (white central piece inside the Feshbach holder), and custom breadboard all fit together. The breadboard was machined to have holes at places that line up with the Feshbach coil in near the middle, a large hole in the center for beam access, holes at the corners for mounting, and four offset holes at the short edges for attaching the shimming field holder directly. **(c, d)** Photographs of the finished magnetic field assembly placed around the science cell. The shimming field coils and MOT coils are wound with 22-gauge copper magnet wire and the Feshbach coils are wound with black plastic heat-shrink wrapped copper tubing. The leads going off to the right are the refrigerator tubing coming from the Feshbach coils. The assembly is mounted on locking adjustable-height posts.

	Helmholtz (G/A)	Anti-Helmholtz (G/cm/A)
Source	4	10.3(4)
Science Shim N/S	3.4	0.79(4)
Science Shim E/W	1.5	0.26(1)
Science Shim U/D	8	0.75(4)
Science MOT	—	8.4(6)
Science MOT X	0.7	—
Feshbach	3.920(3)	—

Table 3.1: Magnetic field values for all the upgraded coils described here. Source refers to the 2D MOT coils. The shorthand N/S, E/W stand for cardinal directions in the laboratory. The shorthand U/D stands for up and down. The science MOT X coil is the few extra turns added around the MOT coil. The character — indicates that the coil is either not designed to operate in this configuration or the number was not measured.

### 3.3.4 Gray Molasses

The last big difference between our approaches to cooling  $^{87}\text{Rb}$  and  $^{39}\text{K}$  is the use of  $D_1$  molasses. Also known as gray molasses, it is based on the same principles as the  $D_2$  molasses discussed in relation to the normal MOT beams but with the added benefit of creating and shelving the atoms in a “dark” state. In normal optical molasses the atoms are always absorbing and reemitting photons, and with an atom that has a well-spaced excited hyperfine manifold this does not prevent sub-Doppler cooling. The states sampled by the atoms in a normal molasses are therefore “bright” states, because an atom scatters light when in them. The working principle of a gray molasses is to realize a specific situation where when an atom stops moving (or comes very close to it) it stops interacting with the laser light all together because it enters a “dark” state. If the atom begins to move again however, it enters a bright state and does interact with the light field such that it feels a force in the opposite direction of its motion. It is this combination of bright and dark states which give gray molasses its name.

This effect was first demonstrated in  $^{87}\text{Rb}$  [118] and cesium [119] and is based on a well known phenomenon in a three level system when exposed to two drive fields. Ref. [111] contains a discussion of this effect and we describe it only briefly here. In a so-called  $\Lambda$  system with two equal-strength drive fields equally blue-detuned from the excited level, a dark state is created. When an atom is in this dark state it becomes decoupled from the light field. Since the presence of this dark state, which is a superposition of the two ground states, depends on the detuning of the two drive fields, if an atom is moving against one beam and into the other the equal detuning condition is broken due to the Doppler shift and the state of the atom becomes bright. Once in a bright state, the atom feels a force in the direction opposite to its motion just as in standard optical molasses and is cooled until it once again enters the dark state and decouples from the light field. At a qualitative level, this gray molasses behaves like velocity-selective coherent population trapping, but at zero velocity.

In  $^{39}\text{K}$  the three levels used are the two  $4^2S_{1/2}$  hyperfine levels  $F = 1$  and  $F = 2$  and the  $4^2P_{1/2}$   $F'' = 2$  state with a  $D_1$  “cycling” beam connecting states  $F = 2 \rightarrow F'' = 2$

and a  $D_1$  “repump” beam connecting states  $F = 1 \rightarrow F'' = 2$  as shown in Fig. 3.11. Since  $^{39}\text{K}$  is not an ideal three-level system however, the situation changes slightly but this is the operating principle nevertheless. An intensity ratio of around 3:1 between the  $D_1$  cycling and  $D_1$  repump is commonly used with an equal blue detuning from the  $F'' = 2$  state of around 5 natural linewidths. The capture range of the  $D_1$  molasses force is quite narrow compared to a normal optical molasses however, which necessitates the use of a standard  $D_2$  optical molasses followed by a  $D_1$  molasses for optimal efficiency. Using this technique,  $^{39}\text{K}$  has been cooled to temperatures  $< 10 \mu\text{K}$  [111, 112] which is easily cold enough to capture an appreciable amount of atoms directly in an optical dipole trap. Then, with the help of the Feshbach resonance to tune the scattering length, all-optical evaporation can be performed to cool the gas to BEC.

### 3.4 Performing an Experiment

Now that we know how our BECs are made, we can discuss how we use them to perform experiments. One major benefit of the momentum-space lattice is the ease with which we are able to “program” new experiments. In general terms, when we perform an experiment we are simply watching what happens to atoms when we modulate a light field to which they are exposed. Our apparatus is designed such that the modulation of that light field (the lattice) is performed by a single AOM with a multifrequency drive as shown in Fig. 3.2. Therefore, all the parameters about the experiment that one would like to change are contained within this electronic multifrequency RF drive. The multifrequency RF drive is created, in turn, by an Arbitrary Waveform Generator (AWG). The AWG simply outputs a list of voltage values that are programmed into it to create any kind of waveform. We control the parameters of the experiment by writing these arbitrary waveforms (“arbs”), hence the phrase “program the experiment.”

### 3.4.1 Arbitrary Waveforms

An arb is essentially just the list of voltages that define the multi-frequency drive that creates our momentum-space lattice. We use Wolfram Mathematica as the platform for creating arbs and below we show an example of Mathematica code which creates an arbitrary waveform. The example creates a 5-site lattice with indices  $n = \{-2, -1, 0, 1, 2\}$ . The tunneling strengths  $V_n$ , tunneling phases  $\varphi_n$ , and site energies are all set (In[7], In[8], and In[9–10] in the code below) to illustrate the control over the experiment. The  $V_n$  and  $\varphi_n$  have been chosen arbitrarily but for ease of illustration the  $\epsilon_n$  have been set to a tilted lattice, with the energy of each site  $+1 E_r$  from its neighbor to the left. Note however that the site energies are defined in terms of the drive field’s detuning from single particle resonance such that we must define another parameter  $\delta_n = \epsilon_{n+1} - \epsilon_n$ . Then at line In[15] the actual sum of sine waves which is sampled to produce the multifrequency field is defined. In plain math it looks like:

$$\sum_{n=-2}^{n=1} V_n \sin([80 \text{ MHz} + \delta_n] 2\pi\tau + \varphi_n), \quad (3.1)$$

which creates the Hamiltonian:

$$H_{\text{arb}} = \sum_{n=-2}^{n=2} \epsilon_n c_n^\dagger c_n + \sum_{n=-2}^{n=1} (t_n e^{-i\phi_n} c_n^\dagger c_{n+1} + \text{H.c.}), \quad (3.2)$$

where  $c_n^{(\dagger)}$  represents the annihilation (creation) operator for a particle at “site”  $n$ ,  $t_n$  is related to  $V_n$  by an overall calibration scaling, and  $\phi_n$  is related to  $\varphi_n$  but incorporates the phase difference between the two Bragg beams.

In the Fourier spectrum of these frequencies (plotted at In[18] and shown in Fig. 3.18) the effects of the custom parameters can be directly observed. The detuning from 80 MHz is shown on the horizontal axis and the vertical axis is an arbitrary peak height relating to the weight at each frequency. The gray grid lines show the two-photon Bragg resonances for the 5-site lattice. The height of the peaks matches with the programmed  $V_n = \{1., 0.6, 0.9, 0.2\}$  and the detunings from resonance for each peak matches with the tilted lattice  $\epsilon_n = \{-2, -1, 0, 1, 2\} E_r$ . Finally, the arb is given a name and an output destination and a custom function creates a .arb file which has the correct syntax to be read

by our specific AWG. The code for this example is reproduced in full below with comments shown in gray and predefined functions shown in red.

```
(* Example arbitrary waveform generator code for a tilted five site lattice with
pseudo random tunneling energies and tunneling phases. Eric J. Meier
2019.09.17 *)

In[3]:= (* The following two functions take in the site indices which one wants
to couple and calculates the two-photon Bragg resonance frequency *)
det[ni_, nf_] := 2 ER1064/(\[Pi] \[HBar]) (ni + nf)
det[ni_] := 2 ER1064/(\[Pi] \[HBar]) (2 ni + 1)

In[5]:= (* "links" defines the size of the system, here I am linking n to n+1 for
sites {-2,-1,0,1} making a 5 site lattice *)
links = Range[-2, 1]

Out[5]= {-2, -1, 0, 1}

In[6]:= (* actually calculating the Bragg resonances *)
DetuningList = det /@ links

Out[6]= {-24333.8, -8111.26, 8111.26, 24333.8}

In[7]:= (* This is a list of the tunneling strengths for each link in the lattice
*)
tn = {1.0, 0.6, 0.9, 0.2}

Out[7]= {1., 0.6, 0.9, 0.2}

In[8]:= (* This is a list of the tunneling phases for the experiment *)
\[Phi]n = {0., \[Pi]/100, \[Pi]/6, \[Pi]}

Out[8]= {0., \[Pi]/100, \[Pi]/6, \[Pi]}

In[9]:= (* This is a list of the site energies to be used in the experiment *)
\[Epsilon]n = {-2., -1.0, 0., 1.0, 2.0} \[\Omega]R1064/(2 \[Pi])

Out[9]= {-4055.63, -2027.81, 0., 2027.81, 4055.63}

In[10]:= (* Since we define the site energies through the link detunings from
Bragg resonance, this calculates those detunings *)
\[Epsilon]ndiff = DetuningList + Differences[\[Epsilon]n]

Out[10]= {-22306., -6083.44, 10139.1, 26361.6}

In[11]:= (* Here I'm setting the total length of the experiment to give the
arbitrary waveform a timebase to define the frequencies and setting the sample
```

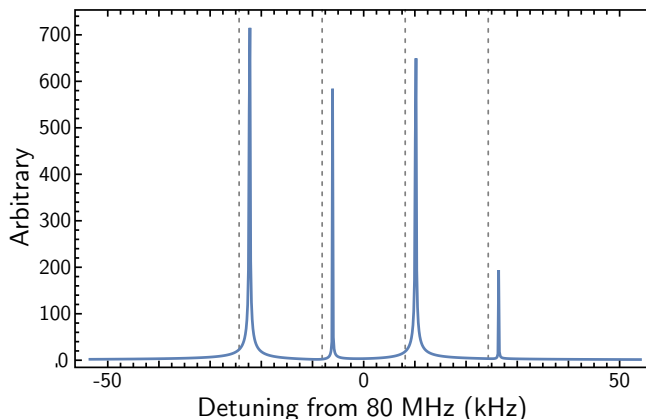


Figure 3.18: Fourier spectrum of example arbitrary waveform. The amplitude is plotted versus frequency (offset from 80 MHz) showing the four peaks for the five site lattice in the example code. The peak height corresponds to the choice of  $V_n$  and the offset from the two-photon Bragg resonances (the gray dashed lines) corresponds to the site energy tilt.

```

    rate of the AWG (with what frequency the voltage points should be output) *)
ArbTime = 6.75 10^-3;
ArbSampleRate = 5.75 10^8;

In[13]:= (* These lines are for calibration purposes. First, the maximum of the
    subsequent function is found and later it is appended (+1) to the list of
    voltages to have a clearly defined maximum value. This ensures that between
    experiments your functions are not rescaled and the tunnelings do not change.
    *)
MaxRFPower = Total[tn];
CalibrationPoint = Round[MaxRFPower + 1];

In[15]:= (* This is the actual function defining the multifrequency drive. A sum
    of sine waves at the right frequency and with the right phase. The 80 MHz
    added to the detuning list is because the AOM has a center frequency of 80 MHz
    . *)
IntermediateArbList[TimeList_] := Sum[tn[[1]]*Sin[(80.*10^6 + \[Epsilon]ndiff[[1
    ]]) 2 \[Pi] TimeList + \[Phi]n[[1]]], {1, 1, Length[links]]}

In[16]:= (* A list of times with which to sample the function is created and the
    function is sampled, generating a list of voltage values. *)
TimeList = Range[0, ArbTime, ArbTime/(ArbTime*ArbSampleRate - 1)];
ArbList = IntermediateArbList[TimeList];

In[18]:= (* using a custom function, the spectrum of the multifrequency drive is
    plotted and checked. *)
FourierPlotter[ArbList, ArbTime, DetuningList]

(* see Fig. 3.18 for Out[18] *)

```

```

In[19]:= (* The calibration points are appended to the voltage list and the arb
file is named and exported. *)
ScaledArbList = Flatten[AppendTo[ArbList, {CalibrationPoint, -CalibrationPoint
}]];
date = today;
(* we set the overall scaling of the AWG here *)
Ch2Vpp = 10.0;
filename = "Example.arb";
expdir = NotebookDirectory[];
(* This is a custom function which formats the list of voltages in the right
syntax to be directly read by the AWG *)
ArbExporter[ScaledArbList, filename, date, Ch2Vpp, ArbSampleRate, expdir]

Out[24]= "Arb Exported as: Example.arb"

```

One important point which is reflected in the code is the calibration of the waveforms amplitude. It is often the case that to set the overall tunneling rate of the Hamiltonian we make a separate calibration waveform. If the calibration waveform and the actual experiment's waveform have different scalings based on some arbitrary maximum of the multifrequency signal, then the calibration will not match the experiment. We get around this by first writing the arb file for the experiment and calculating its maximum value as shown in In[13] of the code. This maximum value (with an added buffer of +1) is then appended to the ends of both the calibration arb and experiment arb (line In[19]) to ensure that they have the same maximum value and therefore the same overall scaling. In this same vein it is also important to define the total length of the experiment, ArbTime at In[11], and the rate at which the AWG will output the arb, ArbSampleRate at In[11]. These two factors essentially define the timebase of the arb, TimeList at In[16], and therefore set the actual frequencies which are written. If the arb is output faster (slower) than expected it will blue (red) shift all the frequencies driving the AOM and completely foil the experiment.

Not shown in the example code above is the use of time dependence in the parameters. This can be extremely useful for creating ramps or loading into eigenstates but can become very complicated. One thing to keep in mind when writing these arbitrary waveforms is that if the Fourier transform does not look as one expects it to, the experiment has not been programmed correctly. For example when performing a ramp of the site energy, the extra time dependence can create a sort of doubling effect in the Fourier transform and this has

to be taken into account in the initial ramp to prevent undesired effects (see Sec. B.5 for details and an example of this).

### 3.4.2 Data Collection and Processing

#### Camera Operation

As alluded to in Subsec. 3.2.4, the final image of a BEC is made out of three individual images of the profile of a resonant laser beam. The first image, the signal, has absorption features at the locations of the atoms in the science cell. The second image, the background, is taken after the atoms fly away and only shows the profile of the laser beam. The third image, the noise, is taken with the laser beam off and the shutter closed and captures the noise level of the camera when the measurement was taken. We use an Andor Neo 5.5 sCMOS [DC-152Q-C00-FI](#) camera to collect the light. The detector area of the camera is essentially an array of light sensitive pixels which read a number proportional to the amount of photons they absorbed during a specific exposure time. The detector is not very color sensitive however, so filters and shutters are used to ensure none of the room lights or other equipment lights affect the image. An exposure time of  $125\ \mu\text{s}$  is used with a time of 80 ms between each of the three images.

The software which controls the camera is not well-suited to this kind of operation but the ability for user customization is practically infinite as the software allows for the writing and implementation of user-made code. The software can run programs written in a proprietary coding language called Andor Basic which is relatively easy to use. The following program was written to accommodate our three-image bursts. To summarize, when the code is first run it does the following:

- (i) First, it asks the user what number image they want to start at.
- (ii) The program then prompts the user to say whether they would like to define a cropping region of interest for the images. If the user responds that they would like to crop the image the program continues to ask them for individual cropping parameters. If not, the program advances to the ready state for taking an image.

- (iii) The program then waits for a trigger from the control software Cicero [as described in Subsec. 3.1.3].
- (iv) After the first image is taken the camera saves that data in temporary storage and readies itself for another exposure which comes shortly thereafter. This is repeated three times total for the three images taken.
- (v) The three images are concatenated to one file and exported to the predetermined destination folder.
- (vi) The camera then cycles back to the beginning of the program and readies itself for another three-shot burst.

The plain text of the program along with several operational notes are provided in full in Sec. A.3.

### Image Processing

Now that we have our three measurements, we can turn them into a proper absorption image. This is done by calculating the optical depth from the three images with the following formula:

$$\text{OD} = \ln \left( \frac{\text{background} - \text{noise}}{\text{signal} - \text{noise}} \right). \quad (3.3)$$

Figure 3.19 shows this calculation in practice. After some evolution in some Hamiltonian, we have population spread out over several lattice sites. We first image them by shining a near-resonant beam on them as discussed in Sec. 3.2.4 and shown in Fig. 3.9(b) to generate the signal image as shown in the top left of Fig. 3.19. If one looks closely, the shadows in the beam can be seen with the most pronounced of these shadows positioned halfway down the image directly under the letter ‘g’ in “Signal”. Then after the atoms fall away we take another image of just the laser beam profile called the background image as shown in the left middle of Fig. 3.19. One might expect to see a nice clean Gaussian profile in this image but imperfections in optics, dust, and thin film effects lead to a complicated interference pattern in the beam profile. Finally, an image is taken with no light hitting the camera at all to

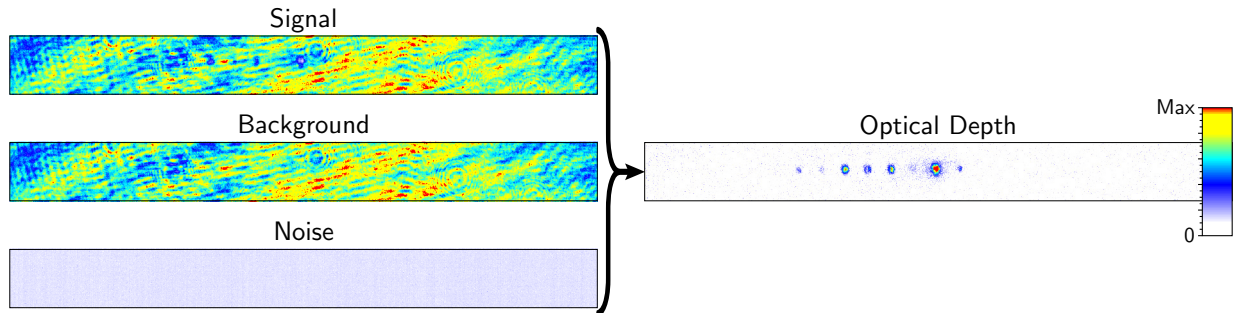


Figure 3.19: Calculation of optical depth from three absorption images. The signal image shows the absorption dips in the profile of the laser beam as little dark spots. The most pronounced of these is halfway down the image just below the ‘g’ in Signal. The background image shows just the profile of the laser after the atoms have fallen out of the frame. The striations and patterns seen here relate to interference of the imaging beam picked up on the way to the camera from dust and imperfect optics as well as interference caused by thin film effects from filters and windows before the detector of the camera. The noise image shows the dark counts of the camera after the laser has been blocked (this image is scaled by a factor of 2 in comparison to the signal and background image). Finally, the optical depth as calculated with Eq. 3.3 is shown with population spread over many lattice sites. The color bar for all four images is shown at right.

capture its dark counts as shown in the bottom left of Fig. 3.19. These three images are combined according to Eq. 3.3 resulting in the optical depth as shown at right and revealing the atomic population distributed across the lattice sites.

These absorption images can be very useful for getting a qualitative sense of what is happening to the condensate wave function. However, for more quantitative analysis these images must be fit such that the relative fraction of the condensate in each lattice site can be extracted. This process begins by summing each column of the image to compress the data into a 1D profile of the lattice populations. We then fit this summed data with a function of the form:

$$\sum_n A_n e^{-\frac{(x-x_{0,n})^2}{2\sigma_n^2}}, \quad (3.4)$$

where  $x$  is the horizontal dimension,  $A_n$  is the amplitude,  $x_{0,n}$  is the position offset, and  $\sigma_n$  is the width, all for specific momentum mode  $n$ . The fitting function (NonlinearModelFit in Mathematica) is provided with initial estimates as well as constraints to ensure a good fit to the data. We then calculate the area  $V_n$  under each momentum state curve with  $V_n = \sqrt{2\pi}A_n\sigma_n$ . This set of areas is then arbitrarily scaled such that  $\sum_n V_n = 1$ . This method of measurement is especially nice because it eliminates the need to ever know how many atoms are actually participating in the experiment, a notoriously difficult thing to

measure precisely.

In the single-particle (*i. e.*, non-interacting) picture each atom independently responds to the Hamiltonian and has its wave function evolve into something of the form  $|\psi_{\text{atom}}\rangle = \sum_n c_n |n\rangle$  where  $|n\rangle$  represents the momentum states and  $|c_n|^2$  the probability that an atom will collapse into that state upon measurement. The “measurement” in this sense occurs when the atom is released from the trap and must decide which way to fly and with what speed, thereby deciding its momentum state  $|n\rangle$ . If we used single atoms to perform this measurement the atom would appear in different momentum states with probability  $|c_n|^2$  upon each measurement, but since there are  $\approx 10^5$  atoms doing this same thing at the same time our final image already has this averaging built in. So what we measure when we take an absorption image of the final distribution of atoms is essentially the set of probabilities  $\{|c_n|^2\}$  which relate directly to the number of atoms which ended up in a given momentum state. Therefore, when we calculate the fraction of atoms in each momentum state  $V_n$  we have actually measured the probability of the wave function *i. e.*,  $V_n = |c_n|^2$ . One drawback of this technique is that it provides no information on any relative phase structure which may or may not be present in the wave function, but we have indirect ways of measuring phase in experiment as detailed in Subsecs. [4.2.2](#) and [7.2.2](#).



# Chapter 4

## Clean Topological Wires

The first experiment we present, clean topological wires, was performed in conjunction with Alex An and under the guidance of Bryce Gadway and we further acknowledge helpful discussions with Taylor Hughes, Ian Mondragon-Shem, and Smitha Vishveshwara. Our discussion of this experiment here is largely a reproduction of Ref. [33] with additional information regarding the implementation of the specific experiments.

### 4.1 Introduction

The polymer *trans*-polyacetylene is normally a simple organic insulator. However, through halogen or alkali metal doping, its conductivity can be increased by over ten orders of magnitude [37, 38, 120]. This unusual electronic property stems from topologically-protected solitonic defects that are free to move along the polymer chain [2, 36]. To account for such behavior, Su, Schrieffer, and Heeger (SSH) proposed a simple one-dimensional (1D) tight-binding model with alternating off-diagonal tunneling strengths to represent doped polyacetylene [2]. The SSH model has since served as a paradigmatic example of a 1D system supporting charge fractionalization [36, 121] and topological character [39].

The emergence of such exotic phenomena in a simple 1D setting has naturally inspired numerous related experimental investigations, including efforts to probe aspects of the SSH model by quantum simulation with pristine and tunable ultracold atomic gases. Recently, using real-space superlattices [122, 123], several bulk characteristics of the SSH model’s topological nature have been explored. These include the measurement of bulk topological indices [29] and the observation of topologically robust charge pumping [124, 125]. Topological pumping has also been observed in a “magnetic lattice” based on internal-state synthetic dimensions [11, 126]. Cold atom experiments have even begun to probe topological boundary

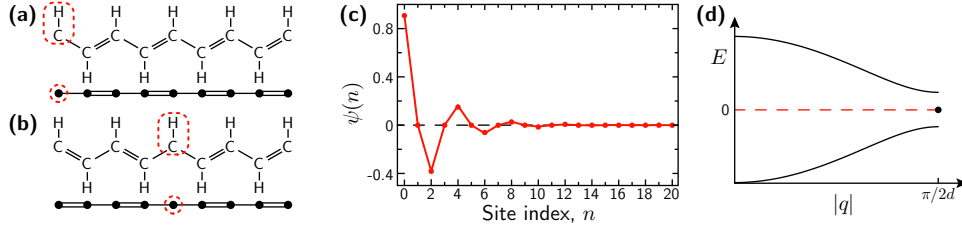


Figure 4.1: The SSH model revisited. **(a)** Top: Chemical structure of *trans*-polyacetylene showing the two-site unit cell structure. The dashed red oval encloses the (edge) defect carbon atom at the left system boundary. Bottom: 1D lattice representation of this molecule. **(b)** The two possible topological phases of polyacetylene joined by a (central) defect at the dashed red oval, with lattice representation below. **(c)** Wavefunction of the localized, zero-energy eigenstate vs. lattice site index, for the edge defect as in **(a)** and  $\Delta/t = 0.41$ . The wavefunction shows population at only even lattice sites (given a defect at site zero) and a  $\pi$  phase inversion (reflected in the sign of the wavefunction) at every other even indexed lattice site. **(d)** Gapped energy dispersion of the SSH model for open boundary conditions and a lattice spacing  $d$ , with a mid-gap state at zero energy. This figure was adapted from Ref. [33].

states, with recent evidence for boundary localization in the related 1D Dirac Hamiltonian with spatially varying effective mass [127]. Highly-tunable photonic simulators [128] have provided a complementary window into the physics of topological systems [129, 130]. In particular, evidence for topological 1D bound states has been found [131] in the discrete quantum walk of light in a Floquet-engineered [132] system resembling the SSH model. Related bound state behavior has also been observed in 1D photonic quasicrystals [133, 134].

The molecule *trans*-polyacetylene consists of a 1D carbon chain connected through alternating single and double bonds. This sublattice bond structure, emblematic of 1D chiral symmetric topological insulators [39], leads to two distinct topological phases. Interesting electronic properties arise when these two phases (or one of the phases and a trivial, non-topological phase) are interfaced. Figure 4.1(a) shows an example of an *edge defect* carbon atom interfacing a polyacetylene chain with the nontopological vacuum. In the case of a *central defect*, the two distinct topological phases of the SSH model are interfaced at a defect carbon atom with two single bonds, as illustrated in Fig. 4.1(b).

Topological polyacetylene chains support zero-energy electronic eigenstates localized to such defects, the basis of which may be found by examining the effective 1D tight-binding model proposed by SSH in [2]. In this simplified picture [see Figs. 4.1(a,b)], the polymer chain's carbon backbone acts as a 1D lattice for electrons, with the alternating double and single bonds represented as strong ( $t + \Delta$ ) and weak ( $t - \Delta$ ) tunneling links, respectively.

The Hamiltonian describing the SSH model is given by

$$H = -(t + \Delta) \sum_{n \in \text{odd}} (c_{n+1}^\dagger c_n + \text{h.c.}) - (t - \Delta) \sum_{n \in \text{even}} (c_{n+1}^\dagger c_n + \text{h.c.}), \quad (4.1)$$

where  $t$  is the average tunneling strength and  $2\Delta$  the tunneling imbalance. This bipartite sublattice structure, the result of a Peierls distortion in the polyacetylene chain, leads to a two-band energy dispersion as in Fig. 4.1(d) with an energy gap  $E_{\text{gap}} = 2\Delta$ . When distinct topological phases of these SSH wires are directly interfaced, spatially localized “mid-gap” eigenstates appear in the middle of this energy gap.

Figure 4.1(c) displays such a localized mid-gap state wavefunction for the case of an edge (site zero) defect as in Fig. 4.1(a), with the particular choice of  $\Delta/t = 0.41$ . Several key features of the topological boundary state are illustrated by Fig. 4.1(c). First, it is localized to the defect site with a characteristic decay length  $\xi/d \sim (\Delta/t)^{-1}$  due to its energetic separation by  $\Delta$  from the dispersive bulk states, where  $d$  is the spacing between lattice sites. Additionally, this topological boundary state exhibits the absence of population on odd lattice sites and a sign inversion of the wavefunction on alternating even sites. Both of these features can be understood from the fact that the state is composed of two quasimomentum states with  $q = \pm\pi/2d$ , leading to a  $\cos(\pi n/2d)$ -like variation of the eigenstate wavefunction underneath the aforementioned exponentially decaying envelope. Below, we directly explore these properties of the mid-gap state wavefunction through single-site injection, multi-site injection, and adiabatic preparation.

## 4.2 Results

### 4.2.1 Single-Site Injection

#### Single-Site Injection: Results

One method for probing topological bound states of the SSH model is to abruptly expose our condensate atoms, initially localized at only a single lattice site, to the Hamiltonian [Eq. 4.1] and observe the ensuing quench dynamics. When population is injected onto a defect site,

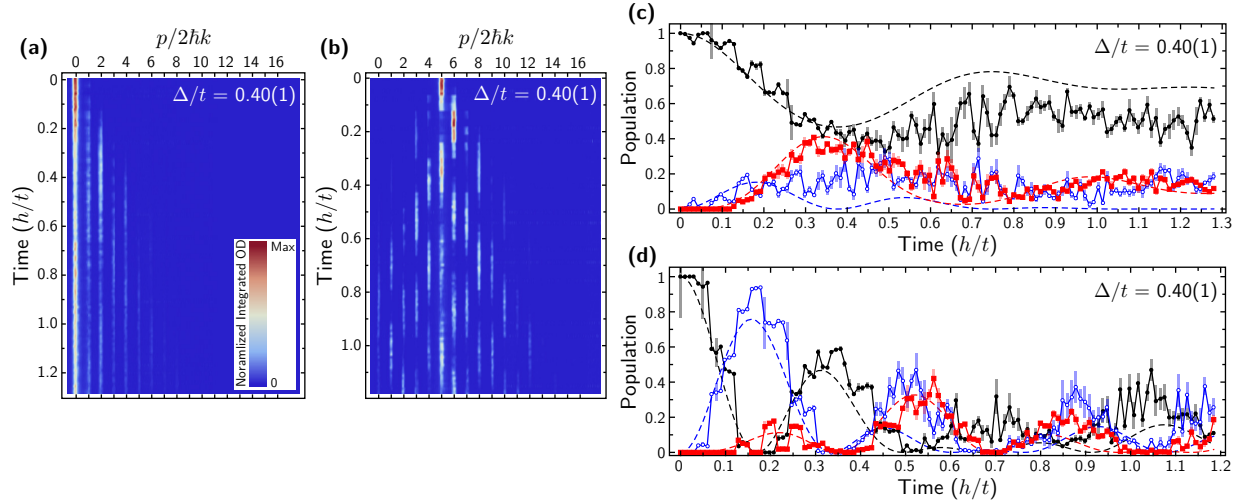


Figure 4.2: Nonequilibrium quench dynamics in the SSH model. **(a)** Integrated absorption images vs. evolution time for population injected at the edge defect and  $\Delta/t = 0.40(1)$ . **(b)** Integrated absorption images vs. evolution time for population injected in the bulk (lattice site five) and  $\Delta/t = 0.40(1)$ . **(c)** Population vs. evolution time for lattice sites zero (black circles), one (red squares), and two (open blue circles) following population injection at the edge defect. **(d)** Population vs. evolution time for lattice sites five (black circles), six (red squares), and seven (open blue circles) following population injection in the bulk. Dashed curves in (c, d) are numerical simulations with no free parameters. All error bars denote one standard error of the mean. This figure was adapted from Ref. [33].

we expect to find a large overlap with the mid-gap state, resulting in a relative lack of dynamics as compared to injection at any other lattice site. Our observations using this quench technique are summarized in Fig. 4.2. In these experiments, population is injected at a single lattice site of our choosing, and the subsequent dynamics are observed with single-site resolution and  $10 \mu\text{s}$  ( $\sim 0.01 h/t$ ) time sampling.

Figure 4.2(a) shows the full dynamics for population injected at the edge defect site, for a lattice characterized by  $\Delta/t = 0.40(1)$ . We observe slow dynamics and significant residual population in the defect site at long times, suggesting localization at the defect. We additionally observe characteristics of the mid-gap state's parity in these dynamics, *i. e.*, the odd lattice sites remain sparsely populated as some atoms spread away from the edge to the second lattice site. Whereas edge injection results in localization, injecting population into the bulk (site five) leads to faster dynamics and increased population spread, as shown in Fig. 4.2(b) for  $\Delta/t = 0.40(1)$ . For these cases of edge and bulk injection, the normalized population dynamics of three sites near the injection point are shown in Figs. 4.2(c,d). The dashed lines represent numerical simulations of Eq. 4.1 with no free parameters, exhibiting

excellent agreement with the data.

### Single-Site Injection: Implementation

For quench experiments starting at the edge of the system a multi-frequency voltage signal was generated with the following form

$$\begin{aligned}
 V(\tau) = & (t + \Delta) \sum_{n=1, n \in \text{odd}}^{19} \sin([2\pi(80 \text{ MHz}) + \omega_n^{\text{res}}] \tau) \\
 & + (t - \Delta) \sum_{n=0, n \in \text{even}}^{18} \sin([2\pi(80 \text{ MHz}) + \omega_n^{\text{res}}] \tau),
 \end{aligned} \tag{4.2}$$

where  $\omega_n^{\text{res}}$  is the resonant frequency linking sites  $n \rightarrow n + 1$  and 80 MHz represents the center frequency of the acousto-optic modulator pair which write this voltage signal onto the laser. This creates a 21-site system as shown in Fig. 4.1(a) with the zero momentum mode, where all atoms in the condensate start, at the edge of the system. Similarly for quench experiments starting somewhere in the bulk, one need only change the indices in the sums to shift the starting position of the atomic population.

The tunneling strengths  $t + \Delta$  and  $t - \Delta$  are measured and calibrated by creating an identical multi-frequency voltage signal but with all the frequencies shifted to unconnected sites except for the one connecting sites  $n = 0 \rightarrow n = 1$  which looks like

$$\begin{aligned}
 V(\tau) = & (t - \Delta) \sin([2\pi(80 \text{ MHz}) + \omega_0^{\text{res}}] \tau) \\
 & + (t + \Delta) \sum_{n=51, n \in \text{odd}}^{69} \sin([2\pi(80 \text{ MHz}) + \omega_n^{\text{res}}] \tau) \\
 & + (t - \Delta) \sum_{n=52, n \in \text{even}}^{68} \sin([2\pi(80 \text{ MHz}) + \omega_n^{\text{res}}] \tau),
 \end{aligned} \tag{4.3}$$

for calibrating  $t - \Delta$  and similarly for calibrating  $t + \Delta$ . Notice the indices in the sums have changed to be between  $n = 50$ – $70$ . The reason for doing it this way is to preserve the total RF power in any given frequency component. In this way we directly measure the Rabi frequency associated with this sole, resonant coupling.

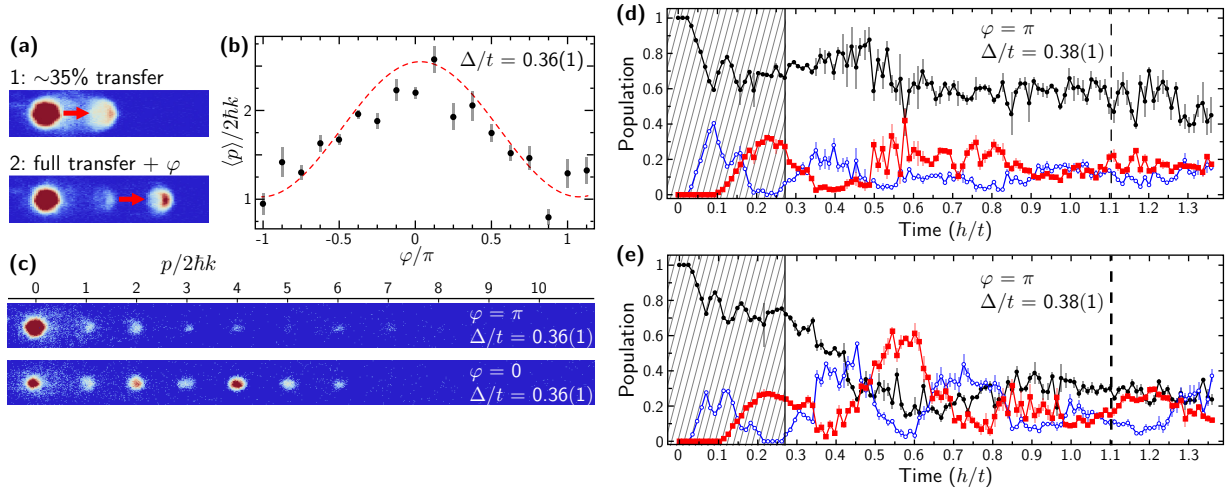


Figure 4.3: Phase-sensitive injection into the SSH model edge state. **(a)** Absorption images detailing the two-stage state initialization sequence. In stage 1,  $\sim 35\%$  of the atoms are transferred from site zero to site one (indicated by the red arrow) with no applied phase shift. In stage 2, nearly all of the atoms in site one are transferred to site two with a controlled phase shift  $\varphi$ . **(b)** The expectation value of the site index  $n$  is plotted vs. the phase  $\varphi$  of initialized states, following a Hamiltonian quench and  $760 \mu\text{s}$  ( $\sim 0.78 h/t$ ) of evolution for  $\Delta/t = 0.36(1)$ . The dashed line corresponds to a numerical simulation given the prepared initial state with no free parameters. **(c)** Absorption images taken after  $760 \mu\text{s}$  ( $\sim 0.78 h/t$ ) of evolution following the initialization and quench, corresponding to phases of  $\varphi = \pi$  (top) and  $\varphi = 0$  (bottom), respectively for  $\Delta/t = 0.36(1)$ . **(d, e)** Population at lattice sites zero (black circles), one (red squares), and two (open blue circles) vs. evolution time for  $\Delta/t = 0.38(1)$  for  $\varphi = \pi$  (d) and  $\varphi = 0$  (e). The shaded regions and dashed lines denote initialization and imaging stages of the experiment, respectively. All error bars denote one standard error of the mean. This figure was adapted from Ref. [33].

## 4.2.2 Phase-Sensitive Injection

### Phase-Sensitive Injection: Results

A more sophisticated probe of the topologically-protected mid-gap state can be achieved through controlled engineering of the atomic population prior to quenching the SSH Hamiltonian. Specifically, we can initialize the atoms to match the defining characteristics of a mid-gap state localized to an edge defect: decay of amplitude into the bulk, absence of population on odd lattice sites, and  $\pi$  phase inversions on successive even sites. We expect that such an initialization should more closely approximate the mid-gap eigenstate, resulting in the near absence of dynamics following the Hamiltonian quench. However, if the relative phases of the condensate wavefunction at different lattice sites are inconsistent with those of the mid-gap state, significant dynamics should ensue.

We prepare the mid-gap state through a two-stage process, as illustrated in Fig. 4.3(a).

In the first stage of the sequence, only sites zero and one are coupled, with roughly 35% of the atomic population transferred to site one with a natural phase shift of  $\pi/2$ , *i. e.*,  $H_{(1)} = -t(c_1^\dagger c_0 + \text{h.c.})$ . Then, in the second stage, sites one and two are coupled to allow full transfer of the population at site one to site two with a chosen phase shift. This second stage is characterized by the Hamiltonian  $H_{(2)} = (te^{-i\varphi}c_2^\dagger c_1 + \text{h.c.})$ , such that the total relative phase between sites zero and two is  $\varphi$ . Thus, this initialization sequence results in appreciable population at lattice sites zero ( $\sim 65\%$ ) and two ( $\sim 35\%$ ) with a chosen phase difference of  $\varphi$  between them.

Figure 4.3(b) summarizes the results of our probing the inherent sensitivity of the mid-gap state to this controlled relative phase  $\varphi$ . Here, the initial state is prepared with some chosen  $\varphi$  and subjected to a quench of the Hamiltonian with  $\Delta/t = 0.36(1)$  for an evolution time of  $\sim 0.78 h/t$ . When the phase difference of the initial state agrees with that of the mid-gap state ( $\varphi = \pm\pi$ ), the average distance from the edge of the system is minimized. Conversely, a phase difference of zero results in population spreading furthest from the defect site. We see excellent agreement between the full dependence on  $\varphi$  and numerical simulations with zero free parameters in Fig. 4.3(b). For the two extremal initialization conditions of  $\varphi = \pi$  and 0, example time of flight images and full quench dynamics are depicted in Figs. 4.3(c-e). The quench dynamics shown in Figs. 4.3(d,e) more fully illustrate and contrast these two cases. A near absence of dynamics is seen when the phase matches that of the mid-gap state ( $\varphi = \pi$ ), while defect-site population is immediately reduced when the phase does not match ( $\varphi = 0$ ).

**Phase-Sensitive Injection: Implementation**

For these experiments, the multi-frequency voltage signal is broken into three distinct parts which are eventually joined via a piece meal function. The first part  $V_1(\tau)$  is given by

$$\begin{aligned}
V_1(\tau) = & + (t + \Delta) \sin ([2\pi(80 \text{ MHz}) + \omega_0^{\text{res}}] \tau) \\
& + (t + \Delta) \sum_{n=53, n \in \text{odd}}^{69} \sin ([2\pi(80 \text{ MHz}) + \omega_n^{\text{res}}] \tau) \\
& + (t - \Delta) \sum_{n=50, n \in \text{even}}^{68} \sin ([2\pi(80 \text{ MHz}) + \omega_n^{\text{res}}] \tau),
\end{aligned} \tag{4.4}$$

which, when considering the atoms, links only sites  $n = 0 \rightarrow n = 1$  with the stronger tunneling  $t + \Delta$  and disconnects all the other links. This performs the first part of the manual preparation sequence. The atoms are exposed to this function for  $60 \mu\text{s}$ , enough time to transfer roughly 35% of the population across this transition.

After this, the function switches to the second part of the preparation stage linking sites  $n = 1 \rightarrow n = 2$

$$\begin{aligned}
V_2(\tau) = & + (t + \Delta) \sin ([2\pi(80 \text{ MHz}) + \omega_1^{\text{res}}] \tau + \varphi) \\
& + (t + \Delta) \sum_{n=53, n \in \text{odd}}^{69} \sin ([2\pi(80 \text{ MHz}) + \omega_n^{\text{res}}] \tau) \\
& + (t - \Delta) \sum_{n=50, n \in \text{even}}^{68} \sin ([2\pi(80 \text{ MHz}) + \omega_n^{\text{res}}] \tau),
\end{aligned} \tag{4.5}$$

where the only differences are the index on  $\omega_1^{\text{res}}$  and the very important phase factor  $\varphi$  now present in the first term. This function is turned on for  $180 \mu\text{s}$  to transfer all the population which was moved to site  $n = 1$  during the first stage to  $n = 2$  and give it a relative phase  $\varphi$ . Once this stage is complete the full Hamiltonian is turned on with a voltage function identical to that shown for the quench experiments. The tunneling energies in these experiments are also calibrated in the same way as for the quench experiments.

### 4.2.3 Adiabatic Preparation

#### Adiabatic Preparation: Results

Lastly, using our full time-dependent control over the system parameters, we directly probe the mid-gap state through a quantum annealing procedure. We begin by exactly preparing the edge mid-gap eigenstate in the fully dimerized limit of the SSH model, *i. e.*, with only the odd tunneling links present at a strength  $t_{\text{odd}} = t + \Delta_{\text{final}}$ . Atomic population is injected at the decoupled zeroth site, identically overlapped with the mid-gap state in this limit. Next, we slowly (over a time  $\tau_{\text{ramp}} = 1$  ms) increase tunneling on the even links from zero to  $t - \Delta_{\text{final}}$ , as depicted by the smooth ramp in Fig. 4.4(a) and described by the time-dependent Hamiltonian

$$H(\tau) = - \sum_{n \in \text{odd}} (t + \Delta_{\text{final}})(c_{n+1}^\dagger c_n + \text{h.c.}) - \sum_{n \in \text{even}} t_{\text{even}}(\tau)(c_{n+1}^\dagger c_n + \text{h.c.}), \quad (4.6)$$

where  $\tau$  denotes time. For adiabatic ramping, the atomic wavefunctions should follow the eigenstate of  $H(\tau)$  from purely localized at time zero to the mid-gap wavefunction (for variable  $\Delta_{\text{final}}/t$ ) at the end of the ramp. In the dimerized limit,  $\Delta_{\text{final}}/t = 1$ , the mid-gap state is isolated from two flat energy bands by a gap energy equal to  $t$ . This energy gap is reduced as  $\Delta_{\text{final}}/t$  decreases, with dispersions as in Fig. 4.1(d) for intermediate values. This gap finally closes and a single dispersive band emerges as  $\Delta_{\text{final}}/t \rightarrow 0$ .

Figure 4.4 summarizes our results using this adiabatic preparation method. Both simulated and averaged experimental absorption images for an adiabatically loaded lattice with the defect on the left edge are shown in Fig. 4.4(b), demonstrating excellent agreement. Adiabatic preparation was also performed for a lattice with a defect at its center, and Fig. 4.4(c) presents simulated and averaged experimental absorption images for this case, also showing good agreement.

As mentioned earlier and shown in Fig. 4.1(c), the amplitude of the mid-gap state wavefunction is largest at the defect site and decays exponentially into the bulk, owing to the energy gap  $\Delta$ . In units of the spacing  $d$  between lattice sites, the decay length  $\xi$  should scale roughly as the inverse of this energy gap (normalized to the average tunneling bandwidth

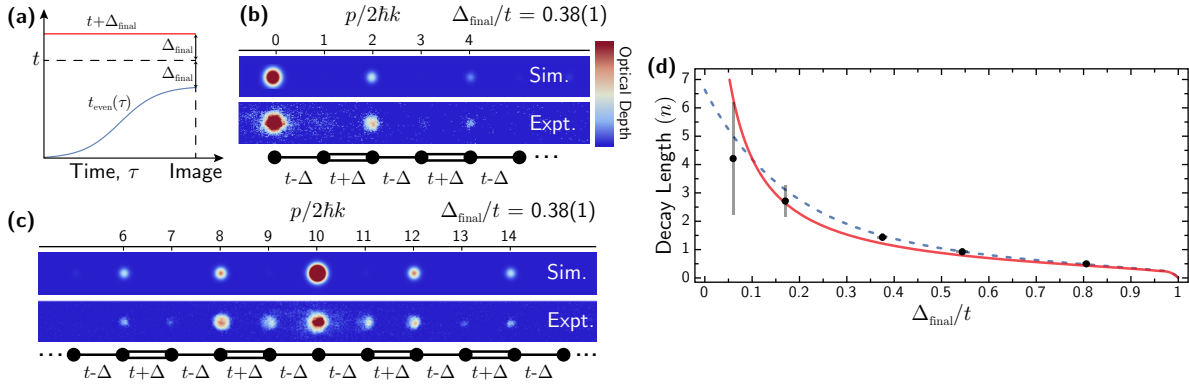


Figure 4.4: Adiabatic preparation of the topological soliton state in the SSH model. **(a)** Time sequence of the smooth, 1 ms-long ramp of the weak tunneling links (blue), holding the strong (red) links fixed. **(b)** Simulated (top) and averaged experimental (bottom) absorption images for an adiabatically loaded edge-defect lattice. **(c)** Same as (b), but for an adiabatically loaded central-defect lattice. **(d)** Decay length of the atomic distribution on even sites of the edge-defect lattice vs.  $\Delta_{\text{final}}/t$ . The dashed blue line represents the results of a numerical simulation of the experimental ramping protocol and the red line shows the exact mid-gap state decay length as a function of  $\Delta/t$  for a 21-site lattice. All error bars denote one standard error of the mean. This figure was adapted from Ref. [33].

$t$ ). We thus expect highly localized mid-gap states for  $\Delta/t \sim 1$  (dimerized limit) and an approach to full delocalization over all 21 sites for  $\Delta/t \ll 1$  (uniform limit). Using our ability to tune the normalized tunneling imbalance, we present in Fig. 4.4(d) a direct exploration of the mid-gap state's localization decay length as a function of  $\Delta_{\text{final}}/t$ . Here, we determine the decay length by fitting the measured atomic populations on even sites at the end of the ramp to an exponential decay. For very small  $\Delta_{\text{final}}/t$ , we expect the observed decay length to differ from that of the true mid-gap state due to deviations of our ramping protocol from adiabaticity with respect to a vanishing energy gap. Specifically, our smooth ramps of  $\Delta_{\text{final}}/t$  should have a duration that greatly exceeds the time scale associated with the smallest energy gap (*i. e.*,  $\tau_{\text{ramp}} \gg \hbar/\Delta_{\text{final}}$ ) to remain fully adiabatic. However, our ramp duration is actually shorter than  $\hbar/\Delta_{\text{final}}$  for the cases when  $\Delta_{\text{final}}/t < 0.13$ , and we should thus expect significant deviation from the predictions for the exact (adiabatic) mid-gap state as we approach small values of  $\Delta_{\text{final}}/t$ . Still, the data in Fig. 4.4(d) are in good qualitative agreement with the simple expectation of an inverse dependence on  $\Delta_{\text{final}}/t$ , and are mostly consistent with both a numerical simulation of the actual experimental ramping protocol (blue dashed line) as well as predictions based on the exact mid-gap state (red line).

### Adiabatic Preparation: Implementation

In these adiabatic preparation experiments we ramp the tunneling strengths to achieve a smooth loading of the mid-gap state. We used a hyperbolic tangent ramp to smoothly vary the tunneling energy of the weak links from zero up to  $t - \Delta$ . The ramp function  $R(\tau)$  we used was

$$R(\tau) = \frac{\tanh\left(\frac{x}{T}(\tau - T/2)\right) + \tanh\left(\frac{x}{2}\right)}{2 \tanh\left(\frac{x}{2}\right)}, \quad (4.7)$$

where  $x$  is a constant (here  $x = 4$  was used) which controls the slope of the ramp at the central portion and  $T$  is the total ramp duration (here 1 ms). To keep the total amplitude of all frequency components constant to ensure the tunneling energy was changing as we expected and not being renormalized we added additional ‘‘compensation links’’. These compensation terms play no role in the experiment other than to ensure that the RF power is not renormalized after the ramp ends. Therefore the multi-frequency voltage function used to drive the acousto-optic modulator looked like

$$\begin{aligned} V_2(\tau) = & + (t + \Delta) \sum_{n=1, n \in \text{odd}}^{19} \sin([2\pi(80 \text{ MHz}) + \omega_n^{\text{res}}] \tau) \\ & + (t - \Delta)R(\tau) \sum_{n=0, n \in \text{even}}^{18} \sin([2\pi(80 \text{ MHz}) + \omega_n^{\text{res}}] \tau) \\ & + (t - \Delta)(1 - R(\tau)) \sum_{n=50.5}^{68.5} \sin([2\pi(80 \text{ MHz}) + \omega_n^{\text{res}}] \tau), \end{aligned} \quad (4.8)$$

where the first term gives the constant strong links, the second term gives the time-varying weak links, and the third term gives the compensation links. This experiment was also calibrated in the same way as the single-site injection experiments already described.

## 4.3 Discussion

Having observed clear evidence for the topological mid-gap state of the SSH model in the non-interacting limit, this work could in the future be extended to study the stability of this state under the influence of nonlinear atomic interactions. Repulsive, long-ranged (in

momentum space) interactions are naturally present in our system due to the atoms' short-ranged interactions in real space, however the data shown here employs large tunneling bandwidths that dominate over the interaction energy scales. Future explorations of interacting topological wires may be enabled by moving to  $^{39}\text{K}$  and accessing the broad Feshbach resonance therein. More easily however, our arbitrary control over the simulated model naturally permits the addition of controlled disorder, enabling investigations of critical behavior and topological phase transitions in disordered topological wires [48, 135].

# Chapter 5

## Disordered Topological Wires

Utilizing our control over each tunneling amplitude and phase we extend our studies on the SSH model through the addition of disorder. This chapter is largely a reproduction of Ref. [48] and its supplement with the addition of data on topological charge pumping and simulations of the interacting SSH model. The experiments shown in this chapter were performed by Alex An and myself under the supervision of Bryce Gadway. The theory work, especially regarding the observable we call the (mean) chiral displacement was done by Alexandre Dauphin, Maria Maffei, and Pietro Massignan and for more information on this observable see the supplement of Ref. [48]. In addition, Taylor L. Hughes was enormously helpful in guiding the experiments from a theoretical standpoint. We also acknowledge helpful discussions with N. Goldman, M. Lewenstein, H. Shapourian, and I. Mondragon-Shem.

### 5.1 Introduction

Topology and disorder share many surprising connections, from the formal similarity of one-dimensional (1D) pseudo-disordered lattices and two-dimensional (2D) integer quantum Hall Hofstadter lattices [133, 136], to the deep connection between the symmetry classes of random matrices [137], and the classification of symmetry protected topological phases [39]. Recently, there has been great interest in exploring both disorder [138] and topology [139] through quantum simulation, stemming from the dramatic influences that these ingredients can have, separately, on the localization properties of quantum particles [15, 41]. When combined, disorder and topology can have a rich and varied influence on quantum transport [140]. Indeed, one of the hallmark features of topological insulators (TIs) is the topologically protected boundary states that are immune to weak disorder [141]. The robust conductance of

such boundary states, such as the 1D edge states of integer quantum Hall systems [15], or the 2D surface states of three-dimensional (3D) TIs [142], serves as an important counterexample to the inevitability of localization in low-dimensional disordered systems [41, 143]. Despite the robustness to weak disorder, a change in topology can result from strong disorder, and unusual critical phenomena related to the unwinding of the topology can accompany such transitions [144, 145].

Surprisingly, static disorder can also induce nontrivial topology when added to a trivial band structure. This disorder-driven topological phase, known as the *topological Anderson insulator* (TAI), was first predicted to occur in metallic 2D HgTe/CdTe quantum wells [42]. There has been much interest in the TAI phase over the past decade [42–44], and many theoretical studies have shown the TAI phenomenon to be quite general, emerging across a range of disordered systems [45–47, 146]. However, due to the lack of precise control over disorder in real materials, and the difficulty in engineering both topology and disorder in most quantum simulators, the TAI has so far evaded experimental realization.

We engineer synthetic 1D chiral symmetric wires with precisely controllable disorder using simultaneous, coherent control over many transitions between discrete quantum states of ultracold atoms. We directly measure the topological index of the synthetic wires through observation of the bulk dynamics of the atomic density following a quench. We observe a robustness of topological wires to weak tunneling (off-diagonal) disorder, while for very strong disorder we observe a transition from topological to trivial. We furthermore observe that a nontrivial topological band structure, the long-sought TAI phase [42], can be induced from an incipient non-topological phase through the addition of static disorder. These transitions, enabled by our unique ability to synthesize many precisely controlled disorder realizations, constitute the first detailed investigations of disorder-driven changes in topology in any experimental system.

The topological band structures we consider are 1D TIs based off the Su–Schrieffer–Heeger model having chiral, or sublattice, symmetry [2, 39, 46, 135]. The rich variety of phenomena associated with 1D TIs (e.g. boundary modes that are stable against disorder, bulk-boundary correspondence, and quantized charge pumping) are easy to visualize in such chiral symmetric wires. We describe this system in terms of a tight-binding model with a

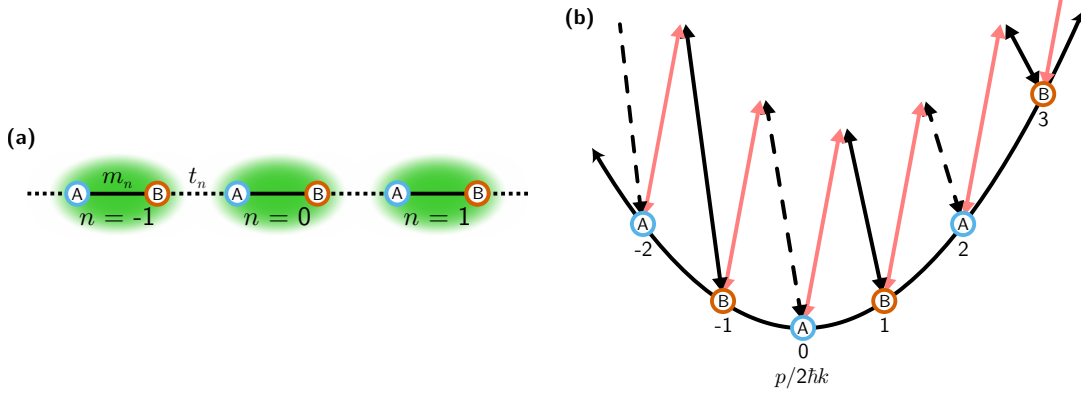


Figure 5.1: Synthetic chiral symmetric wires engineered with atomic momentum states. **(a)** Schematic lattice of the nearest-neighbor-coupled chiral symmetric wire. Site-to-site links within the unit cell (solid) and those connecting different unit cells (dashed) have independent tunneling energies  $m_n$  and  $t_n$ , respectively. **(b)** Schematic of the experimental implementation of the tight-binding model depicted in (a), with tunneling based on two-photon Bragg transitions between discrete atomic momentum states.

two-site unit cell, having sublattice sites  $A$  and  $B$  [depicted in Fig. 5.1]. We consider the Hamiltonian

$$H = \sum_n \left[ m_n c_n^\dagger S c_n + t_n \left( c_{n+1}^\dagger \frac{(\sigma_1 - i\sigma_2)}{2} c_n + \text{h.c.} \right) \right], \quad (5.1)$$

where  $c_n^\dagger = (c_{n,A}^\dagger, c_{n,B}^\dagger)$  creates a particle at unit cell  $n$  in sublattice site  $A$  or  $B$ ,  $c_n$  is the corresponding annihilation operator, and  $\sigma_i$  are the Pauli matrices related to the sublattice degree of freedom [135]. The  $m_n$  and  $t_n$  characterize the intra- and inter-cell tunneling energies. This model can describe chiral wires of the AIII or BDI symmetry classes, by choosing the intra-cell hopping term to be  $S = \sigma_1$  (BDI) or  $S = \sigma_2$  (AIII). Both the AIII (chiral unitary) and the BDI (chiral orthogonal) class models respect chiral symmetry, i.e., they obey  $\Gamma H \Gamma = -H$  with  $\Gamma = \sigma_3 \otimes \mathbb{I}$  the chiral operator, whereas the BDI class also obeys particle-hole and time-reversal symmetry [39]. In this work we choose to study both BDI and AIII class systems because they represent all possible distinguishable chiral classes for which the  $\mathbb{Z}$  topological invariant in one dimension, the winding number, is defined.

The simplicity of chiral symmetric wires, described by just a two-site unit cell with separate intra- and inter-cell hoppings, has allowed for several other realizations based on real-space superlattices [124, 125]. Such studies were restricted to exploring BDI wires, as quantum tunneling between stationary lattice sites is real-valued. In comparison, our use of laser-driven tunneling, which allows an independent and arbitrary control of all tunneling

phases, gives us access to not only the BDI class but also the AIII class, whose recently proposed [147] real-space realization would involve tremendous efforts. Enabled by these controls, we observe a disorder-driven topological to trivial transition in BDI-class wires and also a disorder-driven trivial to topological transition in AIII-class wires, where we find evidence for the TAI phase.

Our ability to create precisely defined disorder in the off-diagonal tunneling terms is crucial for this study. Unlike the site-potential disorder that is more naturally realized in real-space cold atom experiments, e.g., through optical speckle [148] or quasiperiodic lattice potentials [149], pure tunneling disorder is important for preserving the chiral symmetry of our wires [46, 135]. In particular, we let

$$t_n = t(1 + W_1\omega_n), \quad (5.2)$$

$$m_n = t(m + W_2\omega'_n), \quad (5.3)$$

define the variations of our hopping terms, where  $t$  is the characteristic inter-cell tunneling energy,  $m$  is the ratio of intra- to inter-cell tunneling in the clean limit,  $\omega_n$  and  $\omega'_n$  are independent random real numbers chosen uniformly from the range  $[-0.5, 0.5]$ , and  $W_1$  and  $W_2$  are the dimensionless disorder strengths applied to inter- and intra-cell tunneling.

## 5.2 Results

### 5.2.1 Topological to Trivial Transition

We begin by considering the influence of disorder added to a BDI-class wire. The wire is strongly dimerized, as characterized by a small intra- to inter-cell tunneling ratio of  $m = 0.100(5)$  (with  $t/\hbar \approx 2\pi \times 1.2$  kHz), and hence is in the topological regime in the clean limit. We fix the disorder amplitudes to be  $W \equiv W_2 = 2W_1$ , and show in Fig. 5.2(a) the disorder-averaged topological phase diagram of this model as a function of  $W$  and  $m$ , as determined numerically by a real-space calculation of the winding number  $\nu$  for a system with 200 unit cells, together with the critical phase boundary predicted for an infinite system based on the

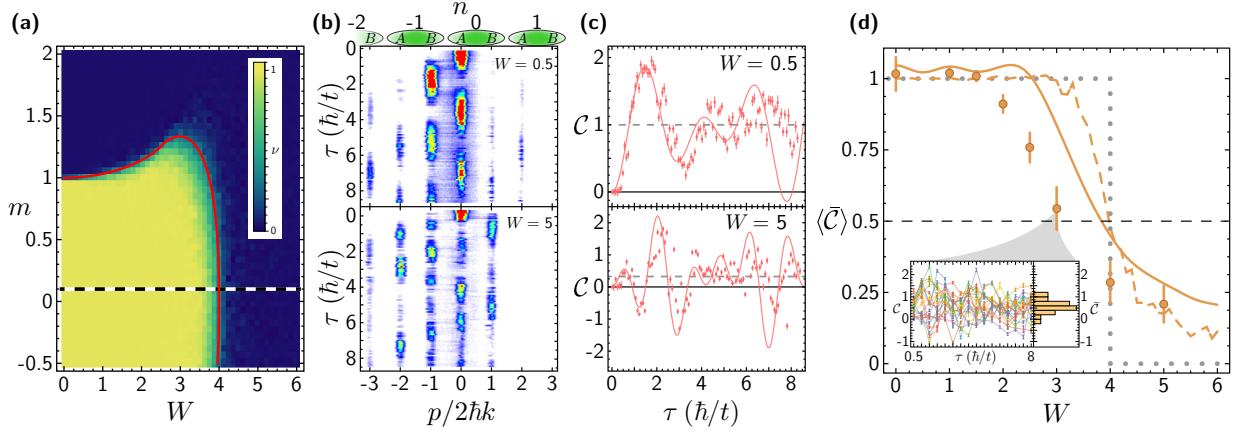


Figure 5.2: Disorder-driven transition from topological to trivial wires. **(a)** Topological phase diagram of the BDI wire model described in Eq. 5.1, showing the winding number  $\nu$  (inset color scale) as a function of disorder strength  $W$  and tunneling ratio  $m$  with tunneling disorder strengths  $W \equiv W_2 = 2W_1$ . The dashed line at  $m = 0.1$  indicates the region explored experimentally. The solid red curve indicates the critical phase boundary. **(b)** Integrated absorption images of the bulk dynamics following a sudden quench of the tunnel couplings, for both weak disorder ( $W = 0.5$ ) and strong disorder ( $W = 5$ ), each for a single disorder configuration. **(c)** Dynamics of  $C$  as calculated from the data shown in (b). The solid red curves are numerical simulations with no free parameters. The dashed gray horizontal lines denote  $\bar{C}$  for each data set. **(d)**  $\langle \bar{C} \rangle$  as a function of  $W$  for  $m = 0.100(5)$ . The data are averaged over 20 independent disorder configurations and times in the range  $0.5$  to  $8 \hbar/t$  in steps of  $0.5 \hbar/t$ . The solid gold line represents a numerical simulation for 200 disorder configurations, but with the same finite time sampling as the data. The dashed gold line is based on the same simulation as the solid gold line, but sampled to much longer times ( $\tau = 1,000 \hbar/t$ ) in a wire with 250 unit cells. The dotted grey curve shows the topological index in the thermodynamic limit [135], which takes a value of  $0.5$  at the critical point, as indicated by the horizontal dashed line. The inset shows  $C$  for  $W = 3$  as a function of time for all 20 disorder configurations with  $\bar{C}$  for each disorder shown in the histogram. All error bars in (c) and (d) denote one standard error of the mean.

divergence of the localization length [135].

The strong dimerization produces a large (in units of the bandwidth) energy gap in the band structure. Such large band gaps are typically favorable for experimentally observing the topological nature of disorder-free nontrivial wires via adiabatic charge pumping [124, 125] or the adiabatic preparation of boundary states [33]. However, it is expected that in disordered chiral symmetric wires the bulk energy gap will essentially vanish at moderate disorder strengths, well below those required to induce a change in topology [135]. The energy gap is replaced by a mobility gap, and the band insulator of the clean system is replaced by an Anderson insulator that remains topological, with topology carried by localized states in the spectrum [135]. Thus, without the spectral gap, experimental probes relying on adiabaticity are expected to fail in evidencing the topology of disordered wires.

We instead characterize the topology of our wires by monitoring the bulk dynamical

response of atoms to a sudden quench. Specifically, we measure the *mean chiral displacement* (MCD) of our atoms. This observable was recently introduced in the context of discrete-time photonic quantum walks [8], and is herein measured for the first time for continuous-time dynamics. We define the expectation value of the chiral displacement operator as

$$\mathcal{C} = 2\langle \Gamma X \rangle, \quad (5.4)$$

given in terms of the chiral operator  $\Gamma$  and the unit cell operator  $X$  [8]. The dynamics of  $\mathcal{C}$  in general display a transient, oscillatory behavior, and its time- and disorder-average  $\langle \bar{\mathcal{C}} \rangle$  converges to the winding number  $\nu$ , or equivalently to the Zak phase  $\varphi_{\text{Zak}}$  divided by  $\pi$ , in both the clean and the disordered cases. At topological critical points, moreover,  $\langle \bar{\mathcal{C}} \rangle$  converges to the average of the invariants computed in the two neighboring phases [8, 30].

For our experiment we begin with all tunnel couplings turned off, and the entire atomic population localized at a single central bulk lattice site (site  $A$  of unit cell  $n = 0$ , for a system with 20 unit cells). We then quench on the tunnel couplings in a stepwise fashion. The projection of the localized initial state onto the quenched system's eigenstates leads to rich dynamics, as depicted in Fig. 5.2(b) for both weak ( $W = 0.5$ ) and strong ( $W = 5$ ) disorder. Such site-resolved dynamics of the atomic population distribution are directly measured by a series of absorption images taken after dynamical evolution under the Hamiltonian of Eq. 5.1 for a variable time  $\tau$  (given in units of the tunneling time  $\hbar/t \approx 130 \mu\text{s}$ ), and after the discrete momentum states separate according to their momenta during a time-of-flight period [51]. From the data shown in Fig. 5.2(b) we calculate  $\mathcal{C}$  as a function of  $\tau$  as shown in Fig. 5.2(c), along with the time average  $\bar{\mathcal{C}}$ . We additionally consider the disorder-averaged topological characterization of the system by averaging  $\bar{\mathcal{C}}$  over many independent disorder configurations.

The dependence of  $\langle \bar{\mathcal{C}} \rangle$  on the strength of applied disorder  $W$  is summarized in Fig. 5.2(d). The inset of Fig. 5.2(d) depicts the determination of  $\langle \bar{\mathcal{C}} \rangle$  (shown for the case  $W = 3$ ), first from the time-average of  $\mathcal{C}$  over 16 values of  $\tau$  evenly spaced between  $0.5 \hbar/t$  and  $8 \hbar/t$ , followed by an average over 20 unique realizations of disorder. We observe a robustness of  $\langle \bar{\mathcal{C}} \rangle$  to weak disorder, maintaining a nearly-quantized value close to one. For strong disorder,

$W \gtrsim 2$ , we observe a relatively steep drop in  $\langle \bar{\mathcal{C}} \rangle$ , with it falling below  $\langle \bar{\mathcal{C}} \rangle = 0.5$  for  $W \gtrsim 3$ . Our observed decrease of  $\langle \bar{\mathcal{C}} \rangle$  with increasing disorder is in reasonably good agreement with a numerical simulation (solid gold line) of the Hamiltonian in Eq. 5.1 for experimental time scales. The observed decay of  $\langle \bar{\mathcal{C}} \rangle$  is associated to a disorder-driven transition between topological ( $W \lesssim 4$ ) and trivial wires ( $W \gtrsim 4$ ). This observed crossover represents the first systematic exploration of a disorder-driven change of topology in any system, enabled by our unique ability to precisely define disorder configurations.

On an infinitely long chain, we would expect to observe a sharp phase transition in the infinite-time limit of our  $\langle \bar{\mathcal{C}} \rangle$  measurement, yielding quantized values of the invariant for all disorders, and half-integer values at the critical phase boundary [150]. However, we instead observe a smooth crossover due to finite-time broadening from our abbreviated period of quench dynamics and the corresponding finite number of sites. The observation of a moderately sharper transition, such as that of the dashed-line numerical simulation in Fig. 5.2(d), would require that we measure at extremely long timescales (shown for 1,000 tunneling times) and for very large systems (shown for 250 unit cells), which at the moment is beyond the capabilities of our experimental technique. The slow convergence of this transition with increasing measurement time and system size is a characteristic feature of random-singlet transitions [145], such as that found in chiral symmetric wires at strong disorder.

## 5.2.2 Observation of the Topological Anderson Insulator

### The TAI in AIII-class Wires

Having demonstrated a disorder-driven change of topology in BDI-class wires, we now turn our attention to AIII-class wires where we investigate the surprising feature that an initially clean, trivial system can be driven topological through the addition of disorder. This phenomenon is manifest in the phase diagram of AIII-class wires in Fig. 5.3(a) for  $m$  just exceeding one. The value  $|m| = 1$  is the critical point between the topological and trivial phase in the clean limit, and values of  $|m| > 1$  are in the trivial phase in the absence of disorder. However, we see that random tunneling disorder induces the TAI phase over a broad

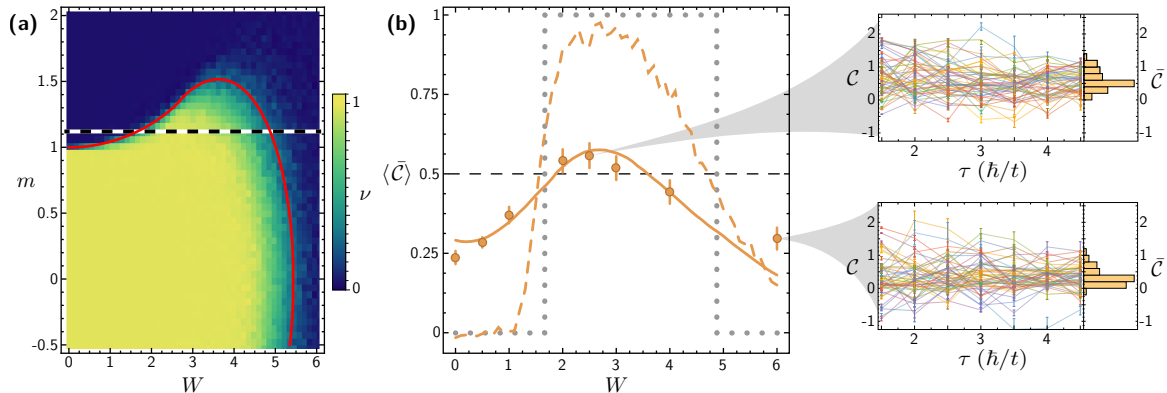


Figure 5.3: Observation of the topological Anderson insulator phase. **(a)** Topological phase diagram of the AIII wire model described in Eq. 5.1, showing the computed winding number (color scale at right) as a function of disorder strength  $W$  and tunneling ratio  $m$  with tunneling disorder strengths  $W \equiv W_2$  ( $W_1 = 0$ ). The striped black and white line at  $m = 1.12$  indicates the region explored experimentally. The solid red curve indicates the critical boundary (i.e. the set of points where the localization length diverges for an infinite chain). **(b)**  $\langle \bar{C} \rangle$  as a function of  $W$  for  $m = 1.12(2)$ . The data are averaged over 50 independent disorder configurations and are averaged in time over the range 1.5 to 4.5  $\hbar/t$  in steps of 0.5  $\hbar/t$ . The solid gold line relates to a numerical simulation for 200 disorder configurations, but with the same finite time sampling as the data. The dashed gold line is based on the same simulation as the solid gold line, but sampled to much longer times ( $\tau = 1,000 \hbar/t$ ) in a 250 unit cell system. The dotted grey curve shows the topological index in the thermodynamic limit [135], which takes a value of 0.5 at the critical points, as indicated by the horizontal dashed line.  $\mathcal{C}$  as a function of time for all 50 disorder realizations is shown at right for  $W = 2.5$  and 6 and  $\bar{C}$  are shown in the histogram to the right of each plot. All error bars in (b) denote one standard error of the mean.

range of weak to moderate  $W$  values, eventually giving way to a trivial Anderson insulator phase again for very large disorder. Beyond numerics, a mechanism for the formation of a TAI phase was first elaborated in Ref. [44] for 2D systems. In that work, disorder is taken into account perturbatively using the self-consistent Born approximation, and was shown to effectively renormalize the parameters in the Hamiltonian (including the parameter(s) that tune between the topological and trivial phases). The TAI phase arises because, as disorder is added to the trivial phase tuned near the clean critical point, the effective Hamiltonian is renormalized through the critical point and into the topological phase. This type of reasoning was adapted and extended to describe the TAI phase in 1D systems including both the BDI- and AIII-class wires that we consider here [46, 150]. Although, strictly speaking, the sharpest results of the latter work can only be applied in a scenario with multiple wires, numerical evidence supports the existence of the TAI even for a single wire [135].

Here, we probe the influence of tunneling disorder on atomic wires of the AIII class. Since we are interested in the TAI phase, we start with a slight dimerization [ $m = 1.12(2)$ ]

that places the system in a trivial phase in the clean limit. We note that being so near the critical point at  $m = 1$  causes the band gap in the clean limit to be much smaller than in the previous experimental setup. The choice of disorder we consider here differs from the previous case: we add disorder only to the intra-cell hopping terms, i.e., setting  $W_1 = 0$  and  $W \equiv W_2$ . We note that the slightly smaller TAI region in the topological phase diagrams for the BDI case (Fig. 5.2(a)) and the AIII case (Fig. 5.3(a)) comes entirely from this change in disorder configuration. In one dimension the topological phase diagrams for BDI and AIII systems are identical when exposed to equivalent disorder configurations ( $W_1$  and  $W_2$  values) and with only nearest neighbor tunnelings present. From Refs. [44, 46, 150] we expect that, for weak disorder of this form, the intra-cell hopping  $m$  should be renormalized toward the topological phase resulting in a TAI. Due to the smaller band gap in this case of reduced dimerization, the effects of off-resonant driving in our system become more pronounced. In order to mitigate these effects, we reduce our tunneling energy to  $t/\hbar \approx 2\pi \times 600$  Hz, resulting in a correspondingly lessened experimental time range of  $\tau = 1.5 \hbar/t$  to  $4.5 \hbar/t$ .

Figure 5.3(b) shows the dependence of  $\langle \bar{\mathcal{C}} \rangle$  on the strength of added disorder in the AIII-class wire. The measured  $\langle \bar{\mathcal{C}} \rangle$  values are obtained, as in the previous case, through the non-equilibrium bulk dynamics of the atoms following a quench of the tunneling. Due to the restricted range of  $\tau$ , we include many more disorder configurations (50) to allow for stable measures of  $\langle \bar{\mathcal{C}} \rangle$ . For weak disorder, we observe that  $\langle \bar{\mathcal{C}} \rangle$  rises and reaches a pronounced maximum at  $W \approx 2.5$ . This is consistent with the expected change in the renormalized  $m$  parameter, i.e., given the negative sign of the lowest-order correction to  $m$ , for weak disorder [44, 46, 150].  $\langle \bar{\mathcal{C}} \rangle$  then decays for very strong applied disorder. This observation of an initial increase of  $\langle \bar{\mathcal{C}} \rangle$  followed by a decrease is indicative of two phase transitions, first from trivial wires to the TAI phase and then to a trivial Anderson insulator at strong disorder, broadened by our finite interrogation time.

Despite the effects of finite-time broadening, we see our measured  $\langle \bar{\mathcal{C}} \rangle$  rise to greater than 0.5 (the infinite-time  $\langle \bar{\mathcal{C}} \rangle$  value associated with the critical point) for  $W \approx 2.5$ , lending further evidence to our observation of the TAI phase. The excellent agreement of our experimental  $\langle \bar{\mathcal{C}} \rangle$  data with a short-time sampled numerical simulation (solid gold line), combined with the sharper transitions expected for long-time measurements based on the same simulations

(dashed gold line for 1,000 tunneling times in a 250 unit cell system), provide strong evidence for the observation of disorder-driven topology in an otherwise trivial band structure.

### The TAI in BDI-class Wires

In addition to the study shown above that explores the influence of tunneling disorder on AIII-class wires, here we study and provide evidence for a TAI phase in BDI-class wires. The case of disordered AIII-class wires utilized disorder that was only applied to the intra-cell tunneling elements, similar to the theory study of Ref. [150]. For these BDI wires we consider the same ratio of disorder strengths on the intra- and inter-cell terms as was examined in theory in Ref. [135] and experimentally for the topological to trivial transition shown in Fig. 5.2, i.e.  $W \equiv W_2 = 2W_1$ . The consequence of this disorder arrangement is that the region of the topological phase diagram relating to the TAI is somewhat smaller than for the scenario in which  $W_1 = 0$ . Because of finite-time broadening, the measurement of  $\langle \bar{\mathcal{C}} \rangle$  takes a smaller maximum value in this case as compared to the case of fully asymmetric ( $W_1 = 0$ ) disorder, as the TAI phase is sandwiched between two trivial regions (for constant tunneling imbalance  $m$  as a function of disorder strength  $W$ ).

The topological phase diagram for the BDI wires as a function of  $m$  and  $W$ , equivalent to that of Fig. 5.2(a) of the BDI case above, is reproduced in Fig. 5.4(a). Here, we measure  $\langle \bar{\mathcal{C}} \rangle$  along the line  $m = 1.12(2)$ , by observing the bulk density response to a quench of the tunneling terms. The bulk response for zero disorder ( $W = 0$ ) and large disorder ( $W = 6$ , for a single configuration of the disorder) are shown in Fig. 5.4(b) and the corresponding  $\mathcal{C}$  measurement is shown in Fig. 5.4(c), where we find good agreement with a zero-free-parameter numerical simulation (blue lines).

The measurements of  $\langle \bar{\mathcal{C}} \rangle$  as a function of  $W$  are shown in Fig. 5.4(d), taken for 50 disorder configurations and for times ranging from  $1.5 \hbar/t$  to  $4.5 \hbar/t$  in steps of  $0.5 \hbar/t$  for  $t/\hbar \approx 2\pi \times 600$  Hz. As in the case of AIII-class wires, here we observe that the addition of weak to moderate disorder leads to an increase in  $\langle \bar{\mathcal{C}} \rangle$ , while strong disorder causes  $\langle \bar{\mathcal{C}} \rangle$  to decay again. The data is in agreement with a numerical simulation (gold solid line in Fig. 5.4(d)) based on the experimental time sampling. The sharp rise and fall of  $\langle \bar{\mathcal{C}} \rangle$  found in

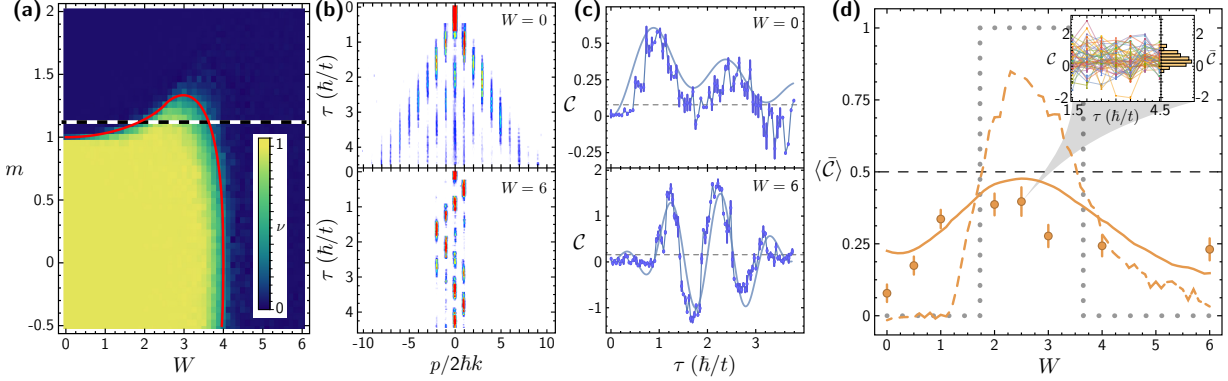


Figure 5.4: Probing the topological Anderson insulating phase in BDI class wires. **(a)** Topological phase diagram of the BDI wire model, showing the computed winding number (inset color scale) as a function of disorder strength  $W$  and tunneling ratio  $m$  with tunneling disorder strengths  $W \equiv W_2 = 2W_1$ . The dashed horizontal line at  $m = 1.12$  indicates the region explored experimentally. The solid red curve indicates the critical boundary. **(b)** Integrated absorption images of the bulk dynamics following a sudden quench of the tunnel couplings, for both zero disorder ( $W = 0$ ) and strong disorder ( $W = 6$ , for a single configuration of the disorder). **(c)** Dynamics of  $\mathcal{C}$  for the same data as in (b). The solid blue curves are numerical simulations with no free parameters. The dashed gray horizontal lines denote  $\bar{\mathcal{C}}$  for the data. **(d)**  $\langle \bar{\mathcal{C}} \rangle$  as a function of  $W$  for  $m = 1.12(2)$ . The data are averaged over 50 disorder configurations and times in the range  $1.5 \hbar/t$  to  $4.5 \hbar/t$  in steps of  $0.5 \hbar/t$ . The solid gold line represents a numerical simulation based on the exact experimental time and disorder averaging. The dashed gold line is based on the same simulation as the solid gold line, but sampled to much longer times ( $\tau = 1,000 \hbar/t$  in a system with 250 unit cells). The dotted grey curve shows the topological index in the thermodynamic limit [135], which takes a value of 0.5 at the critical points, as indicated by the horizontal dashed line. The inset shows  $\mathcal{C}$  as a function of time for all 50 disorder configurations (for  $W = 2.5$ ) and a histogram of the corresponding  $\bar{\mathcal{C}}$  values. All error bars in (c) and (d) denote one standard error of the mean.

simulations extended out to much longer times (dashed gold line, for 1,000 tunneling times) suggest that we are observing successive topological phase transitions that are broadened due to finite time sampling. To note, the maximum  $\langle \bar{\mathcal{C}} \rangle$  measurement and even the equivalent-time theory predictions are slightly less than 0.5 in this case, due to the different ratio of disorder strengths applied to intra- and inter-cell tunnelings as compared to the AIII data of Fig. 5.3.

### 5.2.3 Disordered Topological Charge Pumping

Before we were aware of the chiral displacement observable we probed the topology of our wires by exploring charge pumping. D. J. Thouless originally discovered that when a topological Hamiltonian is cyclically varied it can result in quantized charge pumping [151]. Related to the integer quantum Hall effect, this quantized pumping is directly proportional to the

topological index of the system [14]. Therefore by realizing a Thouless-style charge pump we may indirectly probe the topology of our system. Charge pumps have been realized in the past in quantum dot systems [152, 153] and cold atom systems with both fermions [125] and bosons [124]. Our efforts into measuring topology using this effect were mostly abandoned when we learned of the chiral displacement, which enables a more direct and richer measure of topology in the presence of disorder. Furthermore, because we are not filling a band with fermions, our charge pumping experiments were more in the vein of “geometrical pumping” [154], and there would not necessarily be a direct connection to the quantized topological invariants characterizing the bands. However, we were able to see evidence for a topological crossover in the pumping behavior when adding tunneling disorder to this system, in qualitative agreement with what we may expect based on upon driving the bands topologically trivial by disorder.

The charge pumping Hamiltonian is illustrated in Fig. 5.5(a) and can be written:

$$H_{\text{TP}} = \sum_n \left[ m_n c_{n,\text{B}}^\dagger c_{n,\text{A}} + t_n c_{n+1,\text{A}}^\dagger c_{n,\text{B}} + \text{H.c.} \right] + \sum_n \left[ \epsilon_{\text{A}} c_{n,\text{A}}^\dagger c_{n,\text{A}} + \epsilon_{\text{B}} c_{n,\text{B}}^\dagger c_{n,\text{B}} \right], \quad (5.5)$$

where we use a similar paradigm as in the previous section. To reiterate,  $m_n$  is the intra-cell tunneling strength,  $t_n$  is the inter-cell tunneling strength, and  $c_{n,\text{A}}^\dagger$  ( $c_{n,\text{A}}$ ) creates (annihilates) a particle in site A of unit cell  $n$ . The second term is new, however, and details the site-energy landscape of the lattice.  $\epsilon_{\text{A}}$  gives the energy of all the A sites in all the unit cells and similarly for  $\epsilon_{\text{B}}$ . We further define the parameters which are cyclically varied to be  $\Delta\epsilon = \epsilon_{\text{A}} - \epsilon_{\text{B}}$  and  $\Delta t = m_n - t_n$ .

When the two parameters  $\Delta\epsilon$  and  $\Delta t$  are varied such that they form a loop in parameter space as shown in Fig. 5.5(c, inset) the charge pump is realized. Echoing the discussion of the SSH model from Sec. 1.2, the origin of this parameter space is where the two bands of the system touch and the topology disappears. Therefore, by winding around this point the system remains gapped. Along the horizontal axis when  $\Delta t = 0$  the system is in a topologically trivial phase but remains gapped due to a band insulating phase provided by the site-energy offset  $\Delta\epsilon$ . Our specific cyclic variation during one pump cycle is as follows. First, the lattice begins with a staggered tunneling  $\Delta t/h \approx -1.3$  kHz and the site energy is

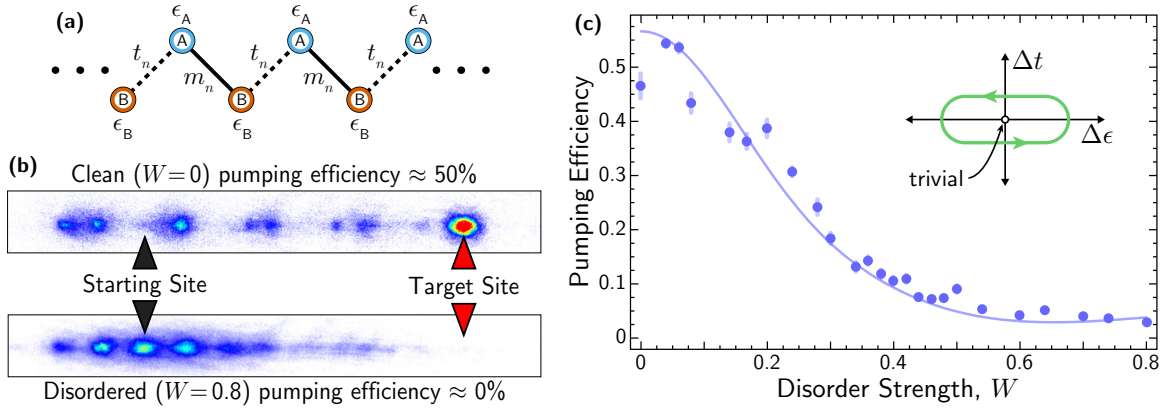


Figure 5.5: Breaking a topological charge pump with tunneling disorder. **(a)** A schematic of the tight-binding model used for the charge pumping experiments. Both the tunneling and site-energy alternate with the A and B sites of the unit cell. **(b)** Absorption images in the zero-disorder limit (top) showing a pumping efficiency of approximately 50%. The pumping efficiency measures the fraction of the initial BEC which makes it to the target site. When tunneling disorder of characteristic strength  $W = 0.8$  is applied we see that virtually none of the atoms make it to the target site (bottom image). **(c)** The pumping efficiency as a function of the disorder strength showing a crossover from a functioning pump (which indicates a topological phase) to an ineffective pump (which indicates a topologically trivial phase). **(c, inset)** The pump breaking down can be understood in terms of the parameter space picture showing the Hamiltonian trajectory winding around the origin once during the pump cycle. When  $\Delta t$  is modified through the addition of disorder to the point where the trajectory no longer winds about the origin, the topology is destroyed and the pump no longer functions.

swept from  $\Delta\epsilon/h = -7 \text{ kHz} \rightarrow +7 \text{ kHz}$ . Then, the tunneling offset is instantaneously jumped to  $\Delta t/h \approx +1.3 \text{ kHz}$  and the site-energy ramp is reversed. At the end of one pump cycle, as long as the band gap does not close, the BEC should have moved over by one unit cell to the left or right depending on the chirality of the trajectory in parameter space. In experiment we find that over 3.5 pump cycles ( $\approx 57 \hbar/|\Delta t_{\text{max}}|$ ) with a maximum  $|\Delta t_{\text{max}}|/h \approx 1.3 \text{ kHz}$  and  $|\Delta\epsilon_{\text{max}}|/h = 7 \text{ kHz}$  we are able to move the population over seven lattice sites with roughly 50% of the initial BEC making it to the target state as shown in Fig. 5.5(b, top). A movie of the time-dependent lattice with population moving through it can be found at the [web address](http://publish.illinois.edu/gadwaylab/files/2016/10/thoulesscartoonred.gif)<sup>1</sup> listed below. Our main source of inefficiency is believed to be a failure to remain adiabatic by deforming the Hamiltonian too quickly. However, if we go slower we lose atoms through mode-changing collisions (*i. e.*, out-coupling to *s*-wave halos). so the parameters used here strike a balance between these two competing sources of atom “loss” and inefficiency.

<sup>1</sup>Movie: <http://publish.illinois.edu/gadwaylab/files/2016/10/thoulesscartoonred.gif>

Now we consider adding tunneling disorder into our charge pump. The disorder values  $\omega_n$  are chosen from a random box distribution between -1 and 1 and are applied to the tunneling terms as:

$$\Delta t(\tau) \rightarrow \Delta t_n(\tau) = \Delta t(\tau) + \omega_n W \Delta t_{\max}, \quad (5.6)$$

where  $W$  is a characteristic disorder strength. Note that the disorder model here is starkly different than in the previous sections. We see that, for large disorder values ( $W = 0.8$  with  $W$  unrelated to the previous sections), the final distribution, after the 3.5 pump cycles are completed, yields an efficiency of virtually zero as shown in Fig. 5.5(b, bottom). Since the pump relies on the inherent topology of the model, its breakdown can be thought to represent an indirect observation of a topological to trivial transition in the system. We can further measure the pumping efficiency continuously as a function of disorder strength as shown in Fig. 5.5(c) where the blue dots are data and the line represents a numerical simulation of the pump. We observe a smooth crossover from a functioning charge pump to an ineffective one as we increase the disorder strength. It is difficult to pinpoint a critical value of disorder from this smooth crossover but  $W \sim 0.25$  appears qualitatively reasonable from this data.

### 5.3 Discussion

Unlike with real condensed matter systems and photonic simulators, where carrier mobility or lattice parameters vary from sample to sample, the spectroscopic control of our atomic physics platform has allowed us to engineer many different, precisely tuned realizations of disorder. In addition to enabling these first explorations of disorder-driven quantum phase transitions in topological wires, this unique level of control will also enable future studies of quantum criticality in disordered topological systems [140, 144]. By simple extension to longer evolution times, we may study in detail the interesting physics of logarithmic delocalization at the random singlet transition [145]. Combined with our ability to engineer tunneling phases [51] and artificial gauge fields [32], our technique may be extended to study disordered quantum Hall systems [144]. And while our present study has been restricted to

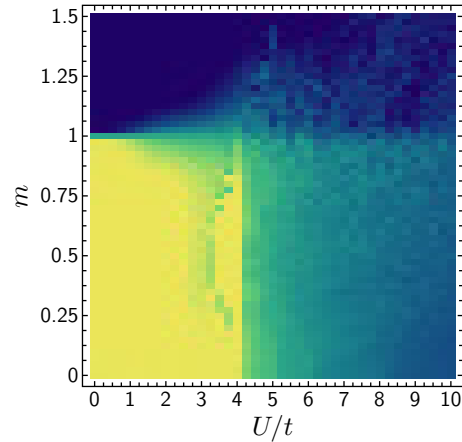


Figure 5.6: Numerical simulation hinting at a possible interaction-induced topological phase transition (or at least the breakdown of the chiral displacement observable). The interaction strength  $U$  is plotted on the horizontal axis and the tunneling imbalance  $m$  is plotted on the vertical axis. The color represents the mean chiral displacement  $\langle \bar{C} \rangle$  with a color scale identical to Fig. 5.3(a).

a regime where interactions are relatively unimportant, the presence of strong interactions in synthetic momentum-space lattices [66] will enable future studies of strongly interacting topological fluids.

It is not known whether the chiral displacement operator as defined in this chapter can be extended to interacting systems. However, we do find that the quantized value of the chiral displacement drops to zero in numerical simulations of Eq. 5.1 with the addition of mean field interactions. Specifically, we present a phase diagram in Fig. 5.6 that shows the mean chiral displacement as a function of the characteristic interaction strength  $U$  and the tunneling imbalance  $m$ . This simulation was performed in a lattice with 200 cells,  $t/h = 1$  kHz, and a total time for averaging of  $40 \hbar/t$  using the Gross–Pitaevskii equation (see Subsec. B.4.2). These results are reminiscent of the phase diagrams shown in Figs. 5.2 and 5.3 but this is now in the zero disorder limit. Still, we find a region of possible topology (as indicated by the mean chiral displacement observable) remaining up to interaction strengths of around  $U/t = 4$  where it appears some transition might occur. Once upgrades to our apparatus are completed, we will be able to experimentally probe this possible transition.



# Chapter 6

## Studying Chaos with a Synthetic Spin

“And now for something completely different.”

---

Monty Python

Diverging drastically from the previous two studies on topological criticality, we now turn our attention to the ability of the momentum-space lattice to mimic a spin system. These experiments were performed by Jackson Ang’ong’a and myself with the technical assistance of Fangzhao Alex An and under the supervision of Bryce Gadway. This chapter is largely a reproduction of Ref. [155] where these results originally appeared.

### 6.1 Introduction

The contrasting behavior of quantum and classical systems is most apparent in their non-linear dynamical response to a periodic drive [156]. While driven classical systems can play host to truly chaotic behavior, including the loss of information about specific initial conditions, it is expected that true memory loss will not occur in closed and bounded quantum systems [157]. This stems from both the unitary nature of closed quantum systems, which strictly forbids memory loss, as well as the relevance of quantum uncertainty and the effective “smearing” of phase space in small quantum systems. This smearing of states in phase space dulls the sensitivity to initial conditions encountered in classically chaotic systems. Over the past few decades a number of experimental systems have illustrated this stark contrast between the nonlinear dynamics of classical and quantum systems, *e.g.* the spectra of atoms in applied electromagnetic fields [158, 159], the response of cold matter waves to time-periodic optical lattices [160–164], and the scattering of complex atoms and molecules in an applied field [165, 166].

The kicked top model, in which the symmetry of a precessing spin is broken by a series of nonlinear “kicks” [156], is one of the most paradigmatic systems giving rise to chaotic behavior. The correspondence between the nonlinear dynamics of classical and quantum systems has been explored through several experimental realizations [167–169] of quantum kicked top models, where the spin is quantized with a finite angular momentum value  $J$ . In a pioneering exploration of chaotic phenomena in quantum systems, Ref. [167] studied the dynamics of the ground hyperfine manifold ( $F = 4$ ) of thermal cesium atoms. The atoms were subjected to a continuous nonlinear twist realized through a state-dependent light shift of the magnetic sublevels ( $m_F$ ) and a periodic linear kick given by a transverse magnetic field. While such studies could be extended to slightly smaller or larger spins with different atomic species or Rydberg atoms [170], a more flexible approach to designing effective spins with tunable size has recently been realized. Using spectrally-resolved addressing of transitions in a multi-level superconducting qudit, Ref. [168] demonstrated the engineering of artificial spin- $J$  systems and control over linear rotations.

Here, in the spirit of creating synthetic spins through coherent control, we engineer a highly-tunable momentum-space lattice [49, 51] with full control over the tunneling and site-energy landscapes. In our approach, the momentum states of a  $(2J + 1)$ -site lattice play the role of angular momentum sublevels  $m_J \in \{-J, J\}$  (see Fig. 6.1(a)), enabling natural control over the size of the spin  $J$ . This simple control over  $J$  allows us to study the crossover from a highly quantum regime (small  $J$ ), where chaotic behavior is mostly suppressed, towards the nearly classical limit (moderate to large  $J$ ), where chaotic behavior is predicted to emerge.

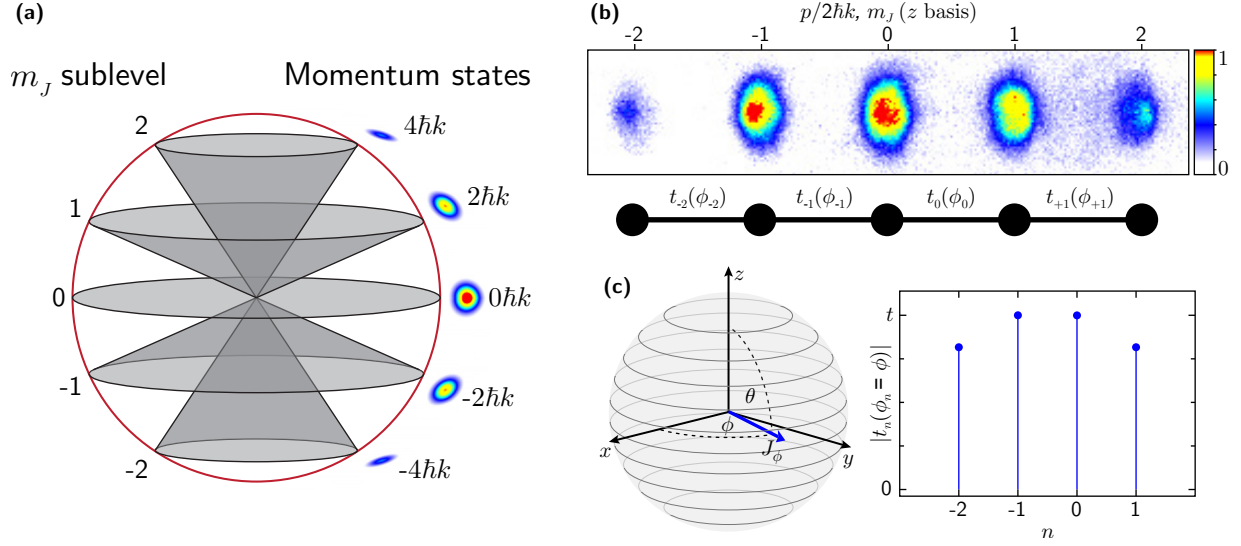


Figure 6.1: Experimental scheme for realizing a synthetic spin. **(a)** Depiction of the projected angular momenta for a spin 2 with the allowed  $m_J$  levels at left and the corresponding momentum states at right. **(b)** Time-of-flight absorption image (top) and cartoon (bottom) depicting a  $J = 2$  lattice where the lattice sites represent the angular momentum sublevels  $m_J$ . **(c)** Arbitrary torque vector on the equator of the Bloch sphere (left) emulated in this system through the tunneling links  $|t_n(\phi_n = \phi)|$  (right).

## 6.2 The Kicked-Top Model

The dynamics of the kicked top system are captured by the time-dependent Floquet Hamiltonian

$$H(\tau) = \frac{\rho}{T} J_x + \frac{\kappa}{2J} J_z^2 \sum_N \delta(\tau - NT), \quad (6.1)$$

where the first term represents continuous rotation about the  $x$  axis at a rate  $\rho/T$  and the second describes a train of effectively instantaneous torsional  $J_z^2$  kicks of strength  $\kappa$  spaced by a period  $T$ , with  $N$  the kick number and  $\tau$  the time variable. In the classical limit, symmetry-breaking by the  $J_z^2$  kicks gives rise to chaotic dynamics for certain initial orientations of the spin, with islands of stability in phase space for moderate nonlinear coupling. As  $\kappa$  is increased, the onset of global chaos leads to the loss of all stable, regular trajectories of the spin. In the limit of small  $J$ , the lack of well-defined spin orientations due to quantum uncertainty results in a general insensitivity to initial conditions and a suppression of chaotic behavior. Specifically, it reduces the sensitivity to initial conditions found in the classical Hamiltonian dynamics.

Connections between classical chaos and the generation of quantum entanglement [171,

[172] add further interest to the interplay between classical and quantum dynamics. For quantum kicked top dynamics in which the spin- $J$  object represents the collective spin of many interacting spin-1/2 particles (*e.g.*, in atomic condensates with a spin degree of freedom [169]) scenarios leading to classical chaos can generate quantum correlations and metrologically useful spin squeezing [173]. Starting from a coherent spin state (CSS) the states of the individual particles become entangled and the many-body state becomes non-separable under the evolution of Eq. 6.1. The direct measurement of multi-particle correlations generated by kicked top dynamics has recently been achieved for the small  $J$  limit, in a system of superconducting qubits with engineered interactions [174].

Here, instead of studying the collective spin of many interacting spin-1/2 particles, we directly mimic the dynamics of a single spin- $J$  quantum object. To successfully explore quantum chaos in this system, we must be able to engineer an effective spin system, realize the kicked top Hamiltonian of Eq. 6.1, accurately prepare initial states of the spin, and measure the final state of the spin after some dynamical evolution. In the following sections, we describe how we achieve these tasks using momentum-space lattice techniques.

### 6.2.1 The Momentum-Space Lattice as a Synthetic Spin

We engineer an artificial spin and realize dynamics governed by Eq. 6.1 by coupling many discrete momentum states in a controlled and time-dependent fashion as described above. By mapping the  $z$ -basis projections of the spin, *i.e.* the  $m_J$  sublevels, onto the momentum states in our lattice, the two terms of Eq. 6.1 allow for a simple realization in terms of lattice dynamics. The  $J_x$  rotation can be viewed as a kinetic evolution enabled by tunneling (undergoing Bragg diffraction) between adjacent sites. The nonlinear  $J_z^2$  kicks are simply instantaneous site-dependent phase shifts, or alternatively represent evolution without tunneling for a fixed time in a quadratic potential of site energies. We realize these elementary processes in a one-dimensional momentum-space lattice [49, 51] populated by atoms from a  $^{87}\text{Rb}$  Bose–Einstein condensate, as depicted in the time-of-flight absorption image shown in Fig. 6.1(b).

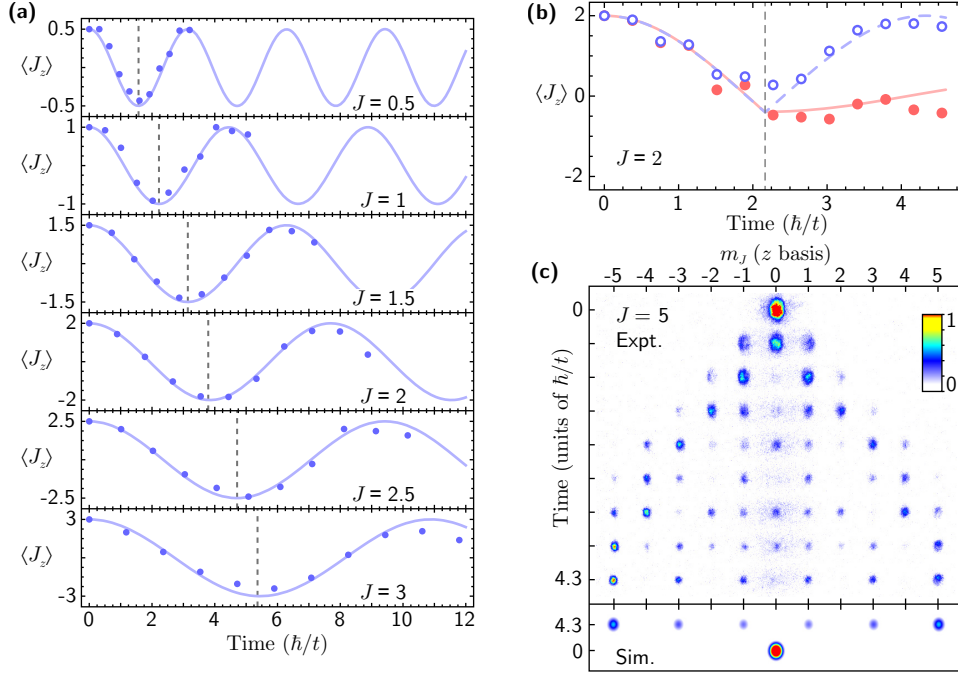


Figure 6.2: Demonstrations of linear rotations. **(a)** Evolution of  $\langle J_z \rangle$  for several spin sizes starting in  $|\theta = 0, \phi = 0\rangle_{\text{CSS}}$  and evolving under a  $J_x$  operator. The solid blue lines are results from simulations of Eq. 6.3 and the dashed gray lines show the theoretical  $\pi$  pulse times. **(b)**  $\langle J_z \rangle$  for a spin-2 state evolving under  $J_x$  until the gray dashed line at  $\approx 2.2 \hbar/t$ . At this time, the operation is switched to either  $J_{-y}$  (red dots and solid red theory line) or  $J_{-x}$  (open blue dots and dashed blue theory line). **(c, top)** Absorption images showing the evolution of a  $J = 5$  spin starting in  $|J = 5, m_J = 0\rangle_z$  and evolving under  $-J_y$ . **(c, bottom)** Simulated absorption images showing the final atomic distribution and the initial state  $|J = 5, m_J = 0\rangle_z$ . All error bars are one standard error of the mean.

### 6.2.2 Linear Spin Operators: Rotations

The linear spin operator  $J_x$  ( $J_y$ ) can be visualized as the rotation of a given spin state about a torque vector lying on the equator ( $\theta = \pi/2$ ) of the Bloch sphere. A CSS  $|\theta, \phi\rangle$  can easily be visualized on the Bloch sphere as well, where the spin is oriented along the polar and azimuthal angles  $\theta$  and  $\phi$ , respectively. While interactions lead to no significant correlated behavior in our system, which is rather based on the direct emulation of a spin- $J$  object, this language of a spin on the Bloch sphere provides for an intuitive picture of the system dynamics. Alternatively,  $J_x$  and  $J_y$  can be understood as the matrix representations of the magnetic dipole operator between different  $|J, m_J\rangle$  states in a transverse magnetic field.

In order to implement generic rotations about equatorial torque vectors pointing along any azimuthal angle  $\phi$ , *i.e.*  $J_\phi = J_x \cos(\phi) + J_y \sin(\phi)$ , we tailor the tunneling amplitudes and phases between adjacent lattice sites as depicted in Fig. 6.1(c). We introduce tunneling

terms  $t_n(\phi_n)$  linking lattice site  $n$  to site  $n + 1$  (or equivalently angular momentum state  $m_J$  to  $m_J + 1$  with tunneling phase  $\phi_n$ , taking the form of the matrix elements of the desired spin operator:

$$t_n(\phi_n) = A\sqrt{J(J+1) - n(n+1)}e^{i\phi_n}. \quad (6.2)$$

Here,  $n \in \{-J, J-1\}$  is the tunneling term index representing a drive-field linking momentum states  $n$  and  $n + 1$  and  $A$  is a constant with units of energy related to the tunneling rate. This tunneling function has a maximum amplitude at the center of the  $m_J$  manifold, which we label  $t$  for convenience (see Fig. 6.1(c)). Using these tunneling links we simulate the tight-binding Hamiltonian

$$H_{\text{tb}}(\phi_n) = \sum_{n=-J}^{J-1} \left( t_n(\phi_n)c_{n+1}^\dagger c_n + \text{h.c.} \right), \quad (6.3)$$

where  $c_n^\dagger(c_n)$  creates (annihilates) a particle at site  $n$ . The tunneling phase  $\phi_n$  determines the direction of the effective torque vector in the  $x$ - $y$  plane, where  $J_x$  and  $J_y$  relate to  $H_{\text{tb}}(\phi_n = 0)$  and  $H_{\text{tb}}(\phi_n = \pi/2)$ , respectively.

Figure 6.2 summarizes our ability to perform these linear, equatorial spin rotations. Beginning from stretched state  $|J, m_J = J\rangle$ , we monitor the  $z$ -axis projection of the spin evolving under a  $J_x$  operator for several values of  $J$  (Fig. 6.2(a)). The observed dynamics are in good agreement with theory, with the observed times of spin-inversion ( $\pi$ -pulse times) matching well with theoretical predictions (dashed lines) for varying  $J$  (in units of  $\hbar/t$ , this time should scale as  $(\pi/2)\sqrt{J(J+1)}$  for integer  $J$  and  $(\pi/2)(J+1/2)$  for half-integer  $J$ ).

We further illustrate our phase- and time-dependent control over spin operations in Fig. 6.2(b). For an initial spin state  $|J = 2, m_J = 2\rangle$ , we first apply a  $J_x$  rotation for a time corresponding to a  $\pi/2$  pulse. We then modify our tunneling parameters to instantly change the direction of the effective torque vector. For a complete inversion of the torque vector to  $-J_x$  (evolution under  $H_{\text{tb}}(\pi)$ , open blue circles), we find that the dynamics of the spin reverse towards the initial state. If we instead shift the torque vector to  $-J_y$  (evolution under  $H_{\text{tb}}(-\pi/2)$ , red filled circles), we find that the dynamics essentially cease, since the spin is aligned along the new torque vector. Continued evolution of the spin as seen in

Fig. 6.2(b) is due to the spin having rotated further than desired prior to the sudden shift of the torque vector.

### 6.2.3 State Preparation

As demonstrated in Fig. 6.2(a,b), we are able to prepare our spin in the stretched state  $|J, m_J = J\rangle$  by a simple definition of the synthetic lattice site index with respect to the discrete momentum values ( $m_J = J + p/2\hbar k$ ), and a corresponding choice of the applied Bragg resonance frequencies. We can furthermore initiate the spin in any state with well-defined angular momentum in the  $z$  basis  $|J, m_J\rangle$  by simply defining the corresponding site of our synthetic lattice to match our zero-momentum condensate. These initial states with  $m_J \neq \pm J$  would represent states that are squeezed with respect to the operators  $J_x$ ,  $J_y$ , and  $J_z$  [175]. While there are no significant correlations between the atoms in these experiments, the ability to prepare arbitrary initial states of our synthetic spin does allow us to explore the evolution of squeezed states under a classically chaotic Hamiltonian. Fig. 6.2(c) shows the evolution of the state  $|J = 5, m_J = 0\rangle$  under a  $-J_y$  spin rotation. This angular momentum state displays interesting dynamics as it is rotated. For example, when measured after a  $\pi/2$  rotation (an evolution time of  $\sim 4.3 \hbar/t$ ) a highly-modulated (population only appearing at every other site)  $m_J$  distribution is observed, in excellent agreement with a direct numerical simulation (bottom plot).

In addition to states with definite  $m_J$ , we may also prepare coherent states pointed in any direction  $|\theta, \phi\rangle$ . To prepare such a state, we start by initializing our atoms at the north pole of the Bloch sphere, *i.e.*  $m_J = J$ . Since this state is equivalent to  $|\theta = 0, \phi = 0\rangle_{\text{CSS}}$ , we can apply a rotation of the spin to transform it to any coherent state. In the following experiments we create arbitrary states with parameters  $|\theta_i, \phi_i\rangle$  by applying tunneling links  $t_n(\phi_i + \pi/2)$  for a time corresponding to a  $\theta_i$  pulse. This takes the initial state, which is aligned at the north pole of the Bloch sphere, down along a constant azimuthal angle  $\phi_i$  to a polar angle  $\theta_i$ . Thus preparing the CSS  $|\theta_i, \phi_i\rangle$ . Figure 6.3(a) shows a series of time-of-flight absorption images illustrating this procedure. The atoms start in  $m_J = 2$  and make their way to  $m_J = -2$  during the pulse duration. The schematic of this procedure on the Bloch

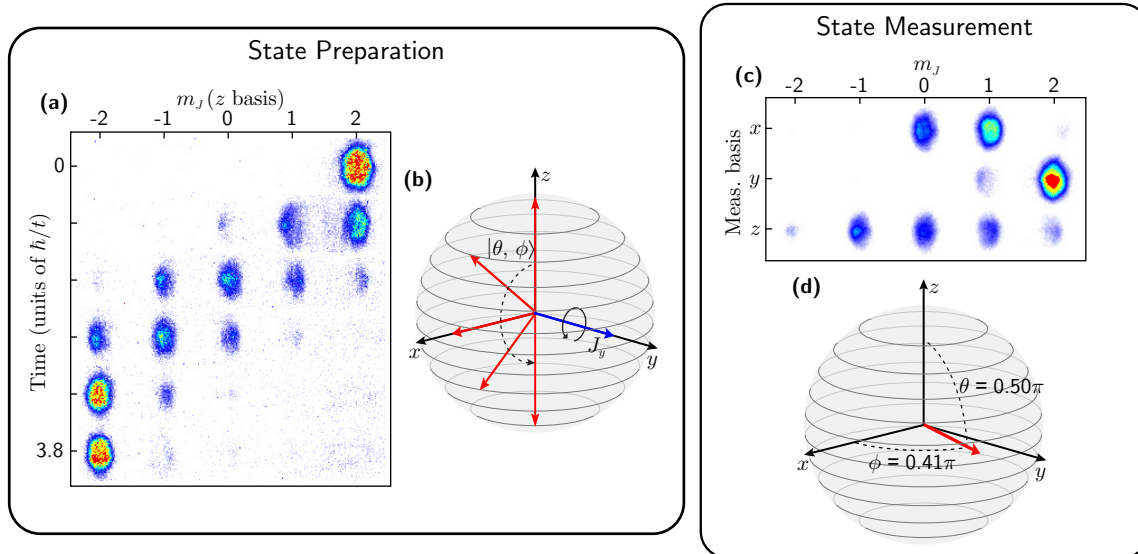


Figure 6.3: State preparation and measurement. **(a)** Absorption images (in the  $z$  basis) of a  $J = 2$  spin rotating from  $|\theta = 0, \phi = 0\rangle_{\text{CSS}}$  to  $|\theta = \pi, \phi = 0\rangle_{\text{CSS}}$  under a  $J_y$  operator. **(b)** Bloch sphere representation of the state rotation shown in (a). The state vector is depicted by the red arrows and the  $J_y$  operator by the blue arrow. **(c)** Images (averaged over many shots) of a  $J = 2$  spin in the state  $|\theta = 0.50\pi, \phi = 0.41\pi\rangle_{\text{CSS}}$  as measured along the  $x$ ,  $y$ , and  $z$  bases. **(d)** Bloch sphere depiction of the measured vector shown in (c).

sphere is shown in Fig. 6.3(b) where the state vector (red arrows) rotates about a  $J_y$  operator (blue arrow) from  $|\theta = 0, \phi = 0\rangle_{\text{CSS}}$  to  $|\theta = \pi, \phi = 0\rangle_{\text{CSS}}$ .

#### 6.2.4 State Measurement

One nice feature of momentum-space lattices is the straightforward ability to measure population at each lattice site directly through time-of-flight absorption imaging. In the context of studying the dynamics of an effective spin- $J$  particle on a  $(2J + 1)$ -site lattice, this relates to directly measuring the  $m_J$  state distribution in the  $z$  basis. Further information about the quantum state of this artificial spin can be accessed by measuring the spin projection along alternative spin axes, *i.e.* along the  $J_x$  and  $J_y$  spin directions. We perform these measurements, related to measuring the coherences between  $z$ -basis states, by applying a linear rotation about a chosen torque vector prior to  $z$ -basis imaging. That is, to measure along the  $x$ ( $y$ ) axis we apply a  $-J_y$ ( $J_x$ ) rotation for a time corresponding to a  $\pi/2$  pulse prior to time-of-flight absorption imaging. Figure 6.3(c) shows a particular CSS as measured in the  $x$ ,  $y$ , and  $z$  spin bases, while Fig. 6.3(d) shows the reconstructed state vector on the Bloch

sphere, relating to mean-values  $\langle J_x \rangle$ ,  $\langle J_y \rangle$ , and  $\langle J_z \rangle$  of this separable CSS. A full reconstruction of the density matrix for a spin of size  $J$  can be accomplished through measurement in an appropriate choice of  $(2J + 1)^2 - 1$  bases, allowing for direct visualization in terms of the experimental Husimi-Q distribution [167].

### 6.2.5 Implementing the Nonlinear Kick Operation

To realize the kicked top model, we additionally need to implement a nonlinear  $J_z^2$  kick. In the context of collective spin states [173], where such a nonlinear spin operation is derived from direct interactions (such as in multi-mode condensates with mode-dependent interactions [169] or through the collective, long-ranged interactions of many ions [176]) or field-mediated interactions (such as for atoms in optical cavities [177]), such a term gives rise to the build up of correlations and entanglement between the constituent particles.

In experiments such as ours that are directly based on effectively spin- $J$  particles [167], the  $J_z^2$  kick term relates instead to engineering a quadratic,  $m_J$ -dependent phase shift to the  $z$ -basis magnetic sublevels, creating nontrivial phase differences between adjacent  $m_J$  states that impact their further evolution under subsequent linear rotations. For the case of emulating an artificial spin within a synthetic lattice of states, such a  $J_z^2$  kick can be created through application of a quadratic potential of the site-energies in the absence of tunneling.

Alternatively, we directly engineer effective instantaneous relative phases at the different  $m_J$  sites. This is accomplished by suddenly shifting the tunneling phase between two adjacent  $m_J$  states to reflect the phase difference acquired during the instantaneous  $J_z^2$  kick. This approach is unique to systems based on driven tunneling, which allow phase-dependent control of tunneling. As a concrete example for  $J = 2$ , a  $J_z^2$  kick with  $\kappa = \pi/8$  leads to a relative phase accrual of  $3\pi/8$  between the states  $m_J = 1$  and  $m_J = 2$ . In our system, this phase difference is implemented by instantaneously shifting the phase of the  $m_J = 1 \rightarrow m_J = 2$  tunneling link as  $t_1(\phi_1) \rightarrow t_1(\phi_1 + 3\pi/8)$ , or more generally  $\phi_n \rightarrow \phi_n + (2n + 1)\kappa$  for the  $n \rightarrow n + 1$  tunneling phase.

## 6.3 Results

### 6.3.1 Nonlinear Dynamics of the Effective Spin

We first examine the dynamics of our artificial spin under evolution governed by an effective squeezing Hamiltonian  $H_{\text{sq}} = \alpha_0 J_z^2$ . For any initial state, the  $m_J$  population distribution will be unaffected in the  $z$  basis. Therefore to explore the influence of the  $J_z^2$  term, we measure the  $x$  and  $y$  spin distributions by rotating into these measurement bases. The phase accrual of the  $z$ -basis  $m_J$  states is accounted for by an appropriate modification of the phase terms of the various tunneling elements used to rotate the spins for measurement of  $J_x$  and  $J_y$ .

For certain initial states  $|\theta, \phi\rangle$ , evolution under  $H_{\text{sq}}$  leads to the generation of correlations in the uncertainty of the spin value along the  $x$ ,  $y$ , and  $z$  directions. With increasing evolution time, the spin distribution undergoes periodic cycles of becoming squeezed (having reduced spread along one spin direction, with increased uncertainty along another) and then returning to a simple CSS. We again emphasize that no significant correlations between the atoms are induced by these dynamics, but nonetheless, correlations of the (single-atom) spin distributions along the different spin projection axes can be induced by the nonlinear  $J_z^2$  term. To characterize this behavior, we directly measure the spin distributions along the different spin directions  $J_x$ ,  $J_y$ , and  $J_z$ . We combine these measurements to determine the spin length

$$L = \frac{\langle J_x \rangle^2 + \langle J_y \rangle^2 + \langle J_z \rangle^2}{J^2} \quad (6.4)$$

of our artificial spin. For initial CSSs, the length of the spin vector is  $J$  and the spin length is one, and these properties would be unchanged by simple linear rotations. When the net length of the spin vector becomes zero, the spin length  $L$  takes a value of zero. In Fig. 6.4(d) we show the dependence of the spin length  $L$  with increasing effective evolution time  $\tau$ , *i.e.* as the parameter  $\alpha \equiv \alpha_0 \tau / \hbar$  increases. These measurements were carried out for two different initial states: the CSS  $|\theta = \pi/2, \phi = -\pi/2\rangle_{\text{CSS}}$  and the  $J_z$  eigenstate  $|J = 2, m_J = 0\rangle_z$ .

The  $y$ -basis spin dynamics of the initial CSS are shown in Fig. 6.4(a). Initially aligned along the  $-y$  axis (at  $\alpha = 0$ ), the CSS (red squares in Fig. 6.4(d)) should have a spin length of one. In experiment, imperfections in the state preparation and measurement rotations cause

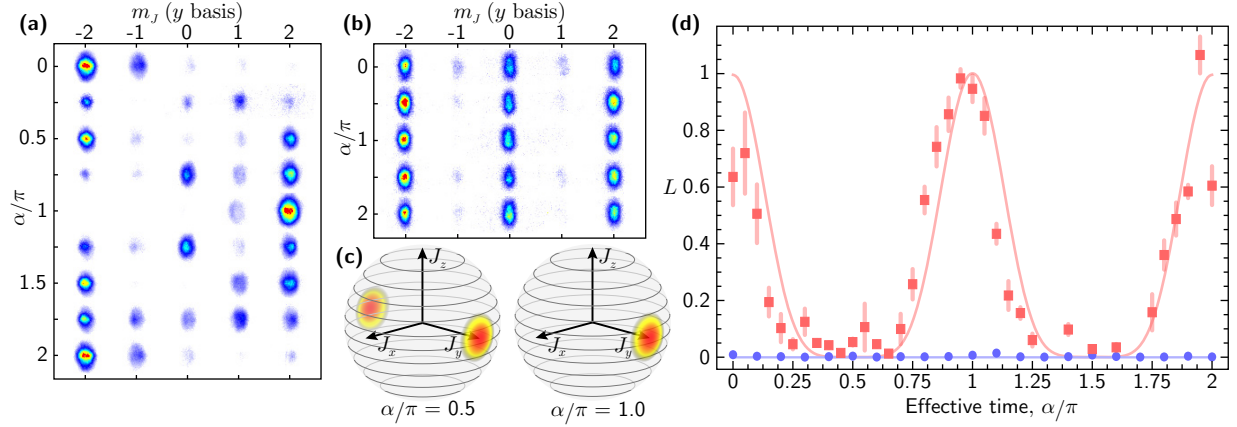


Figure 6.4: Squeezing of the artificial spin. Absorption images of the  $y$ -basis spin projection as a function of the effective squeezing time  $\alpha$  when starting in **(a)**  $|\theta = \pi/2, \phi = -\pi/2\rangle_{\text{CSS}}$  and **(b)**  $|J = 2, m_J = 0\rangle_z$ . **(c)** Density distributions for initial state  $|\theta = \pi/2, \phi = -\pi/2\rangle_{\text{CSS}}$  shown at effective time  $\alpha/\pi = 0.5$  (left) and  $\alpha/\pi = 1.0$  (right). **(d)** Spin length  $L$  versus the effective squeezing time  $\alpha$ . The red squares and simulation line are for initial state  $|\theta = \pi/2, \phi = -\pi/2\rangle_{\text{CSS}}$  and the blue dots and simulation line are for  $|J = 2, m_J = 0\rangle_z$ . All error bars are one standard error of the mean.

deviation of the measurements at  $\alpha = 0$ . At a larger effective evolution time ( $\alpha = \pi/2$ ), the spin has rearranged itself such that half of the probability density is concentrated on each of the  $-y$  and  $+y$  axes (Fig. 6.4(c), left) resulting in a minimum spin length. Later, at  $\alpha = \pi$ , the spin realigns along the  $+y$  axis and forms the state  $|\theta = \pi/2, \phi = +\pi/2\rangle_{\text{CSS}}$ , as depicted in Fig. 6.4(c). This process is also demonstrated in the  $y$ -basis absorption images shown in Fig. 6.4(a). We note that the slight offset of the data in Fig. 6.4(d) is primarily due to an additional phase shift caused by atomic interactions in the synthetic lattice of momentum states (see Ref. [66] for more information).

In contrast to these dynamics of the CSS, the  $J_z$  eigenstate  $|J = 2, m_J = 0\rangle_z$  is entirely unaffected by the  $J_z^2$  operation, as by definition this state can support no important relative phase structure. This independence is illustrated by the data shown in Fig. 6.4(b) where the  $y$ -basis absorption images reflect no change across the entire range of  $\alpha$  values. Likewise, as seen in Fig. 6.4(d) (blue dots), the spin length of this non-CSS remains fixed at  $L = 0$  for all values of the effective evolution time  $\alpha$ .

While the initial CSS and non-CSS show wildly disparate dynamical behavior in their spin length under the nonlinear spin Hamiltonian, they surprisingly behave quite similarly when considering instead the evolution of their out-of-time-ordered correlation functions

(OTOCFs) [178]. These functions have been proposed as a suitable measure of dynamically-generated entanglement and the scrambling of information in complex, many-body systems [177, 179, 180], possibly even serving as a probe of many-body localization in disordered systems with interactions [181, 182]. Recently OTOCFs have been measured in ion based systems [183, 184] and in nuclear magnetic resonance systems [185, 186]. Here, we use the wide tunability of our synthetic lattice parameters to measure OTOCFs for the first time with an atomic quantum gas. In particular, we demonstrate the suitability of this measure for tracking the complex evolution of arbitrary initial states, including non-CSSs.

Essentially, OTOCFs probe the overlap between an initial state and that same state after some complex evolution characterized by a series of forward- and reverse-time operations. Following the terminology of Ref. [177], we define the OTOCF as

$$F(\alpha) = \langle W_\alpha^\dagger V^\dagger W_\alpha V \rangle, \quad (6.5)$$

where

$$W_\alpha = U(-\alpha) W U(\alpha) \quad (6.6)$$

and

$$U(\alpha) = e^{-i\alpha J_z^2}, \quad (6.7)$$

for commuting operators  $W$  and  $V$ , which we set to be  $W = V = e^{-i\frac{\pi}{4\hbar}J_x}$ . We perform the  $J_z^2$  operations with an effective evolution parameter  $\alpha$  as described above. Each of the  $V$  and  $W_\alpha$  operations involves tunneling for a time equivalent to a  $\pi/4$  rotation, such that the full experimental duration (ignoring state preparation and readout) is equivalent to that of a global  $\pi$  pulse. For a given initial state  $|\Psi\rangle$ , we measure  $|F(\alpha)|^2$  by first applying the operator  $F(\alpha)$  (by stepwise Hamiltonian evolution realizing the operators  $V$ ,  $W_\alpha$ ,  $V^\dagger$ , and  $W_\alpha^\dagger$ ), then rotating to a measurement basis in which  $|\Psi\rangle$  is an eigenstate, and finally determining the fraction of the condensate wavefunction which overlaps with the initial

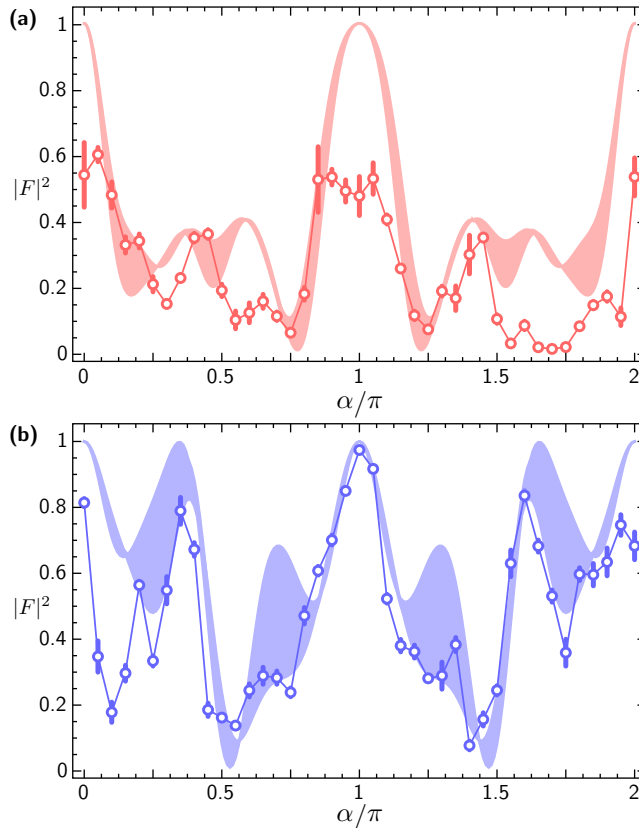


Figure 6.5: Out-of-time-ordered correlation function.  $|F|^2$  for initial states **(a)**  $|\theta = \pi/2, \phi = -\pi/2\rangle_{\text{CSS}}$  and **(b)**  $|J = 2, m_J = 0\rangle_z$  as a function of the effective dynamics time  $\alpha$ . Shaded regions indicate the results of numerical simulations incorporating the uncertainty in the calibrated tunneling rate. All error bars are one standard error of the mean.

state  $|\Psi\rangle$ . The OTOCF distinguishes between regular and chaotic dynamics by exhibiting exponential decay under chaotic conditions. In the large-spin limit, the exponential decay of OTOCFs under chaotic conditions can be related to the Lyapunov exponent of the associated classical map [187]. Here, we expect that the numerical value of the OTOCF will generally be near one if simple, regular dynamics occur (perfect overlap  $|F(\alpha = 0)|^2 = 1$  if there is no dynamical evolution) and nearer to zero if complex dynamics take place (somewhat similarly to the behavior of the spin length  $L$ ).

In Fig. 6.5 we measure the OTOCF under evolution of our squeezing Hamiltonian for the same two initial states discussed previously:  $|\theta = \pi/2, \phi = -\pi/2\rangle_{\text{CSS}}$  and  $|J = 2, m_J = 0\rangle_z$ . In the case of an initial CSS (Fig. 6.5(a)), the effective squeezing dynamics reflect those seen in the spin length, with  $|F(\alpha)|^2$  taking a maximum value at  $\alpha/\pi = \{0, 1, 2\}$ . For an initial non-CSS, however, while the spin length was completely invariant as a function of

$\alpha$ , the OTOCF measurement in Fig. 6.5(b) shows complex nontrivial dynamics. Thus, the OTOCF serves as a suitable probe for complex dynamics of the underlying Hamiltonian for more general initial states.

We note that the deviations between data and theory in the case of Fig. 6.5(a) (especially for  $\alpha = 0$  and  $\pi$ ) cannot be explained solely by incorrect pulse timing stemming from tunneling rate instabilities (which are approximately 4%). Rather, these deviations are due primarily to the loss of coherence between the sites of the synthetic lattice due to increasing spatial separation of the different momentum states. Since the state  $|\theta = \pi/2, \phi = -\pi/2\rangle_{\text{CSS}}$  requires a state preparation and readout pulse, the momentum states have more experimental time to separate than in the case for  $|J = 2, m_J = 0\rangle_z$ , where a state preparation and readout is not necessary. This conclusion is supported by Fig. 6.5(b) which shows much better agreement between theory and data for the initial state  $|J = 2, m_J = 0\rangle_z$  than for  $|\theta = \pi/2, \phi = -\pi/2\rangle_{\text{CSS}}$ . Additionally, we have verified through numerical simulations including mean-field effects that the deviations between data and theory in Fig. 6.5(a) for  $\alpha = 0$  and  $\pi$  are not caused by coherent interactions. We find that including mean-field effects in our simulations at the level appropriate for our system only slightly changes the expected result in a way that is not qualitatively important for the present work.

### 6.3.2 Chaotic Behavior in the Kicked-Top Model

Having demonstrated all of the necessary ingredients to simulate kicked tops with our artificial spins, we now engineer the full kicked top model and use it to explore unique aspects of chaotic behavior in a well controlled quantum system. For different initial CSSs and spin sizes  $J$ , we study the spin length following evolution under Eq. 6.1. In Fig. 6.6(a), for a spin size  $J = 2$  and the initial state  $|\theta = \pi/2, \phi = -\pi/2\rangle_{\text{CSS}}$ , we show the dynamics of the spin length as a function of the number of applied kicks. Evolution under two different sets of kicked top parameters are shown: the filled orange circles relate to  $(\rho, \kappa/2J) = (\pi/8, \pi/5)$  and the open blue circles relate to  $(\rho, \kappa/2J) = (\pi/8, \pi/2)$ . In both cases, the spin length almost immediately decreases to near minimum after a single kick, showing the chaotic nature of the system under these conditions.

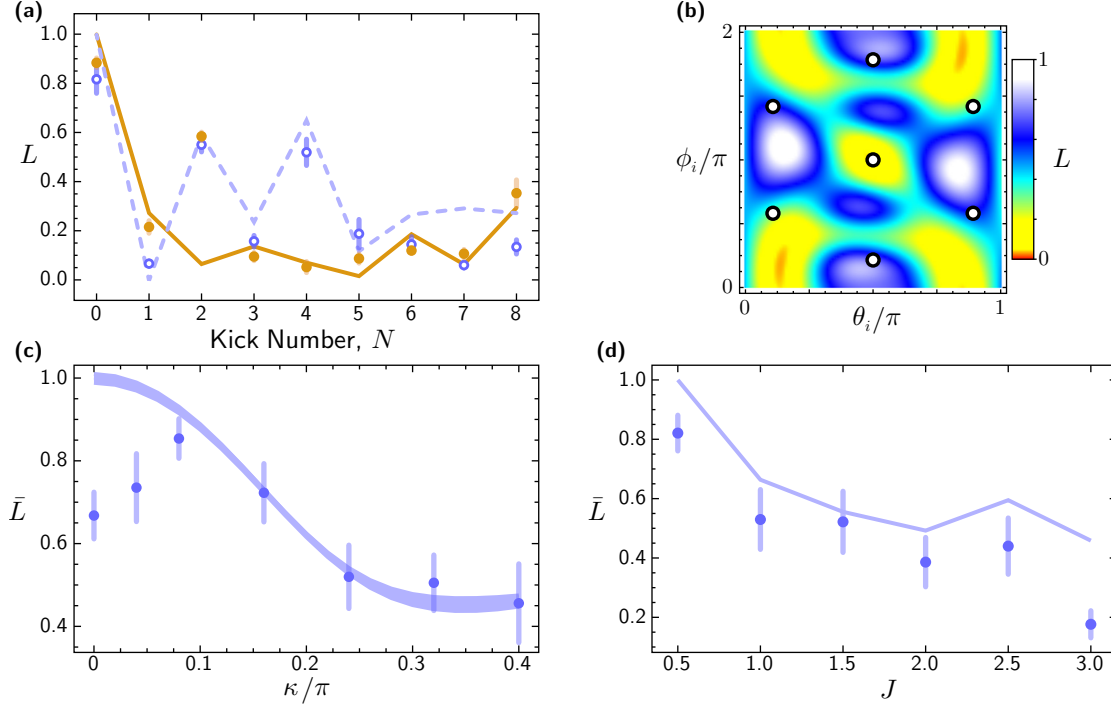


Figure 6.6: Chaotic behavior in the kicked-top model. **(a)** Spin length  $L$  for initial state  $|\theta = \pi/2, \phi = -\pi/2\rangle_{\text{CSS}}$  measured after each kick in a set of eight kicks. The open blue dots and dashed blue simulation line are  $(\rho, \kappa/2J) = (\pi/8, \pi/5)$  and the closed orange dots and solid orange simulation line are  $(\rho, \kappa/2J) = (\pi/8, \pi/2)$ . **(b)** Simulated spin length of the effective spin for different initial states. The color represents spin length averaged over  $N \in \{5, 6\}$  kicks, with respect to the color bar at right. The seven open black dots represent the measurements taken to calculate the averaged spin length  $\bar{L}$ . **(c)**  $\bar{L}$  as a function of the kick strength  $\kappa$  for  $(\rho, J) = (\pi/8, 2)$ . Shaded regions indicate results from a numerical simulation incorporating the uncertainty in the calibrated tunneling rate. **(d)**  $\bar{L}$  as a function of the size of the spin  $J$  for  $(\rho, \kappa/2J) = (\pi/8, \pi/2)$ . Solid line connects points obtained from a numerical simulation. All error bars are one standard error of the mean.

Our realization of the quantum kicked top model allows us to access the complete range of nonlinear coupling strengths. This is in contrast to studies with cesium atoms [167] and with superconducting qubits [174], where only limited ranges of kick strength were explored. Using this full control of  $\kappa$ , we explore the onset of chaotic behavior as the nonlinear coupling strength  $\kappa$  is increased. Because the presence of chaotic behavior in the system is very sensitive to the initial state, and because the classical phase-space boundaries (in terms of  $\phi$  and  $\theta$ ) between stable islands and chaotic regions change with increasing  $\kappa$ , we seek to reconstruct a global picture of how a typical initial state would evolve under given kicked top parameters. We sample seven representative initial CSSs  $|\theta = \theta_i, \phi = \phi_i\rangle_{\text{CSS}}$  spread throughout phase space (illustrated in Fig. 6.6(b)), and measure the spin length averaged

over these different cases. Moreover, to account for the fact that the dynamics of  $L$  for a given orbit do not necessarily reach some constant value independent of the kick number, but in general undergo a complex evolution, we additionally average over the measured spin length  $L$  for five and six kicks. The averaged (over initial state and kick number) spin length  $\bar{L}$  is plotted as a function of nonlinear coupling strength  $\kappa$  in Fig. 6.6(c). A general agreement with the theoretical prediction (solid line) is observed, with a steady decay towards a smaller spin length for increasing  $\kappa$ , signaling the onset of chaotic behavior. For small values of  $\kappa$  the discrepancy between the theory and the data may be due to the lack of tunneling stability in our system (of approximately 4%) which causes incorrect pulse timing, leading to an accumulation of error following many kick periods, state preparation, and state readout.

Finally, we use our unique ability to tune the size of our artificial spin to explore the crossover from the fully quantum regime towards the onset of classically chaotic behavior. For increasing  $J$  values, where the initial CSSs become more and more sharply defined in terms of their  $J_x$ ,  $J_y$ , and  $J_z$  expectation values (normalized to  $J$ ), one expects to reach a point where classical-like sensitivity to initial conditions can manifest even in quantized systems. A general correspondence between the onset of classical chaos and the development of high entanglement entropy in a quantum system has been observed for systems as small as  $J = 3/2$  [174]. Likewise, in the related chaotic system of kicked rotors, classical diffusive behavior has been observed for quantum systems of just two interacting rotors [164]. In Fig. 6.6(d), we look at the decay of the averaged spin length  $\bar{L}$  for a wide range of  $J$  values from  $1/2$  to  $3$ , for the case of  $(\rho, \kappa/2J) = (\pi/8, \pi/2)$ . For the smallest case of  $J = 1/2$  the spin should remain in a state with unity spin length at all times and for all initial states. As the system size grows, however, theoretical calculations (solid line) predict a steady trend towards smaller averaged spin length, signaling a crossover to increasingly classical-like chaotic behavior. We indeed observe a similar trend in the dynamical evolution of our artificial spins, with mostly regular evolution for small  $J$  giving way to significantly smaller spin length for larger  $J$ .

## 6.4 Discussion

Our study based on Hamiltonian engineering in a synthetic lattice offers a new approach to exploring the correspondence between quantum and classical dynamics, offering the possibility of directly tuning the size of a driven synthetic spin. Here, we have been limited to exploring only modest values of  $J$ , due to the increasing duration required for rotations of the effective spin for increasing  $J$  values. However, straightforward improvements to our experiment should allow us to probe signatures of chaos in artificial spins of size  $J \sim 10 - 20$ . Currently, we believe we are limited primarily by the spatial separation of the wavepackets relating to the many discrete momentum orders. This loss of near-field coherence may be mitigated in the future, however, by creating more spatially extended condensates, or through refocusing (echo) protocols.

Our demonstration of a synthetic lattice approach to kicked top studies also suggests that related platforms, having similar levels of local and dynamical parameter control, could also be used to explore quantum chaos. In particular, the high degree of control in discrete photonic systems [188] should enable similar explorations, perhaps with extensions to much larger effective spin sizes.

In addition to the tunable size of our spins, the wide control afforded by synthetic lattice techniques should also enable further studies on the dynamics of modified kicked tops belonging to distinct symmetry classes [189]. Going beyond the somewhat artificial construction of a synthetic spin, this system also allows for generic studies of Floquet systems. In particular, for regimes in which the atomic interactions are important [66], this system can be used to probe Bose-Hubbard Floquet dynamics. Synthetic lattices should even enable the precise implementation of random unitary operations at the single-particle level. This raises the interesting prospect of exploring boson sampling problems [190] with few-particle Fock states in synthetic lattices.

Lastly, we remark on the influence of atomic interactions on the dynamics in our kicked top. Under present experimental conditions, the tunneling energy  $t$  dominates heavily over the mean-field interaction energy of our condensate atoms  $U$  (with  $t/U \gtrsim 5$ ), such that we do not expect any large modification of the dynamics as compared to non-interacting particles.

However, by working at smaller values of  $t$ , we can enter the regime where interactions lead to correlated dynamics. That is, cold collisions give rise to an effective nonlinear interaction in the collective spin of many spin-1/2 particles [169] (*i.e.* nonlinear interactions in a momentum-space double well [66]). The use of a synthetic spin, as compared to a real spin, also opens up the intriguing possibility of exploring the driven dynamics of a system of many collectively interacting large- $J$  particles, in which the atomic interactions enrich the system with effective spin-spin interactions. In particular, recent studies of double well momentum space systems [66] can be easily extended to triple well systems and beyond.

# Chapter 7

## Counter-Diabatic Driving

We've got a long way to go and a short time to get there.

---

“East Bound and Down” by Jerry Reed

In this chapter we turn our attention to finding shortcuts to beat the adiabatic speed limits for our system. We use a scheme known as counter-diabatic driving, which is a type of shortcut-to-adiabaticity protocol [191]. These experiments were performed under the supervision of Bryce Gadway with theory assistance from Dries Sels and Kinfung Ngan. They are based in large part on the paper by Dries Sels and Anatoli Polkovnikov on this topic [192].

### 7.1 Introduction

Quantum state transformations that are robust to experimental imperfections are important for applications in quantum information science and quantum sensing. Counter-diabatic (CD) approaches [191, 193–195], which use knowledge of the underlying system Hamiltonian to actively correct for diabatic effects, are powerful tools for achieving simultaneously fast and stable state transformations even in larger systems in which adiabaticity is challenged. Protocols for CD driving have thus far been limited in their experimental implementation to discrete systems with just two or three levels, as well as bulk systems with particular scaling symmetries. Here, we extend this control to a discrete synthetic lattice system composed of as many as nine states. Although this system has a vanishing gap and thus no adiabatic support in the thermodynamic limit, we show that CD approaches can still give a substantial improvement in the fidelity of state preparation as compared to adiabatic transformations.

Adiabatic Hamiltonian transformation means changing a Hamiltonian slowly enough such that a particle in a certain eigenstate at the beginning of the change will stay in that eigenstate. A useful classical analogy of this idea is to imagine a server carrying a glass of

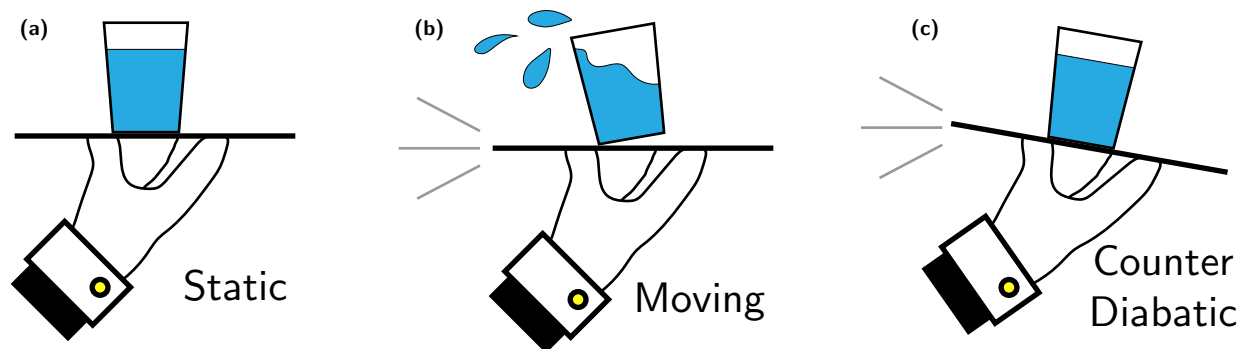


Figure 7.1: The counter-diabatic server. **(a)** A server holds a glass of water level to the floor. **(b)** The server then begins to move while holding the glass level and it spills everywhere! However, if the waiter moved slowly enough they could maintain adiabaticity and not spill the water. **(c)** The server employs CD driving and the water level in the glass is unperturbed as they jog across the room. This figure is adapted from Ref. [192].

water across a room as shown in Fig. 7.1. If the server moves slowly enough while holding the cup level to the floor, no water will spill out of the cup. But if they move too quickly, the water will spill. The critical speed at which water begins to spill from the cup is called the adiabatic limit. In this case, this limit sets how fast the server may walk across the room to deliver the glass of water. Now imagine that the server has filled the glass almost to the brim. The adiabatic limit becomes much longer and the server may have to take several minutes to cross the room with the glass and not spill any water. So far, we have assumed that the server has kept the glass level to the floor at all times. If we relax this constraint however the server may walk much faster than the adiabatic limit if they tilt the cup of water in the direction they are traveling as shown in Fig. 7.1(c). This powerful trick allows the server to bypass the adiabatic limit and still arrive at the table with the glass of water in the appropriate stationary state that it started in. Hopefully the server has earned themselves a big tip, but our motivation is to prepare interesting and exotic quantum states which would normally be adiabatically prohibited.

The water in the glass spills if the adiabatic limit is broken because, in its reference frame, it is no longer in a stationary state of the instantaneous Hamiltonian. When the glass began to move, new terms appeared in the water's Hamiltonian in the shifted reference frame which were capable of making it undergo a diabatic transition out of the glass. The same thing happens to a quantum particle in an eigenstate of a Hamiltonian. Initially the particle may

be in a stationary state, but when the Hamiltonian begins to change in time it acquires new terms in its reference frame which may couple different instantaneous eigenstates and cause a breakdown in adiabaticity. When the server tilts the glass what they have done is manually introduce a term to the Hamiltonian which, when we enter the shifted reference frame, cancels with the newly acquired diabatic terms. This is the idea of counter-diabatic driving. The diabatic terms which appear when the Hamiltonian is changed are solved for ahead of time (assuming knowledge of the Hamiltonian and its time variations) and directly countered.

Such shortcuts have been theoretically investigated in a physical context since the mid 2000s beginning with work by Demirplak, *et al.* [193, 194] and Berry [195]. Theoretical formulations have been found for two and three level adiabatic rapid passages [196], systems hosting a scale invariance [197], modifying a BEC trapping potential [198], and generating and manipulating vortices in BECs [199, 200]. The experimental realizations of these, or any, protocols have been markedly lacking however due to the general difficulty in both calculating the proper counter-diabatic terms to be used and finding an experimental platform with the level of control needed to implement them. However, there has been experimental progress using two level nitrogen vacancy centers [201] with the formulation of Demirplak, *et al.* [193] and in the context of cold atoms, Bason, *et al.* [202] performed several different CD schemes on a BEC in an optical lattice which vastly outperformed adiabatic protocols. More recently, CD protocols have been used in superconducting qubits for implementing high-fidelity quantum gates [203], observing work fluctuations [204], and measurement of the Berry phase [205]. Similarly, the Chern number was also measured in a superconducting qubit acting as a synthetic spin- $1/2$  by Schroer, *et al.* [206], based on connections to the physics of CD driving. Specifically, the diabatic terms generated in a time-deformed Hamiltonian can be connected to *effective* topological invariants of the underlying parameter space [206–210]. On the subject of topology, it has been theorized that CD Floquet driving fields can create synthetic topological band structures for few-level quantum systems [211]. Further proving their general usefulness, counter-diabatic techniques have also been proposed for quantum state transfer in quantum networking [212] and in the general context of quantum computation [213]. There has also been a fair amount of interest

in the extension of counter-diabatic protocols to quantum many-body systems [214, 215] including the Lipkin–Meshkov–Glick model of interacting fermions in a two-level system [216] as well as the Ising model [217] and bosonic Josephson junctions [218]. Finally, CD driving has been shown to outperform [219] the popular example of quantum optimization based on extracting information from crowd-sourced gaming [220].

The variety of these examples of CD driving give a picture of how universally useful the technique is. Still, most experiments are not well suited to implementing complex CD protocols—even when they can be solved for—due to the high level of local control generally required. For example, in the measurements described here the different tunneling strengths and phases need to be tuned on an independent site-by-site basis to implement the CD protocol. This level of control is relatively rare in experimental systems, making the momentum-space lattice a prime test bed for exploring and using CD protocols. Our control allows us to demonstrate the first implementation of CD driving in a system larger than three quantum states.

## 7.2 Results

We perform two basic experiments to demonstrate the power of this technique for state manipulation and preparation. The first is the inversion of a tilted lattice where all population moves from one end to the other. The second is the preparation of the five eigenstates of a discretized particle in a “box” (a five-site lattice with open boundary conditions). For both experiments the Hamiltonian can be written as:

$$H_0 = - \sum_n (t_n c_n^\dagger c_{n+1} + \text{H.c.}) + \sum_n V_n c_n^\dagger c_n, \quad (7.1)$$

where  $t_n$  is the real, positive tunneling energy associated with a particle making the transition between sites  $n \rightarrow n + 1$ ,  $c_n^{(\dagger)}$  is the annihilation (creation) operator at site  $n$ , and finally  $V_n$  is the energy of the site  $n$ .

We consider attempting to make an adiabatic change to this Hamiltonian by changing the parameters  $V_n$  and  $t_n$  as a function of the external parameter  $\lambda(\tau)$  where  $\tau$  represents

time, such that they become:

$$V_n \rightarrow V_n(\lambda) \quad (7.2)$$

$$t_n \rightarrow t_n(\lambda). \quad (7.3)$$

The parameter  $\lambda$  encapsulates the time-dependence of the Hamiltonian but could in principle be a function of an external field or any other variable. In the moving reference frame of the atoms, the Hamiltonian acquires additional terms [192–195] which are capable of coupling the instantaneous eigenstates of the system and allowing the initial state to become a superposition. We name these additional terms the “diabatic” terms because they are what drive the system out of adiabaticity when it is changed too quickly. For this particular Hamiltonian, the diabatic terms  $\alpha_n$  can be found by solving the following set of equations.

$$-t_n \partial_\lambda (V_{n+1} - V_n) = \alpha_n (V_{n+1} - V_n)^2 + \alpha_n (t_{n+1}^2 + 4t_n^2 + t_{n-1}^2) - 3t_n (t_{n+1}\alpha_{n+1} + t_{n-1}\alpha_{n-1}), \quad (7.4)$$

where every term is a function of  $\lambda$  and so the explicit  $(\lambda)$  notation has been suppressed. This set of equations was derived by undergraduate Kinfung Ngan based on the outline in the supplementary information of Ref. [192]. For simplicity this set of equations only includes the spatial dependence of the tunneling terms and not the time-dependence. For the experiments performed here, the diabatic effects come almost entirely from the time-dependence of the site energies and not the tunneling terms which only negligibly change the  $\alpha_n$ .

The diabatic terms  $\alpha_n$  are then added directly back into the Hamiltonian on the tunneling strengths and phases as:

$$H_{\text{CD}}(\lambda) = - \sum_n (t_{n,\text{CD}}(\lambda) e^{-i\phi_{n,\text{CD}}(\lambda)} c_n^\dagger c_{n+1} + \text{H.c.}) + \sum_n V_n(\lambda) c_n^\dagger c_n, \quad (7.5)$$

where the new terms  $\phi_{n,\text{CD}}(\lambda)$  and  $t_{n,\text{CD}}(\lambda)$  are given by

$$t_n(\lambda) \rightarrow t_{n,\text{CD}}(\lambda) = \sqrt{t_n(\lambda)^2 + (\alpha_n(\lambda)\partial_\tau\lambda(\tau))^2}, \quad (7.6)$$

$$\phi_n \rightarrow \phi_{n,\text{CD}}(\lambda) = \arctan\left(\frac{t_n(\lambda)}{\alpha_n(\lambda)\partial_\tau\lambda(\tau)}\right). \quad (7.7)$$

This formalism using the additional variable  $\lambda$  may seem cumbersome and unnecessary but it has the advantage of allowing one to solve Eq. 7.4 without prior knowledge of the explicit functional form of the time-dependence. As long as it is known how  $t_n$  and  $V_n$  relate to  $\lambda$ , the functional form of  $\lambda$  can be changed without re-solving for the  $\alpha_n(\lambda)$ . Equations 7.6 and 7.7 illustrate why it is difficult for most experiments to implement this form of CD correction. The  $\alpha_n$  are generally different for each  $n$  and therefore implementing them requires local control over the tunneling strength and phase. This stringency is somewhat relaxed by remapping the corrections through a gauge transformation which allows them to be applied solely to the site energies. Even so, independent control over each site energy is still challenging in many experimental platforms. We choose to perform the ungauged version of the protocol for simplicity, given our natural ability to engineer tunneling phases.

### 7.2.1 Lattice Tilt Inversion

Our first demonstration of how CD driving can provide a shortcut to adiabaticity is in the context of a tilted lattice. We begin with all the population in the highest excited state of a lattice with a variable total number of sites  $L$  as depicted in Fig. 7.2(a). In the absence of CD driving, we linearly ramp the lattice from a positive tilt to a negative tilt thus making the initial, highest-energy state the lowest in the final configuration. The ramp, which has a duration  $T$ , has the exact form

$$\lambda(\tau) = 1 - \frac{\tau}{T}, \quad (7.8)$$

which is incorporated into  $t_n$  and  $V_n$  as

$$t_n(\lambda) = t(1.1 - \lambda) = t \left( 0.1 + \frac{\tau}{T} \right) \quad (7.9)$$

$$V_n(\lambda) = nV_0 2(\lambda - 1/2) = nV_0 \left( 1 - \frac{2\tau}{T} \right), \quad (7.10)$$

where  $t$  is the characteristic tunneling scale of the lattice at the end of the ramp and  $V_0$  is the initial site energy slope. The tunneling is offset by 0.1 so that we may begin in an eigenstate of the tilted Hamiltonian with couplings present. Notice that the tunneling is independent of  $n$  meaning that each link always has the same tunneling strength (in the adiabatic protocol) whereas the site energy is linear with  $n$  such that the lattice is tilted with slope  $V_0$  at  $\tau = 0$  and  $-V_0$  when  $\tau = T$ . The correction factors  $\alpha_n$  as calculated from Eq. 7.4 are plotted along with the modified tunneling strength and phase (from Eqs. 7.6 and 7.7) in Figs. 7.2(b-d) as an example of the type of correction generated by this procedure.

The calculated  $\alpha_n$  values shown are for a five-site lattice undergoing this inversion in a time  $T = 2$  ms with an initial offset  $V_0/h \approx 4$  kHz and a characteristic tunneling  $t/h \approx 1$  kHz. The  $\alpha_n$  terms are then used to calculate the CD tunneling strength  $t_{n,\text{CD}}(\lambda)$  and phase  $\phi_{n,\text{CD}}(\lambda)$ . The diabatic terms  $\alpha_n$  are symmetric about the center of the lattice in this case and so  $\alpha_{-1} = \alpha_0$  (blue dashed line) and  $\alpha_{-2} = \alpha_1$  (solid yellow line) as shown in Fig. 7.2(b). This symmetry propagates onto the tunneling and phase as well, as shown in matching style in Figs. 7.2(c, d). The uncorrected tunneling and phase are also shown in these figures as a gray dashed line for comparison.

If this procedure were done slowly enough to respect adiabaticity conditions, all population would remain in the highest-energy eigenstate resulting in the localized wavefunction moving from the right-most site to the left-most site of the lattice. However, if ramped too quickly, this adiabatic limit breaks down and the condensate ends up in a superposition of eigenstates of the final lattice. Figure 7.2(e) shows this effect in the averaged absorption image data for  $L = 5$ ,  $t/h \approx 1$  kHz,  $V_0/h \approx 4$  kHz, and  $T = 2$  ms. With CD driving (the left image in the panel) nearly all of the atoms appear in the left-most target state of the five states after starting in the right-most state. Without CD driving however (the right image in the panel), we detect almost no atoms at the target state due to a breakdown in

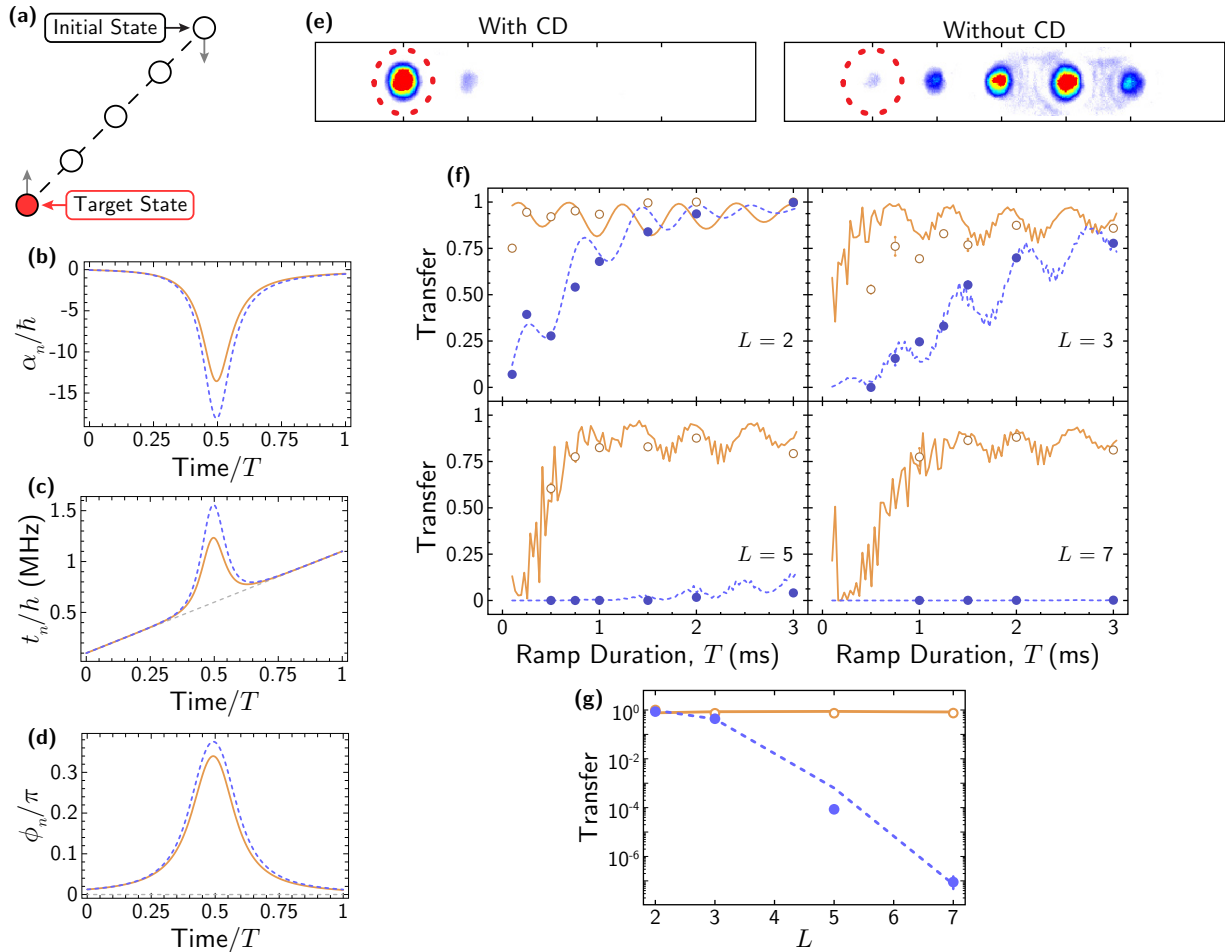


Figure 7.2: Enhancement of population transfer by CD driving. **(a)** Cartoon depiction of the initial, highest-energy state and the target state for data shown in **(b)**. **(b–d)** The  $\alpha_n$ ,  $t_{n,\text{CD}}$ , and  $\phi_{n,\text{CD}}$  for a five site lattice with  $n \in \{-2, -1, 0, 1, 2\}$  and  $T = 2$  ms. The blue dotted line represents the terms for the transitions  $-1 \rightarrow 0$  and  $0 \rightarrow 1$  and the gold solid line is for  $-2 \rightarrow -1$  and  $1 \rightarrow 2$ . The gray dashed lines in **(c)** and **(d)** show  $t_n$  and  $\phi_n$  without CD corrections. **(e)** Averaged (over eight measurements) absorption images for a  $T = 2$  ms ramp in an  $L = 5$  site lattice with  $V_0/h \approx 4$  kHz and  $t_n/h \approx 1$  kHz. The procedure is performed both with CD driving (left) and without (right). The target state is circled with the red dotted line on the left and the starting state is on the far right. **(f)** The population transferred from the initial state to the target state at the end of the ramp versus the total ramp duration,  $T$ . Open orange circles and solid orange lines represent data and simulation when implementing CD driving during the ramp. Filled blue circles and dashed blue lines represent data and simulation without implementing CD driving during the ramp. We perform the protocol with  $L = 2$ ,  $L = 3$ ,  $L = 5$ , and  $L = 7$ . **(g)** Log of population fraction transferred to the target state as a function of system size  $L$  for a  $T = 2$  ms ramp. Open orange circles and solid orange line are data and simulation when using CD driving during the ramp. Filled blue circles and dashed blue line are data and simulation without CD driving during the ramp. All error bars indicate one standard error of the mean. The data shown here were taken with  $t/h \approx 1$  kHz and the simulations use an average mean-field interaction of  $U/h = 1.25$  kHz.

adiabaticity. In fact, most atoms remain within one to two sites of the starting state.

We perform this lattice inversion experiment as a function of both ramp duration  $T$  and system size  $L$  and present the results in Fig. 7.2(f). On the vertical axis we plot the transfer (the fractional amount of atoms which ended up in the target state) against the ramp duration  $T$  on the horizontal axis. Focusing on the  $L = 2$  case presented in the upper left, we find that implementing CD driving results in a substantial increase in the transferred fraction for shorter ramps as reflected in the data (open orange circles) and simulation (solid orange line) over the case without CD driving (solid blue dots and dashed blue theory line). We do see that we are eventually able to reach adiabaticity for ramp durations  $T > 2$  ms. Indeed, in this limit for such a small system size the CD driving terms become negligible and the two ramps are essentially identical.

We also perform this lattice transfer experiment as a function of the system size  $L$  working with sizes  $L = \{2, 3, 5, 7\}$ . We observe, unsurprisingly, that without CD driving it becomes more difficult to maintain adiabaticity as the system size is increased. This is reflected in the increasingly low transferred fraction for the blue curves/points at a 3 ms ramp duration shown in the four panels of Fig. 7.2(f). When using CD driving however, we are able to prepare the target state with  $> 80\%$  fidelity for all four system sizes given a long enough ramp duration. We do observe another effect showing up for short ramp durations which results in decreased transfer when using CD driving. This is due to the CD corrections becoming so large that they exceed the operational limits of our synthetic lattice of momentum states and off-resonantly couple all the different lattice states in a way that prevents us from accurately modeling the desired Hamiltonian. In general any limits on how fast these protocols can be carried out tend to be practical rather than fundamental.

In Fig. 7.2(g) we condense the information of Fig. 7.2(f) into a single plot. We show the population transferred to the target state as a function of system size for a  $T = 2$  ms ramp duration for all four system sizes on a semi-log scale. We observe that the CD driving (open orange circles) results in very near to perfect transfer for all lattice sizes, whereas the case without CD driving (solid blue dots) results in a transfer which decreases very quickly with system size, eventually reaching the  $10^{-11}$  level with  $L = 7$ . This plot emphasizes the enormous benefits of using CD driving when performing a non-trivial operation in a system

containing an adiabatic limit that scales poorly with system size (*i. e.*, no adiabatic support in the thermodynamic limit).

### 7.2.2 Preparing the Eigenstates of a 1D Square Well

To display the versatility of both the CD driving technique and our synthetic momentum-space lattice we now move to studying the preparation of more interesting eigenstates. The starting configuration is a 5-site lattice with the same initial positive slope used in the previous experiment. In this case, however, we stop the ramp when the different sites of the lattice all have zero energy as illustrated in Fig. 7.3(a). The forms of the ramp function  $\lambda(\tau)$  and tunneling  $t_n(\lambda)$  are identical to the previous case shown in Eqs. 7.8 and 7.9 but now we ramp the site energies as

$$V_n(\lambda) = nV_0\lambda = nV_0 \left(1 - \frac{\tau}{T}\right), \quad (7.11)$$

where  $n$  is the site index,  $V_0$  is initial slope of the tilted lattice,  $T$  is the ramp duration, and  $\tau$  the time variable. The diabatic terms and corrected tunnelings and phases for this experiment look identical to the first half of those for the lattice inversion experiment shown in Figs. 7.2(b–d). This new ramp results in an initial positive slope of  $V_0$  at  $\tau = 0$  but instead of fully inverting at  $\tau = T$  the site energies become zero resulting in a uniform flat lattice.

The eigenstates of this uniform lattice are essentially just the lowest five eigenstates of a particle in a box, with the wavefunction sampled at five locations throughout the system corresponding to the five sites of the synthetic lattice as shown in Fig. 7.3(b). We further note that even though the wavefunctions have more nodes for eigenstates 4 and 5, their probability densities look identical to eigenstates 1 and 2 when considering this discretization caused by the lattice. Furthermore, using our ability to choose which lattice sites we connect, we can prepare any of the five possible eigenstates by simply shifting our lattice around the initially zero-momentum condensate. That is, by linking sites -2 to 2 the condensate starts at the center of the lattice which ramps into the middle-energy state of the final configuration. But if we link sites 0 to 4 then we start in the lowest energy state at the left edge of the lattice and we ramp into the lowest energy state of the final configuration. In this way we can

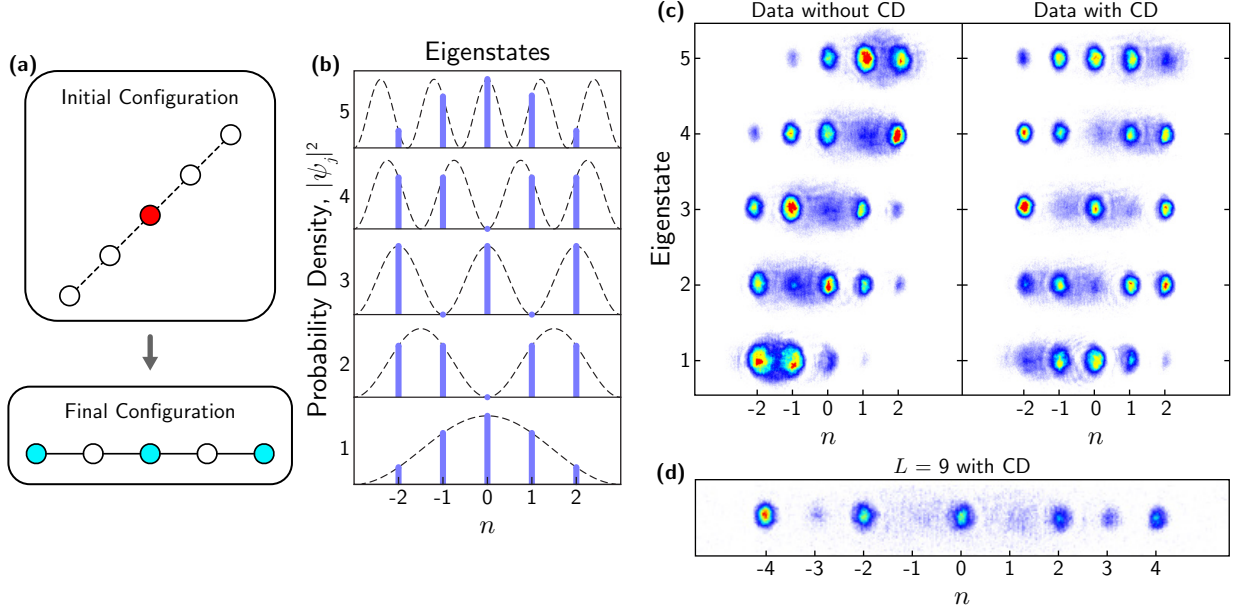


Figure 7.3: Preparing the eigenstates of an  $L$ -site lattice with counter-diabatic driving. **(a)** Depiction of the ramp protocol for eigenstate preparation. We start in a single site of the initial configuration and the choice of this site dictates which eigenstate of the final configuration is prepared. We show, for example, starting in the middle of the initial configuration and ending in the middle eigenstate of a five-site lattice. **(b)** The first five eigenstates for a particle in a box. The dashed lines indicate the probability for a continuous space whereas the blue bars show the discretized amplitudes that would be measured in a five-site lattice. **(c, left)** Absorption images for the attempted preparation of all five eigenstates without CD driving. We compare the theoretical probability distribution and our adiabatically prepared probability distribution by calculating the “efficiency”  $F_j^{\text{adi}} = \{0.722(24), 0.555(11), 0.282(15), 0.619(9), 0.808(7)\}$  for each of the five eigenstates. **(c, right)** Absorption images for the preparation of all five eigenstates with CD driving during the ramp. For these five states, the associated preparation “efficiencies” are  $F_j^{\text{cd}} = \{0.983(5), 0.861(5), 0.865(3), 0.911(8), 0.987(2)\}$ . Data shown in (c) were taken with a ramp time of 1 ms and a final tunneling of  $t/h = 950$  Hz. **(d)** Absorption image showing the preparation of the middle-energy state for a nine-site lattice taken with a ramp time of 1 ms and a final tunneling of  $t/h = 1$  kHz. We additionally note the presence of the thermal cloud in all the absorption images shown here. The thermal atoms are in a different place in each image because the starting location of the BEC is different for each of the five eigenstate ramps.

prepare all five eigenstates  $|\psi_j\rangle$  of the lattice.

We first attempt this experiment without CD driving as shown in Fig. 7.3(c, left) with the parameters  $V_0/h \approx 4$  kHz,  $t/h \approx 0.95$  kHz, and  $T = 1$  ms. It is qualitatively clear from the absorption images that the procedure without CD driving failed to prepare any of the eigenstates, as the probability densities do not match the expected eigenstates shown in Fig. 7.3(b). More to the point, the atomic distribution has not spread out much from the initial zero-momentum condensate that was first populated. Quantitatively, we compare the theoretical probability distribution and our adiabatically prepared probability distribution by calculating the “efficiency”. We calculate the efficiency in terms of the normalized number

of atoms detected at each lattice site  $n$  and for each state  $j$  which we define as  $P_n^j$ . The “efficiency”  $F$  is calculated from these probability distributions by

$$F_j = \left( \sum_n \sqrt{P_n^{j, \text{theory}} P_n^{j, \text{expt}}} \right)^2 \quad (7.12)$$

in terms of the experimental and predicted theoretical probability distributions. In the adiabatic case  $F_j^{\text{adi}} = \{0.722(24), 0.555(11), 0.282(15), 0.619(9), 0.808(7)\}$  for each of the five eigenstates. To note, the adiabatic approach works most efficiently for the highest and lowest energy states, which have the fewest neighboring (in energy) eigenstates to which they could undergo diabatic transitions. We observe that a marked improvement is obtained by applying CD driving to this state preparation protocol, keeping all other parameters the same.

We are able to prepare probability distributions which agree well with the desired distributions, with  $F_j^{\text{cd}} = \{0.983(5), 0.861(5), 0.865(3), 0.911(8), 0.987(2)\}$  for eigenstates 1-5, with corresponding experimental absorption images shown in Fig. 7.3(c, right). Thus the average efficiency for preparing states via the adiabatic method is 0.60(5), with an improvement to an average efficiency of 0.92(3) via the CD method. Just as for the state transfer across the lattice, this preparation of eigenstates delocalized across the sites can also be extended to larger system sizes. Fig. 7.3(d) shows (via absorption image) the preparation of the middle-energy eigenstate for an  $L = 9$  site lattice, which should have the same alternating probability density structure as the middle-energy in Fig. 7.3(b).

These measurements show that we are able to accurately prepare a state which has the same probability density as the desired eigenstate. However, they do not prove that the prepared state has the correct phase structure. We cannot directly measure the relative phases between the momentum states in the lattice so instead we devise an indirect test of the phase structure. This test is performed by observing the evolution of the probability density of the wavefunction after the ramp has ended. If the state is prepared with the correct probability density and amplitude, it will not evolve in time under the Hamiltonian because it is in an eigenstate. However, if the phase or probability density differs from the eigenstate, we will observe continued dynamics after the ramp period. So, if we accurately

prepare the desired eigenstate we will see a static distribution of atoms in the lattice after the ramp period.

Figure 7.4 summarizes our tests of the phase structure of the prepared states. We perform the same protocol used to prepare the eigenstates of the 5-site lattice but with parameters  $V_0/h \approx 4$  kHz,  $t/h \approx 900$  Hz, and  $T = 0.75$  ms. We attempt to prepare eigenstate 3 of the 5-site lattice as shown in Fig. 7.3 both with and without CD driving with the added step of keeping the Hamiltonian on and static after the ramp period for an additional time  $T$ . Without CD driving, we observe continued dynamics after the end of the ramp as shown in Fig. 7.4(a). This indicates that we have failed to prepare the eigenstate, which is no surprise since the probability density of the prepared state did not match the eigenstate at the end of the ramp (black dashed line). In addition, the data agree qualitatively with a numerical simulation of the ramp as shown in Fig. 7.4(b). But when we prepare the eigenstate more accurately using CD driving, we find that the dynamics that take place after the ramp has ended are much more subdued as shown in the data and simulations shown in Figs. 7.4(c, d). There is still some minor time dependence stemming from the fact that the eigenstate was not prepared with 100% fidelity. Atomic interactions, which are tuned to be relatively unimportant for this work, also contribute to the residual dynamics because they were not taken into account for the CD protocol. This signifies that we have nearly correctly prepared the desired eigenstate in both the probability amplitude and phase structure.

A further test that we have actually prepared the desired eigenstate is to examine the long time behavior of the momentum states after the middle-energy state has been prepared. In this case we are looking to see whether the state we prepared is a dressed state of the lattice. If we prepare the atoms in the middle-energy eigenstate of the lattice they will have a momentum  $\langle p \rangle = 0$  due to their symmetric wavefunction and as such will not move in space even after many milliseconds of exposure to the lattice. But if the state is prepared and then the lattice is turned off, the atomic density will evolve in real space as well, with the various “wave packets” relating to the different momentum orders separating in space. To put this more carefully, when an atom from the condensate is prepared in eigenstate 3 of the uniform lattice it will have a wavefunction which can be written in terms of the site

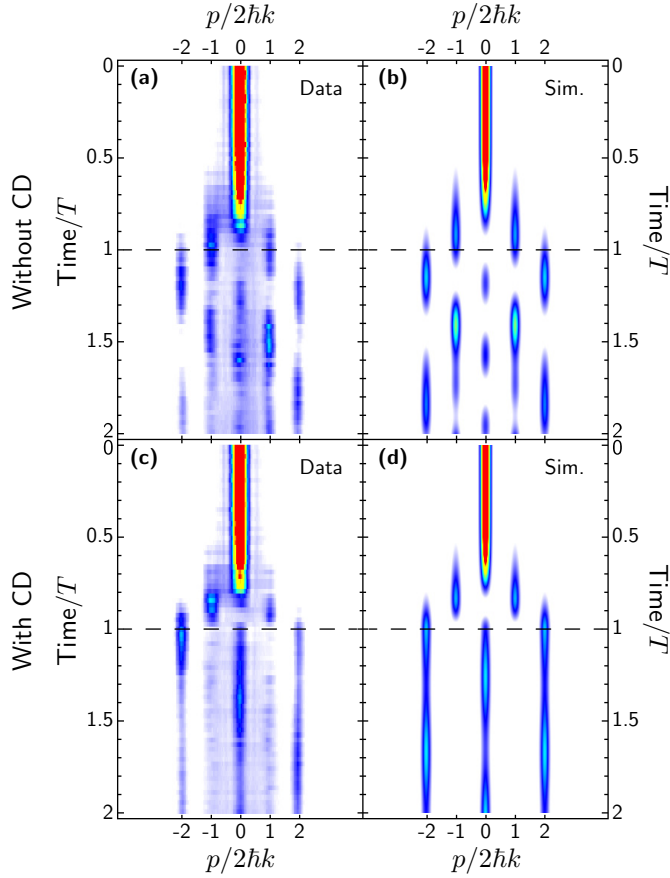


Figure 7.4: Testing the phase structure of the counter-diabatically prepared eigenstates. Observations of any dynamics after the ramp when preparing the middle-energy state of a five-site lattice for ramps without CD driving [data in **(a)** and simulation in **(b)**] and for ramps with CD driving [data in **(c)** and simulation in **(d)**]. The dashed lines in all four panels indicate the end of the ramp. Data shown here were taken with a ramp time  $T = 0.75$  ms and a final tunneling  $t/h = 900$  Hz.

index basis states  $|n\rangle$  as

$$|\psi_3\rangle = \frac{1}{\sqrt{3}} (|-2\rangle + |0\rangle + |2\rangle). \quad (7.13)$$

This state has equal population in the three sites  $n = \{-2, 0, 2\}$  as shown in Fig. 7.3(b). Recalling that our sites in this system are momentum states, an atom in this state will be found with a momentum  $p = 2\hbar k\{-2, 0, 2\}$  with equal probability upon measurement. If the lattice is turned off, these various momentum modes will evolve in real space, leading to separating wave packets. However, if the coupling light field is left on, the atoms remain in a “dressed state” of the field and the atomic momentum states. The momentum components of these dressed states do not separate in real space, due to the presence of the light field

(in much the same way that atoms adiabatically loaded into a standing-wave optical lattice will have projection onto multiple discrete momentum states when released in time-of-flight, but these orders do not disperse).

Our investigation of this dressed state effect is shown in Fig. 7.5 where we prepare the middle energy state of the five site lattice with CD driving and then institute a hold time equal to  $T$  after the ramp with parameters  $V_0/h \approx 4$  kHz,  $t/h \approx 950$  Hz, and  $T = 1$  ms. Figures 7.5(a, b) show the middle energy state with wavefunction given in Eq. 7.13 being prepared for the first 1 ms of time for both cases followed by a 1 ms hold time. We observe that when the lattice is left on for the entire hold time the momentum space distribution of the atoms is static with no spreading present. However, when the lattice is turned off as soon as the ramp ends at 1 ms the momentum orders begin to move out away from their  $\tau = 0$  locations as shown in Fig. 7.5(b). The effect is relatively slight on this scale, given the additional 18 ms of time-of-flight expansion, but with respect to the vertical dashed lines indicating  $p/2\hbar k = \pm 2$  it can be readily seen that the dressed state atoms lie on this line for the entire duration of the experiment whereas the non-dressed state atoms deviate from the line. The deterioration of the dressed state during the hold time is, we believe, an artifact of mode changing collisions causing atoms at higher momenta to preferentially scatter to non-lattice values.

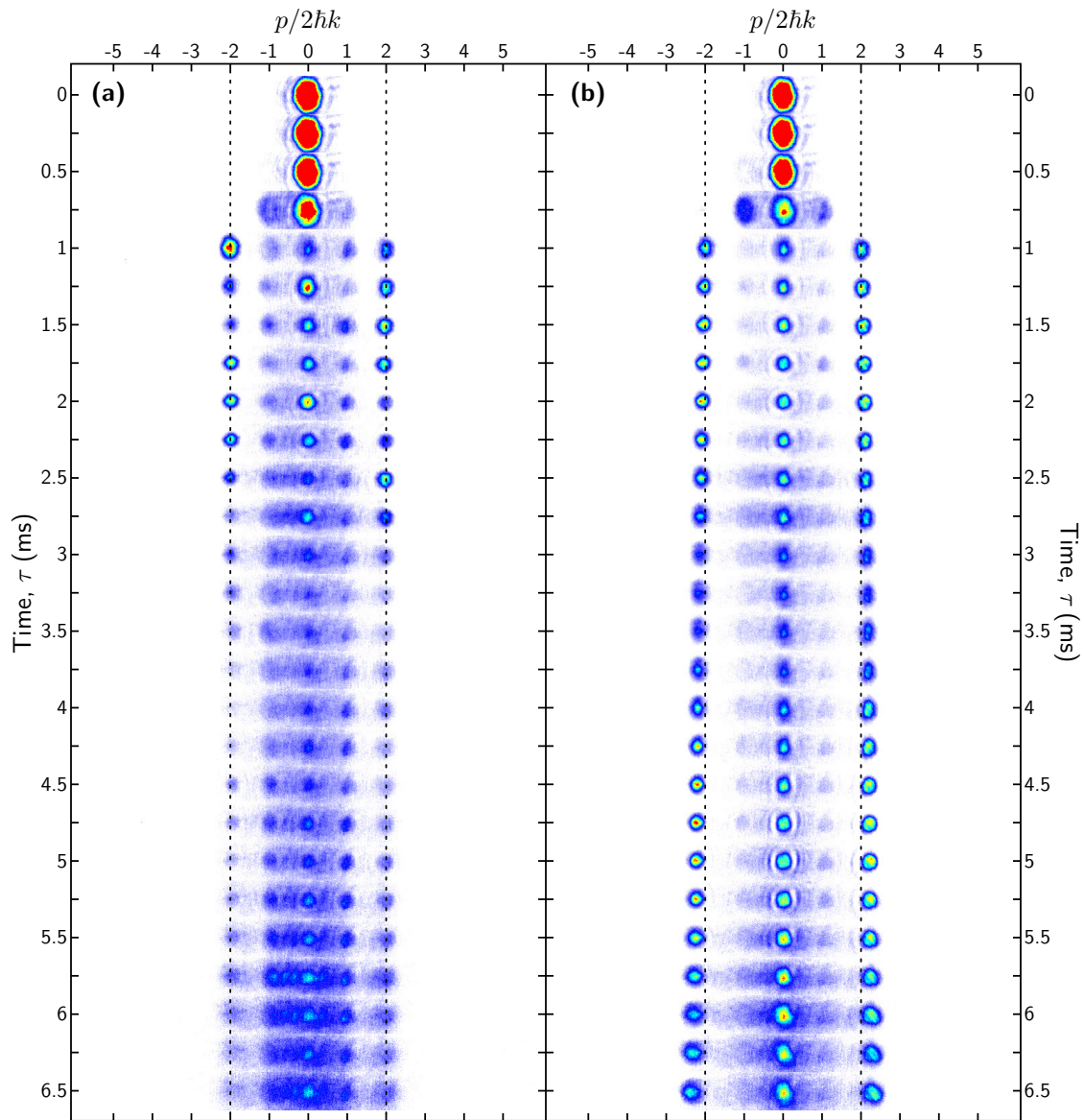


Figure 7.5: Evidence for dressed states of the lattice with CD driving. The middle energy state of a 5-site uniform lattice is prepared with CD driving over the first 1 ms of both **(a)** and **(b)** before the condensate is exposed to a 5.5 ms hold time. In **(a)** the Hamiltonian is left on during this hold time and the dressed state of the lattice keeps the atoms in place at the correct momentum values. However, in **(b)** the Hamiltonian is switched off immediately after the state is prepared and thus no dress state is prepared resulting in the atoms spreading apart during the hold time.

## 7.3 Discussion

We have shown the ability for CD driving to improve upon the adiabatic transformation of multi-site lattice systems through several state preparation and transformation experiments. We showed that the CD technique is capable of creating interesting and rich eigenstates such as dressed states of a lattice. In our particular case, without the use of CD driving, we would not be able to perform these experiments, as the rate-limiting adiabatic conditions make the experiment too long to perform. These experiments represent the first implementation of a truly non-trivial shortcut to adiabaticity protocol to our knowledge, *i. e.*, in a system beyond just two or three states that does not possess scaling symmetry. As such they prove the power of this technique to transform systems with small gaps or poor adiabatic scaling. Indeed, this regime of many-level systems is where the use of these shortcuts yields the most dramatic improvements over adiabatic protocols. These fast, robust, and efficient manipulations may prove particularly useful in the context of atom interferometry for example.

We would also like to comment on the presence of atomic interactions in the data shown here. While atomic interactions can play a non-trivial role in the dynamics of atoms in the momentum-space lattice, for these experiments we operated in a regime where they did not substantially affect the results. In some of the data there are effects which may be attributed to atomic interactions, such as asymmetries when ramping different directions in the lattice inversion experiment and asymmetries in the prepared eigenstates of the uniform lattice. However, these effects were small enough such that they could not be unilaterally attributed to the presence of interactions over other experimental imperfections. This being said, the simulations shown in Fig. 7.2(f) take into account atomic interactions at a level similar to the tunneling strength via a mean-field, Gross–Pitaevskii simulation which yields better agreement with the data. In the future, once upgrades to our apparatus are complete, we plan to revisit the open question of finding optimal CD driving protocols in the presence of nonlinear interactions [214, 215, 218].



# Appendix A

## Custom Lab Hardware and Software

This appendix details a few minor pieces of equipment/software which I have principally designed, written, and/or constructed during the course of this work which were not worthy of the main body of this thesis.

### A.1 Analog Isolation Circuit

Electrical isolation of signals traveling to the apparatus is important for both signal quality as well as protecting the relatively expensive equipment which produces the signals. To make sure that a surge can never travel back to the computer or NI chassis (see Sec. 3.1.3) from the apparatus we use optical isolators which ensure one-way signal propagation. The idea is to take the analog signal and convert it to an optical signal with a Light-Emitting Diode (LED). The brightness of the LED is read by a photodiode in the same integrated circuit (IC) as the LED and re-outputs the signal. This allows the input of the isolator to be completely electrically disconnected from the output and the one-way propagation of the LED-photodiode pair ensures no electricity may flow from the output to the input of the circuit.

Figure A.1(a) shows the actual circuit from an electronics perspective and Fig. A.1(b) shows the circuit with the ICs and pins labeled for ease of reconstruction. The circuit features two operational amplifiers (Analog Devices [LT1097](#)), the optical isolator chip (Broadcom Limited [HCNR201](#)), a diode (Vishay [1N4150](#)), a trimmer potentiometer (Bourns Inc. [3296Y-1-503LF](#)), a transistor (ON Semiconductor [2N3906TFR](#)), and various resistors and capacitors. Since the input and output halves of the circuit must be kept electrically isolated for the circuit to serve its purpose, the  $\pm 15\text{ V}$  signals, which power the op-amps, and the grounds must be isolated as well. To accomplish this we use separate power supplies on dif-

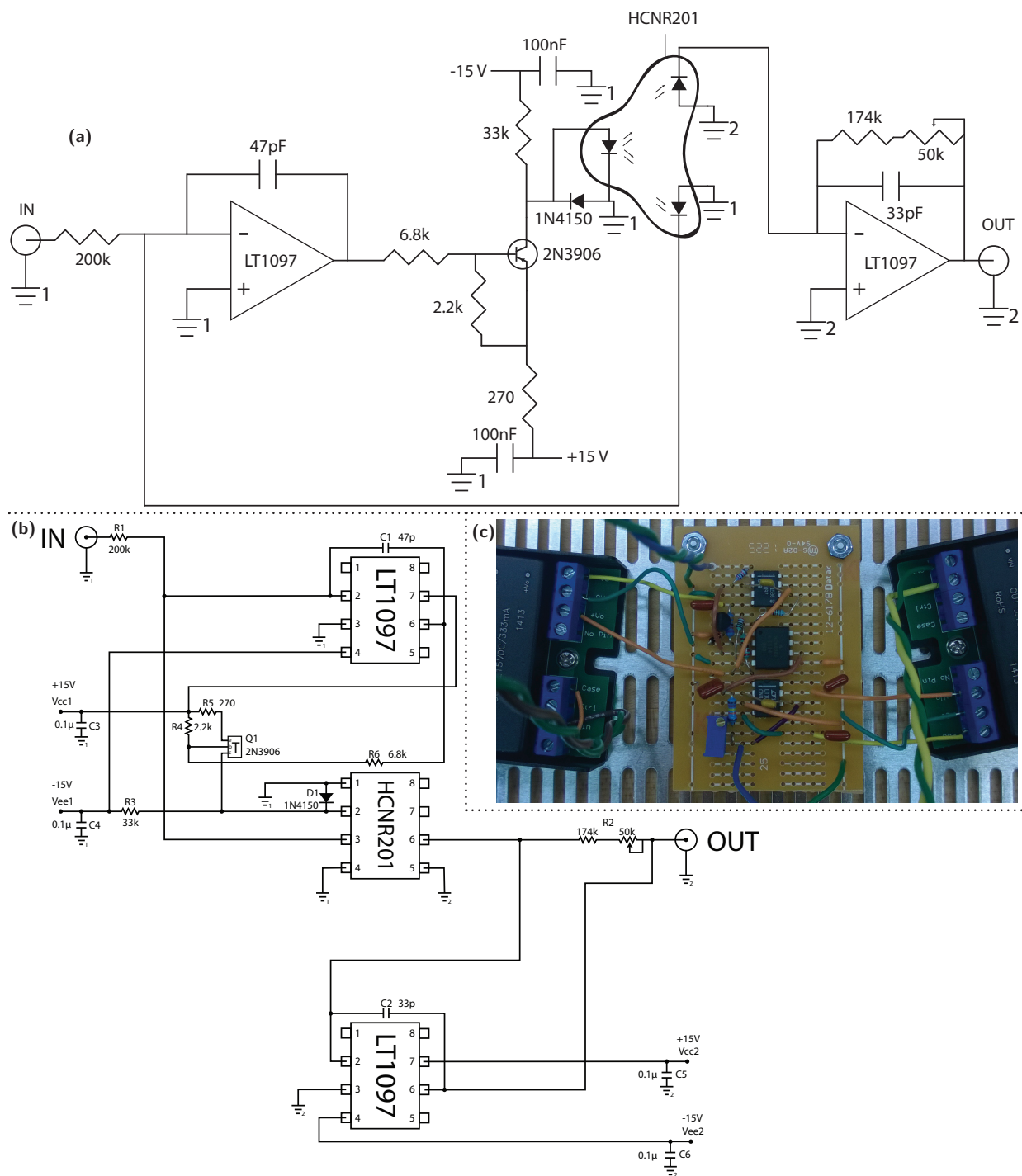


Figure A.1: Circuit diagrams for the analog isolator. **(a)** Circuit diagram for the analog isolator with part numbers and resistances and capacitances given. This diagram was made by Michael Highman. **(b)** Wiring schematic to aid reconstruction of the circuit. Dots indicate connections when two wires cross. **(c)** Picture of a completed circuit showing the DC-DC converters for the two isolated halves of the circuit on the left and right. The circuit is laid out similarly to the diagram with the op amps on top and bottom and the isolator in the center. The trim pot, diode, and transistor are all on the left side of the board.

ferent circuits for the two halves as well as DC-DC converters (CUI Inc. [PYB10-Q24-D15-U](#)) with high isolation between the power supplies and circuits. This is reflected in Fig. [A.1](#) by the 1 and 2 labels on the power supplies Vcc and Vee to the op amps as well as grounds. An example of a constructed circuit is shown in Fig. [A.1\(c\)](#). The DC-DC converters are the large black rectangles on either side of the circuit. The circuit in the picture is laid out similarly to Fig. [A.1\(b\)](#) with the op amps on top and bottom and isolator chip in the center. The transistor is at the upper-left of the isolator chip with the diode partially obscured below it. The trim pot is the blue rectangle at the extreme lower-left of the circuit. The trim pot allows one to tune an offset voltage applied to the output. This is for “calibrating” the circuit because the output signal may be slightly offset from the input signal. So for each constructed circuit, the output must be tested and adjusted to match the input as closely as possible. This has a significant ramification in that the voltage one programs into the computer to control some piece of hardware will not be the actual voltage applied. This is usually irrelevant however since most things are optimized while only ever looking at the voltage set by the computer. This can become very important if a sensitive piece of hardware is being controlled by an analog voltage and must be moved to a new circuit for some reason. The new circuit will have a different offset and so the voltage from the computer must be changed or reoptimized to reflect this.

## A.2 Laser Offset Locking Scheme

For our  $^{87}\text{Rb}$  repump laser we use a scheme for fixing its frequency with relation to atomic resonance called an “offset lock” [[221](#), [222](#)]. Our offset lock was originally designed and implemented by Derek Ping and myself in 2016. We first lock the separate cycling laser to an atomic transition based off of polarization spectroscopy in a  $^{87}\text{Rb}$  vapor cell. With that laser locked, we generate a locking signal for the repump laser based on comparing the difference between the repump and cycling frequencies to a fixed offset value. This is called an “offset lock” because we are locking one laser to an arbitrary value which is offset from another laser. For  $^{87}\text{Rb}$  we need to lock the repump laser frequency  $\omega_{\text{rep}}$  about 6.5 GHz above the cycling laser frequency  $\omega_{\text{cyc}}$ . First, we take a small amount of light from both

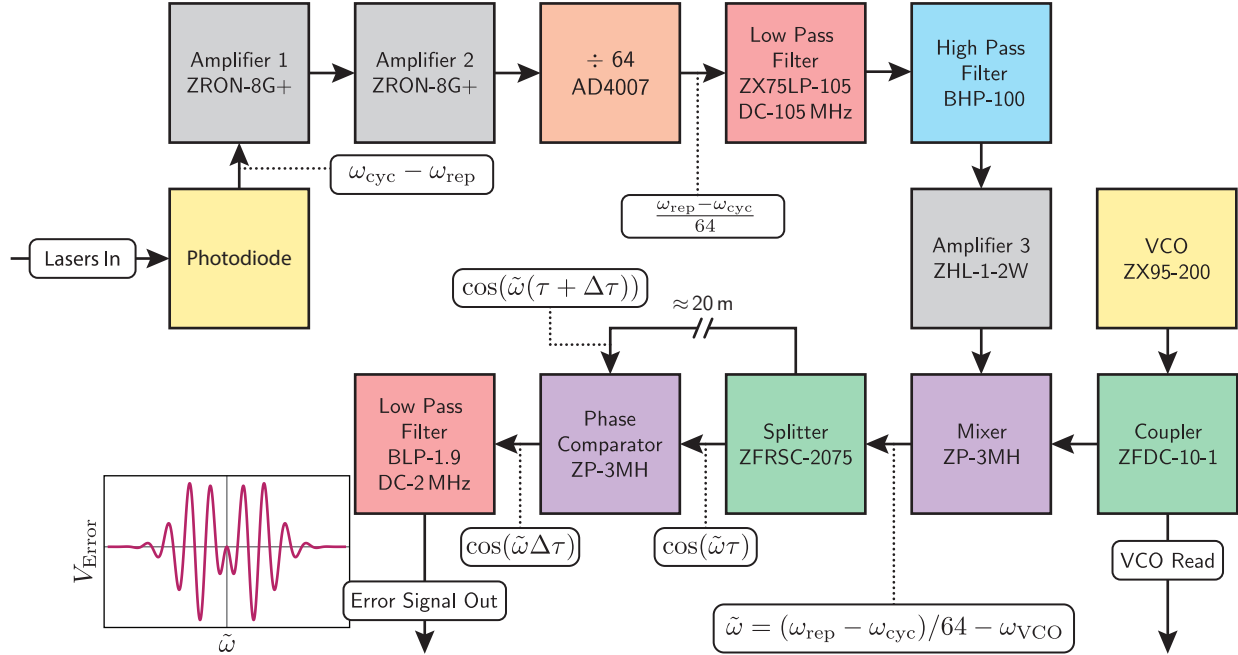


Figure A.2: Block diagram of electronics for the  $^{87}\text{Rb}$  offset lock. The repump and cycling lasers are free space coupled onto a photodiode which reads only their difference frequency. The signal is then amplified, divided by 64, filtered, amplified again, and then mixed with a signal from a VCO. The mixed signal is split and one path is sent directly into a phase comparator and the other into the phase comparator after a time delay  $\Delta\tau$ . The signals on the two arms of the phase comparator have the same frequency so the output just corresponds to the frequency-dependent phase shift on the signal which went through the delay line. The error signal is passed through one final filter and sent to the locking circuitry. An approximation of the error signal is shown at the bottom left versus the frequency  $\tilde{\omega}$ . The coupler serves to measure and adjust the VCO frequency without disassembling the circuit.

lasers ( $\approx 500 \mu\text{W}$ ) and combine them in fiber to optically mix them. The output of the fiber has both the sum and difference frequencies and is aligned through free space onto a fast photodiode (Newport [818-BB-45](#)). The photodiode is considered fast because it has a high enough bandwidth to read the difference frequency between the two  $\sim 100$  THz frequencies. Thus it essentially acts as a low-pass filter and only converts  $\omega_{\text{rep}} - \omega_{\text{cyc}}$  into an electronic signal.

This electronic signal is fed into the offset lock which we show in Fig. [A.2](#). First, the difference signal is amplified with two Mini Circuits [ZRON-8G+](#). It is then passed to a frequency divider (Analog Devices [AD4007](#)) that we set to give a division of 64, thus bringing our 6.5 GHz signal down to roughly 102 MHz. After filtering the signal to eliminate any undesired frequencies from passing through, the signal is once again amplified (Mini Circuits [ZHL-1-2W](#)) and then is passed to a mixer (Mini Circuits [ZP-3MH](#)). At this point

the difference signal divided by 64 is mixed with a voltage controlled oscillator (VCO, Mini Circuits ZX95-200) with a tunable frequency  $\omega_{\text{VCO}}$ . At the output of the mixer the difference frequency is again kept yielding  $(\omega_{\text{rep}} - \omega_{\text{cyc}})/64 - \omega_{\text{VCO}}$ . This signal is then split (Mini Circuits ZFRSC-2050). One path is sent directly into a phase comparator which, in this case, is just a mixer (Mini Circuits ZP-3MH). The other path from the splitter is sent through a roughly 20 m long cable before entering the phase comparator. The purpose of the path length difference is to give one signal a phase shift with respect to the other which is subsequently read by the phase comparator. Importantly, the amount that the phase on the signal going down the long path gets shifted also depends on the frequency of that signal. Finally, the signal is filtered once again and then sent to the locking circuitry (a PID circuit built into the Toptica laser controller). The entire system is made from block, plug-and-play electronic components and BNC cables, and is housed in a metallic enclosure. We found that eliminating all adapters and other sources of loss from the output of the photodiode was all but necessary to achieve a stable, reliable error signal and so the front panel of the enclosure simply has a hole for the SMA cable to pass through. Also on the front panel is a BNC jack for reading the VCO frequency, a trim pot for adjusting the VCO frequency, BNC jacks for powering the circuit, and finally a BNC jack which outputs the final error signal.

Mathematically, the signal going directly into the phase comparator can be written  $V_1 = \cos(\tilde{\omega}\tau)$  and the delayed signal can be written  $V_2 = \cos(\tilde{\omega}(\tau + \Delta\tau))$  where  $\tilde{\omega} = (\omega_{\text{rep}} - \omega_{\text{cyc}})/64 - \omega_{\text{VCO}}$ , and  $\Delta\tau$  is the added time taken for the signal to travel the roughly 20 m delay line. When the difference between these two signals is taken by the phase comparator we get  $V_{\text{Error}}(\omega_{\text{rep}}) = \cos(\tilde{\omega}\Delta\tau)$  where we have ignored a constant phase shift due to the path length difference. Thus the output of the phase comparator is a constant value corresponding to the frequency difference between the three oscillators  $\tilde{\omega}$ . If any of the the three frequencies are changed, the output of the phase comparator changes. However, when locking the repump laser, the cycling laser must already be locked and the VCO must be fixed such that  $\omega_{\text{cyc}}$  and  $\omega_{\text{VCO}}$  are constants. Therefore, when  $\omega_{\text{rep}}$  is scanned it causes the relative phase between the two arms of the phase comparator to change and, more importantly,  $V_{\text{Error}}$  crosses zero as shown in the approximation of the error signal in the bottom left of Fig. A.2. The zero-crossings of  $V_{\text{Error}}$  occur whenever  $\tilde{\omega}\Delta\tau = 2n\pi$  with  $n$  a positive or negative integer.

Given  $\Delta\tau \sim 100$  ns the zero crossings are spaced by  $\sim 10$  MHz. The decaying envelope around the signal corresponds to the filtering performed to limit  $(\omega_{\text{rep}} - \omega_{\text{cyc}})/64$  to the range 100–105 MHz as shown in Fig. A.2. When locked,  $\tilde{\omega}$  only changes due to any drifts in  $\omega_{\text{rep}}$  and so the locking circuitry adjusts the current in the diode to keep  $V_{\text{Error}}(\omega_{\text{rep}}) = 0$ . Any of these zero crossings may be used for locking the laser but by convention we typically use the first zero crossing to the right of the origin. To get the lock frequency just right with respect to the atomic transition, the VCO frequency may be tuned to shift the error signal.

### A.3 Andor Neo Camera Program

The program text shown below is written in a proprietary language called Andor Basic and only designed to work specifically with the Andor Neo 5.5 sCMOS camera. To summarize the code, it performs the following actions:

- (i) It starts by asking the user what number image they want to start at (line 48). The naming scheme for files can be altered in the base code but we use the convention “YYYY-MM-DD-image#” with the file extension .asc (ASCII file type). The program does not automatically start at image number 1 because if the program is stopped and restarted it may overwrite images already taken that day so instead it is up to the user to prevent this from happening (lines 47–93). If the user selects a number which already exists in the current export folder it prompts them to confirm that they would like to overwrite the files in that folder as an added safeguard against losing data.
- (ii) The program then prompts the user to say whether they would like to define a cropping region of interest for the images (lines 100–152). The files can always be cropped later if no cropping is done here but we find it is best for analyzing the data later to keep the file sizes as small as possible. If the user responds that they would like to crop the image the program continues to ask them for individual cropping parameters. If not, the program advances to the ready state for taking an image.
- (iii) The program then waits for a trigger (line 167) from the control software Cicero [as described in Subsec. 3.1.3] after having a few of its settings about the image defined

(lines 159–162). This trigger is sent to the camera 27.5430 ms before the actual picture is taken to allow the camera time to drain any built-up charge before the image is taken. We set the camera to the external trigger exposure time mode such that it starts the exposure when a signal from the computer goes high and ends the exposure when it goes low again. Since the camera is set at line 161 to take three frames for a single measurement, the program waits at line 167 until it receives three triggers and takes three images.

- (iv) The three images are concatenated in one file and exported to the predetermined destination (line 169). This can cause problems because while the software is busy writing this file it cannot ready the camera for another exposure. This only really becomes an issue when a full-size image is being taken faster than every 5 seconds or so. Given our experimental cycle time of  $\approx 25$  s and that we typically use cropped images, this does not pose an issue.
- (v) The camera then cycles back to the beginning of the steady-state loop (line 165) and readies itself for another three-shot burst.

```
// Andor Loop Program version 4.1 - Eric J. Meier - 2017.08.25 1
// This version autosaves data files in ASCII format as well as including 2
// automated region of interest (ROI) settings and was
// written for a 1920x1080 screen (relevant for window placement within the 3
// program).
//2015.10.26 - Wrote a line to output crop settings 4
//2015.10.28 - Wrote a line to output crop settings in two ways and changed ROI 5
// interface to accept 'n' for a full image instead of all ones. Added some
// common cropping settings that output when 'y' is entered when asked if you
// want to set an ROI.
//2016.03.29 - changed some of the suggested settings; added commands to set acq. 6
// mode, trig mode, kin. ser. length, and num. accum.
//2016.03.31 - Fixed the (H,B,W,L) crop settings calculations. 7
//2016.06.28 - updated common cropping settings 8
//2016.08.31 - updated common cropping settings and added option to input '18ms' 9
// into hc selection window to get common 18 ms TOF settings of (hc,vc)
// =(1000,1080)
//2017.01.17 - added a temperature controller line to heading to set cooler to on 10
// and temp to -40
//2017.08.25 - updated common cropping settings and made the cropping settings 11
// output when program aborted
```

```

cooler(1) // turns on the TEC for the camera 12
SetTemperature(-40) // sets the target temperature 13
outputfont = 12 //define font size for output window 14
output(0,0,750,400) // define size of output window 15
base$="C:\Users\labuser2\Desktop\data\" // directory for exporting data 16
ext$=".asc" // file extension 17
year$=mid$(date$,1,4) // extracts the year from the computer date 18
month$=mid$(date$,6,2) // extracts the month from the computer date 19
day$=mid$(date$,9,2) // extracts the day from the computer date 20
// create a directory on the computer to save the data in (if one does not 21
    already exist) 22
MakeDirectory(base$+year$+"\") 23
MakeDirectory(base$+year$+"\ "+month$+"\") // 24
base$=base$+year$+"\ "+month$+"\ "+day$+"\ " 25
MakeDirectory(base$) 26
name$=base$+date$()+"-image" // define the file naming scheme 27
28
//prints the date used for the images (in case the computer date got changed 29
    erroneously) and tells the user where the files will be saved
Print() 30
Print() 31
Print() 32
Print() 33
Print() 34
Print("-----") 35
Print("-----Gadway Lab-----") 36
Print("-----") 37
Print("") 38
Print("Image date extension is set to: "+date$()) 39
Print("Base directory (based on computer date) is set to: " +name$) 40
Print("Edit program directly to alter the base directory.") 41
Print() 42
Print("-----") 43
44
// The following while loop is used to interface with the user to pick an image 45
    starting number. When a number is input the computer checks whether such a
    file already exists in the current working directory. If it does, the program
    prompts the user to confirm that they would like to overwrite that file when
    the next picture is taken. This is a safeguard against accidentally
    overwriting data. It then tells the user the full path and name for the first
    image to be taken.
j=0 // set the while loop variable 46
while (j==0) // enter while loop 47
    input("What number do you want to start at? (Numbering begins at 1)", i) 48
    path$= (name$+i)+ext$ // ask the user for an image number variable and 49
        define the path and name for the first image to be taken.

```

```

// check if the path already exists. If it does, ask the user if they
// would like to overwrite. If not, do nothing.
if (exist(path$)) then
    fileexist$="File already exists. Would you like to overwrite for
    the entire series? (y/n) "
    input(fileexist$, ow$)
endif

// if the user accidentally enters '0' the program politely reminds them
// that we start counting with the number '1'.
if (i==0) then
    Print("Numbering starts at 1")
    j=0
endif

// If the file does not already exist we inform the user that the file
// name is valid and set the while loop condition to exit.
if !(i==0) && !(exist(path$)) then
    Print ("File name checks out.")
    j=1
    ow$="z"
endif

// This line resets the while loop if the user has picked a file number
// which already exists but decides they do not want to overwrite that
// file.
if (strcmp(ow$,"n",1)==0) then
    j=0
endif

// Prints a confirmation that the user has requested to overwrite existing
// data and sets the while loop condition to exit.
if (strcmp(ow$,"y",1)==0) then
    Print("Overwriting Requested")
    j=1
endif

// If the user makes a typo this resets the loop.
x=abs(strcmp(ow$,"n",1)) and abs(strcmp(ow$,"y",1)) and abs(strcmp(ow$
,"z",1))
if (x==1) then
    j=0
    Print("Unrecognized input, try again.")
endif

// Upon successfully setting a file name and before exiting the loop, the

```

```

        full path and name are printed for the user's reference.
    if (j==1) then
        print("First Picture will be saved to: " + path$)
    endif

wend

Print()
Print("-----")
Print()

// This while loop is used to set a region of interest (ROI) for the images to be
// taken. It first asks the user if they want to use an ROI or not. If they do,
// it asks them for a few dimensions to define the ROI for our specific camera
// detector size. Since most of the time when we are taking data it is of a BEC
// after 18ms time of flight it is in the same vertical location on the camera.
// So, there is a default escape key to get around setting those parameters by
// entering '18ms'. It then sets these settings using the 'SetImage' command and
// prints them for future reference.
m=0
while (m==0) // enter loop

    input("Would you like to set an ROI? Respond 'n' for a full image. (y/n)",
    l$) // ask the user if they want an ROI and save the response in the
    string variable 'l'

    // if the user does not want to set an ROI then the camera is set to
    // record a full image and the loop is exited.
    if (strcmp(l$,"n",0)==0) then
        SetImage()
        m=1
    endif

    // if the user does want to set an ROI, they are prompted with several
    // questions about the dimensions of the ROI
    if (strcmp(l$,"y",0)==0) then
        Print("18 ms TOF: (x, y) = (958, 1212)") // This prints a reminder
        for the pre-measured BEC position after the normally used 18ms
        time of flight.
        input("Enter the horizontal center of the desired ROI. (Enter '18ms
        ' to use the common settings)", hc$) // ask the user for the
        horizontal center of the image and also accept the default
        token '18ms'

        // if '18ms' is selected this sets the horizontal and vertical
        // center to the position of the BEC.
        if (strcmp(hc$,"18ms",0)==0) then

```

```

        hc=958
        vc=1212
    else // if the user enters a number for the horizontal center we
        enter this section
        hc=val(hc$) // convert the input string to a float
        input("Enter the vertical center of the desired ROI.", vc)
        // ask the user for a vertical center
    endif

    input("Enter the desired Height.", h) // ask the user for a height
    of the image
    input("Enter the desired Width.", w) // ask the user for the width
    of the image

    // the following four lines convert the user friendly measurements
    above to coordinates that the software understands based on our
    custom rotation of the camera and the detector size.
    hs = 2560-vc-Floor(h/2)
    he = hs + h-1
    vs = hc - Floor(w/2)
    ve = vs + w-1

    SetImage(hs,he,1,vs,ve,1) // set the final cropping parameters
    m=1
endif

// a catch for typos
if !(strcmp(l$, "n", 0) == 0) && !(strcmp(l$, "y", 0) == 0) then
    m=0
    Print("Unrecognized Input.")
endif

// print the crop settings for the user's reference
if (strcmp(l$, "n", 0) == 0) then
    Print("Crop Settings: full image")
else
    Print("Crop Settings: (H, B, W, L) = "+"(str$(w)+", "+str$(hc-
        Floor(w/2))+", "+str$(h)+", "+str$(2560-vc-Floor(h/2))+")")
    Print("Crop Settings: (Xc, Yc, H, W) = "+"(str$(hc)+", "+str$(vc)
        +", "+str$(h)+", "+str$(w)+")")
endif

wend

Print()
Print("-----")
Print()

```

```

// Now we are done with the user input section of the code and on to the steady- 157
state running section. 158
SetAcquisitionMode(3) // This sets the acquisition mode of the camera to 'Kinetic 159
Series'. A mode which tells the software that you will be taking a certain
number of images as part of a single measurement. Very useful for the three-
image procedure of absorption imaging.
SetTriggerMode(7) // This sets the trigger to external, which we supply by the 160
computer which runs the rest of the apparatus.
SetKineticNumber(3) // This sets the number of images in the Kinetic Series to 161
three. The signal, background, and noise images.
SetAccumulateNumber(1) // Tells the camera there will be one frame taken per 162
image. i.e. no averaging. 163
// The following while loop sets the camera to ready itself for a three-image 164
burst and then write those images to disk and then ready itself again. There
are no stop conditions for the program it must be manually stopped by the user
when desired.
while (1) // set the while loop to run indefinitely 165
    Print("Ready for trigger...") // inform the user that the camera is ready 166
    and waiting for a trigger
    run() // set the camera to its ready state. This is where the image is 167
    actually taken. The program sits at this line until it receives the
    number of triggers set above in 'SetKineticNumber', 3 in this case.
    Print("Exporting...") // Now that it has recorded three frames, the camera 168
    informs the user that it will begin exporting the data.
    SaveASCIIXY(#0,path$,4,0,0) // the command to actually write the file to 169
    disk.
    Print("Picture saved as: "+path$) // A confirmation of the successful 170
    saving of the file and its full path.
    beep() // emit a sound to let the user know the file was saved. 171
    i=i+1 // increase the image number variable for the next image to be taken 172
    path$=(name$+i)+ext$ // reset the image path with new image number 173
    variable
wend 174

```

## A.4 Magnetic Field Estimation

This section gives equations and examples of code for estimating the field from square coils in general as well as our Feshbach coils specifically.

### A.4.1 Feshbach Coils

The Feshbach coils are modeled as 72 individual circular loops of wire. Because the wire is actually refrigerator tubing and is quite thick, the size of one loop is a large fraction of the size of the whole coil. So each of the 72 loops has its radius and offset from the center defined individually. The Mathematica code shown below models the field from these coils using the basic form for the on-axis field from one circular loop:

$$B(I) = \frac{\mu_0}{4\pi} I \frac{2\pi r^2}{(d^2 + r^2)^{3/2}}, \quad (\text{A.1})$$

where  $\mu_0$  is the permeability of free space,  $I$  is the current,  $r$  is the radius of the loop, and  $d$  is the on-axis distance to the point where the field is measured. With all the dimensions of the coil holders plugged in from Fig. 3.16, Eq. A.1 simplifies to  $B/I = 3.799 \text{ G/A}$ .

```
(* Feshbach coil field estimator. This code estimates the field from the Feshbach
   coils with the dimensions as laid out in Fig. 3.16. Eric J. Meier 2019.10.09
   *)
In[1]:= CellClearance = 2.0; (*Free space between the coils in inches*)
\[Mu]0 = 4*\[Pi]*10^-7;
intom = 0.0254;
WrappedTubeOD = 0.15*intom; (*Diameter of the refrigerator tubing with shrink
   wrap in meters*)
HolderOD = 2.262*intom; (*Diameter of the spool part of the holder which the
   first column of turns is wrapped around in meters*)
HolderCapThickness = 0.2*intom; (*Thickness of the top cap support of the spool
   in meters*)
HolderSeparation = CellClearance*intom + HolderCapThickness; (*Space between the
   spool parts of the coils*)
HolderCavityHeight = 1.02*intom; (*Height of the spool area (on axis of loops) in
   meters*)
FirstColumnRadius = (HolderOD + WrappedTubeOD)/2; (*Radius of the smallest column
   of turns in meters*)
LastColumnRadius = 4.15/2*intom - WrappedTubeOD/2; (*Radius of the largest column
   of turns in meters*)
FirstRowDistance = HolderSeparation/2 + WrappedTubeOD/2; (*On-axis distance of
   the closest row of turns in meters*)
LastRowDistance = HolderSeparation/2 + HolderCavityHeight - WrappedTubeOD/2; (*On
   -axis distance of the furthest row of turns in meters*)

In[5]:= ColumnRadii = Range[FirstColumnRadius, LastColumnRadius, (
   LastColumnRadius - FirstColumnRadius)/5] (* Defines the radii of the six
   columns of loops *)
```

```

Out[5]= {0.0306324, 0.0346659, 0.0386994, 0.042733, 0.0467665, 0.0508}

In[6]:= RowDistances = Range[FirstRowDistance, LastRowDistance, (LastRowDistance
- FirstRowDistance)/5] (* Defines the distances from the field center of the
six rows of loops *)

Out[6]= {0.029845, 0.0342646, 0.0386842, 0.0431038, 0.0475234, 0.051943}

In[7]:= BTurn[II_, r_, d_] := \[Mu]0/(4 \[Pi])*II*(2 \[Pi] r^2)/(d^2 + r^2)^(3/2)
*10000; (*This is for the on-axis field of a single loop with radius r a
distance d away in Gauss*)

In[8]:= TurnPositions = Delete[Flatten[Table[Table[{ColumnRadii[[i]],
RowDistances[[j]]}, {j, Length[RowDistances]}], {i, Length[ColumnRadii]}], 1],
-6]; (*List of all the positions of the individual turns with the closest
turn deleted to account for the fact that we only got 35 turns in*)

In[9]:= TotalBField[II_] := 2*Total[BTurn[II, #[[1]], #[[2]]]&/@TurnPositions] (*
The total field produced by the 70 individual loops of wire in Gauss. Factor
of two because there are two coils.*)

```

#### A.4.2 Square Coil Formulae

The equations we use to estimate the magnetic field at a point in space  $(x, y, z)$  due to a rectangular current loop of dimensions  $2b \times 2a$  as taken from Ref. [223] are:

$$B_x = \frac{\mu_0}{4\pi} I \sum_{k=1}^4 \frac{(-1)^{k+1} z}{r_k(r_k + d_k)} \quad (\text{A.2})$$

$$B_y = \frac{\mu_0}{4\pi} I \sum_{k=1}^4 \frac{(-1)^{k+1} z}{r_k(r_k + c_k)} \quad (\text{A.3})$$

$$B_z = \frac{\mu_0}{4\pi} I \sum_{k=1}^4 (-1)^k \left( \frac{c_k}{r_k(r_k + d_k)} + \frac{d_k}{r_k(r_k + c_k)} \right), \quad (\text{A.4})$$

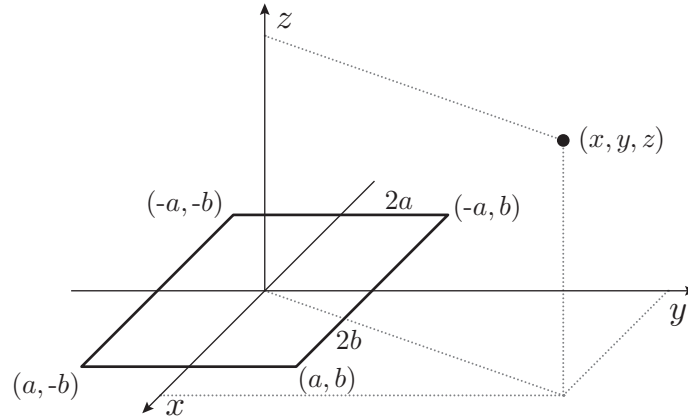


Figure A.3: Dimensional layout for a square coil. The coil lays in the  $x - y$  plane with its center at the origin and has dimensions  $2b \times 2a$ . This figure adapted from [223].

where  $B_i$  represent the components of the full  $\mathbf{B}$  vector and

$$c_1 = c_4 = x + a, \quad (\text{A.5})$$

$$c_2 = c_3 = x - a, \quad (\text{A.6})$$

$$d_1 = d_2 = y + b, \quad (\text{A.7})$$

$$d_3 = d_4 = y - b, \quad (\text{A.8})$$

$$r_k = \sqrt{c_k^2 + d_k^2 + z^2}. \quad (\text{A.9})$$

In the above equations, the geometry of the loop is assumed to be as shown in Fig. A.3. That is to say, a loop lying in the  $x-y$  plane with its center at the origin. The length of the rectangle in the  $x$  direction is  $2b$  and in the  $y$  direction is  $2a$ . The equations essentially just assume four straight wire segments carrying current  $I$ . For more than one turn, the result is simply multiplied by the number of turns. These equations are used to calculate the full magnetic field from the 2D MOT coils [see Fig. 3.13] and 3D MOT shimming fields which are both rectangular.



# Appendix B

## Simulation Techniques

Nearly all of the computer simulations which are compared to experiment in this thesis were performed by me and are written for Wolfram Mathematica. For the more repetitious measurements of the SSH model (particularly in the presence of disorder or interactions) Mathematica seemed to suffer from some instabilities causing the program to freeze. In these cases (specifically the simulations shown in Figs. 5.2(d), 5.3(b), 5.4(d), and 5.6) Python was used instead. Below, we give examples for several different types of simulation in both of these languages.

For all the examples we will be considering a 5-site lattice centered about zero such that  $n \in \{-2, -1, 0, 1, 2\}$ . Also, for fun, we will use the following pseudorandom values for the tunneling strengths  $t_n$ , tunneling phases  $\varphi_n$ , and site energies  $\epsilon_n$ .

$$\begin{aligned}\epsilon_n &= \{0.3, 0.2, -0.4, 0.0, 0.666\}E_r, \\ t_n &= \{0.4, 0.666, 0.5, 0.05\}E_r, \\ \varphi_n &= \{0.2, 0.1, 1.0, 1.5\}\pi,\end{aligned}\tag{B.1}$$

where  $E_r = h^2/(2M_{\text{Rb}}\lambda^2) \simeq h \times 2027.8 \text{ Hz}$  is the recoil energy of an atom emitting a photon of the lattice laser light with  $\lambda = 1064 \text{ nm}$ . Recall that  $t_n$  and  $\varphi_n$  have only four terms because they are properties of the links between sites  $n \rightarrow n + 1$  and as such there are only  $N - 1$  of them. We will additionally use the initial condition that all population will start in site  $n = 0$  for all the simulations here.

### B.1 Ideal Approximation Simulations

The starting off point when we want to investigate a new project with computer simulation is typically with the “ideal” form of our system. That is to say, the fully approximated

Hamiltonian:

$$H^{\text{ideal}} \approx \sum_{n=N_i}^{N_f} \epsilon_n c_n^\dagger c_n + \sum_{n=N_i}^{N_f-1} \left( t_n e^{i\varphi_n} c_{n+1}^\dagger c_n + \text{H.c.} \right) \quad (\text{B.2})$$

where  $\epsilon_n$  gives the site energy,  $t_n$  gives the tunneling strength,  $\varphi_n$  is the tunneling phase,  $N_i$  and  $N_f$  relate to the first and last site in the system with the total number of sites given by  $N = N_f - N_i + 1$  as shown in Fig. 2.1(d). Each term in the second sum of the Hamiltonian links sites  $n$  and  $n + 1$  and therefore the sum runs to the second-to-last site, resulting in the next site being the final site in the system.

Now let us consider simulating our  $N = 5$  site lattice with the parameters as listed in Eqs. B.1. Given these parameters we can write the Hamiltonian as:

$$H^{\text{ideal}} = \begin{pmatrix} \epsilon_{-2} & t_{-2}e^{i\varphi_{-2}} & 0 & 0 & 0 \\ t_{-2}e^{-i\varphi_{-2}} & \epsilon_{-1} & t_{-1}e^{i\varphi_{-1}} & 0 & 0 \\ 0 & t_{-1}e^{-i\varphi_{-1}} & \epsilon_0 & t_0e^{i\varphi_0} & 0 \\ 0 & 0 & t_0e^{-i\varphi_0} & \epsilon_1 & t_1e^{i\varphi_1} \\ 0 & 0 & 0 & t_1e^{-i\varphi_1} & \epsilon_2 \end{pmatrix} \quad (\text{B.3})$$

$$= \begin{pmatrix} 0.3 & 0.4e^{i0.2\pi} & 0 & 0 & 0 \\ 0.4e^{-i0.2\pi} & 0.2 & 0.666e^{i0.1\pi} & 0 & 0 \\ 0 & 0.666e^{-i0.1\pi} & -0.4 & -0.5 & 0 \\ 0 & 0 & -0.5 & 0 & 0.05e^{i1.5\pi} \\ 0 & 0 & 0 & 0.05e^{-i1.5\pi} & 0.666 \end{pmatrix} E_r. \quad (\text{B.4})$$

In the basis of the momentum states used in the experiment  $|n\rangle$  we consider the arbitrary state  $|\psi(\tau)\rangle = \sum_n c_n(\tau)|n\rangle$ . Solving for the dynamics of a given initial state then corresponds to finding the set of  $c_n(\tau)$  which correspond to the occupation of each momentum mode. We

can simulate the dynamics of this initial state with the time-dependent Schrödinger equation:

$$i\hbar\partial_\tau|\psi(\tau)\rangle = H|\psi(\tau)\rangle \quad (\text{B.5})$$

$$i\frac{\hbar}{E_r} \begin{pmatrix} \dot{c}_1(\tau) \\ \dot{c}_2(\tau) \\ \dot{c}_3(\tau) \\ \dot{c}_4(\tau) \\ \dot{c}_5(\tau) \end{pmatrix} = \begin{pmatrix} 0.3 & 0.4e^{i0.2\pi} & 0 & 0 & 0 \\ 0.4e^{-i0.2\pi} & 0.2 & 0.666e^{i0.1\pi} & 0 & 0 \\ 0 & 0.666e^{-i0.1\pi} & -0.4 & 0.2e^{i0.666\pi} & 0 \\ 0 & 0 & 0.2e^{-i0.666\pi} & 0 & 0.5e^{i1.5\pi} \\ 0 & 0 & 0 & 0.5e^{-i1.5\pi} & 0.666 \end{pmatrix} \begin{pmatrix} c_1(\tau) \\ c_2(\tau) \\ c_3(\tau) \\ c_4(\tau) \\ c_5(\tau) \end{pmatrix}. \quad (\text{B.6})$$

Solving this system of equations for the set  $c_n(\tau)$  will yield the evolution of the wave function in terms of the momentum states for this particular Hamiltonian. In most cases we use the initial conditions that the population starts in the zero momentum mode with no phase which I will here define to be site  $n = 0$ ,  $c_n(\tau = 0) = \{0, 0, 1, 0, 0\}$ . Once  $|\psi(\tau)\rangle$  is known, other things can be calculated like the average position  $\langle n \rangle(\tau) = \langle \psi(\tau) | n | \psi(\tau) \rangle$ , or the momentum width  $\sigma_p(\tau) = \sqrt{\langle p^2 \rangle - \langle p \rangle^2}$ , or the fidelity with some target state, etc. For this specific situation, solving Eq. B.6 yields the dynamics as shown in Fig. B.1(a). The population moves around in the lattice in a complex pattern owing to our random selections for the system parameters. One thing to note is that site  $n = 5$  is virtually never populated because it is only connected by the weak tunneling  $t_5 = 0.05E_r$ . In Fig. B.1(b) we show what this might look like as integrated absorption images by adding an artificial width to the  $|c_n|^2(\tau)$  shown in Fig. B.1(a). Below we display the Mathematica code used to simulate these dynamics and generate the plot shown in Fig. B.1(a). Note that in the code the  $n$  basis is shifted for convenience and  $\hbar$  is dropped everywhere to make the numbers easier for the computer to work with.

```
(* Ideal simulation of Eq. B.6 written for Mathematica by Eric J. Meier.
2019.10.10 *)
Ns = 5; (* Number of sites in the system *)
FinalTime = 10.0 10^-3./(2 Pi); (* time to solve for dynamics over *)
Er = 2 Pi 2027.8138181797337; (* the recoil energy for a rubidium atom and a 1064
nm laser in Hz*)
t = {0.4, 0.666, 0.5, 0.05} Er; (* The tunneling energies *)
epsilon = {0.3, 0.2, -0.4, 0.0, 0.666} Er; (* the site energies *)
```

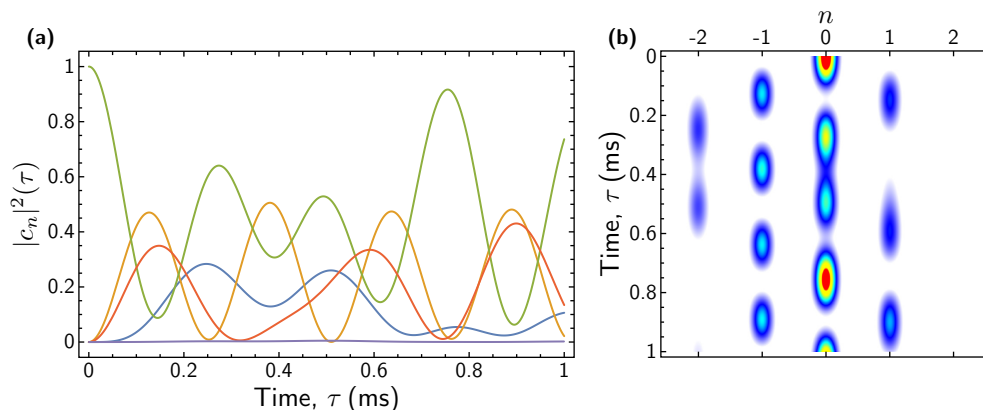


Figure B.1: Population dynamics for example ideal simulation. **(a)** The probabilities of the wavefunction  $|c_n|^2$  for all five sites as a function of time  $\tau$ . The line colors correspond to the states  $n$  as  $\{-2, -1, 0, 1, 2\}$  in  $\{\text{blue, yellow, green, red, purple}\}$ . **(b)** A replotting of the data shown in (a) with arbitrary momentum width to look similar to absorption images. The color scale is as given in Fig. 6.1(b).

```

phi = {0.2, 0.1, 1.0, 1.5} Pi ; (* the tunneling phases *)

(* Here we define the Hamiltonian *)
H = Normal[SparseArray[Join[
  Table[{n, n} -> epsilon[[n]], {n, Ns}],
  Table[{n + 1, n} -> t[[n]] Exp[-I phi[[n]]], {n, Ns - 1}],
  Table[{n, n + 1} -> t[[n]] Exp[I phi[[n]]], {n, Ns - 1}]]];

(* set our initial conditions, all population starting in site 3 *)
InitialConditions = {c[1][0.] == 0., c[2][0.] == 0., c[3][0.] == 1.,
  c[4][0.] == 0., c[5][0.] == 0.};

(* Use NDSolve to solve to numerically solve the differential equations and then
  massage them into functional forms *)
solution = NDSolveValue[{-I D[Table[c[n][\Tau]], {n, Ns}], \Tau] == H.Table[c[
  n][\Tau]], {n, Ns}], InitialConditions, Table[c[n], {n, Ns}], {\Tau, 0.,
  FinalTime}];
Coeff[\Tau_] := #[\Tau] & /@ solution
ProbAmp[\Tau_] := Abs[#[\Tau]]^2 & /@ solution

(* Plot the probabilities of the wavefunction [plot shown in Fig. B.1(a)] *)
Plot[Evaluate[ProbAmp[\Tau] 10^-3], {\Tau, 0., FinalTime/10^-3}, Frame ->
  True, Axes -> False, FrameStyle -> Directive[Black, 16]]

```

This method can be extended to  $\approx 40$  sites before Mathematica starts to slow down (depending on the computer of course) and as long as the Hamiltonian does not change in time. The Hamiltonian is free to change in time however since we have that ability in experiment and use it often. To modify the above formulation the  $\epsilon_n$ ,  $t_n$ , and/or  $\varphi_n$  just

become functions of time in whatever way is desired and the Mathematica code is modified to include this time dynamics by making the Hamiltonian a function of time as well. This tends to greatly extend the solving time in Mathematica though.

## B.2 Non-Approximated Simulations

While the ideal simulations capture the physics we want to probe, we typically also perform non-approximated solutions of our system either as a check or as a way to help explain deviations between the experiment and the ideal simulations. By a non-approximated simulation we refer to solving the “full” Hamiltonian (not making the rotating wave approximation) given by

$$H^{\text{full}}(\tau) = \sum_n (\chi(\tau)|\psi_n\rangle\langle\psi_{n+1}| + \chi^*(\tau)|\psi_{n+1}\rangle\langle\psi_n|) + \sum_n E_n|\psi_n\rangle\langle\psi_n|, \quad (\text{B.7})$$

where  $E_n = 2n^2k^2\hbar^2/M_{\text{Rb}}$  is the energy associated with the momentum states  $n$  and

$$\chi(\tau) = \sum_j t_j e^{i\varphi_j} e^{-i\tilde{\omega}_j\tau}. \quad (\text{B.8})$$

The  $\tilde{\omega}_j$  are the transition frequencies which address the two-photon Bragg transitions between momentum states, and  $t_n$  and  $\varphi_n$  are the same as in the ideal case, the tunneling strengths and phases with which the transitions are driven. For more information on where this Hamiltonian comes from see the opening and first section of Chap. 2.

Let us again consider an  $N = 5$  site lattice centered at site zero and with parameters shown in Eq. B.1. The Hamiltonian now can be written in terms of the recoil energy

$E_n = 4n^2 E_r$  as

$$H^{\text{full}}(\tau) = \begin{pmatrix} -16E_r & \chi(\tau) & 0 & 0 & 0 \\ \chi^*(\tau) & -4E_r & \chi(\tau) & 0 & 0 \\ 0 & \chi^*(\tau) & 0 & \chi(\tau) & 0 \\ 0 & 0 & \chi^*(\tau) & 4E_r & \chi(\tau) \\ 0 & 0 & 0 & \chi^*(\tau) & 16E_r \end{pmatrix}. \quad (\text{B.9})$$

We can go about solving this Hamiltonian in the exact same way as in the ideal case shown in Eq. B.6. Here, however, we must also define the frequency of the drive fields in addition to the other parameters. Also, the site energies must come in on the detunings from resonance rather than on the diagonal of the Hamiltonian. For convenience let us redefine  $\tilde{\omega}_j = \omega_{j,j+1}^{\text{res}} - \delta_j$  where  $\omega_{j,j+1}^{\text{res}} = 4E_r((j+1)^2 - j^2)/\hbar = 4E_r(2j+1)/\hbar$  (which is commonly known as An's Law after eminent scholar Fangzhao Alex An) and  $\delta_j$  is the detuning of the drive field from resonance. Note however, that there are only four drive fields to link a 5 site lattice. So we choose the convention  $\delta_j = \epsilon_{n+1} - \epsilon_n$  with  $\epsilon_n$  as defined in Eq. B.2 as the site energies.

Calculating  $\delta_j$  from our site energies listed in Eq. B.1 as used in the ideal case above, yields

$$\delta_j = \{-0.1, -0.6, 0.4, 0.666\}E_r. \quad (\text{B.10})$$

The tunneling strength and phase may remain the same however, because they are already defined as parameters of the driving field. Plugging this into the time-dependent Schrödinger equation as before results in a set of equations which when solved yield the coefficients of the wavefunction  $c_n(\tau)$ . Performing this simulation numerically as before with the same initial conditions yields dynamics as shown in Fig. B.2. We find that given these parameters the two simulations are quite similar as can be seen in Fig. B.2(a) by comparing the solid lines (full simulation) to the dotted lines (ideal simulation reproduced from Fig. B.1(a)). The jumpiness in the full simulation results from the fact that we did not make the rotating-wave approximation so the states are subjected to high-frequency wiggles on top of their net

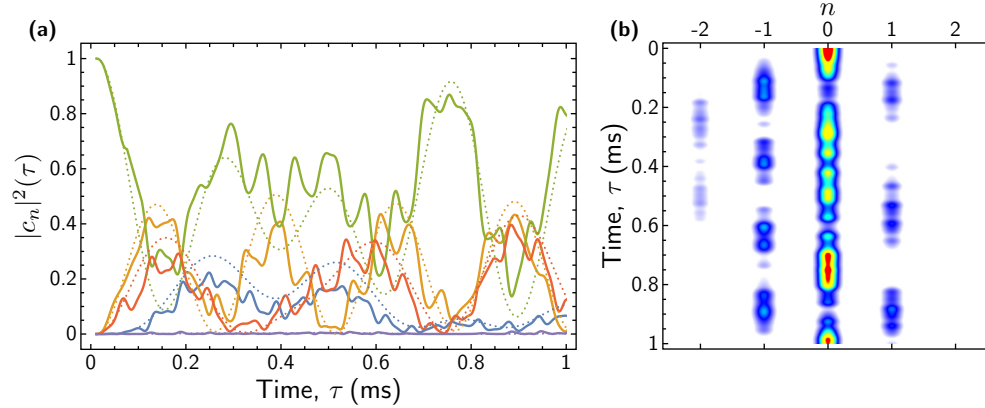


Figure B.2: Population dynamics for example full simulation. **(a)** The probabilities of the wavefunction  $|c_n|^2$  for all five sites as a function of time  $\tau$ . The line colors correspond to the states  $n$  as  $\{-2, -1, 0, 1, 2\}$  in  $\{\text{blue, yellow, green, red, purple}\}$ . The dotted lines in the background are the ideal simulation from Fig. B.1(a) for comparison. **(b)** A replotting of the data shown in (a) with arbitrary momentum width to look similar to absorption images. The color scale is as given in Fig. 6.1(b).

motion. If we were to run the simulation again with no phases on the drive frequencies these wiggles would be even more pronounced and step-like as the drive frequencies all come into phase with one another at the same time and push the state forward. Figure B.2(b) shows what the simulation would look like if it were data by adding an arbitrary momentum width to it. Below we show the Mathematica code which simulates this system and generates Fig. B.2.

```
(* Full simulation of Eq. B.7 written for Mathematica by Eric J. Meier.
2019.10.10 *)
Ns = 5; (* Number of sites in the system *)
FinalTime = 1.0 10^-3.; (* time to solve for dynamics over *)
Er = 2 Pi 2027.8138181797337; (* the recoil energy for a rubidium atom and a 1064
nm laser in Hz*)
t = {0.4, 0.666, 0.5, 0.05} Er; (* The tunneling energies *)
epsilon = {0.3, 0.2, -0.4, 0.0, 0.666} Er; (* the site energies *)
phi = {0.2, 0.1, 1.0, 1.5} Pi ; (* the tunneling phases *)
delta = Differences[epsilon]; (* define the detunings of the drive fields *)

ResDriveFreq = Table[4 Er (2 n + 1), {n, -2, 1}]; (* define the resonant drive
frequencies *)

StateEnergies = Table[4 Er n^2, {n, -2, 2}]; (* define the energies of the 5
states *)

chi[\[Tau]_] := Sum[t[[j]] Exp[-I phi[[j]]] Exp[-I (ResDriveFreq[[j]] - delta[[j]]
)] \[Tau], {j, Ns - 1} (* The common tunneling term  $\chi(\tau)$  as defined in
Eq. B.8 *)
```

```

(* Here we define the Hamiltonian *)
H[\[Tau]_] := Normal[SparseArray[Join[
  Table[{n, n} -> StateEnergies[{n}], {n, Ns}],
  Table[{n + 1, n} -> chi[\[Tau]]\[Conjugate], {n, Ns - 1}],
  Table[{n, n + 1} -> chi[\[Tau]], {n, Ns - 1}]]]];

(* set our initial conditions, all population starting in site 3 *)
InitialConditions = {c[1][0.] == 0., c[2][0.] == 0., c[3][0.] == 1., c[4][0.] ==
  0., c[5][0.] == 0.};

(* Use NDSolve to solve to numerically solve the differential equations and then
  massage them into functional forms *)
solution = NDSolveValue[{-I D[Table[c[n][\[Tau]], {n, Ns}], \[Tau]] == H[\[Tau]].
  Table[c[n][\[Tau]], {n, Ns}], InitialConditions}, Table[c[n], {n, Ns}], {\[Tau]
  ], 0., FinalTime];
Coeff[\[Tau]_] := #[\[Tau]] & /@ solution
ProbAmp[\[Tau]_] := Abs[#[\[Tau]]]^2 & /@ solution

(* Plot the probabilities of the wavefunction. The output of this line is shown
  as Fig. B.2(a) *)
Plot[Evaluate[ProbAmp[\[Tau] 10^-3]], {\[Tau], 0., 10}, Frame -> True, Axes ->
  False, FrameStyle -> Directive[Black, 16]]

```

### B.3 Simulations with Interactions

When we suspect that there is some non-negligible effect of interactions in our data, we also incorporate interactions into our simulations. We do this by solving a non-linear Schrödinger equation known as the Gross–Pitaevskii (GP) equation which incorporates interactions as a mean-field effect. We define the GP equation as:

$$i\partial_{\tau}\psi(\tau) = H\psi(\tau) - U|\psi(\tau)|^2\psi(\tau), \quad (\text{B.11})$$

where  $U$  encapsulates the effectively attractive interactions inherently present in our system (see Sec. 2.7 for more details). Since this is only incorporated in the differential equations to be solved, it changes nothing about the setup shown in the two previous sections for ideal or full simulations. Therefore, it can be used with either ideal or full simulations. For simplicity we will consider an ideal simulation identical to that performed above but

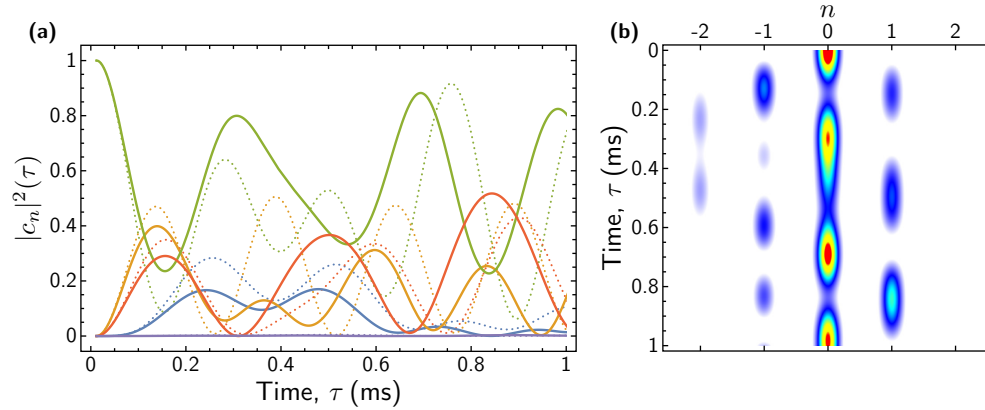


Figure B.3: Population dynamics for example interacting ideal simulation. **(a)** The probabilities of the wavefunction  $|c_n|^2$  for all five sites as a function of time  $\tau$  with a mean-field interaction strength of  $U = E_r$ . The line colors correspond to the states  $n$  as  $\{-2, -1, 0, 1, 2\}$  in  $\{\text{blue, yellow, green, red, purple}\}$ . The dotted lines in the background are the ideal simulation from Fig. B.1(a) for comparison. **(b)** A replotting of the data shown in (a) with arbitrary momentum width to look similar to absorption images. The color scale is as given in Fig. 6.1(b).

with interactions of a strength  $U = E_r$ . We still use our parameters as given in Eqs. B.1 and the same initial conditions as the previous two simulations but numerically solve the GP equation above. We find dynamics as shown by the solid lines in Fig. B.3(a) which deviate significantly from the non-interacting case (dotted lines) due to the presence of the interactions. Figure B.3(b) shows the dynamics as if they were absorption images for clarity. Below we show the Mathematica code used to simulate the GP equation and generate the dynamics shown in Fig. B.3. Note that the system of equations defined by the GP equation is now separated from the NDSolve function for convenience.

```
(* Interacting Ideal simulation of Eq. B.11 written for Mathematica by Eric J.
Meier. 2019.10.11 *)
Ns = 5; (* Number of sites in the system *)
FinalTime = 1.0 10^-3.; (* time to solve for dynamics over *)
Er = 2 Pi 2027.8138181797337; (* the recoil energy for a rubidium atom and a 1064
nm laser in Hz*)
t = {0.4, 0.666, 0.5, 0.05} Er; (* The tunneling energies *)
epsilon = {0.3, 0.2, -0.4, 0.0, 0.666} Er; (* the site energies *)
phi = {0.2, 0.1, 1.0, 1.5} Pi; (* the tunneling phases *)
U = 1.0 Er; (* the interaction strength *)

(* Here we define the Hamiltonian *)
H = Normal[SparseArray[Join[
  Table[{n, n} -> epsilon[[n]], {n, Ns}],
  Table[{n + 1, n} -> t[[n]] Exp[-I phi[[n]]], {n, Ns - 1}],
  Table[{n, n + 1} -> t[[n]] Exp[I phi[[n]]], {n, Ns - 1}]]];
```

```

(* set our initial conditions, all population starting in site 3 *)
InitialConditions = {c[1][0.] == 0., c[2][0.] == 0., c[3][0.] == 1., c[4][0.] ==
  0., c[5][0.] == 0.};

(* define the system of differential equations defined by the GP equation (
  Eq. B.11) *)
gpe = Table[-I c[n]'[\[Tau]] == H[[n]].Table[c[n][\[Tau]], {n, 5}] - U Abs[c[n]
  ][\[Tau]]^2 c[n][\[Tau]], {n, Ns}];

(* Use NDSolve to solve to numerically solve the differential equations and then
  massage them into functional forms *)
solution = NDSolveValue[{gpe, InitialConditions}, Table[c[n], {n, Ns}], {\[Tau],
  0., FinalTime}];
Coeff[\[Tau]_] := #[\[Tau]] & /@ solution
ProbAmp[\[Tau]_] := Abs[#[\[Tau]]]^2 & /@ solution

(* Plot the probabilities of the wavefunction. The output of this line is shown
  in Fig. B.3*)
Plot[Evaluate[ProbAmp[\[Tau] 10^-3]], {\[Tau], 0., FinalTime/10^-3}, Frame ->
  True, Axes -> False, FrameStyle -> Directive[Black, 16]]

```

## B.4 Python Simulations

Mathematica is the default lab program for simulations, arbitrary waveform generation, data analysis, and plotting. In all of these tasks it usually performs quite well. However, there have been a few simulations which we have done in Python because of some limitations to Mathematica. First, when running a very long simulation in Mathematica, say one that will take 10 hours or more, we have noticed that the program seems to just stop with no errors or crashing—it just runs forever, long after it should be finished. We get around this occasionally by breaking the simulation up into smaller pieces and writing the results to disk and then recombining them after it is all done. But if the simulation can be rewritten in Python relatively quickly it may be more advantageous to do that. A second quirk of Mathematica is a strange numerical instability that pops up on occasion. The same simulation can be run in Mathematica and Python and whereas the Python data shows a smooth trend, the Mathematica data will be jumpy but show the same general trend. The jumpiness in the Mathematica simulations is repeatable but not physical to the best of our

knowledge. For these reasons it is sometimes worth it for a Mathematica expert to run a Python simulation. Indeed, in the case of the simulations shown in Chap. 5, we needed to perform large-system, long-time simulations with disorder averaging. Mathematica proved to be slow and prone to freezing up for this specific simulation so we turned to Python.

Let us now consider our example system with Python as in the cases above. We will show simulations in Python using both the [QuTiP](#) package [224] and the [QuSpin](#) package [225]. QuTiP is, in general, more developed and has more functionality but I find QuSpin easier and more transparent to work with for the kind of simulations we do. The following two code examples are simulations of the ideal system (Eq. B.6) using the parameters defined in Eqs. B.1 and the same initial conditions as before (all population starting in the middle site of a 5-site lattice) first with the QuTiP package and then with the QuSpin package. Full simulations may be incorporated into either of these packages similarly to the way it is done above in Mathematica.

### B.4.1 QuTiP

We begin by showing an example using the QuTiP package. Lines 6–11 are basically the same as all the other Mathematica simulations—just defining parameters to be used later on. The Hamiltonian is defined using for loop architecture in lines 14–19 and then converted to a QuTiP object (Qobj) in line 20. The initial conditions are defined in line 23. QuTiP forces the user to define the discrete list of times they want to solve the Hamiltonian for (whereas Mathematica does it behind the scenes in NDSolve unless explicitly defined) and this is done in line 26. The solving of the time-dependent Schrödinger equation is done in line 29 which outputs an object with several properties. The empty lists in the q.mesolve function can be filled with operators which one wants to solve for which is a nice feature. The object result.states contains the Qobj state arrays at each time in “times” and it must be first stripped of its Qobj status so that it can be transposed which is done in lines 32–34. Then the coefficients  $c_n(\tau)$  and the probabilities  $|c_n|^2(\tau)$  are defined in lines 36 and 37. Finally the dynamics are plotted in lines 39–43. We do not show the output of this as a figure here because it is identical to Fig. B.1(a).

```

1 # Ideal simulation of Eq. B.6 for Python using the QuTiP package by Eric J. Meier
  2019.10.11
2 import numpy as np
3 import qutip as q
4 import matplotlib.pyplot as plt
5
6 Ns=5 # number of sites in the system
7 FinalTime=1.0*10**(-3) # time to solve dynamics over
8 Er=2*np.pi*2027.8138181797337 # the recoil energy for a rubidium atom and a 1064
  nm laser in Hz
9 t=np.array([0.4,0.666,0.5,0.05])*Er # tunneling energies
10 epsilon=np.array([0.3,0.2,-0.4,0.0,0.666])*Er # site energies
11 phi=np.array([0.2,0.1,1.0,1.5])*np.pi # tunneling phases
12
13 # define the Hamiltonian
14 H = [[0 for x in range(Ns)] for y in range(Ns)]
15 for i in range(0,Ns-1):
16     H[i][i+1]=t[i]*np.exp(1j*phi[i])
17     H[i+1][i]=np.conj(t[i]*np.exp(1j*phi[i]))
18 for i in range(0,Ns):
19     H[i][i]=epsilon[i]
20 H=q.Qobj(H)
21
22 # define the initial conditions
23 psi0=q.basis(Ns,2)
24
25 # create a list of times to solve for the states at
26 times=np.linspace(0.,FinalTime,num=501,endpoint=True)
27
28 # solve the time dependent schrodinger equation
29 result = q.mesolve(H, psi0, times, [], [])
30
31 # massage the state vectors into numpy manipulable objects
32 states=[]
33 for i in result.states:
34     states.append(i[:])
35
36 coeff=np.transpose(states)[0] # define the coefficients
37 proamp=np.abs(coeff)**2 # define the probabilities
38
39 for pp in proamp:
40     plt.plot(times,pp)
41 plt.xlabel('Time, (ms)')
42 plt.ylabel('|c_n|^2 (Time)')
43 plt.show()

```

## B.4.2 QuSpin

Now we will perform the same exact simulation but in the QuSpin package. It looks a little more complex than the QuTiP code but that is because it is more upfront and explicit in my opinion. For example, we may manually define the Schrödinger equation and evolve a state using it with this package which makes for more clarity and ease especially when incorporating interactions. The code begins the same way with parameters being defined in lines 9–14. Then we move into defining the Hamiltonian. QuSpin’s method for defining the Hamiltonian is a little more involved than for QuTiP. Tunneling terms (lines 18 and 19) are defined by creating a list item of the form  $[t_{n_i, n_f}, n_i, n_f]$  where  $t_{n_i, n_f}$  sets the tunneling term between sites  $n_i$  and  $n_f$ . Similarly, the energies are defined (line 22) by a list of the form  $[\epsilon_n, n]$  where  $\epsilon_n$  is the energy of site  $n$ . Next these parameters are incorporated into lists using the keywords  $+ -$  for tunneling in the direction  $n_i \rightarrow n_f$  and  $- +$  for the opposite direction in line 25. Additionally, the site energies are coded in with the keyword  $n$  followed by the site energy parameter list. After defining the basis in line 29, these lists are passed to the Hamiltonian building function in line 32. Incorporating dynamic Hamiltonians is relatively easy in this architecture as well by using the list named “dynamic” which we leave empty in line 26. Next, we define a function for the Schrödinger equation in lines 38–44. Then the state is evolved for the discrete time list defined in line 47 by the “evolve” function called in line 50 with the initial state defined in line 35. This yields the coefficients  $c_n(\tau)$  directly and the probabilities  $|c_n|^2(\tau)$  are calculated from them in line 53. Lines 55–60 plot the result which we do not show here because it is identical to Fig. B.1(a). Interactions may be incorporated very easily into this code by uncommenting the non-linear term to the Schrödinger equation defined in line 40.

```

1 # Ideal simulation of Eq. B.6 for Python using the QuSpin package by Eric J.
  Meier 2019.10.11
2 from quspin.operators import hamiltonian # Hamiltonians and operators
3 from quspin.basis import boson_basis_1d # Hilbert space boson basis
4 from quspin.tools.evolution import evolve # nonlinear evolution
5 import numpy as np # generic math functions
6 import matplotlib.pyplot as plt # plotting library
7 from six import iteritems # loop over elements of dictionary
8
9 Ns=5 # number of sites in the system

```

```

10 FinalTime=1.0*10**(-3) # time to solve dynamics over
11 Er=2*np.pi*2027.8138181797337 # the recoil energy for a rubidium atom and a 1064
    nm laser in Hz
12 t=np.array([0.4,0.666,0.5,0.05])*Er # tunneling energies
13 epsilon=np.array([0.3,0.2,-0.4,0.0,0.666])*Er # site energies
14 phi=np.array([0.2,0.1,1.0,1.5])*np.pi # tunneling phases
15
16 ##### construct single-particle Hamiltonian #####
17 # define site-coupling lists in the form [t_n, ni, nf]
18 hop_t=[[t[i]*np.exp(1j*phi[i]),i,(i+1)] for i in range(Ns-1)]
19 conjhop_t=[[t[i]*np.exp(-1j*phi[i]),i,(i+1)] for i in range(Ns-1)]
20
21 #define the site energies
22 pot=[[epsilon[i],i] for i in range(Ns)]
23
24 # define static and dynamic lists to be fed into the QuSpin hamiltonian function
25 static=[["+-",hop_t],["-+",conjhop_t],['n',pot]]
26 dynamic=[]
27
28 # define basis of the hamiltonian in terms of 1D bosons
29 basis=boson_basis_1d(Ns,Nb=1)
30
31 # build real-space Hamiltonian
32 Hsp=hamiltonian(static,dynamic,basis=basis,dtype=np.complex64,check_symm=True,
    check_herm=True,check_pcon=False)
33
34 # define initial conditions
35 psi0=np.array([0.,0.,1.,0.,0.])
36
37 #define the time-dependent Schrodinger equation as a function
38 def TDSE(time,psi):
39     # solve static part of TDSE
40     psi_dot = Hsp.static.dot(psi)#-U*np.abs(psi)**2*psi
41     # solve dynamic part of TDSE
42     for f,Hd in iteritems(Hsp.dynamic):
43         psi_dot += f(time)*Hd.dot(psi)
44     return -1j*psi_dot
45
46 # define the list of times to solve the hamiltonian for
47 times=np.linspace(0.,FinalTime,501)
48
49 # time-evolve state according to TDSE with the QuSpin evolve function and define
    the states, coefficients, and probabilities
50 psi_t = evolve(psi0,times[0],times,TDSE,atol=1E-12,rtol=1E-12)
51 states=np.transpose(psi_t)
52 coeff=psi_t
53 proamp=abs(psi_t)**2

```

```

54
55 # plot the resulting probabilities as a function of time
56 for pp in proamp:
57     plt.plot(times,pp)
58 plt.xlabel('Time, (s)')
59 plt.ylabel('|c_n|^2(Time)')
60 plt.show()

```

## B.5 Corrections for Time Dependent Lattices

It is important to keep in mind that the Fourier transform of the applied drive field to the atoms is more important than the instantaneous frequency. That is to say that one should pay extra attention to making sure the Fourier transform looks right instead of assuming since the instantaneous drive frequency is always doing what you think it should that it is correct. In this section we present an example of this pitfall based on an adiabatic rapid passage in a two-level system using full simulation techniques. We will begin with what I call the naïve case, where we simply program what we believe to be the correct instantaneous frequency.

We will use the following parameters for our simulation:

$$t = 0.2E_r, \quad (\text{B.12})$$

$$\epsilon_n(\tau) = \left\{ \frac{\epsilon_f - \epsilon_i}{\tau_{\text{ramp}}}\tau + \epsilon_i, 0 \right\}, \quad (\text{B.13})$$

$$\delta(\tau) = -\frac{\epsilon_f - \epsilon_i}{\tau_{\text{ramp}}}\tau - \epsilon_i, \quad (\text{B.14})$$

where  $\epsilon_i = -4E_r$ ,  $\epsilon_f = +4E_r$ , and  $\tau_{\text{ramp}} = 10$  ms. These equations describe a two-site system ( $|0\rangle$  and  $|1\rangle$ ) with constant tunneling  $t$ . The energy of site  $|0\rangle$  is zero at all times but the energy of site  $|1\rangle$  is a linear ramp from  $\epsilon_i$  to  $\epsilon_f$  in a time  $\tau_{\text{ramp}}$  as shown in Fig. B.4(a). As in the previous sections,  $\delta(\tau) = \epsilon_1 - \epsilon_0$  is the time-dependent energy difference between the two sites, which will be incorporated into the drive field. In the naïve case,  $\delta(\tau)$  extends from  $-\epsilon_i$  to  $-\epsilon_f$ , crossing the resonance condition halfway through the ramp as shown in

Fig. B.4(b). The drive field  $\chi(\tau)$  can be written as

$$\chi(\tau) = t e^{-i(\omega_{0,1}^{\text{res}} + \delta(\tau))\tau}, \quad (\text{B.15})$$

where  $\omega_{0,1}^{\text{res}} = 4E_r \approx 2\pi \times 8111.26 \text{ Hz}$  is the Bragg resonance frequency for connecting momentum modes  $|0\rangle$  and  $|1\rangle$ . This gives us a Hamiltonian of

$$H_{\text{naïve}} = \begin{pmatrix} 0 & \chi(\tau) \\ \chi^*(\tau) & 4E_r \end{pmatrix}. \quad (\text{B.16})$$

Using the time-dependent Schrödinger equation (Eq. B.5) to evolve the initial state  $\psi(\tau = 0) = |0\rangle$  according to this Hamiltonian gives the dynamics shown in Fig. B.4(c). What we should expect to see with this experiment is the population starting in site 0 being moved over to site 1 centered at a time when the two sites are resonant with one another, which in this case is when  $\delta = 0$  halfway through the ramp. However, we instead see that the population transfers early, at roughly  $\tau = \tau_{\text{ramp}}/4$ . This problem is further reflected in the Fourier transform shown in Fig. B.4(d). The frequency sweep shown there begins at the correct frequency denoted by the gray vertical line on the left at  $\omega_{0,1}^{\text{res}} + \epsilon_i$ . The problem is that our sweep is not centered about resonance. Instead, it extends from  $\omega_{0,1}^{\text{res}} + \epsilon_i$  to  $\omega_{0,1}^{\text{res}} + 3\epsilon_f$  (the gray vertical line at the left), which is twice the range that the ramp should extend.

I have not formulated any universal fix for this problem. In this case, however, we modify the site energy ramp by reducing its rate of change by a factor of  $1/2$  such that

$$\delta^c(\tau) = -\frac{\epsilon_f - \epsilon_i}{2\tau_{\text{ramp}}}\tau - \epsilon_i \quad (\text{B.17})$$

as is shown in Fig. B.4(e). This is counter-intuitive because, from the instantaneous frequency perspective, the drive field never crosses resonance but actually ends there. This fixes the problem however, as is shown by the dynamics in Fig. B.4(f) where the population beginning in state  $|0\rangle$  (blue line) is transferred to state  $|1\rangle$  (orange line) at the proper time  $\tau = 0.5\tau_{\text{ramp}}$ . Further, the Fourier transform of the drive field with this corrected site-energy ramp [Fig. B.4(g)] also shows the desired behavior. The ramp begins at  $\omega_{0,1}^{\text{res}} + \epsilon_i$  and ends

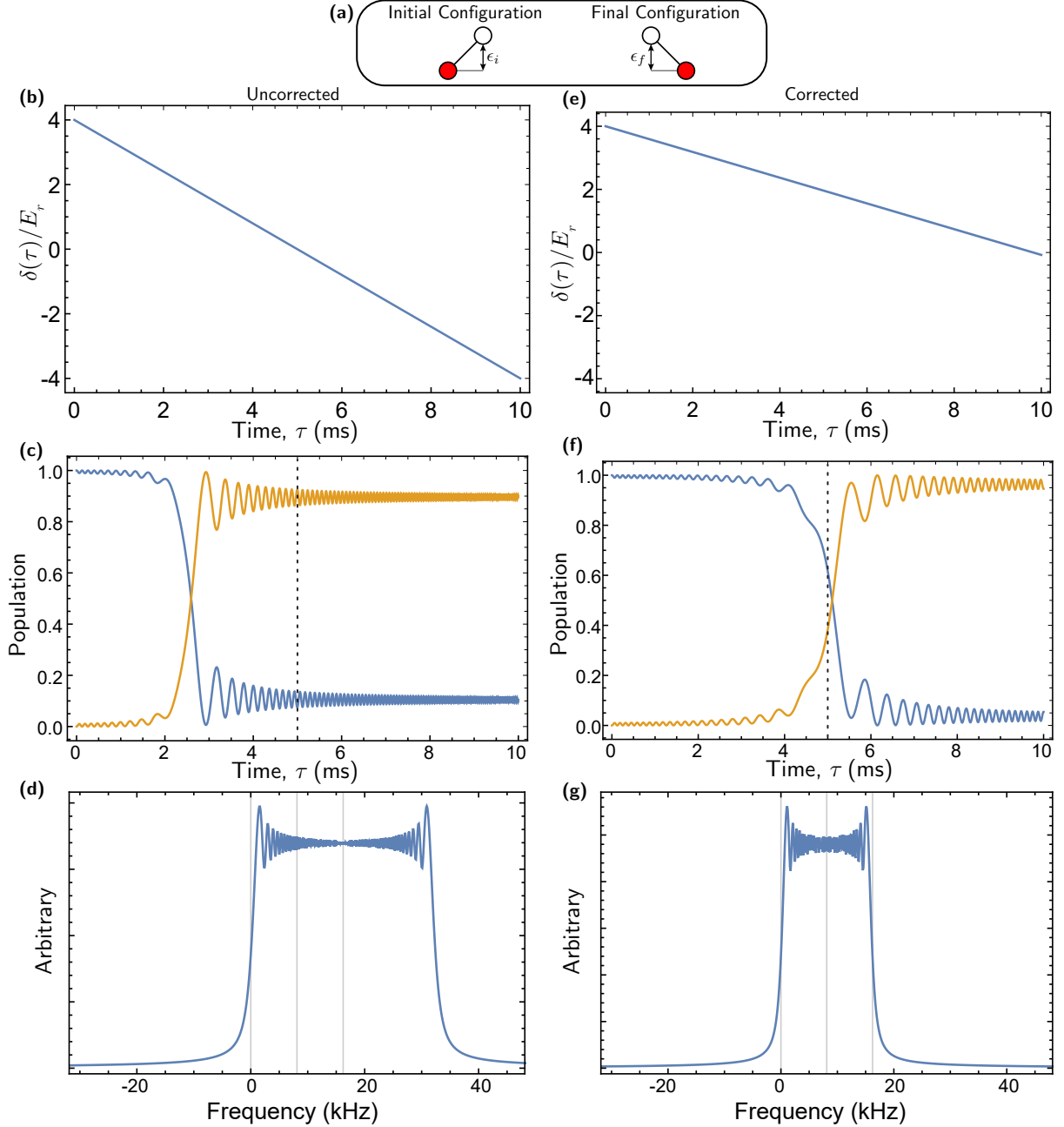


Figure B.4: Corrections for time dependent lattices. **(a)** Cartoon of the lattice showing the initial and final configurations. **(b)** The site energy difference  $\delta(\tau)$  showing the naïve ramp through resonance. **(c)** The resulting dynamics for the naïve ramp. The population transfers from site  $|0\rangle$  (blue line) to  $|1\rangle$  (orange line) at roughly  $\tau = 0.25\tau_{\text{ramp}}$ , a factor of two before it should. **(d)** Discrete Fourier transform of Eq. B.15 using the site energy ramp shown in (b). The ramp starts at the correct frequency  $\omega_{0,1}^{\text{res}} + \epsilon_i$  (left-most gray vertical line) but extends twice as far as desired, ending at  $\omega_{0,1}^{\text{res}} + 3\epsilon_f$ . In the naïve picture this spectrum should be centered at  $\omega_{0,1}^{\text{res}}$  and vary from this by  $+\epsilon_i$  to  $+\epsilon_f$ . **(e)** The correction to the site energy ramp. The rate of change of the site-energy difference is reduced by a factor of  $1/2$ , which results in it counter-intuitively stopping on resonance. **(f)** The dynamics for the corrected site-energy ramp shown in (e). The population is transferred from site  $|0\rangle$  (blue line) to  $|1\rangle$  (orange line) at  $\tau = 0.5\tau_{\text{ramp}}$ , which is the expected behavior. **(g)** The discrete Fourier transform in the corrected case now looks as we desired, extending from  $\omega_{0,1}^{\text{res}} + \epsilon_i$  to  $\omega_{0,1}^{\text{res}} + \epsilon_f$ . The parameters for all sub-panels are  $t/E_r = 0.2$  and  $\epsilon_i = \epsilon_f = 4E_r$ .

at  $\omega_{0,1}^{\text{res}} + \epsilon_f$  such that it has the correct width and end points.

There is one more very important practical detail about this problem. The counter-intuitive modifications are *only* necessary during the ramp. If one wanted to institute some hold time or expose the system to a different Hamiltonian after the ramp, then the drive field should jump to the desired frequencies with no corrections (but it should account for the ensuing time of the ramp). For example, consider the case presented here with an extra hold time after the experiment. The site energy difference at the end of the corrected ramp are zero ( $\delta^c(\tau_{\text{ramp}}) = 0$ ). According to the Fourier transform and the results of the experiments, there is a site-energy offset of  $\epsilon_f$  however. So  $\delta^c(\tau)$  must be instantaneously jumped to  $\epsilon_f$  during the hold time so that the sites do not become resonantly coupled. If this is done properly in this context, the population will remain in state  $|1\rangle$ . If  $\delta^c$  remains unchanged at zero during the hold time the two states will be resonantly coupled and Rabi oscillations will ensue.

Below we show the Mathematica code used to generate the plots shown in Fig. B.4. The static parameters are defined in lines 2–8 followed by the definition of  $\epsilon(\tau)$  in line 10 and  $\delta(\tau)$  in line 12. The output of the Plot function in line 14 is shown as Figs. B.4(b/e).  $\omega_{0,1}^{\text{res}}$  is defined in line 16 and the energies of the states are defined in line 18. The drive field  $\chi(\tau)$  is defined in line 20 followed by the Hamiltonian in lines 23–26. NDSolve is used to find the dynamics [shown in Figs. B.4(c/f)] of the state populations in lines 32–34 with the initial conditions defined in line 29. Lines 40–51 discretize the drive field and plot its Fourier transform as shown in Figs. B.4(d/g). The code is displayed currently in the naïve format. To correct it the factor of 2 in the denominator of  $\delta(\tau)$  can be uncommented in line 10.

```

1 (* Mathematica code displaying the correction for time dependent lattices. Eric J
   . Meier 2019.10.25 *)
2 Ns = 2; (* Number of sites in the system *)
3 FinalTime = 10.0 10^-3.; (* time to solve for dynamics over *)
4 Er = 2 \[Pi] 2027.8138181797337'; (* the recoil energy for a rubidium atom and a
   1064 nm laser*)
5 t = {0.2} Er; (* The tunneling energies *)
6 epsilon0 = -4.0 Er; (* the initial site energy *)
7 epsilonf = +4.0 Er; (* the final site energy *)
8 phi = {0.0} Pi ; (* the tunneling phases *)
9
10 epsilon[\[Tau]_] := {(epsilonf - epsilon0)/(*2*)FinalTime \[Tau] + epsilon0, 0.0}

```

```

(* the site energies as a function of time including the ramp *)
11
12 delta[\[Tau]_] := Differences[epsilon[\[Tau]]];(* define the detunings of the
    drive fields *)
13
14 Plot[delta[\[Tau]/10^3]/Er, {\[Tau], 0, 10.}]
15
16 ResDriveFreq = {4 Er (2 n + 1)} /. {n -> 0}; (* define the resonant drive
    frequencies *)
17
18 StateEnergies = 4 Er n^2 /. {n -> {0, 1}}; (* define the energies of the 2 states
    *)
19
20 chi[\[Tau]_] := Sum[t[[j]] Exp[-I phi[[j]]] Exp[-I (ResDriveFreq[[j]] - delta[\[
    Tau]][[j]]) \[Tau]], {j, Ns - 1}] (* define the drive field itself *)
21
22 (* Here we define the Hamiltonian *)
23 H[\[Tau]_] := Normal[SparseArray[Join[
24     Table[{n, n} -> StateEnergies[[n]], {n, Ns}],
25     Table[{n + 1, n} -> chi[\[Tau]]\[Conjugate], {n, Ns - 1}],
26     Table[{n, n + 1} -> chi[\[Tau]], {n, Ns - 1}]]]];
27
28 (* set our initial conditions, all population starting in site 1 *)
29 InitialConditions = {c[1][0.] == 1., c[2][0.] == 0.};
30
31 (* Use NDSolve to solve to numerically solve the differential equations and then
    massage them into functional forms *)
32 solution = NDSolveValue[{-I D[Table[c[n][\[Tau]], {n, Ns}], \[Tau]] == H[\[Tau]].
    Table[c[n][\[Tau]], {n, Ns}], InitialConditions}, Table[c[n], {n, Ns}], {\[Tau]
    ], 0., FinalTime];
33 Coeff[\[Tau]_] := #[\[Tau]] & /@ solution
34 ProbAmp[\[Tau]_] := Abs[#[\[Tau]]]^2 & /@ solution
35
36 (* Plot the probability amplitude of the wavefunction *)
37 Plot[Evaluate[ProbAmp[\[Tau] 10^-3]], {\[Tau], 0., 10}, Frame -> True, Axes ->
    False, FrameStyle -> Directive[Black, 16]]
38
39 (* in the following block we calculate the discrete Fourier transform of the
    drive field as if it were an arbitrary waveform with the 80 MHz AOM frequency
    *)
40 ArbSampleRate = 5.75 10^8;
41 TimeList = Range[0, FinalTime, FinalTime/(FinalTime*ArbSampleRate - 1)];
42 arbchi[\[Tau]_] := Sum[2 t[[j]] Sin[(phi[[j]] + (2 \[Pi] 80.0 10^6 + ResDriveFreq
    [[j]] - delta[\[Tau]][[j]]) \[Tau]], {j, Ns - 1}]
43 ArbList = arbchi[TimeList];
44 DetuningList = ResDriveFreq/(2 \[Pi]);
45 ArbTime = FinalTime;

```

```

46 MaxSpectRange = Ceiling[Max[{Abs[Min[DetuningList]], Max[DetuningList]}]/(80
    10^3)] + 1;
47 ArbSpectrumY = Abs[Fourier[ArbList]][[Round[80 10^3*ArbTime (10^3 - MaxSpectRange
    ) + 1] ;; Round[80 10^3*ArbTime (10^3 + MaxSpectRange) + 1]]];
48 ArbSpectrumX = ((# - #[[-1]]/2.) & /@ {Range[0, Length[ArbSpectrumY] - 1]/(
    ArbTime 10^3)}][[1]];
49 ArbSpectrumXY = Transpose[{ArbSpectrumX, ArbSpectrumY}];
50 ListLinePlot[ArbSpectrumXY, PlotRange -> {{Min[DetuningList]/10^3 - 40,
51     Max[DetuningList]/10^3 + 40}, All}, GridLines -> {Join[Flatten[DetuningList
    ]/10^3, {(ResDriveFreq[[1]] + epsilon0)/(2 \[Pi] 10^3), (ResDriveFreq[[1]]
    + epsilonf)/(2 \[Pi] 10^3)}], {}}, FrameLabel -> {"Detuning from 80 MHz (
    kHz)"}, FrameStyle -> Directive[Black]]

```

# References

- [1] R. P. Feynman, *Int. J. Theor. Phys.* **21**, 467 (1982).
- [2] W. P. Su, J. R. Schrieffer, and A. J. Heeger, *Phys. Rev. Lett.* **42**, 1698 (1979).
- [3] J. Vila, G. H. Paulino, and M. Ruzzene, *Phys. Rev. B* **99**, 125116 (2019).
- [4] M. Serra-Garcia, V. Peri, R. Süsstrunk, O. R. Bilal, T. Larsen, L. G. Villanueva, and S. D. Huber, *Nature* **555**, 342 (2018).
- [5] S. Stützer, Y. Plotnik, Y. Lumer, P. Titum, N. H. Lindner, M. Segev, M. C. Rechtsman, and A. Szameit, *Nature* **560**, 461 (2018).
- [6] M. Milićević, G. Montambaux, T. Ozawa, O. Jamadi, B. Real, I. Sagnes, A. Lemaître, L. Le Gratiet, A. Harouri, J. Bloch, and A. Amo, *Phys. Rev. X* **9**, 031010 (2019).
- [7] S. Mittal, V. V. Orre, D. Leykam, Y. D. Chong, and M. Hafezi, *Phys. Rev. Lett.* **123**, 043201 (2019).
- [8] F. Cardano, A. D’Errico, A. Dauphin, M. Maffei, B. Piccirillo, C. de Lisio, G. De Filippis, V. Cataudella, E. Santamato, L. Marrucci, M. Lewenstein, and P. Massignan, *Nat. Commun.* **8**, 15516 (2017).
- [9] T. Ozawa, H. M. Price, A. Amo, N. Goldman, M. Hafezi, L. Lu, M. C. Rechtsman, D. Schuster, J. Simon, O. Zilberberg, and I. Carusotto, *Rev. Mod. Phys.* **91**, 015006 (2019).
- [10] B. M. Anderson, R. Ma, C. Owens, D. I. Schuster, and J. Simon, *Phys. Rev. X* **6**, 041043 (2016).
- [11] A. Celi, P. Massignan, J. Ruseckas, N. Goldman, I. B. Spielman, G. Juzeliūnas, and M. Lewenstein, *Phys. Rev. Lett.* **112**, 043001 (2014).
- [12] M. Mancini, G. Pagano, G. Cappellini, L. Livi, M. Rider, J. Catani, C. Sias, P. Zoller, M. Inguscio, M. Dalmonte, and L. Fallani, *Science* **349**, 1510 (2015).
- [13] J. H. E. Cartwright and D. L. Gonzalez, *Math. Intelligencer* **38**, 69 (2016).
- [14] D. J. Thouless, M. Kohmoto, M. P. Nightingale, and M. den Nijs, *Phys. Rev. Lett.* **49**, 405 (1982).
- [15] K. von Klitzing, G. Dorda, and M. Pepper, *Phys. Rev. Lett.* **45**, 494 (1980).

- [16] B. A. Bernevig, T. L. Hughes, and S.-C. Zhang, *Science* **314**, 1757 (2006).
- [17] L. Fu, C. L. Kane, and E. J. Mele, *Phys. Rev. Lett.* **98**, 106803 (2007).
- [18] J. E. Moore and L. Balents, *Phys. Rev. B* **75**, 121306 (2007).
- [19] A. B. Bernevig and T. L. Hughes, *Topological insulators and topological superconductors* (Princeton University Press, Princeton, NJ, 2013).
- [20] B. Bradlyn, L. Elcoro, J. Cano, M. G. Vergniory, Z. Wang, C. Felser, M. I. Aroyo, and B. A. Bernevig, *Nature* **547**, 298 (2017).
- [21] M. G. Vergniory, L. Elcoro, C. Felser, N. Regnault, B. A. Bernevig, and Z. Wang, *Nature* **566**, 480 (2019).
- [22] M. V. Berry, *Proc. R. Soc. Lond. A* **392**, 1802 (1984).
- [23] D. Xiao, M.-C. Chang, and Q. Niu, *Rev. Mod. Phys.* **82**, 1959 (2010).
- [24] J. Zak, *Phys. Rev. Lett.* **62**, 2747 (1989).
- [25] L. A. Ponomarenko, R. V. Gorbachev, G. L. Yu, D. C. Elias, R. Jalil, A. A. Patel, A. Mishchenko, A. S. Mayorov, C. R. Woods, J. R. Wallbank, M. Mucha-Kruczynski, B. A. Piot, M. Potemski, I. V. Grigorieva, K. S. Novoselov, F. Guinea, V. I. Fal'ko, and A. K. Geim, *Nature* **497**, 594 (2013).
- [26] C. R. Dean, L. Wang, P. Maher, C. Forsythe, F. Ghahari, Y. Gao, J. Katoch, M. Ishigami, P. Moon, M. Koshino, T. Taniguchi, K. Watanabe, K. L. Shepard, J. Hone, and P. Kim, *Nature* **497**, 598 (2013).
- [27] M. Aidelsburger, M. Lohse, C. Schweizer, M. Atala, J. T. Barreiro, S. Nascimbène, N. R. Cooper, I. Bloch, and N. Goldman, *Nat. Phys.* **11**, 162 (2014).
- [28] N. Fläschner, B. S. Rem, M. Tarnowski, D. Vogel, D.-S. Lühmann, K. Sengstock, and C. Weitenberg, *Science* **352**, 1091 (2016).
- [29] M. Atala, M. Aidelsburger, J. T. Barreiro, D. Abanin, T. Kitagawa, E. Demler, and I. Bloch, *Nat. Phys.* **9**, 795 (2013).
- [30] M. Maffei, A. Dauphin, F. Cardano, M. Lewenstein, and P. Massignan, *New J. Phys.* **20**, 013023 (2018).
- [31] B. K. Stuhl, H.-I. Lu, L. M. Aycock, D. Genkina, and I. B. Spielman, *Science* **349**, 1514 (2015).
- [32] F. A. An, E. J. Meier, and B. Gadway, *Science Advances* **3**, e1602685 (2017).
- [33] E. J. Meier, F. A. An, and B. Gadway, *Nat. Commun.* **7**, 13986 (2016).
- [34] T. Ozawa and H. M. Price, *Nat. Rev. Phys.* **1**, 349 (2019).

- [35] N. R. Cooper, J. Dalibard, and I. B. Spielman, [Rev. Mod. Phys. \*\*91\*\*, 015005 \(2019\)](#).
- [36] A. J. Heeger, S. Kivelson, J. R. Schrieffer, and W. P. Su, [Rev. Mod. Phys. \*\*60\*\*, 781 \(1988\)](#).
- [37] H. Shirakawa, E. J. Louis, A. G. MacDiarmid, C. K. Chiang, and A. J. Heeger, [J. Chem. Soc., Chem. Commun. , 578 \(1977\)](#).
- [38] A. J. Heeger, [Rev. Mod. Phys. \*\*73\*\*, 681 \(2001\)](#).
- [39] S. Ryu, A. P. Schnyder, A. Furusaki, and A. W. W. Ludwig, [New J. Phys. \*\*12\*\*, 065010 \(2010\)](#).
- [40] D. S. Fisher, [Phys. Rev. B \*\*51\*\*, 6411 \(1995\)](#).
- [41] P. W. Anderson, [Phys. Rev. \*\*109\*\*, 1492 \(1958\)](#).
- [42] J. Li, R.-L. Chu, J. K. Jain, and S.-Q. Shen, [Phys. Rev. Lett. \*\*102\*\*, 136806 \(2009\)](#).
- [43] H. Jiang, L. Wang, Q.-f. Sun, and X. C. Xie, [Phys. Rev. B \*\*80\*\*, 165316 \(2009\)](#).
- [44] C. W. Groth, M. Wimmer, A. R. Akhmerov, J. Tworzydło, and C. W. J. Beenakker, [Phys. Rev. Lett. \*\*103\*\*, 196805 \(2009\)](#).
- [45] H.-M. Guo, G. Rosenberg, G. Refael, and M. Franz, [Phys. Rev. Lett. \*\*105\*\*, 216601 \(2010\)](#).
- [46] A. Altland, D. Bagrets, L. Fritz, A. Kamenev, and H. Schmiedt, [Phys. Rev. Lett. \*\*112\*\*, 206602 \(2014\)](#).
- [47] C. Liu, W. Gao, B. Yang, and S. Zhang, [Phys. Rev. Lett. \*\*119\*\*, 183901 \(2017\)](#).
- [48] E. J. Meier, F. A. An, A. Dauphin, M. Maffei, P. Massignan, T. L. Hughes, and B. Gadway, [Science \*\*362\*\*, 929 \(2018\)](#).
- [49] B. Gadway, [Phys. Rev. A \*\*92\*\*, 043606 \(2015\)](#).
- [50] “Fastest snail racing,” (1995).
- [51] E. J. Meier, F. A. An, and B. Gadway, [Phys. Rev. A \*\*93\*\*, 051602 \(2016\)](#).
- [52] Y. Aharonov, L. Davidovich, and N. Zagury, [Phys. Rev. A \*\*48\*\*, 1687 \(1993\)](#).
- [53] M. Karski, L. Förster, J.-M. Choi, A. Steffen, W. Alt, D. Meschede, and A. Widera, [Science \*\*325\*\*, 174 \(2009\)](#).
- [54] F. Zähringer, G. Kirchmair, R. Gerritsma, E. Solano, R. Blatt, and C. F. Roos, [Phys. Rev. Lett. \*\*104\*\*, 100503 \(2010\)](#).
- [55] A. Schreiber, K. N. Cassemiro, V. Potoček, A. Gábris, P. J. Mosley, E. Andersson, I. Jex, and C. Silberhorn, [Phys. Rev. Lett. \*\*104\*\*, 050502 \(2010\)](#).

- [56] M. A. Broome, A. Fedrizzi, B. P. Lanyon, I. Kassal, A. Aspuru-Guzik, and A. G. White, *Phys. Rev. Lett.* **104**, 153602 (2010).
- [57] F. Bloch, *Z. Phys.* **52**, 555 (1929).
- [58] C. Zener, *Proc. R. Soc. London Ser. A* **145**, 523 (1934).
- [59] C. Waschke, H. G. Roskos, R. Schwedler, K. Leo, H. Kurz, and K. Köhler, *Phys. Rev. Lett.* **70**, 3319 (1993).
- [60] M. Ben Dahan, E. Peik, J. Reichel, Y. Castin, and C. Salomon, *Phys. Rev. Lett.* **76**, 4508 (1996).
- [61] R. Sapienza, P. Costantino, D. Wiersma, M. Ghulinyan, C. J. Oton, and L. Pavesi, *Phys. Rev. Lett.* **91**, 263902 (2003).
- [62] J. Floß, A. Kamalov, I. S. Averbukh, and P. H. Bucksbaum, *Phys. Rev. Lett.* **115**, 203002 (2015).
- [63] P. M. Preiss, R. Ma, M. E. Tai, A. Lukin, M. Rispoli, P. Zupancic, Y. Lahini, R. Islam, and M. Greiner, *Science* **347**, 1229 (2015).
- [64] I. Solomon, *Phys. Rev. Lett.* **2**, 301 (1959).
- [65] F. A. An, E. J. Meier, and B. Gadway, *Phys. Rev. X* **8**, 031045 (2018).
- [66] F. A. An, E. J. Meier, J. Ang'ong'a, and B. Gadway, *Phys. Rev. Lett.* **120**, 040407 (2018).
- [67] R. P. Smith, R. L. D. Campbell, N. Tammuz, and Z. Hadzibabic, *Phys. Rev. Lett.* **106**, 250403 (2011).
- [68] R. Ozeri, N. Katz, J. Steinhauer, and N. Davidson, *Rev. Mod. Phys.* **77**, 187 (2005).
- [69] M. Anderlini, P. J. Lee, B. L. Brown, J. Sebby-Strabley, W. D. Phillips, and J. V. Porto, *Nature* **448**, 452 (2007).
- [70] A. M. Kaufman, B. J. Lester, M. Foss-Feig, M. L. Wall, A. M. Rey, and C. A. Regal, *Nature* **527**, 208 (2015).
- [71] J. Larson, A. Collin, and J.-P. Martikainen, *Phys. Rev. A* **79**, 033603 (2009).
- [72] J. Stenger, S. Inouye, A. P. Chikkatur, D. M. Stamper-Kurn, D. E. Pritchard, and W. Ketterle, *Phys. Rev. Lett.* **82**, 4569 (1999).
- [73] R. Lopes, C. Eigen, A. Barker, K. G. H. Viebahn, M. Robert-de Saint-Vincent, N. Navon, Z. Hadzibabic, and R. P. Smith, *Phys. Rev. Lett.* **118**, 210401 (2017).
- [74] S. Baharian and G. Baym, *Phys. Rev. A* **87**, 013619 (2013).

- [75] L. Fallani, L. De Sarlo, J. E. Lye, M. Modugno, R. Saers, C. Fort, and M. Inguscio, *Phys. Rev. Lett.* **93**, 140406 (2004).
- [76] S. B. Koller, E. A. Goldschmidt, R. C. Brown, R. Wyllie, R. M. Wilson, and J. V. Porto, *Phys. Rev. A* **94**, 063634 (2016).
- [77] C. Chin, R. Grimm, P. Julienne, and E. Tiesinga, *Rev. Mod. Phys.* **82**, 1225 (2010).
- [78] C. D'Errico, M. Zaccanti, M. Fattori, G. Roati, M. Inguscio, G. Modugno, and A. Simoni, *New J. Phys.* **9**, 223 (2007).
- [79] A. Keshet and W. Ketterle, *Rev. Sci. Instrum.* **84**, 015105 (2013).
- [80] C. Wieman and T. W. Hänsch, *Phys. Rev. Lett.* **36**, 1170 (1976).
- [81] S. N. Bose, *Z. Phys.* **26**, 178 (1924).
- [82] A. Einstein, *Preuss. Akad. Wiss* **261** (1924).
- [83] M. H. Anderson, J. R. Ensher, M. R. Matthews, C. E. Wieman, and E. A. Cornell, *Science* **269**, 198 (1995).
- [84] K. B. Davis, M. O. Mewes, M. R. Andrews, N. J. van Druten, D. S. Durfee, D. M. Kurn, and W. Ketterle, *Phys. Rev. Lett.* **75**, 3969 (1995).
- [85] C. C. Bradley, C. A. Sackett, J. J. Tollett, and R. G. Hulet, *Phys. Rev. Lett.* **79**, 1170 (1997).
- [86] V. Bagnato, D. E. Pritchard, and D. Kleppner, *Phys. Rev. A* **35**, 4354 (1987).
- [87] D. A. Steck, available online at [steck.us/alkalidata](http://steck.us/alkalidata) (revision 2.1.5, 13 January 2015).
- [88] S. Bize, Y. Sortais, M. S. Santos, C. Mandache, A. Clairon, and C. Salomon, *Europhys. Lett* **45**, 558 (1999).
- [89] J. Ye, S. Swartz, P. Jungner, and J. L. Hall, *Opt. Lett.* **21**, 1280 (1996).
- [90] P. D. Lett, R. N. Watts, C. I. Westbrook, W. D. Phillips, P. L. Gould, and H. J. Metcalf, *Phys. Rev. Lett.* **61**, 169 (1988).
- [91] S. J. Park, J. Noh, and J. Mun, *Opt. Commun.* **285**, 3950 (2012).
- [92] W. Petrich, M. H. Anderson, J. R. Ensher, and E. A. Cornell, *J. Opt. Soc. Am. B* **11**, 1332 (1994).
- [93] C. G. Townsend, N. H. Edwards, C. J. Cooper, K. P. Zetie, C. J. Foot, A. M. Steane, P. Szriftgiser, H. Perrin, and J. Dalibard, *Phys. Rev. A* **52**, 1423 (1995).
- [94] W. Ketterle, K. B. Davis, M. A. Joffe, A. Martin, and D. E. Pritchard, *Phys. Rev. Lett.* **70**, 2253 (1993).

- [95] M. H. Anderson, W. Petrich, J. R. Ensher, and E. A. Cornell, *Phys. Rev. A* **50**, R3597 (1994).
- [96] R. Grimm, M. Weidemüller, and Y. B. Ovchinnikov, *Advances in Atomic Molecular and Optical Physics* **42**, 95 (2000).
- [97] C. J. Foote, *Atomic Physics* (Oxford University Press, 2014).
- [98] T. Kraemer, J. Herbig, M. Mark, T. Weber, C. Chin, H.-C. Nägerl, and R. Grimm, *App. Phys. B* **79**, 1013 (2004).
- [99] W. Petrich, M. H. Anderson, J. R. Ensher, and E. A. Cornell, *Phys. Rev. Lett.* **74**, 3352 (1995).
- [100] L. De Sarlo, P. Maioli, G. Barontini, J. Catani, F. Minardi, and M. Inguscio, *Phys. Rev. A* **75**, 022715 (2007).
- [101] M. Prevedelli, F. S. Cataliotti, E. A. Cornell, J. R. Ensher, C. Fort, L. Ricci, G. M. Tino, and M. Inguscio, *Phys. Rev. A* **59**, 886 (1999).
- [102] H. Wang, A. N. Nikolov, J. R. Ensher, P. L. Gould, E. E. Eyler, W. C. Stwalley, J. P. Burke, J. L. Bohn, C. H. Greene, E. Tiesinga, C. J. Williams, and P. S. Julienne, *Phys. Rev. A* **62**, 052704 (2000).
- [103] M. Ueda and A. J. Leggett, *Phys. Rev. Lett.* **80**, 1576 (1998).
- [104] Y. Kagan, G. V. Shlyapnikov, and J. T. M. Walraven, *Phys. Rev. Lett.* **76**, 2670 (1996).
- [105] J. M. Gerton, D. Strekalov, I. Prodan, and R. G. Hulet, *Nature* **408**, 692 (2000).
- [106] J. L. Roberts, N. R. Claussen, S. L. Cornish, E. A. Donley, E. A. Cornell, and C. E. Wieman, *Phys. Rev. Lett.* **86**, 4211 (2001).
- [107] G. Roati, M. Zaccanti, C. D'Errico, J. Catani, M. Modugno, A. Simoni, M. Inguscio, and G. Modugno, *Phys. Rev. Lett.* **99**, 010403 (2007).
- [108] C. Fort, A. Bambini, L. Cacciapuoti, F. S. Cataliotti, M. Prevedelli, G. M. Tino, and M. Inguscio, *Eur. Phys. J. D* **3**, 113 (1998).
- [109] M. Landini, S. Roy, L. Carcagní, D. Trypogeorgos, M. Fattori, M. Inguscio, and G. Modugno, *Phys. Rev. A* **84**, 043432 (2011).
- [110] V. Gokhroo, G. Rajalakshmi, R. K. Easwaran, and C. S. Unnikrishnan, *J. Phys. B: At. Mol. Opt. Phys.* **44**, 115307 (2011).
- [111] D. Nath, R. K. Easwaran, G. Rajalakshmi, and C. S. Unnikrishnan, *Phys. Rev. A* **88**, 053407 (2013).

- [112] G. Salomon, L. Fouché, P. Wang, A. Aspect, P. Bouyer, and T. Bourdel, *Europhys. Lett.* **104**, 63002 (2013).
- [113] M. Landini, S. Roy, G. Roati, A. Simoni, M. Inguscio, G. Modugno, and M. Fattori, *Phys. Rev. A* **86**, 033421 (2012).
- [114] M. Inguscio and L. Fallani, *Atomic Physics* (Oxford University Press, 2013).
- [115] T. G. Tiecke, available online at [tobiastiecke.nl/archive/PotassiumProperties.pdf](http://tobiastiecke.nl/archive/PotassiumProperties.pdf) (revision 1.03, June 2019).
- [116] S. Falke, E. Tiemann, C. Lisdat, H. Schnatz, and G. Grosche, *Phys. Rev. A* **74**, 032503 (2006).
- [117] E. Arimondo, M. Inguscio, and P. Violino, *Rev. Mod. Phys.* **49**, 31 (1977).
- [118] A. Hemmerich, M. Weidemüller, T. Esslinger, C. Zimmermann, and T. Hänsch, *Phys. Rev. Lett.* **75**, 37 (1995).
- [119] D. Boiron, C. Triché, D. R. Meacher, P. Verkerk, and G. Grynberg, *Phys. Rev. A* **52**, R3425 (1995).
- [120] C. K. Chiang, C. R. Fincher, Y. W. Park, A. J. Heeger, H. Shirakawa, E. J. Louis, S. C. Gau, and A. G. MacDiarmid, *Phys. Rev. Lett.* **39**, 1098 (1977).
- [121] R. Jackiw and C. Rebbi, *Phys. Rev. D* **13**, 3398 (1976).
- [122] S. Fölling, S. Trotzky, P. Cheinet, M. Feld, R. Saers, A. Widera, T. Müller, and I. Bloch, *Nature* **448**, 1029 (2007).
- [123] J. Sebby-Strabley, M. Anderlini, P. S. Jessen, and J. V. Porto, *Phys. Rev. A* **73**, 033605 (2006).
- [124] M. Lohse, C. Schweizer, O. Zilberberg, M. Aidelsburger, and I. Bloch, *Nat. Phys.* **12**, 350 (2016).
- [125] S. Nakajima, T. Tomita, S. Taie, T. Ichinose, H. Ozawa, L. Wang, M. Troyer, and Y. Takahashi, *Nat. Phys.* **12**, 296 (2016).
- [126] H.-I. Lu, M. Schemmer, L. M. Ayccock, D. Genkina, S. Sugawa, and I. B. Spielman, *Phys. Rev. Lett.* **116**, 200402 (2016).
- [127] M. Leder, C. Grossert, M. Sitta, Lukas Genske, A. Rosch, and M. Weitz, *Nat. Commun.* **7**, 13112 (2016).
- [128] A. Szameit and S. Nolte, *J. Phys. B* **43**, 163001 (2010).
- [129] M. Hafezi, S. Mittal, J. Fan, A. Migdall, and J. M. Taylor, *Nat. Photonics* **7**, 1001 (2013).

- [130] M. C. Rechtsman, J. M. Zeuner, Y. Plotnik, Y. Lumer, D. Podolsky, F. Dreisow, S. Nolte, M. Segev, and A. Szameit, *Nature* **496**, 196 (2013).
- [131] T. Kitagawa, M. A. Broome, A. Fedrizzi, M. S. Rudner, E. Berg, I. Kassal, A. Aspuru-Guzik, E. Demler, and A. G. White, *Nat. Commun.* **3**, 882 (2012).
- [132] T. Kitagawa, M. S. Rudner, E. Berg, and E. Demler, *Phys. Rev. A* **82**, 033429 (2010).
- [133] Y. E. Kraus, Y. Lahini, Z. Ringel, M. Verbin, and O. Zilberberg, *Phys. Rev. Lett.* **109**, 106402 (2012).
- [134] M. Verbin, O. Zilberberg, Y. E. Kraus, Y. Lahini, and Y. Silberberg, *Phys. Rev. Lett.* **110**, 076403 (2013).
- [135] I. Mondragon-Shem, T. L. Hughes, J. Song, and E. Prodan, *Phys. Rev. Lett.* **113**, 046802 (2014).
- [136] D. R. Hofstadter, *Phys. Rev. B* **14**, 2239 (1976).
- [137] A. Altland and M. R. Zirnbauer, *Phys. Rev. B* **55**, 1142 (1997).
- [138] L. Sanchez-Palencia and M. Lewenstein, *Nat. Phys.* **6**, 87 (2010).
- [139] N. Goldman, J. C. Budich, and P. Zoller, *Nat. Phys.* **12**, 639 (2016).
- [140] F. Evers and A. D. Mirlin, *Rev. Mod. Phys.* **80**, 1355 (2008).
- [141] X.-L. Qi and S.-C. Zhang, *Rev. Mod. Phys.* **83**, 1057 (2011).
- [142] Y. L. Chen, J. G. Analytis, J.-H. Chu, Z. K. Liu, S.-K. Mo, X. L. Qi, H. J. Zhang, D. H. Lu, X. Dai, Z. Fang, S. C. Zhang, I. R. Fisher, Z. Hussain, and Z.-X. Shen, *Science* **325**, 178 (2009).
- [143] E. Abrahams, P. W. Anderson, D. C. Licciardello, and T. V. Ramakrishnan, *Phys. Rev. Lett.* **42**, 673 (1979).
- [144] H. Aoki, *J. Phys. C: Solid State Phys.* **16**, L205 (1983).
- [145] D. S. Fisher, *Phys. Rev. B* **50**, 3799 (1994).
- [146] P. Titum, N. H. Lindner, M. C. Rechtsman, and G. Refael, *Phys. Rev. Lett.* **114**, 056801 (2015).
- [147] C. G. Velasco and B. Paredes, *Phys. Rev. Lett.* **119**, 115301 (2017).
- [148] J. Billy, V. Josse, Z. Zuo, A. Bernard, B. Hambrecht, P. Lugan, D. Clément, L. Sanchez-Palencia, P. Bouyer, and A. Aspect, *Nature* **453**, 891 (2008).
- [149] G. Roati, C. D’Errico, L. Fallani, M. Fattori, C. Fort, M. Zaccanti, G. Modugno, M. Modugno, and M. Inguscio, *Nature* **453**, 895 (2008).

- [150] A. Altland, D. Bagrets, and A. Kamenev, *Phys. Rev. B* **91**, 085429 (2015).
- [151] D. J. Thouless, *Phys. Rev. B* **27**, 6083 (1983).
- [152] M. Switkes, C. M. Marcus, K. Campman, and A. C. Gossard, *Science* **283**, 1905 (1999).
- [153] M. D. Blumenthal, B. Kaestner, L. Li, S. Giblin, T. J. B. M. Janssen, M. Pepper, D. Anderson, G. Jones, and D. A. Ritchie, *Nat. Phys.* **3**, 343 (2007).
- [154] H.-I. Lu, M. Schemmer, L. M. Aycock, D. Genkina, S. Sugawa, and I. B. Spielman, *Phys. Rev. Lett.* **116**, 200402 (2016).
- [155] E. J. Meier, J. Ang'ong'a, F. A. An, and B. Gadway, *Phys. Rev. A* **100**, 013623 (2019).
- [156] F. Haake, *Quantum Signatures of Chaos*. (Springer, 2001).
- [157] T. Hogg and B. A. Huberman, *Phys. Rev. Lett.* **48**, 711 (1982).
- [158] E. J. Galvez, B. E. Sauer, L. Moorman, P. M. Koch, and D. Richards, *Phys. Rev. Lett.* **61**, 2011 (1988).
- [159] M. Courtney, N. Spellmeyer, H. Jiao, and D. Kleppner, *Phys. Rev. A* **51**, 3604 (1995).
- [160] F. L. Moore, J. C. Robinson, C. F. Bharucha, B. Sundaram, and M. G. Raizen, *Phys. Rev. Lett.* **75**, 4598 (1995).
- [161] W. K. Hensinger, H. Häffner, A. Browaeys, N. R. Heckenberg, K. Helmerson, C. McKenzie, G. J. Milburn, S. L. Phillips, W. D. Rolston, H. Rubinsztein-Dunlop, and B. Urcroft, *Nature* **412**, 52 (2001).
- [162] D. A. Steck, W. H. Oskay, and M. G. Raizen, *Science* **293**, 274 (2001).
- [163] J.-C. Garreau, *C. R. Phys.* **18**, 31 (2017).
- [164] B. Gadway, J. Reeves, L. Krinner, and D. Schneble, *Phys. Rev. Lett.* **110**, 190401 (2013).
- [165] J. L. Bohn, A. V. Avdeenko, and M. P. Deskevich, *Phys. Rev. Lett.* **89**, 203202 (2002).
- [166] A. Frisch, M. Mark, K. Aikawa, F. Ferlaino, J. L. Bohn, C. Makrides, A. Petrov, and S. Kotochigova, *Nature* **507**, 475 (2014).
- [167] S. Chaudhury, A. Smith, B. E. Anderson, S. Ghose, and P. S. Jessen, *Nature* **461**, 768 (2009).
- [168] M. Neeley, M. Ansmann, R. C. Bialczak, M. Hofheinz, E. Lucero, A. D. O'Connell, D. Sank, H. Wang, J. Wenner, A. N. Cleland, M. R. Geller, and J. M. Martinis, *Science* **325**, 722 (2009).

- [169] J. Tomkovič, W. Muessel, H. Strobel, S. Löck, P. Schlagheck, R. Ketzmerick, and M. K. Oberthaler, *Phys. Rev. A* **95**, 011602 (2017).
- [170] A. Facon, E.-K. Dietsche, D. Grosso, S. Haroche, J.-M. Raimond, M. Brune, and S. Gleyzes, *Nature* **535**, 262 (2016).
- [171] W. H. Zurek and J. P. Paz, *Phys. Rev. Lett.* **72**, 2508 (1994).
- [172] K. Furuya, M. C. Nemes, and G. Q. Pellegrino, *Phys. Rev. Lett.* **80**, 5524 (1998).
- [173] M. Kitagawa and M. Ueda, *Phys. Rev. A* **47**, 5138 (1993).
- [174] C. Neill, P. Roushan, M. Fang, Y. Chen, M. Kolodrubetz, Z. Chen, A. Megrant, R. Barends, B. Campbell, B. Chiaro, A. Dunsworth, E. Jeffrey, J. Kelly, J. Mutus, P. J. J. O'Malley, C. Quintana, D. Sank, A. Vainsencher, J. Wenner, T. C. White, A. Polkovnikov, and J. M. Martinis, *Nat. Phys.* **12**, 1037 (2016).
- [175] S. Chaudhury, S. Merkel, T. Herr, A. Silberfarb, I. H. Deutsch, and P. S. Jessen, *Phys. Rev. Lett.* **99**, 163002 (2007).
- [176] J. G. Bohnet, B. C. Sawyer, J. W. Britton, M. L. Wall, A. M. Rey, M. Foss-Feig, and J. J. Bollinger, *Science* **352**, 1297 (2016).
- [177] B. Swingle, G. Bentsen, M. Schleier-Smith, and P. Hayden, *Phys. Rev. A* **94**, 040302 (2016).
- [178] S. H. Shenker and D. Stanford, *J. High Energy Phys.* **2014**, 67 (2014).
- [179] Y. Sekino and L. Susskind, *J. High Energy Phys.* **2008**, 065 (2008).
- [180] P. Hosur, X.-L. Qi, D. A. Roberts, and B. Yoshida, *J. High Energy Phys.* **2016**, 4 (2016).
- [181] R. Fan, P. Zhang, H. Shen, and H. Zhai, *Sci. Bull.* **62**, 707 (2017).
- [182] X. Chen, T. Zhou, D. A. Huse, and E. Fradkin, *Annal. der Phys.* **529**, 1600332 (2017).
- [183] M. Gärttner, J. G. Bohnet, A. Safavi-Naini, M. L. Wall, J. J. Bollinger, and A. M. Rey, *Nat. Phys.* **13**, 781 (2017).
- [184] K. A. Landsman, C. Figgatt, T. Schuster, N. M. Linke, B. Yoshida, N. Y. Yao, and C. Monroe, *Nature* **567**, 61 (2019).
- [185] J. Li, R. Fan, H. Wang, B. Ye, B. Zeng, H. Zhai, X. Peng, and J. Du, *Phys. Rev. X* **7**, 031011 (2017).
- [186] K. X. Wei, C. Ramanathan, and P. Cappellaro, *Phys. Rev. Lett.* **120**, 070501 (2018).
- [187] E. B. Rozenbaum, S. Ganeshan, and V. Galitski, *Phys. Rev. Lett.* **118**, 086801 (2017).

- [188] R. Keil, A. Perez-Leija, F. Dreisow, M. Heinrich, H. Moya-Cessa, S. Nolte, D. N. Christodoulides, and A. Szameit, *Phys. Rev. Lett.* **107**, 103601 (2011).
- [189] M. Kuś, R. Scharf, and F. Haake, *Z. Phys. B* **66**, 129 (1987).
- [190] A. P. Lund, M. J. Bremner, and T. C. Ralph, *npj Quant. Inf.* **3**, 15 (2017).
- [191] E. Torrontegui, S. Ibáñez, S. Martínez-Garaot, M. Modugno, A. del Campo, D. Guéry-Odelin, A. Ruschhaupt, X. Chen, and J. G. Muga, in *Advances in Atomic, Molecular, and Optical Physics*, Vol. 62, edited by E. Arimondo, P. R. Berman, and C. C. Lin (Academic Press, 2013) pp. 117 – 169.
- [192] D. Sels and A. Polkovnikov, *Proc. Natl. Acad. Sci.* **114**, E3909 (2017).
- [193] M. Demirplak and S. A. Rice, *J. Phys. Chem. A* **107**, 9937 (2003).
- [194] M. Demirplak and S. A. Rice, *J. Phys. Chem. B* **109**, 6838 (2005).
- [195] M. V. Berry, *J. Phys. A Math. Theor.* **42**, 365303 (2009).
- [196] X. Chen, I. Lizuain, A. Ruschhaupt, D. Guéry-Odelin, and J. G. Muga, *Phys. Rev. Lett.* **105**, 123003 (2010).
- [197] S. Deffner, C. Jarzynski, and A. del Campo, *Phys. Rev. X* **4**, 021013 (2014).
- [198] A. del Campo, *Phys. Rev. Lett.* **111**, 100502 (2013).
- [199] S. Masuda, U. Güngördü, X. Chen, T. Ohmi, and M. Nakahara, *Phys. Rev. A* **93**, 013626 (2016).
- [200] T. Ollikainen, S. Masuda, M. Möttönen, and M. Nakahara, *Phys. Rev. A* **95**, 013615 (2017).
- [201] J. Zhang, J. H. Shim, I. Niemeyer, T. Taniguchi, T. Teraji, H. Abe, S. Onoda, T. Yamamoto, T. Ohshima, J. Isoya, and D. Suter, *Phys. Rev. Lett.* **110**, 240501 (2013).
- [202] M. G. Bason, M. Viteau, N. Malossi, P. Huillery, E. Arimondo, D. Ciampini, R. Fazio, V. Giovannetti, R. Mannella, and O. Morsch, *Nat. Phys.* **8**, 147 (2012).
- [203] T. Wang, Z. Zhang, L. Xiang, Z. Jia, P. Duan, W. Cai, Z. Gong, Z. Zong, M. Wu, J. Wu, L. Sun, Y. Yin, and G. Guo, *New J. Phys.* **20**, 065003 (2018).
- [204] Z. Zhang, T. Wang, L. Xiang, Z. Jia, P. Duan, W. Cai, Z. Zhan, Z. Zong, J. Wu, L. Sun, Y. Yin, and G. Guo, *New J. Phys.* **20**, 085001 (2018).
- [205] Z. Zhang, T. Wang, L. Xiang, J. Yao, J. Wu, and Y. Yin, *Phys. Rev. A* **95**, 042345 (2017).
- [206] M. D. Schroer, M. H. Kolodrubetz, W. F. Kindel, M. Sandberg, J. Gao, M. R. Vissers, D. P. Pappas, A. Polkovnikov, and K. W. Lehnert, *Phys. Rev. Lett.* **113**, 050402 (2014).

- [207] M. Kolodrubetz, [Phys. Rev. Lett. \*\*117\*\*, 015301 \(2016\)](#).
- [208] V. Gritsev and A. Polkovnikov, [Proc. Nat. Acad. Sci. \*\*109\*\*, 6457 \(2012\)](#).
- [209] S. Sugawa, F. Salces-Carcoba, A. R. Perry, Y. Yue, and I. B. Spielman, [Science \*\*360\*\*, 1429 \(2018\)](#).
- [210] P. Roushan, C. Neill, Y. Chen, M. Kolodrubetz, C. Quintana, N. Leung, M. Fang, R. Barends, B. Campbell, Z. Chen, B. Chiaro, A. Dunsworth, E. Jeffrey, J. Kelly, A. Megrant, J. Mutus, P. J. J. O'Malley, D. Sank, A. Vainsencher, J. Wenner, T. White, A. Polkovnikov, A. N. Cleland, and J. M. Martinis, [Nature \*\*515\*\*, 241 \(2014\)](#).
- [211] P. J. D. Crowley, I. Martin, and A. Chandran, [Phys. Rev. B \*\*99\*\*, 064306 \(2019\)](#).
- [212] A. Baksic, H. Ribeiro, and A. A. Clerk, [Phys. Rev. Lett. \*\*116\*\*, 230503 \(2016\)](#).
- [213] A. C. Santos and M. S. Sarandy, [Sci. Reports \*\*5\*\*, 15775 \(2015\)](#), article.
- [214] H. Saberi, T. c. v. Opatrný, K. Mølmer, and A. del Campo, [Phys. Rev. A \*\*90\*\*, 060301 \(2014\)](#).
- [215] M. Bukov, D. Sels, and A. Polkovnikov, [Phys. Rev. X \*\*9\*\*, 011034 \(2019\)](#).
- [216] S. Campbell, G. De Chiara, M. Paternostro, G. M. Palma, and R. Fazio, [Phys. Rev. Lett. \*\*114\*\*, 177206 \(2015\)](#).
- [217] T. Hatomura, [J. Phys. Soc. Japan \*\*86\*\*, 094002 \(2017\)](#).
- [218] T. Hatomura, [New J. Phys. \*\*20\*\*, 015010 \(2018\)](#).
- [219] D. Sels, [Phys. Rev. A \*\*97\*\*, 040302 \(2018\)](#).
- [220] J. J. W. H. Sørensen, M. K. Pedersen, M. Munch, P. Haikka, J. H. Jensen, T. Planke, M. G. Andreassen, M. Gajdacz, K. Mølmer, A. Lieberoth, and J. F. Sherson, [Nature \*\*532\*\*, 210 \(2016\)](#).
- [221] G. Ritt, G. Cennini, C. Geckeler, and M. Weitz, [App. Phys. B \*\*79\*\*, 363 \(2004\)](#).
- [222] T. Uehlinger, *A 2D Magneto-Optical Trap as a High-Flux Source of Cold Potassium Atoms*, [Ph.D. thesis](#), Institute for Quantum Electronics, Department of Physics, Swiss Federal Institute of Technology Zurich (2008).
- [223] D. Herceg, A. Juhas, and M. Milutinov, [Facta universitatis - series: Electronics and Energetics \*\*22\*\*, 285 \(2009\)](#).
- [224] J. Johansson, P. Nation, and F. Nori, [Computer Phys. Commun. \*\*184\*\*, 1234 \(2013\)](#).
- [225] P. Weinberg and M. Bukov, [SciPost Phys. \*\*2\*\*, 003 \(2017\)](#).

# Index

- ac Stark Shift, 65
- Acousto-Optic Modulators, 48
- Alkali Metal Dispensers, 45
- Analog Isolation, 161
- Andor Neo Camera Program, 166
- Arbitrary Waveforms, 88
  - Arbitrary Waveform Generator, 51
  - Calibration, 91
  - Example Code, 89
  - Fourier Transform, 88
- Band Structure, 2
- Bloch Oscillations, 31
- Bose–Einstein Condensate, 53
  - Phase-Space Density, 53
- Bragg Diffraction, 20
- Camera Operation, 92
- Chaos, 125
- Cicero Word Generator, 47
- Compressed Magneto-Optical Trap, 62
- Continuous-Time Quantum Walk, 29
- Counter-Diabatic Driving, 143
  - Defining Equations, 147
  - Dressed States, 157
  - Eigenstate Preparation, 152
  - Lattice Tilt Inversions, 149
  - Phase Structure, 155
- Cycle Time, 46
- Cycling Transition
  - $^{87}\text{Rb}$ , 55
- Dark Spontaneous-Force Optical Trap, 62
- Disordered SSH Model, 109
  - Topological Anderson Insulator, 110
  - Topological Anderson Insulator Observation, 116
  - Topological Charge Pumping, 120
  - Topological Transitions, 113
- Evaporative Cooling, 65
  - $^{39}\text{K}$ , 69
- Feshbach Resonance, 69, 71
- Fourier Transform, 10
- Gray Molasses, 70, 86
- Gross–Pitaevskii Equation, 184
- Ideal Simulations, 178
- Imaging, 67, 93
  - Optical Depth, 93
  - Processing, 93
- Interacting Simulations, 184
- Interacting Su–Schrieffer–Heeger Model, 123
- Lasers, 48
  - Locking (Frequency Stabilization), 50
  - Offset Locking, 50
  - Polarization Spectroscopy, 50
- Magnetic Field Systems for  $^{39}\text{K}$ , 75
  - Atom Source, 75
  - Science Cell Feshbach Coil, 82, 173
  - Science Cell MOT Coil, 81
  - Science Cell Shimming Fields, 79
  - Summary of Values, 84
- Magnetic Levitation, 64
- Magneto-Optical Trap, 55
  - $^{39}\text{K}$ , 74
  - $^{87}\text{Rb}$  2D, 58
  - $^{87}\text{Rb}$  3D, 56
- Momentum-Space Lattice, 19
  - Experimental Realization, 51
  - Interactions, 36
  - Limitations, 26
  - Tight-Binding Approximation, 24

- Tunability, 24
- Tunneling Limitation, 23
- Next-Nearest-Neighbor Tunneling, 33
  - Unintentional Couplings, 34
- Non-Approximated Simulations, 181
- Offset Lock, 164
- Optical Dipole Trap, 65
- Optical Molasses, 56
- Optical Pumping, 63
- Outline, 18
- Phase Reversal, 32
- PID Circuit, 49
- Python Simulations, 187
- QuSpin, 189
- QuTiP, 187
- Radio Frequency Control
  - Crystal Oscillator, 50
  - Switches, 51
  - Voltage Controlled Oscillator, 50
  - Voltage Variable Attenuators, 51
- Repump Transition
  - $^{87}\text{Rb}$ , 56
- Rotating Wave Approximation, 22
- Scattering Length, 69, 72
- Shutters, 49
- Simulation Techniques, 177
  - Ideal Simulations, 178
  - Interacting Simulations, 184
  - Non-Approximated Simulations, 181
  - Python Simulations, 187
    - QuSpin, 189
    - QuTiP, 187
- Square Coil Magnetic Field Estimation, 175
- Su–Schrieffer–Heeger Model, 2, 8, 97
  - Adiabatic Preparation, 105
  - Band Gap, 12
  - Band Structure, 12
  - Chemical Basis, 9
  - Edge States, 14
  - Phase Sensitive Injection, 102
  - Single-Site Injection, 100
  - Winding Number, 13
- Sympathetic Cooling of  $^{39}\text{K}$ , 69
- Synthetic Dimension, 3, 19
- Synthetic Spins
  - Chaotic Behavior, 138
  - Coherent Spin States, 128
  - Husimi-Q Distribution, 133
  - Out-of-Time-Ordered Correlation Function, 136
  - Rotations, 129
  - Squeezing, 135
  - State Measurement, 132
  - State Preparation, 131
- The Kicked-Top Model, 127
- Time-Dependent Lattice Corrections, 191
- Topological Anderson Insulator, 17, 110
  - Observation of, 116
- Topology, 4
  - Möbius Strip, 4
  - Techniques for Measuring, 6
  - Topological Index, 4
- Vacuum Chamber, 42
  - Cleaning and Baking, 44
- William Morong, 1